Title	Damage and permeability in linerless composite cryogenic tanks
Author(s)	Grogan, David M.
Publication Date	2015-09-29
Item record	http://hdl.handle.net/10379/5279

Damage and permeability in linerless composite cryogenic tanks

David M. Grogan

Supervisors: Prof. Sean B. Leen and Prof. Conchúr M. Ó Brádaigh

A thesis submitted to the National University of Ireland as fulfilment of the requirements for the Degree of Doctor of Philosophy.

Mechanical Engineering,

National University of Ireland, Galway.

September 2015

Contents

Contents

Contents

Contents

Abstract

Carbon fibre reinforced polymers (CFRP) are one of the prospective material families being investigated for use in the fuel tanks of future reusable launch vehicles (RLVs). The extreme cryogenic thermo-mechanical loading that these structures experience can lead to damage build-up in the CFRP in the form of microcracking and delamination, which can lead to increased laminate permeability. This work presents a combined experimental and numerical approach for predicting damage and permeability in composite laminates and linerless cryogenic tanks.

A novel extended finite element (XFEM)-based methodology for the combined simulation and prediction of thermal fatigue delamination for identification of delaminated crack opening displacement (DCOD) and, hence, composite laminate permeability is presented first. The methodology is validated through simulation of standardised static and fatigue delamination test methods, using computationally efficient modelling techniques. Delamination growth in a quasi-isotropic laminate under cryogenic fatigue loading is used to examine the effects of initial interlaminar defects on subsequent crack growth, as well as the relationship between delamination length and material permeability based on DCOD values predicted by the new methodology.

An experimental investigation into damage formation in CF /PEEK laminates before, during and after cryogenic cycling, using optical microscopy and three-dimensional X-ray computed tomography (CT), is conducted. Thicker laminates were found to exhibit significantly greater microcrack density and delamination when compared to thinner laminates, with lay-up and material type also being important contributing

Abstract

factors. Microcracking induced by thermal residual stresses was also observed in thicker laminates following processing. 3-D rendering software was used to establish the presence of through thickness crack networks within the laminates, as well as the extent of cracking through the specimen width. Crack opening in inner and off-axis ply groups was found to be significantly less than in outer plies, indicating the importance of these plies for limiting laminate permeability. The presence of voids was found to influence crack nucleation and growth paths within the laminates, with full void volume characterisation presented.

A novel computational methodology for predicting three-dimensional microcracking and permeability in composite laminates is presented based on experimental observations and established numerical methods. The methodology simulates (i) microcrack initiation and propagation using XFEM, and (ii) delamination, using a mixed-mode cohesive zone model. Random microcrack initiation is modelled using a random (Weibull) distribution of fracture strengths. The Weibull distribution is adjusted to account for specimen volume, allowing mesh independent crack density predictions. An alternative method is also investigated, based on an elemental representation of defects using measured void geometry. The predicted microcracking and damage distributions are shown to correlate closely with 3-D X-ray CT scans of cryogenically cycled specimens. Crack opening displacements are consistent with laminate test measurements. Permeabilities, based on the dimensions of the leak paths, were found to be within the measured range for various CF/PEEK materials.

Finally, a combined experimental and numerical approach to the design and analysis of tape-laid composite cryogenic tanks is presented. A detailed material and defect characterisation of automated tape-laid CF/PEEK was undertaken using optical micrography and 3-D X-ray CT, as well as cryogenic testing to investigate damage formation. Resulting material data is used as input to a novel XFEM-cohesive zone methodology which is used to predict intra- and inter-ply damage in an internally pressurised cryogenic tank. An optimised tank lay-up is presented and tested using the numerical method to ensure resistance to microcrack formation and fuel leakage through the tanks walls under operating loads.

Acknowledgements

Acknowledgements

At NUI Galway I would like to thank Justin Dunleavy for his excellent work in developing a cryogenic fatigue rig for use in this work, with help from the technical staff including William Kelly and Pat Kelly. Thanks to Dr. Pat McGarry for his support as part of my graduate research committee and for his direct contribution to the development of novel numerical methods in this work. I would like to thank all my friends at NUI Galway, who were always ready to provide a helping hand, as well as my friends in the outside world, for providing the tonic to academic life. In particular, thanks to Brendan, who over the last four years has been with me everywhere from canal boats in Amsterdam to mustangs in Texas.

Finally, to my parents, brothers James and Niall and long-suffering girlfriend Eimear: your technical, emotional and moral support underpins all my work.

List of Publications

The work presented in this thesis comprises the following journal publications:

Chapter 3: Grogan D.M., Leen S.B. & Ó Brádaigh C.M. An XFEM-based methodology for fatigue delamination and permeability of composites. *Composite Structures*, **107**, 205-218, 2014.

Chapter 4: Grogan D.M., Leen S.B., Semprimoschnig C.O.A. & Ó Brádaigh C.M. Damage characterisation of cryogenically cycled carbon fibre/PEEK laminates. *Composites Part A: Applied Science and Manufacturing*, **66**, 237-250, 2014.

Chapter 5: Grogan D.M., Ó Brádaigh C.M. & Leen S.B. A combined XFEM and cohesive zone model for composite laminate microcracking and permeability. *Composite Structures*, **120**, 246-261, 2015.

Chapter 6: Grogan D.M., McGarry J.P., Ó Brádaigh C.M. & Leen S.B. Damage and permeability in tape-laid thermoplastic composite cryogenic tanks. *Composites Part A: Applied Science and Manufacturing*, **78**, 390-402, 2015.

Note: D.M. Grogan is the primary author for each publication

1. Introduction

1.1 Chapter summary

An order of magnitude drop in launch costs is an objective of the next generation of space launch vehicles. The reduction of vehicle structural weight is one of the ways of achieving this aim. Carbon-fibre composites are seen as a light-weight alternative to traditional metallic alloys in the aerospace industry and their use could lead to significant weight savings, specifically in relation to the large cryogenic fuel tanks used for these vehicles.

Given the novelty of these composite materials and their associated processing techniques, their performance under the extreme thermo-mechanical loading experienced within a cryogenic tank is poorly understood. These materials are particularly susceptible to sub-critical damage modes which can lead to the formation of extensive crack networks through the tank wall, facilitating fuel leakage. The accurate prediction of damage accumulation and permeability in composite materials is therefore essential to the safe and economical design of these structures.

An overview of current space transportation methods and costs is provided in **Section** 1.2. **Section** 1.3 describes cryogenic fuel tank design, while **Section** 1.4 discusses the damage modes which can arise due to the thermo-mechanical loading of composites and their effect on tank permeability. **Section** 1.5 provides a summary of methods used to numerically model damage formation in composite laminates.

Section 1.6 gives an overview of the main thesis objectives and aims, whereas **Section** 1.7 outlines the contents of each chapter of the thesis.

1.2 Space transportation and associated costs

Transporting a payload from earth into orbit remains an exceedingly complex task, despite being several decades since it was first achieved. The vast resources and infrastructure required to facilitate routine space launches has meant that space transportation, and human space exploration in general, has been confined to all but the largest nation states. However, the recent growth of the commercial space industry, including the use of privately built launch systems [1], has renewed the need for safe and economical space launch solutions.

Since the beginning of the space age, the primary mode of space transportation has been expendable chemical rockets. Such launch systems are typically comprised of solid rocket boosters and/or external fuel and oxidiser tanks attached to the launch vehicle. These components are then jettisoned before the vehicle attains orbit. The current cost of transporting payload to space using this method is approximately €15,000/kg [2]. Through their respective future launch vehicle programs [3, 4], the National Aeronautics and Space Administration (NASA) and the European Space Agency (ESA) have communicated the need to move towards more cost effective and sustainable launch systems. Specifically, NASA requires its 2nd generation launch system to reduce costs by a factor of 10 over its predecessor [3].

The development of reusable launch vehicles (RLVs) is key to achieving these dramatic cost savings, with an increase in launch frequency being linked to lower overall transport costs per launch [5]. A significant reduction in vehicle structural weight is also required, which will rely on the development of new materials, technologies and processing techniques. Due to the relative contribution of the tank to the total vehicle dry weight, which currently stands at up to 50% [6], a durable and lightweight fuel tank design will be central to meeting these requirements.

1.3 Fuel tank design

Fuel tanks are a major structural component of all space launch vehicles (SLVs) and are critical to the safe and efficient operation of these vehicles. Their design is primarily influenced by payload requirements, propellant choice, construction materials and manufacturing processes.

1.3.1 Rocket engine propellant

Solid and liquid propellant chemical rockets are two of the most widely used forms of propulsion for SLVs. Due to their higher propellant density, solid propellant rockets offer the advantages of compact design and ease of storage. However, for high performance applications including the Space Shuttle and Ariane V, the greater specific impulse offered by liquid propellants such as a liquid hydrogen (LH_2) and liquid oxygen (LO_2) combination is necessary [7]. Crucially for RLVs, liquid propellant rockets are controllable and can be shut down and restarted when necessary.

As a fuel, LH_2 has the benefit of an extremely high specific energy. However, its low specific density offsets this to an extent, resulting in a relatively low volumetric energy density. This requires LH_2 to be stored in a deeply cryogenic state (-253 °C) in order to minimise storage volume. Significant insulation around the tank is also needed to slow boil-off of the liquid, which can contribute to internal tank pressure loads in excess of 200 kPa [8]. The propellant oxidiser, LO_2, has similar storage requirements, albeit at a higher temperature of (-183 °C).

1.3.2 Construction materials and processes

Liquid propellant fuel tanks essentially act as cryogenic pressure vessels. The construction materials used for these vessels must be capable of resisting extreme cryogenic temperatures, high internal pressure loads and operational loads associated with take-off and landing. They must also be impermeable and chemically resistant to the contained cryogens.

1. Introduction

Metallic alloys are currently the material of choice for cryogenic tanks in the space industry. In particular, aluminium/lithium (Al/Li) alloys have found favour in more recent applications, including the Space Shuttle's 'superlightweight' (SLWT) main liquid fuel tanks [9]. These high strength and high fracture toughness materials offer good damage resistance, despite the extreme operating conditions. They also show minimal susceptibility to hydrogen embrittlement [10, 11]. The processing and development costs associated with these alloys are relatively low, due to well established forming practices for metallic pressure vessels and general familiarity with the material behaviour. However, despite the suitability of these advanced alloys for cryogenic fuel storage, metallic materials remain a relatively high-weight solution.

In order to achieve the significant weight savings required for next generation SLVs, the aerospace industry has turned to carbon-fibre reinforced polymer (CFRP) composite materials. Like existing Al/Li alloys, CFRPs have high strength and stiffness, high toughness and good chemical resistance. However, they are also extremely light-weight materials, meaning they can offer similar performance to metallic alloys, with a substantial weight saving. The advantage of CFRPs over other aerospace materials in terms of specific stiffness is shown in Fig. 1.1.
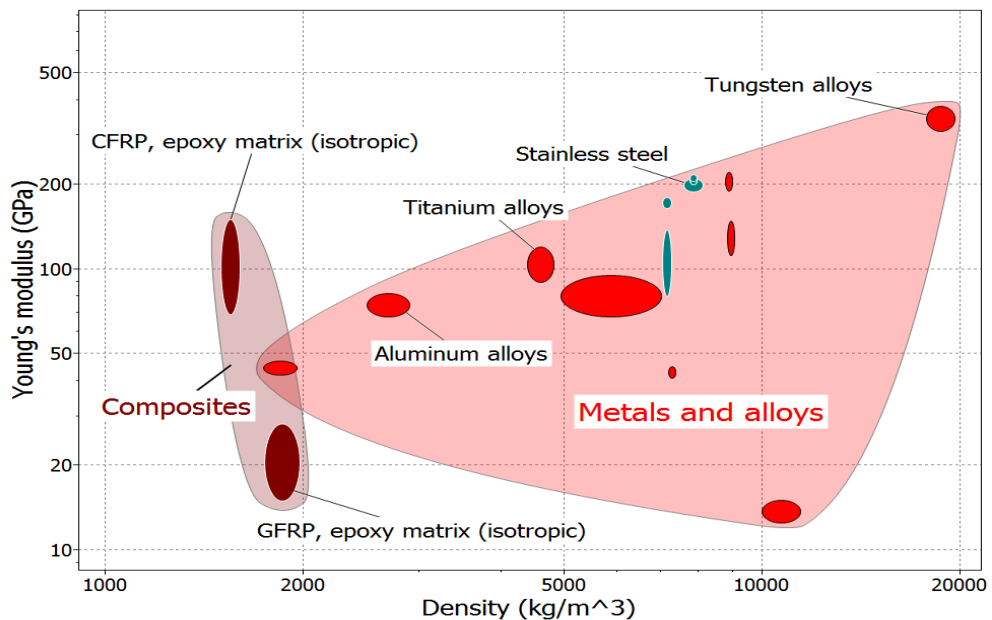
Figure 1.1 An Ashby plot of Young's modulus against density for a range of aerospace materials using properties from [12].

1. Introduction

Specifically, composites such as carbon-fibre PEEK (CF/PEEK) are being investigated for use in cryogenic fuel tanks. CF/PEEK is a high-performance thermoplastic carbon-composite material. Thermoplastic composites offer a number of advantages over thermosetting composites in terms of the improved range of mechanical properties and processing techniques available. Thermoplastic composites also offer advantages in terms of component reformability and reusability, due to the consistent chemical composition of thermoplastic resins throughout processing. Crucially, CF/PEEK exhibits significantly higher fracture toughness values when compared to CF/epoxy materials. For instance, Mode I fracture toughness values lie in the range of 190 to 400 jm^{-2} for CF/epoxy materials and 1,062 to 1,990 jm^{-2} for CF/PEEK materials [13, 14]. This translates to increased resistance to damage propagation [15]. Thermoplastics also allow the use of out-of-autoclave processing techniques such as automated tape laying (ATL), which is based on the in-situ heating, melting and consolidation of overlapping composite plies. This technique facilitates the manufacturing of large structures, like cryogenic-tanks, without the capital investment required for an autoclave several metres in diameter.

Figure 1.2 A 5.5m diameter composite cryogenic tank prototype under development by Boeing [16]. The tank was manufactured using automated tape placement of thermoset composites.

However, the use of CFRPs for extreme aerospace applications is not without its problems. Such materials have a propensity to undergo sub-critical damage build-up, in the form of microcracking and delamination, due to severe thermo-mechanical loading. Predicting these damage modes and determining their influence on the structural performance of components and material behaviour in general, remains a difficult task. An example of this is the case of the composite cryogenic fuel tank prototype developed for use in the Lockheed Martin X-33 RLV, a demonstrator for the VentureStar orbital vehicle. The tank structure comprised inner and outer walls separated by a core and was manufactured from a CF/epoxy material, IM7/977-2 [17]. Tank failure occurred during physical testing due to permeation of LH_2 through the inner wall of the structure. Subsequent expansion of the cryogen within the core lead to an increase in core pressure and catastrophic failure of the entire structure. One of the main contributing factors to this failure was found to be the presence of an extensive network of microcracks through the thickness of the tank wall, which formed a leak path for the cryogen to escape [17]. Further testing confirmed that the permeability of the pristine tank walls increased from approximately 3×10^{-6} to 3×10^{-3} scc/sec-in.^{2} when the tank underwent fuelling. This complex interaction of damage modes was not anticipated by designers. The test programme was cancelled in 2001, leading to a surge in interest in the cryogenic performance of composite materials, in particular microcracking and permeability.

1.4 Damage and failure of composite cryogenic tanks

Following the failure of the X-33 RLV fuel tank, there has been renewed interest in the damage accumulation behaviour of composites under severe thermal and mechanical loading. This incident revealed the major impact that sub-critical damage, in the form of microcracking and delamination, can have on composite structures. Taken by themselves, these damage modes do not typically constitute full structural failure. However, this damage build-up can lead to a number of undesirable effects such as a multi-directional reduction in strength and stiffness, increased susceptibility to attack from solvents and the formation of gas leakage paths through the material.

1.4.1 Transverse microcracking

Intra-laminar failure, in the form of transverse microcracking in off-axis plies, is usually the first noticeable damage mode encountered in composite laminates. These cracks typically form transverse to the direction of loading and run parallel to the fibre direction in a composite laminate. This damage mode is confined to the matrix of a composite material and generally occurs at a load level far below that required for fibre failure. A detailed overview of matrix microcracking in composite materials is given by Nairn [18]. Fig. 1.3 shows a cross-section view of a transverse microcrack in a damaged laminate.
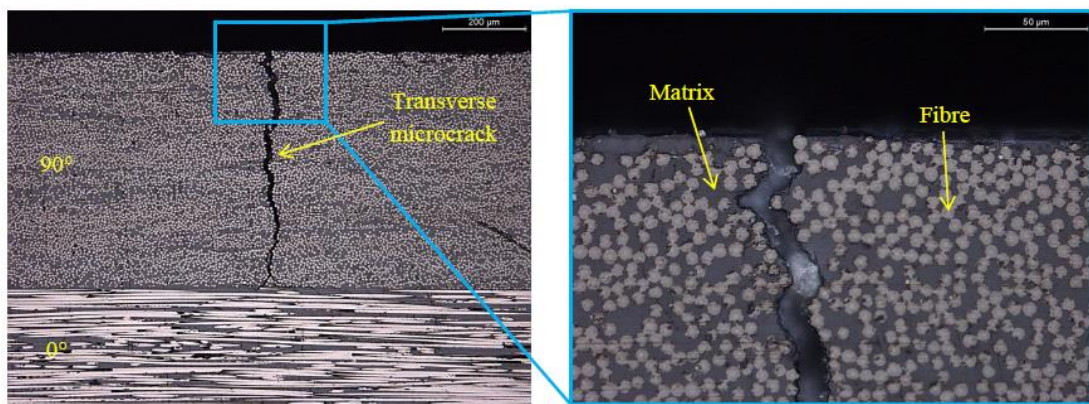
Figure 1.3 An optical micrograph of a transverse microcrack running through the matrix in the outer ply of a damaged laminate. The fibres in the outer 90° ply are orientated perpendicular to those in the adjacent 0° ply and to the plane of the cross-section cut.

Due to the multi-axial nature of the thermo-mechanical loading experienced in cryogenic tanks, transverse microcracks may form in both the outer and inner ply groups of laminates simultaneously [18, 19]. The inherent inhomogeneity of composite materials and the presence of manufacturing defects can mean that these microcracks may form below the failure strength of the bulk material [20]. Factors such as laminate stacking sequence, laminate thickness and component geometry can also affect transverse microcrack initiation and propagation in composites [21-23].

1.4.2 Delamination

Delamination is a form of inter-laminar damage. It typically occurs after an initial level of microcracking has developed, due to increased amplitude of loading or the occurrence of subsequent thermo-mechanical load cycles. Like transverse microcracking, delamination involves the matrix of a composite. However, delaminations tend to initiate and propagate along the interface between two adjacent ply groups and arise due to the action of tensile and/or shear forces. Fig. 1.4 shows a delamination at the free edge of a laminate, between two ply groups.
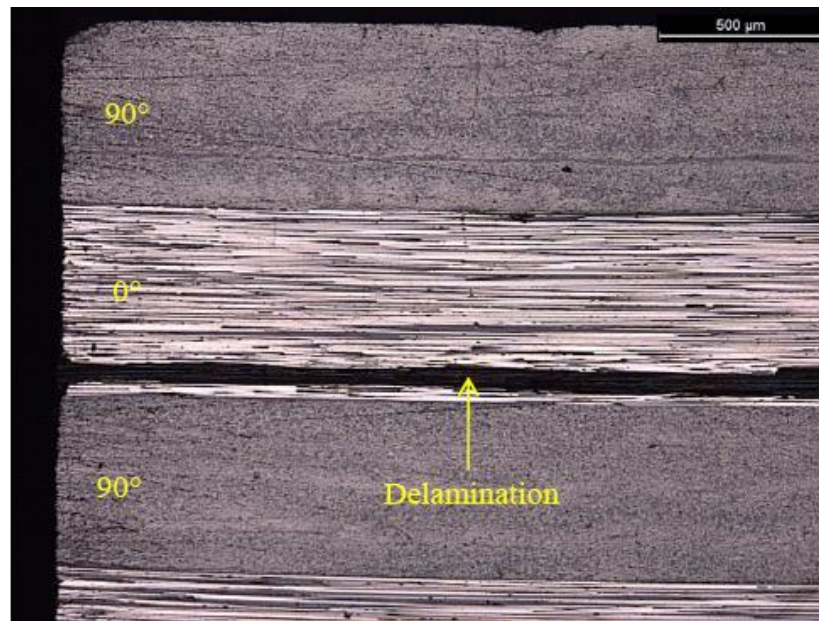
Figure 1.4 An optical micrograph of delamination between 0° and 90° ply groups in a damaged laminate.

Delaminations may initiate from existing transverse cracks or from the free edges of laminates. Laminate delamination is a more severe mode of damage due the multi-directional loss of stiffness that results from the debonding of plies. This is in contrast to transverse microcracking, where the laminate structure remains intact despite a localised stiffness reduction. They also play a role in the formation of crack networks through the thickness of laminates by connecting staggered microcracks in adjacent plies.

1.4.3 Crack networks and permeability

The leakage of liquid or gas from a cryogenic fuel tank constitutes structural failure and can have serious implications for mission safety. Although it is possible for leakage to occur through pristine laminates via natural diffusion processes, the presence of damage drastically increases permeability. This is because the formation of through-thickness crack networks allows a direct path for fluid to flow through the tank wall, as shown in Fig. 1.5.
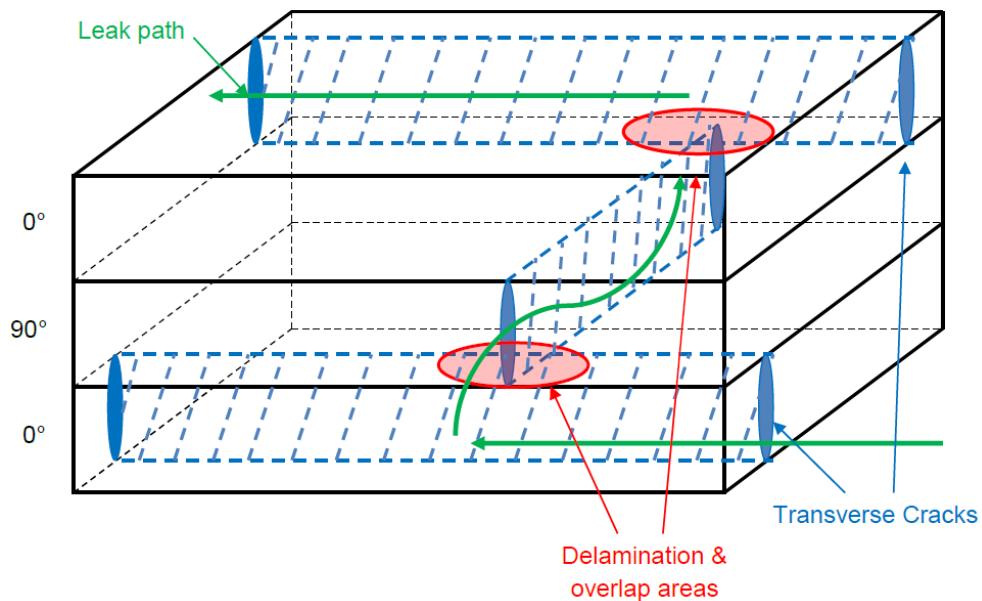
Figure 1.5 Overlapping transverse microcracks leading to the formation of a leak path through a laminate.

Although the existence of delaminations are not a prerequisite for the formation of these leak paths, their interaction with other damage modes can lead to increased permeability. For instance, delaminations which have initiated and propagated in the vicinity of transverse microcracks have been found to increase the crack opening displacement (COD) of these transverse cracks [24, 25]. This increased crack opening, or delaminated crack opening displacement (DCOD), as shown in Fig. 1.6, in turn leads to larger overlap areas between microcracks in adjacent plies, allowing higher leak rates. Delaminations can also act to link non-overlapping transverse

microcracks, thereby ensuring the continuation of a leak path which otherwise would have been arrested at a ply interface.
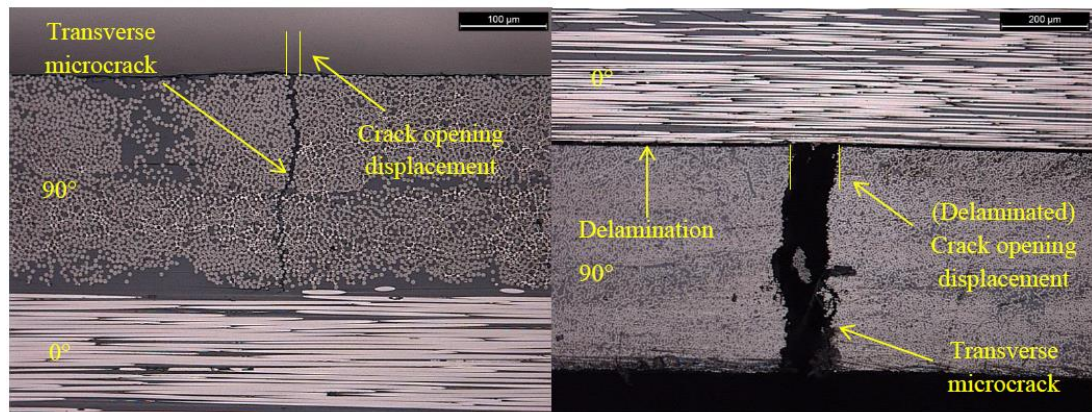
Figure 1.6 Optical micrographs showing the measurement of the crack opening displacement of a transverse microcrack (COD) (left) and the delaminated crack opening displacement of a transverse microcrack (DCOD) (right).

1.5 Numerical modelling of damage in composites

Due to the complex, orthotropic behaviour of fibre-matrix materials, predicting the performance of composite structures generally requires significant computational effort. Thus, finite element analysis (FEA) is commonly used to model composite materials. This analysis technique allows designers to simulate full-scale testing of components without the need for costly physical testing over many design iterations and is of particular benefit for large structures such as cryogenic fuel tanks.

Detecting sub-critical damage accumulation, in the form of microcracking and delamination, in composite components is a difficult and time consuming task [26, 27]. In some cases, due to crack closure or because of thick laminate sections, damage may be undetectable by ultrasound or X-ray scanning techniques. This highlights the need for accurate crack initiation and propagation prediction during the design process. Prior knowledge of which composite lay-ups best resist microcrack initiation, of how through-thickness crack networks will form, or even where damage is most likely to occur first within a structure, will lead to safer and more cost-effective designs.

Although damage modelling for composites can be carried out at micro- and macro-levels, a meso-level, or ply-by-ply approach, allows the simulation of individual damage modes such as transverse microcracking and delamination, whilst still remaining applicable to large-scale structures. A detailed review of meso-level modelling of failure in composite laminates is given by van der Meer [28]. Due to the quasi-brittle nature of many composite materials, linear elastic fracture mechanics (LEFM) is often used to model crack growth. Cohesive zone modelling, based on traction-separation curves to describe failure behaviour, has also been applied extensively to composite materials.

Numerous challenges exist in modelling the multiple interacting damage modes in composites simultaneously. Specific techniques used to model inter-laminar failure include the virtual crack closure technique (VCCT) and the use of special cohesive elements at the interface region. Predicting delamination growth is simplified by the fact that the crack path is generally constrained to the interface region of the laminate, but its initiation point must still be determined. Simulating transverse microcrack initiation and growth is a more complex task, due to the inherently random nature of crack nucleation, whereby multiple microcracks may grow in different directions through a laminate. However, the recent development of the extended finite element method (XFEM) has removed the need for crack initiation points and propagation paths to be defined a-priori, leading to the possibility of combined, random, intra and inter-laminar damage models for composite laminates.

1.6 Thesis motivation and aims

In order to substantially reduce launch costs, the next generation of RLVs must offer extensive weight savings over current designs. The development of light-weight composite cryogenic fuel tanks using advanced materials is key to achieving this goal. In order to understand and predict the performance of these composite structures, new modelling techniques are necessary. This thesis aims to address the micro-damage effects of the launch vehicle fuel on thermoplastic cryogenic tanks through novel numerical models for the prediction of microcracking and delamination and the resulting permeability of thermoplastic materials.

The main aims of the thesis are:

1. To develop a numerical methodology to model delamination in composite materials and to validate and calibrate the model with experimental test data.

2. To experimentally characterise the general structure and defects present in CF/PEEK laminates and to fully characterise damage formation in these laminates under representative cryogenic loading.

3. To develop a novel, full 3-D numerical methodology capable of accurately predicting microcracking, delamination and permeability in composite laminates and to compare output with experimental data generated during the course of the work and from industry collaborators for CF/PEEK materials.

4. To scale the developed methodology to predict the permeability of linerless composite cryogenic tanks processed using out-of-autoclave technologies and to design an optimised tank lay-up to minimise cryogen leakage under expected operating loads.

By achieving these aims, this thesis presents a novel methodology for damage and permeability prediction in composite materials, allowing for safer, more economical cryogenic fuel tank design.

1.7 Thesis overview

Chapter 2 provides a review of the relevant experimental and numerical methods used in the analysis of damage and permeability in composite materials. **Chapter** 3 introduces a novel two-dimensional XFEM-based methodology for the combined simulation and prediction of thermal fatigue delamination for identification of delaminated crack opening displacement (DCOD) and, hence, composite laminate permeability. This method improves on existing permeability prediction techniques by allowing direct simulation of delamination growth and DCOD at transverse microcracks, in place of assuming a fixed delamination length prior to an analysis.

Chapter 4 describes the cryogenic testing of CF/PEEK laminates. A detailed analysis of the results of this experimental work, including defect distributions within the material and damage accumulation due to cryogenic cycling, is presented.

In **Chapter** 5, a fully three-dimensional modelling methodology for predicting transverse microcracking, delamination and permeability of composite laminates is developed. The methodology simulates microcrack initiation and propagation using XFEM and delamination using a mixed-mode cohesive zone model. Random microcrack initiation is modelled using a random (Weibull) distribution of fracture strengths and also by an alternative method based on an elemental representation of defects using measured defect geometry.

Chapter 6 examines the use of tape-laid CF/PEEK for cryogenic tanks. Detailed material characterisation is carried out using methods similar to those described in **Chapter** 4. The methodology developed in **Chapter** 5 is expanded upon and used to model damage accumulation in tape-laid cryogenic tanks, with the resulting damage and permeability being compared with cryogenically cycled test specimens. The main results of the thesis are discussed in **Chapte**r 7 and include design recommendations for composite cryogenic fuel tanks for RLVs.

1.8 References

[1] Anderson C. Rethinking public-private space travel. *Space Policy*, **29**, 266-271, 2013.

[2] Coopersmith J. The cost of reaching orbit: Ground-based launch systems. *Space Policy*, **27**, 77-80, 2011.

[3] Lamoreaux A.J. Final report on audit of the space launch initiative: Primary requirements for a 2nd generation reusable launch vehicle. Report number IG-02-028, Office of Inspector General, The National Aeronautics and Space Administration, Washington, DC, USA, 2002.

[4] Letourneur Y., Leleu F., Pinard D., Krueger J. & Balduccini M. Status of next generation expendable launchers concepts within the FLPP program. *Acta Astronautica,* **66**, 1404-1411, 2010.

[5] Koelle D.E. The cost-optimal size of future reusable launch vehicles. *Acta Astronautica*, **47**(2-9), 205-213, 2000.

[6] Xu J., Sankar B.V. & Bapanapalli S. Finite element based method to predict gas permeability in cross-ply laminates. *Journal of Composite Materials*, **42**(9), 849-864, 2008.

[7] Amri R. & Rezoug T. Numerical study of liquid propellants combustion for space applications. *Acta Astronautica*, **69**, 485-498, 2011.

[8] Abumeri G.H., Kosareo D.N. & Roche J.M. Cryogenic composite tank design for next generation launch technology. In *40th AIAA/ASME/SAE/ASEE Joint Propulsion Conference and Exhibit*, AIAA, Fort Lauderdale, Florida, USA, 2004.

[9] Nemeth M.P., Young R.D., Collins T.J. & Starnes J.H. Effects of initial geometric imperfections on the non-linear response of the Space Shuttle superlightweight liquid-oxygen tank. *International Journal of Non-Linear Mechanics*, **37**, 723-744, 2002.

[10] Verstraete D., Hendrick P., Pilidas P. & Ramsden K. Hydrogen fuel tanks for subsonic transport aircraft. *International Journal of Hydrogen Energy*, **35**, 11085-11098, 2010.

[11] Vander Kooi D.C., Park W. & Hilton M.R. Characterization of cryogenic mechanical properties of aluminium-lithium alloy C-458. *Scripta Materialia*, **41**(11), 1185-1190, 1999.

[12] Material database from CES EDUPack 2012. Granta's CES EduPack, Granta Material Intelligence, Granta Design Limited, 2012.

[13] Aoki T., Ishikawa T., Kumazawa H. & Morino Y. Mechanical behaviour of CF/polymer composite laminates under cryogenic environment. *Proceedings of the 12th International Conference on Composite Materials*, Paris, France, 1997.

[14] Yoon H. & Takahashi K. Mode I interlaminar fracture toughness of commingled carbon fibre/PEEK composites. *Journal of Materials Science*, **28**, 1849-1855, 1993.

[15] Crick R.A., Leach D.C., Meakin P.J. & Moore D.R. Interlaminar fracture morphology of carbon fibre/PEEK composites. *Journal of Materials Science*, **22**, 2094-2104, 1987.

[16] Image from: http://gcd.larc.nasa.gov (Accessed June 2014).

[17] Final Report of the X-33 Liquid Hydrogen Tank Test Investigation Team. The National Aeronautics and Space Administration, Marshall Space Flight Center, Huntsville, Alabama, USA, 2000.

[18] Nairn J.A. Matrix microcracking in composites. In *Polymer matrix composites*, Ch. 13, Pergamon, 2001.

[19] Henaff-Gardin C., LaFarie-Frenot C.M. & Gamby D. Doubly periodic matrix cracking in composite laminates Part 2: Thermal biaxial loading. *Composite Structures*, **36**(1-2), 131-140, 1996.

[20] Berthelot J.M. & LeCorre J.F. Statistical analysis of the progression of transverse cracking and delamination in cross-ply laminates. *Composites Science and Technology*, **60**, 2659-2669, 2000.

[21] Kumazawa H., Aoki T. & Susuki I. Influence of stacking sequence on leakage characteristics through CFRP composite laminates. *Composites Science and Technology*, **66**, 2107-2115, 2006.

[22] Bechel V.T. & Kim R.Y. Damage trends in cryogenically cycled carbon/polymer composites. *Composites Science and Technology*, **64**, 1773-1784, 2004.

[23] Park C.H. & McManus H.L. Thermally induced damage in composite laminates: predictive methodology and experimental investigation. *Composites Science and Technology*, **56**, 1209-1219, 1996.

[24] Roy S. & Benjamin M. Modelling of permeation and damage in graphite/epoxy laminates for cryogenic fuel storage. *Composites Science and Technology*, **64**, 2051–2065, 2004.

[25] Nair A. & Roy S. Modelling of permeation and damage in graphite/epoxy laminates for cryogenic tanks in the presence of delaminations and stitch cracks. *Composite Science and Technology*, **67**(11-12), 2592–2605, 2007.

[26] Todoroki A., Tanaka Y. & Shimamura Y. Delamination monitoring of graphite/epoxy laminated composite plate of electric resistance change method. *Composite Science and Technology*, **62**(9), 1151-1160, 2002.

[27] Bois C. & Hochard C. Monitoring of Laminated Composites Delamination Based on Electro-mechanical Impedance Measurement. *Journal of Intelligent Material Systems and Structures*, **15**(1), 59-67, 2004.

[28] Van der Meer F.P. Mesolevel modelling of failure in composite laminates: constitutive, kinematic and algorithmic aspects. *Archives of Computational Methods in Engineering*, **19**(3), 381-425, 2012.

2. Background

2.1 Chapter summary

Research into advanced polymer composite materials has increased substantially in recent years as such material systems have emerged as viable alternatives to traditional metallic materials in a range of industries. The inherent complexity of composite materials has required the adoption of existing experimental characterisation techniques to better understand material behaviour, as well as the development of novel simulation techniques capable of predicting multiple damage modes simultaneously. This chapter provides an overview of the main developments and remaining gaps in the area of composite damage research from both experimental (**Section** 2.2) and numerical modelling (**Section** 2.3) viewpoints.

Section 2.2.1 describes techniques which have been used to investigate the internal structure of composite materials, including characterising the defects present in processed laminates. **Section** 2.2.2 summarises previous work into damage formation in composite laminates due to cryogenic loading, with **Section** 2.2.3 focusing on studies which have linked damage formation to permeability in physically tested specimens. **Section** 2.3.1 introduces some of the commonly used methods for numerical prediction of delamination in composite laminates, as well as the limitations of these techniques with respect to modelling other failure modes. The challenges associated with developing combined damage models which can account for both intra- and inter-laminar failure are discussed in **Section** 2.3.2, while

Section 2.3.3 focuses on the gap between existing permeability prediction techniques and developments in realistic crack network simulation methods.

2.2 Experimental characterisation of cryogenically cycled laminates

In recent years, aerospace applications such as cryogenic fuel tanks have driven much of the research into the effects of cryogenic temperatures on composite materials. Due to the relative novelty and complexity of advanced composites such as CF/PEEK, the damage initiation and growth mechanisms for these materials remain poorly understood, particularly in low temperature environments. Research to date has generally been focused on the cryogenic cycling of composite laminates in order to induce sub-critical damage, primarily in the form of matrix microcracking. Permeability testing of cryogenically cycled laminates often takes place in conjunction with microcrack analysis. However, the difficulty in detecting the presence of internal through-thickness crack networks in damaged laminates has hindered progress in relating the level of microcracking in a damaged laminate to its permeability. A thorough understanding of the formation of these crack networks, and their relationship with laminate permeability, is critical to the design of composite cryogenic fuel tanks and is being actively pursued.

2.2.1 Characterisation of composite materials

The physical properties of composite laminates are highly dependent on processing techniques and parameters. Ply-level defects such as voids, inclusions and resin-rich areas (Fig. 2.1), which may arise during the autoclave or tape-laying processes, can alter the thermo-mechanical response of the laminate as a whole. Additionally, the presence of significant thermal residual stresses in thermoplastic composites such as CF/PEEK can lead to damage formation in laminates prior to testing. Detailed characterisation of the general structure of laminates post-processing is, therefore, an important step in determining the damage accumulation behaviour of the material

upon physical testing and is essential to development of representative numerical models.
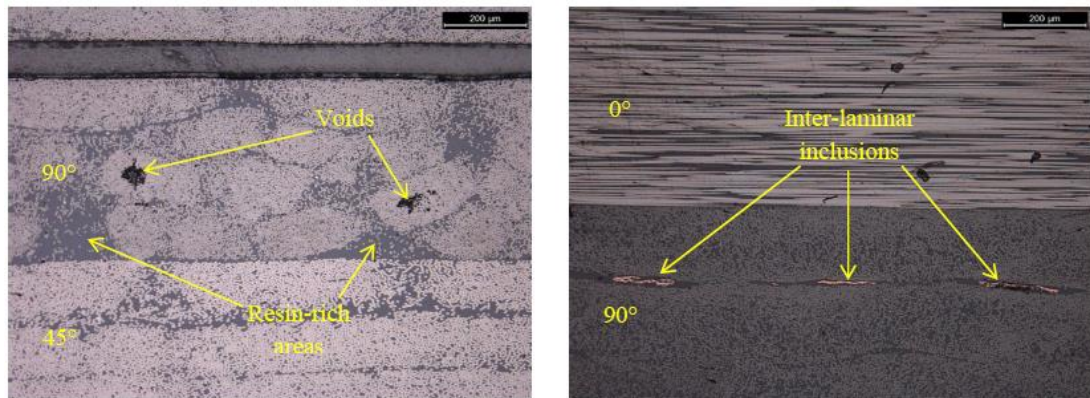
Figure 2.1 An optical micrograph of a CF/PEEK laminate showing some common defects including voids, resin-rich areas and inclusions.

The influence of micro-defects on the macro properties of laminates is a well-studied topic. Voids, often being the most numerous and detrimental discontinuity present in composites, have received the most attention. Void formation occurs due to the presence of entrapped air within the prepreg and between plies as well as volatiles within the material, which are released during the curing cycle. Volatiles can take the form of residual solvents used in the manufacturing of the prepreg as well as volatiles which have been absorbed into the resin during pre-processing. The level of volatiles within a prepreg can depend on whether a thermoset or thermoplastic resin is used, with levels typically far higher in thermosetting resins due to the chemical changes which occur in these materials during processing. These voids can act as crack nucleation points within the laminate and can alter the properties of a laminate to a large degree, depending on the total void content present. A number of studies have shown that increased porosity in laminates leads to reductions in strength and modulus of up to 25% for void volume contents greater than 3% [1-6], as well as to changes in thermal expansion behaviour [7]. Furthermore, the spatial distribution and the effect of void morphology on properties must also be considered. Numerical simulations have been carried out showing the influence of individual void orientation and aspect ratio on inter-laminar crack growth [8, 9] and laminate moduli in the longitudinal and transverse directions [10]. However, it is only recently that

2. Background

advances in non-destructive testing (NDT) techniques, such as 3-D X-ray computed tomography (CT), have allowed full spatial and morphological characterisation of voids, therefore experimental verification of these models remains lacking in the literature.

The porosity of laminates is generally characterised in terms of void volume content as a percentage of the total specimen volume. Void volume contents on the order of several % are acceptable for some non-critical applications; however porosity levels above 1% are generally not considered acceptable for the aerospace industry [1]. Numerous methods exist to evaluate composite porosity, with varying accuracy. NDT techniques such as optical microscopy and X-ray CT (Section 3.3) have been shown to provide greater accuracy over other conventional characterisation techniques such as Archimedes Theoretical versus Actual Density [11] and destructive techniques such as matrix burn-off and matrix digestion [12].

Optical microscopy is widely used due to the relative simplicity of the technique and the equipment required for analysis. However, due to the 2-D nature of the technique, multiple cross-sections of the material are required in order to achieve a representative sample for void characterisation [11, 13]. This can lead to a time consuming analysis process, as well as leaving the technique open to the inherent 2-D bias of cross-section analysis. Advances in technology and reduction in equipment costs has seen the emergence of 3-D X-ray CT as the pre-eminent method of void characterisation. This technique, which is based on the attenuation of X-rays as they pass through phases of differing density in a scanned specimen, allows voids to be isolated from the bulk material. The principal advantage of 3-D X-ray CT is that it allows a full spatial and morphological characterisation of all voids within a given specimen volume. Void characterisation studies have been carried out for carbon/epoxy materials using 3-D X-ray CT [11, 14], with the technique consistently providing higher fidelity void data when compared to other methods such as optical microscopy. The technique has also been used to investigate the role of void volume and void morphology in damage initiation and propagation, with studies relating the reduction in fatigue life to larger voids for glass/epoxy wind turbine blades [15] and the reduction in strength of carbon-epoxy curved beams to certain critical areas of porosity [16]. Although 3-D X-Ray CT offers extremely powerful material characterisation capabilities, detailed void characterisation data for a range of

composite materials, particularly thermoplastics, remains unavailable at this time, due to the novelty and relative complexity of the approach.

Foreign matter can be unintentionally introduced into composite laminates during manufacturing and processing. Like voids, inclusions can act as crack initiation points within laminates and are generally seen as detrimental to the mechanical properties of a composite. Foreign objects such as metallic scrap material and backing paper can sometimes be found embedded within a ply or between plies. The accidental inclusion of foreign material is more common during the hand lay-up of laminates when compared to more modern, machine-based, processing techniques due to the increased likelihood of operator error in following processing instructions. Processing composites in a cleanroom can help reduce the likelihood of foreign matter inclusion within processed laminates. Inclusion characterisation can be carried out in tandem with void characterisation, with a distinction between the defects being made on the basis on density in the case of 3-D X-ray CT. There exists minimal published research on full inclusion characterisation for composite materials, with a recent investigation into damage evolution in metal matrix composites [17], shown in Fig. 2.2, being the exception. Despite this, quantifying the volume and distribution of foreign matter within a laminate remains an important step in the material characterisation process.
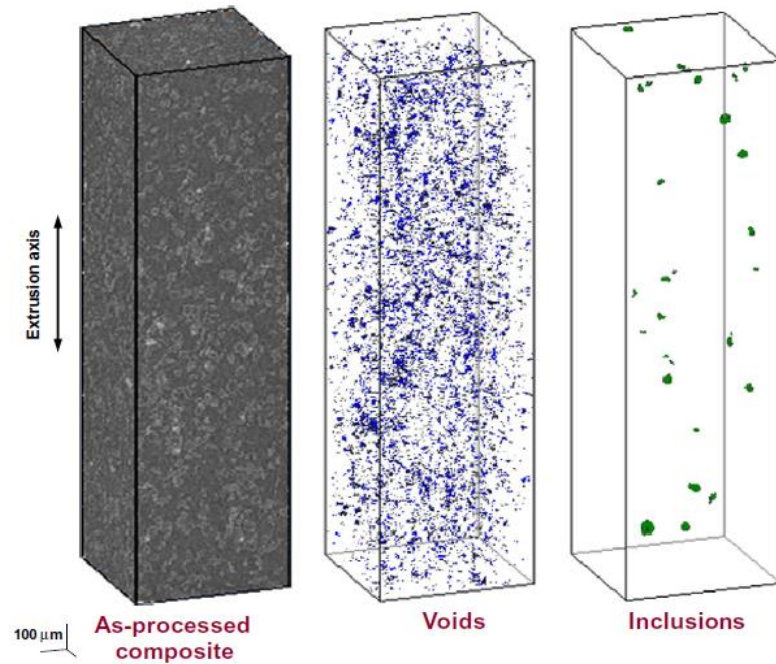
Figure 2.2 3-D microstructure of a metal-matrix composite obtained using X-ray CT showing voids and inclusions [17].

Resin-rich areas are another form of material discontinuity commonly observed in composites and are defined as regions where there is an excess of polymer compared to fibres. These resin areas represent zones of low modulus and strength when compared to the laminate as a whole and can therefore influence damage accumulation behaviour. As with voids and inclusions, the aforementioned NDT techniques can be used to identify and characterise these resin zones. However, due to the ill-defined boundaries of these areas, precise dimensions for individual resin areas can be difficult to discern. Resin-rich areas, identified by optical microscopy and ultrasonic c-scans, have been shown to lead to delamination initiation in carbon/epoxy specimens tested in tension [18]. These regions have also proved important to the study of failure mechanisms in 3-D woven composites [19]. Due to the fundamental structure of multi-axial stitched composites, the resulting resin-rich regions are typically larger than those found in more traditional composites. 3-D X-ray CT has been employed for such material types to identify and characterise resin-rich areas, with individual resin channels on the order of several mm being observed [20] and total resin-rich content on the order of 5% of the total specimen volume [21].

Thermal residual stresses, which arise during the cool-down of laminates from processing temperatures, can significantly alter the performance of composite materials. The magnitude and source of these stresses can vary depending on process parameters, material type and laminate lay-up amongst other factors. A detailed review of residual stresses in thermoplastic composites is given in [22-24]. CF/PEEK composites, due to their high processing temperatures, are particularly susceptible to the formation of these stresses. Numerous studies have shown that the magnitude of thermal residual stresses in CF/PEEK laminates can represent a significant proportion of the transverse and inter-laminar strength [25-28] and in some cases exceed it [29, 30]. Reductions in fracture toughness of up to 35% have also been recorded for cross-ply lay-ups when compared to uni-directional laminates, due to the presence of sizeable residual stress gradients [31]. Therefore, in addition to the aforementioned defects, the post-processing characterisation of composite laminates must include residual stress induced damage modes including microcracking and delamination.

2.2.2 Cryogenically induced microcracking and delamination in laminates

Research into the formation of sub-critical damage modes in composite materials covers a wide range of applications and load cases. Extensive work has been carried out into microcracking and delamination of laminates under static and fatigue mechanical and thermal loading. Despite the broad area of study, a number of key factors which influence damage formation in laminates have been identified. The stacking sequence and lay-up of laminates has consistently been shown to affect the crack density of similarly loaded specimens [32, 33], with laminates containing blocked plies generally offering reduced microcrack resistance [34]. Microcrack initiation is known to be dependent on total laminate thickness and individual ply thickness, with the strain to crack nucleation decreasing with increasing ply thickness for a range of glass/epoxy and carbon/epoxy materials [35, 36]. A number of researchers have attributed this to the statistical size effect [37-39], whereby the probability of failure is higher in a larger volume of material due to the increased presence of defects. The role of edge effects in damage initiation for laminates under

a variety of thermo-mechanical load cases has also been established [40-43], with cracks generally forming at stress levels below the bulk failure strength of the material and propagating towards the centre of the specimen upon increased loading.

The development of cryogenic fuel tanks has been the main driver of research into the effects of cryogenic temperatures on composite materials. Being a form of thermal loading, the damage accumulation behaviour observed in cryogenically cycled specimens exhibits many of the trends outlined above. For cost and safety reasons, liquid nitrogen (LN_2) is often used in the cryogenic cycling process, although some studies have used more exotic cryogens [44]. Bechel *et al* have carried out significant work in this area [32, 45] on a range of carbon/epoxy and carbon/bismaleimide materials, cycling specimens between room temperature and -196 °C up to 1,000 times. Using optical microscopy and 2-D X-ray scans to observe microcrack formation, they made a number of conclusions about damage formation in composite laminates. Outer ply crack densities were found to be significantly higher than those in inner ply groups. The blocking of laminate plies was also found to contribute to increased microcrack densities when compared to inter-laced stacking sequences. Adjacent ply groups which were 90° out of phase were also found to help arrest through thickness crack formation. In terms of cycling, once microcrack initiation had occurred, steady damage accumulation was observed over several hundred cycles until ply-level saturation had occurred. Laminates of two different thicknesses were also compared, with the thinner being more resistant to damage initiation in the early stages of cycling. However, differences in crack densities between thicker specimens were found to lessen with increasing cycles.

The amplitude of the cryogenic cycle used in testing has been shown to be an important factor in damage formation in laminates, with no ply-level cracking observed in some carbon composites after cycling between room temperature and LN_2/liquid helium temperature, but steady crack growth observed when using elevated temperature cycles [40, 46]. The role of cure temperature as part of the overall cryogenic cycle has also been identified as playing a role in damage formation, with materials having a higher stress free temperature being susceptible to more severe microcracking and delamination [47], as shown in Fig. 2.3. The method of cooling specimens to cryogenic specimens has also been questioned; although no detailed study has been performed examining the effect of cooling rates on damage

24

formation. However, clear differences in crack growth have been observed in similar materials that have been slow-cooled [48, 49] as opposed to the more conventional method of direct immersion in the cryogen [32].
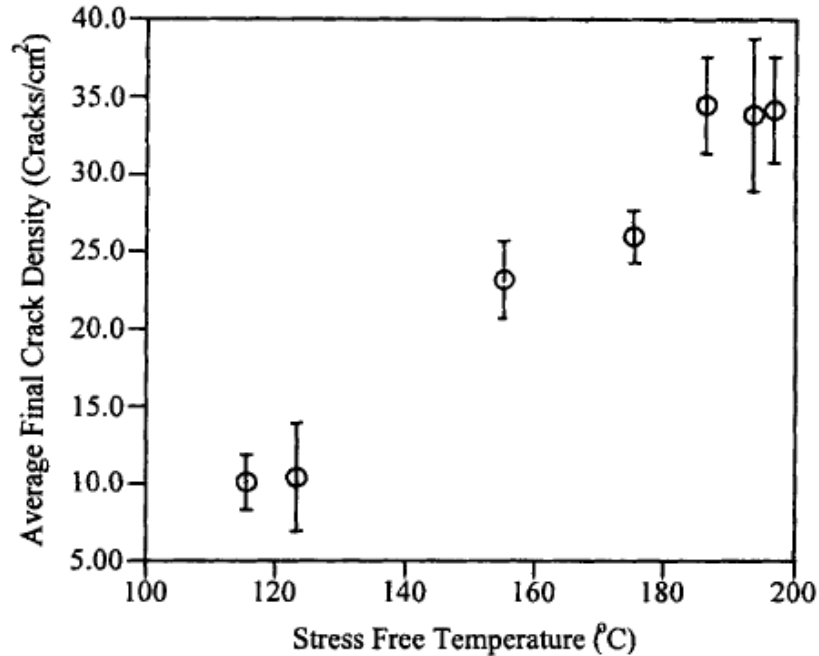
Figure 2.3 Variation in crack density with stress free temperature for cryogenically cycled carbon/epoxy materials [47].

Cryogenic temperatures can alter the fundamental material properties of composites. The increase in composite laminate transverse and interlaminar strength with decreasing temperature is a well-known phenomenon for certain materials and has been predicted to strongly influence microcrack and delamination initiation in cryogenically cycled laminates [50]. The effect of cryogenic temperatures on laminate fracture toughness is highly dependent on material type, with contrasting effects, in terms of increased and decreased toughness with temperature change, often encountered [51, 52]. Damage accumulation at cryogenic temperatures is also dependent on fibre properties; increased microcracking is linked with stiffer fibres and with poor fibre/matrix adhesion [53, 54] for example.

Little work has been carried out on the cryogenic behaviour of CF/PEEK or thermoplastics in general, despite the unique set of properties and opportunities these materials offer. Experimental testing of APC-2/AS4 CF/PEEK laminates at room

and cryogenic temperatures has shown the stiffness and strength properties to remain relatively stable over a wide range of temperatures, with only a slight increase in laminate transverse strength [55]. However, other studies have shown significant decreases in the damage initiation threshold for both microcracking and delamination in CF/PEEK specimens tested in tension and impact at cryogenic temperatures [56, 57] (Fig. 2.4). Specific material type, processing conditions, laminate stacking sequence and the magnitude of the cryogenic cycle used during testing all likely contribute to discrepancies in experimental test data.
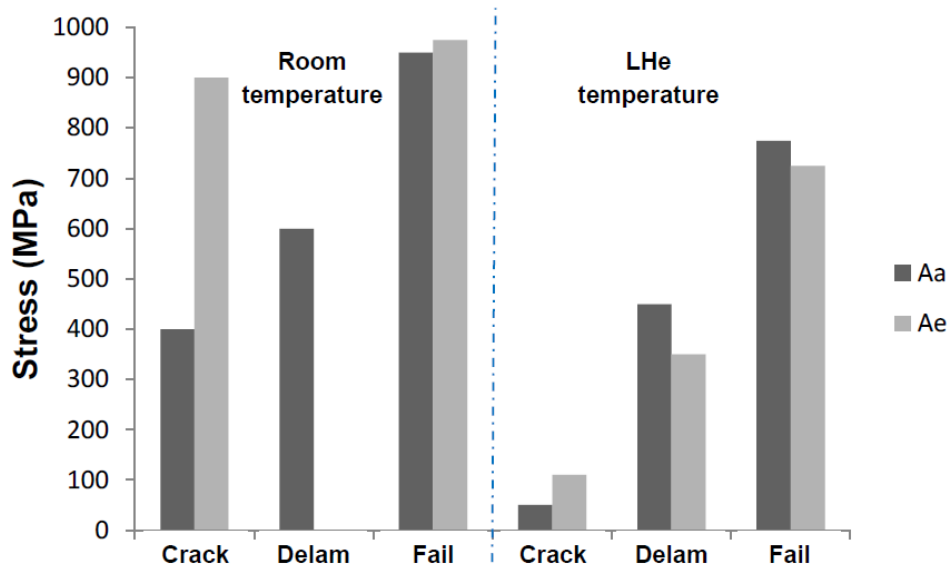
Figure 2.4 Stress to damage initiation (cracking and delamination) and final failure for intermediate modulus CF/epoxy (Aa) and CF/PEEK (Ae) quasi-isotropic laminates at room temperature and liquid helium (LHe) temperature, adapted from [56].

The work of Kobayashi *et al* [58] remains the only recent work which investigates damage growth in CF/PEEK laminates in detail under purely cryogenic loading. Here, two cross-ply lay-ups of $[0°_2/90°_3/0°_2]$ and $[0°_2/90°_4/0°_2]$ were each cycled from LN_2 temperature up to either 150 °C or 250 °C. It should be noted that the glass transition temperature for CF/PEEK is 143 °C, above which crystallisation of the matrix can occur. Therefore, cycling laminates above this temperature can lead to cold crystallisation, where the crystallinity and, hence, properties of the matrix material can change with respect to laminates cycled below the glass transition

temperature. Without explicitly tracking changes to the crystallinity content of the laminates due to cold crystallisation, direct comparisons of damage formation with laminates cycled at lower temperatures are not meaningful. Optical microscopy and 2-D radiography were used to examine microcrack growth. As expected, laminates exposed to the higher amplitude cycle (up to 250 °C) developed a greater crack density and reached saturation in less than 500 cycles, with rapid crack initiation being observed over the first 100 cycles. The lower amplitude cycle laminates underwent steady crack growth over 1,000 cycles. Interestingly, the total damage and the damage growth rate were found to be higher in the thinner laminates. Larger thermal residual stress normal to the fibre direction in the thinner laminates was cited as a contributing factor for this discrepancy in microcrack formation. It should also be noted that the thinner laminates employed an unbalanced lay-up. Higher crack densities were observed in the inner 90° plies for all laminates, with delaminations initiating from matrix cracks in the 0° plies. The analysis also included a basic numerical methodology, which predicted decreasing residual stresses within the laminates with increasing microcrack density. Further research is required in order to fully understand damage formation in cryogenically cycled composites, particularly for thermoplastics.

2.2.3 Leak paths and permeability of cryogenically cycled laminates

The multi-axial nature of cryogenic loading can facilitate the development of contiguous cracking, and thus cryogen leak paths, through the thickness of composite laminates. These leak paths are key contributors to laminate permeability. For this reason, permeability testing of composite laminates is often carried out in conjunction with cryogenic cycling and microcrack analysis, although permeability characteristics of laminates can be inferred though microcrack analysis alone, provided the analysis is informed by a complete 3-D characterisation of the microcracking throughout the specimen. Bechel *et al* [59] exposed cross-ply and quasi-isotropic bismaleimide and epoxy carbon composite laminates to LN_2 only and elevated thermal cycles of up to 177 °C. Through-thickness cracking was found to occur far more frequently in the elevated cycle specimens. The presence of leak

paths within these specimens was predicted based on the presence of microcracks in each ply group as observed under an optical microscope. However, it was unclear at which cycle the cracks in the 0° and 90° plies had fully propagated across the width of the specimens or as to the extent of the short stitch cracks [60, 61] in the off-axis plies. Thus, a complete characterisation of leak path formation in these laminates was not possible.

Many researchers have conducted physical leak tests on damaged laminates. Helium gas is generally used to test for leakage, being a safer alternative to hydrogen. Fig. 2.5 shows a schematic of a typical permeability test rig.
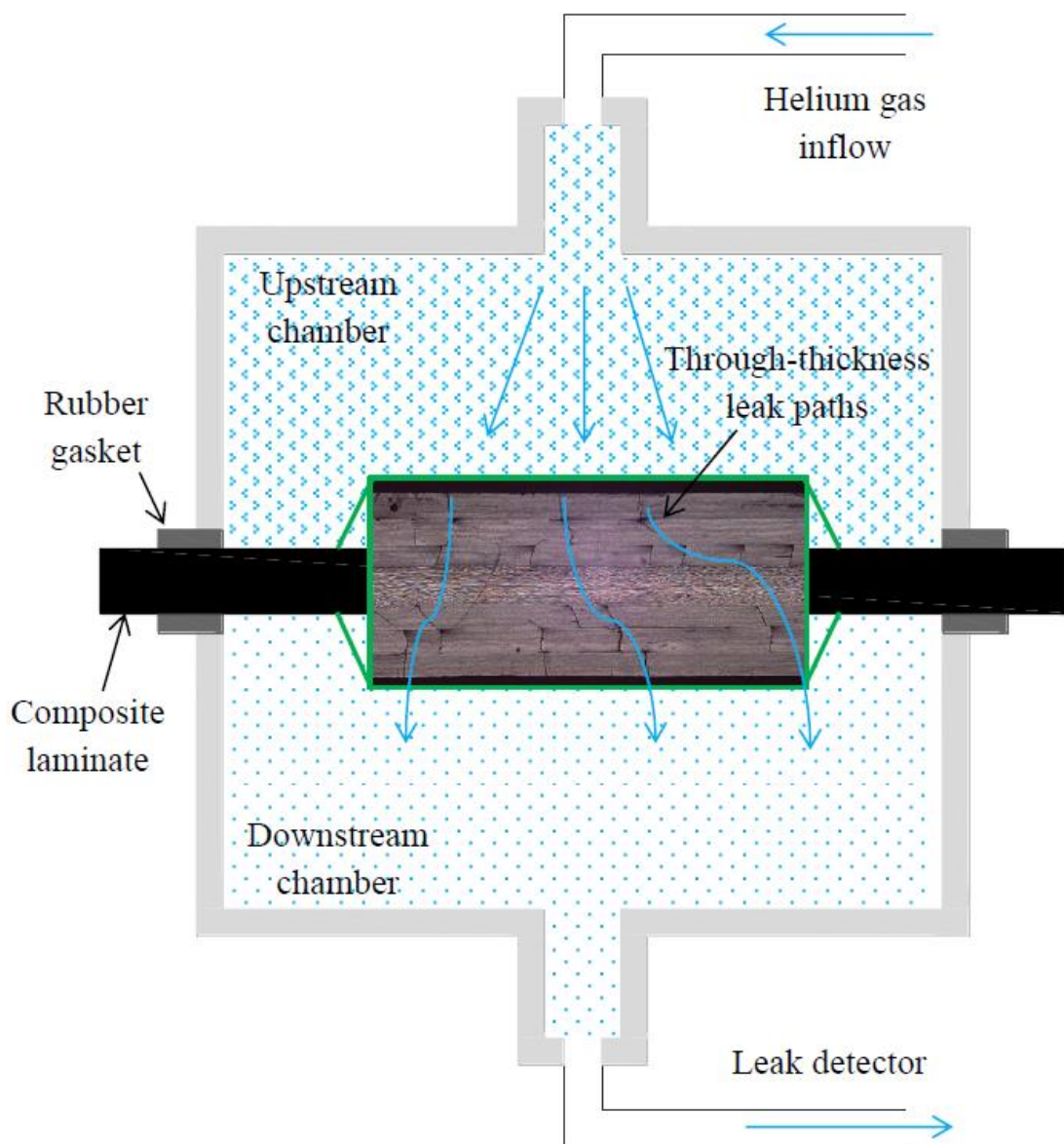
Figure 2.5 Schematic of a typical permeability test rig for composite specimens.

2. Background

Kumazawa *et al* looked at microcracking and permeability in carbon/epoxy cross-ply and quasi-isotropic laminates under uniaxial and biaxial mechanical loading at room temperature [62, 63]. Thin, inter-laced, cross-ply laminates were consistently found to have the lowest permeability and generally resisted the formation of through-thickness crack networks. Quasi-isotropic laminates were found to be more permeable that cross-ply laminates, even for specimens with similar crack densities, which were analysed using ultrasonic C-scans. Greater crack opening in damaged laminates was observed with increased loading, which in turn increased the measured leak rate. However, the mechanisms leading to increased crack opening were not identified. Other work on carbon/epoxy systems has also shown reduced permeability in thin, un-blocked cross-ply laminates [64].

Further work by Bechel *et al* [65], on the aforementioned cross-ply and quasi-isotropic bismaleimide and epoxy carbon materials, showed significantly reduced permeability for cryogenically cycled cross-ply lay-ups when compared to quasi-isotropic laminates. The pristine laminates were permeability tested before cryogenic cycling, however, the flow rate due to natural diffusion was below the resolution of the test apparatus and deemed negligible. Only bulk flow of fluid was detectable in damaged specimens, due to the presence of through-thickness leak paths. Microcrack analysis of the laminates revealed far fewer through-thickness crack networks in the cross-ply laminates. The presence of short stitch cracks was believed to contribute to increased permeability in the laminates with off-axis plies, based on previous 2-D X-ray scans of crack intersection areas (Fig. 2.6).
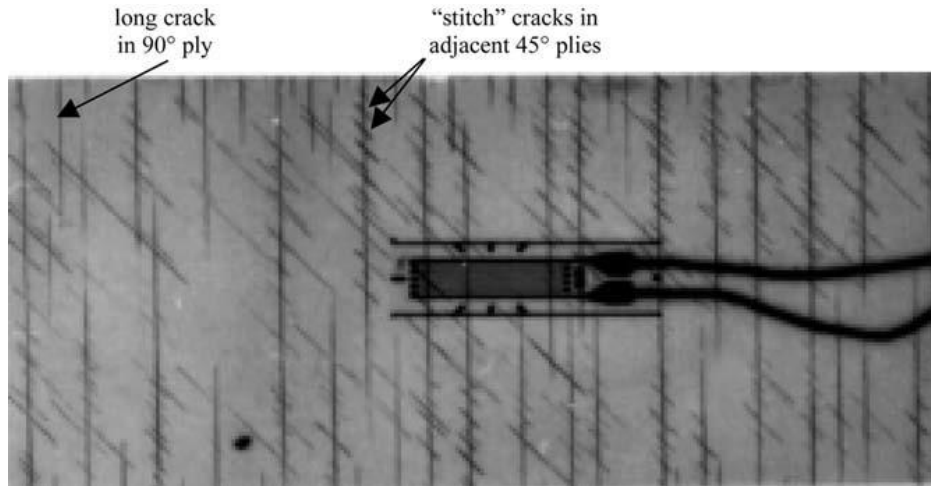
Figure 2.6 2-D X-ray scan of overlapping transverse long and stitch cracks in a composite laminate [66].

The influence of delamination on crack opening and permeability was also postulated; however, difficulties in observing delaminations at crack intersection areas prevented a conclusive investigation of this effect. Yokozeki *et al* have also investigated gas leakage in CF/epoxy IM600/133 laminates exposed to cryogenic temperatures and under mechanical loading [67, 68]. They found little change in laminate permeability between room temperature and LN_2 temperature; however, a clear trend of increasing leak rate with increasing mechanical load, in three-point bending and uniaxial tension, was observed. A trend of increasing leak conductance rate with decreasing crack intersection angle was also observed, with a leak conductance model being used to explain this trend. However, again due to difficulties in determining the extent and role of delamination at intersection areas, inaccuracies in conduction predictions were encountered for certain crack types. Research conducted at NASA's Langley Research Center [44, 69] into the permeability of toughened carbon/epoxy laminates follows a similar trend to the previous works, with increasing microcracking and permeability at cryogenic temperatures under cyclic loading. Subsequent analysis again relies on estimating crack lengths and crack opening areas at intersections areas.

In summary, the study of leak path formation and permeability in composite laminates is a relatively under-studied topic. The use of 2-D characterisation techniques to extrapolate trends in microcracking through the entire laminate width

for damaged specimens often leads to incomplete analysis of leak rates and no clear link between crack density and measured permeability. The role of delamination in increasing crack openings at overlap areas is also poorly understood, yet is often cited as a significant contributing factor to leak rates. The use of 3-D imaging techniques to identify and full characterise crack networks is seen as essential in developing this research area. Although the effect of stacking sequence on crack network formation has been well covered, the influence of thermal gradients and ply thickness is less understood, with no studies looking at the damage in directly scaled laminates. As with cryogenically induced damage in general, thermoplastic composites have received little attention, with no known studies investigating crack networks or permeability in cryogenically cycled CF/PEEK.

2.3 Numerical modelling of damage and permeability in laminates

Given the multi-phase nature of composite materials, modelling damage initiation and growth in composite structures is particularly challenging. In addition to the usual complexities inherent in the field of damage prediction, simulation of damage formation in composite materials must account for the action of multiple damage modes in multiple materials, often occurring simultaneously and interacting with one another. Recent developments in FEA and associated hardware have helped to considerably reduce the computational expense of composite damage simulations, leading to a corresponding jump in research in the area. Myriad methods of modelling inter- and intra-laminar failure have since been developed, with varying levels of success reported. A brief summary of the main simulation techniques used in the field follows.

2.3.1 Delamination modelling

Delamination, or inter-laminar failure, is perhaps the most studied composite damage mode. This is driven in part by the difficulty in detecting the presence of

delamination in laminates, thus requiring robust predictive methodologies to design against failure. However, delamination is arguably one of the more straightforward composite damage modes to model due to crack growth largely being confined to a pre-defined, planar area. Detailed reviews of delamination modelling, encompassing a wide range of inter-related techniques including damage mechanics, fracture mechanics and cohesive zone approaches, have been carried out by the following authors [70-74]. In terms of the FE implementation of these techniques, two methods stand out as being the most widely used: a linear elastic fracture mechanics (LEFM) approach (often using a form of the Virtual Crack Closure Technique (VCCT)) and a cohesive interface approach using the concepts of damage mechanics.

LEFM, which follows from Griffith's original work [75], relies on predicting crack growth based on the energy required to create a new fracture surface in a material. For composite materials, a material parameter G_c is often quoted, which represents the ability of the material to resist fracture. Numerical simulations of crack propagation using this method calculate the strain energy release rate (SERR), also G, at the crack front and compare it to G_c of the composite, with growth occurring if $G > G_c$. The VCCT [76, 77] is a popular and robust non-singular-field method of applying LEFM principles to the FE modelling of delamination in composites and bi-material interfaces in general. The technique is based on the premise that the strain energy required to open a new crack surface by a certain length is the same as the energy required to close the crack by the same length. The strain energy release rate at the crack tip is calculated as a function of the force at the tip and the crack opening displacement (COD). If $G > G_c$, then nodal separation (delamination) will occur.

Recently, Wimmer [79] and Krueger [80, 81] have investigated the use of the VCCT in commercial FE software packages for static and fatigue delamination of composites, with reasonable success. However, the use of the technique with a conventional finite element mesh can limit the value of the approach, as summarised in [74]. LEFM-based methods require crack growth to initiate from a pre-defined crack seam or flow, about which the mesh must conform. The level of mesh-refinement and the associated transverse cracking in adjacent plies may also influence the solution.

A damage mechanics approach to crack growth modelling relates the increase in damage in a material to the reduction in certain material properties, such as stiffness. The principles of damage mechanics are often implemented in FEA though the use of a cohesive zone or elements along the ply interface of a laminate [82-85]. Unlike the VCCT, cohesive zone modelling doesn't require extensive mesh refinement or re-meshing to account for crack growth. The approach also allows the modelling of both damage initiation and progression, with a reduction in element stiffness usually occurring after initiation in accordance with a pre-defined damage evolution law.

Research in the field has also progressed to incorporating aspects of fracture mechanics theory into the cohesive approach [86, 87], whereby the work done in reducing the stiffness of a cohesive element directly corresponds to the critical energy release rate of the material. One of the main issues with using cohesive models is the difficulty in determining appropriate damage evolution and stiffness relations, some of which cannot be obtained experimentally. Also, like the VCCT, the cohesive approach within conventional FEA generally relies on a pre-defined crack growth path. While this is not always a critical issue for planar damage modes such as delamination, it does limit the flexibility of the approach.

The recent development of the extended finite element method (XFEM) [88], which incorporates concepts relating to the partition of unity [89] in the finite element mesh, offers an alternative to the aforementioned techniques. With this method, crack growth is no longer confined to element boundaries or special purpose interface elements, allowing the modelling of arbitrary crack formation and growth without the need to pre-define the path or constantly re-mesh the area of interest. Both methods of crack modelling outlined above are also possible using this approach [90, 91]. Due to the novelty of the approach, research into static [92-96] and particularly fatigue delamination [97, 98] using XFEM is quite sparse. A further description of the method is provided in Section 2.3.2.

2.3.2 Microcracking and combined damage models

Intra-ply failure modes are often treated in a separate manner from delamination. The range of failure modes which can occur at a ply level, in terms of both matrix

and fibre failure, means the modelling of discrete fracture processes at a meso-level is a complex task. However, extensive effort has been invested into ply-level failure theories for many years. Numerous failure criteria have been developed taking into account fibre and matrix failure in tension and compression including the commonly used criteria developed by Hashin [99], Tsai-Wu [100] and Puck [101]. A detailed review of ply-level failure criterion is available in [73]. The FE implementation of such a continuum approach typically involves smearing damage over the mesh, without modelling physical cracking. While such methods can be used in combined composite damage simulation [102-104], without the ability to model COD and the presence of overlapping crack networks they have limited use in permeability prediction simulations.

Given the focus on sub-critical damage formation for permeability modelling, matrix microcracking and its interaction with delamination are prioritised. Matrix microcracking presents a particular problem for conventional modelling techniques due to its inherently random nature. The method of pre-defining crack propagation areas and paths, as is often done for delamination, has been applied to transverse cracking [105-108]. However, realistic 3-D simulations cannot be reasonably undertaken through this a-priori definition of crack paths using interface elements. As introduced in the previous section, the recent development of XFEM and partition of unity methods in general have helped to alleviate some of the issues inherent in microcrack modelling. With XFEM, the discontinuity is defined separately from the mesh, allowing a crack of arbitrary shape and location to be modelled effectively without re-meshing and without the usual extensive mesh refinement required to pre-define the discontinuity.

The enrichment functions for a general crack growth problem are contained in the finite element approximation of the displacement field and typically comprise of functions which capture the singularity at a crack tip and represent the displacement jump between crack faces. The flexibility this technique offers has paved the way for more realistic and sophisticated methods of simulating microcracking [110], as well as a small number of fully fledged meso-level combined damage models. Work by der Meer, Ahmed and Sluys [111-113] at the Delft research group is prominent in this new area. Combined microcracking and delamination models, based on phantom node and cohesive element methods respectively, show good agreement with

mechanical tensile and impact tested physical specimens. Microcrack initiation is determined by a pre-defined crack-spacing parameter, with cracks being inserted parallel to fibres upon initiation. However, it is not clear if this spacing parameter has a firm basis in the physical reality of the material. It is also not clear as to what extent the physical crack opening of propagated cracks is accounted for, as well as the interaction between overlapping cracks. The use of a custom FE code and interface elements at each ply also has implications for the flexibility and scalability of the model. A mesh-independent combined damage model has also been developed by Iarve *et al* [114, 115]. The model was shown to capture many of the damage trends associated with several mechanical load types, including interaction between microcracks and delamination. Matrix cracks are inserted into the mesh based on a random distribution of strengths, which is seen as broadly representative of the physical phenomena driving random crack growth. Again, it is not clear how capable the model is to represent distinct COD values, with the traditional XFEM Heaviside discontinuous step function being replaced by a continuous function, resulting in cracks surfaces being replaced with a gradient zone. However, efforts from both the Delft group and Iarve *et al* have helped place such combined numerical damage models to the fore of meso-level damage simulation, with widespread adoption of similar techniques envisaged.

2.3.3 Permeability prediction

Predicting the permeability of composite laminates based on numerical damage models represents a significant challenge due to the highly complex damage formation and interaction mechanisms. Discrete cracking needs to be modelled in order to determine COD values, ruling out many well established continuum damage modelling techniques [116]. As mentioned in the previous section, combined damage models capable of simulating intra- and inter-laminar remain extremely sparse, with no known technique proven capable of simulating the formation of crack opening and overlap areas through the thickness of laminates. For this reason, existing permeability models rely on a unit-cell approach to permeability prediction, based on pre-defined microcracks and delaminations.

2. Background

Early work in the area was carried out by Roy and Benjamin [117], who, based on an existing theoretical approach [118], predicted the opening displacement of transverse cracks, using ply crack density and adjoining delamination length as input for prescribed thermal and mechanical loads. They also modelled the through-thickness delaminated crack opening displacement (DCOD) distribution for a composite, subjected to thermal and mechanical loading, using both a mathematical model and a two-dimensional FE model of a composite laminate. These models were then used to predict laminate permeability based on the existence of overlap areas between transverse cracks and delaminations. Using crack densities taken from [65] and an estimation of the variation of delamination length with thermal cycles as input, Nair and Roy [119] developed a repeating two-dimensional FE unit cell geometry. Permeability predictions based on this model were then compared to experimental results from [65] with reasonable success. However, no experimental verification of the COD predictions was given. Yokozeki *et al* [67, 68] have also developed a basic analytical method to determine trends in gas leakage based on experimental inputs. Experimental trends were captured quite well for gas leak through tensile specimens except for cases where delamination was known to play a role in crack opening. The models predicted an inverse relationship between crack overlap angle and leak rate.

A small number of more sophisticated, three-dimensional FE based unit-cell models have also been developed recently [120-122], which rely on variation of parameters, such as crack density and delamination length, to determine their effect on laminate permeability. As expected, these models consistently predict greater permeability with increased crack density, as well as wider crack openings in the presence of delamination. Such unit-cell models have also been used in conjunction with fluid analyses in order to determine leak rate trends [123, 124]. However, due to the sensitivity of predictions to many parameters including crack morphology and assumed delamination lengths, leak rate predictions were often found to exceed experimental observations. The dependency of these modelling techniques (Fig. 2.7) on experimental input in the form of delamination length and crack density seriously limits their applicably to large scale damage and permeability simulations. This is further compounded by the lack of published data on the role of delamination in COD and crack network formation in general. Random microcrack initiation, delamination growth and the interaction between various damage modes are all

critical to predicting laminate permeability. Thus, the need for a flexible, three-dimensional globally-applicable modelling technique, capable of capturing the interaction between random intra- and inter-laminar cracking, is essential to progress in the area.
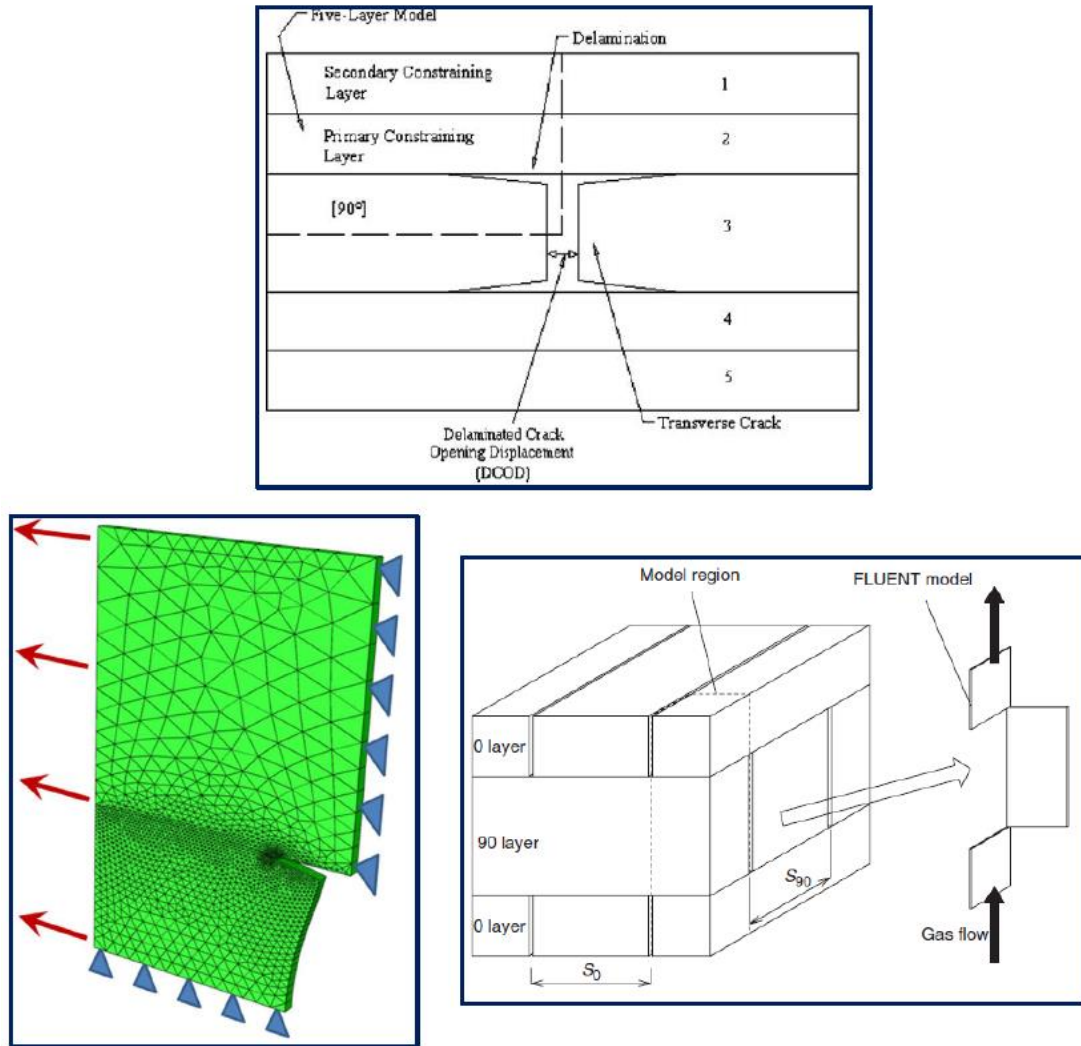

Figure 2.7 Selection of images showing the current state-of-the-art for laminate permeability prediction models. A common theme among existing simulation techniques is a unit-cell approach to analysis, based on pre-defined microcracks and delaminations at crack overlap areas. Clockwise from top: [119], [124] and [122].

2.4 References

[1] Liu L., Zhang B.M., Wang D.F. & Wu Z.J. Effects of cure cycles on void content and mechanical properties of composite laminates. *Composite Structures*, **73**, 303-309, 2006.

[2] Bowles K.J. & Frimpong S. Void effects on the interlaminar shear strength of unidirectional graphite-fiber-reinforced composites. *Journal of Composite Materials*, **26**(10), 1487-1509, 1992.

[3] Hernánderz S., Sket F., Molina-Aldareguia J.M. & González C. Effect of curing cycle on void distribution and interlaminar shear strength in polymer-matrix composites. *Composites Science and Technology*, **71**(10), 1331-1341, 2011.

[4] Madsen B. & Lilholt H. Physical and mechanical properties of unidirectional plant fibre composites—an evaluation of the influence of porosity. *Composites Science and Technology*, **63**, 1265-1272, 2003.

[5] Zhu H., Wu B., Dihong L., Zhang D. & Chen Y. Influence of voids on the tensile performance of carbon/epoxy fabric laminates. *Journal of Materials Science & Technology*, **27**(1), 69-73, 2011.

[6] De Almeida S.F.M & Neto Z.S.N. Effect of void content on the strength of composite laminates. *Composite Structures*, **28**, 139-148, 1994.

[7] Hatta H., Takei T. & Taya M. Effects of dispersed microvoids on thermal expansion behavior of composite materials. *Materials Science and Engineering*, **A285**, 99-110, 2000.

[8] Zhuang L. & Talreja R. Effects of voids on postbuckling delamination growth in unidirectional composites. *International Journal of Solids and Structures*, **51**(5), 936-944, 2014.

[9] Ricotta M., Quaresimin M. & Talreja R. Mode I strain energy release rate in composite laminates in the presence of voids. *Composites Science and Technology*, **68**(13), 2616-2623, 2008.

[10] Huang H. & Talreja R. Effects of void geometry on elastic properties of unidirectional fiber reinforced composites. *Composites Science and Technology*, **65**(13), 1964-1981, 2005.

[11] Little J.E., Yuan X. & Jones M.I. Characterisation of voids in fibre reinforced composite materials. *NDT&E International*, **46**, 122-127, 2014.

[12] Standard test methods for constituent content of composite materials. Designation D3171–09. American Society for Testing of Materials (ASTM).

[13] Paciornik S. & D'Almeida J.R.M. Measurement of void content and distribution in composite materials through digital microscopy. *Journal of Composite Materials*, **43**(2), 101-112, 2009.

[14] Nikishkov Y., Airoldi L. & Makeev A. Measurement of voids in composites by X-ray computed tomography. *Composites Science and Technology*, **89**, 89-97, 2013.

[15] Lambert J., Chambers A.R., Sinclair I. & Spearing S.M. 3D damage characterisation and the role of voids in the fatigue of wind turbine blade materials. *Composites Science and Technology*, **72**, 337-343, 2012.

[16] Nikishkov Y., Seon G. & Makeev A. Structural analysis of composites with porosity defects based on X-ray computed tomography. *Journal of Composite Materials*, **48**(17), 2131-2144, 2014.

[17] Williams J.J, Flom Z., Amell A.A., Chawla N., Xiao X. & De Carlo F. Damage evolution in SiC particle reinforced Al alloy matrix composites by X-ray synchrotron tomography. *Acta Materialia* **58**, 6194-6205, 2010.

[18] Feraboli P., Cleveland T., Ciccu M., Stickler P. & DeOto L. Defect and damage analysis of advanced discontinuous carbon/epoxy composite materials. *Composites Part A: Applied Science and Manufacturing*, **41**, 888-901, 2010.

[19] Callus P.J., Mouritz A.P., Bannister M.K. & Leong K.H. Tensile properties and failure mechanisms of 3D woven GRP composites. *Composites Part A: Applied Science and Manufacturing*, **30**, 1277-1287, 1999.

2. Background

[20] Mahadik Y., Brown K.A.R. & Hallett S.R. Characterisation of 3D woven composite internal architecture and effect of compaction. *Composites Part A: Applied Science and Manufacturing*, **41**(7), 872-880, 2010.

[21] Liotier P.J., Alain V. & Christine D. Characterization of 3D morphology and microcracks in composites reinforced by multi-axial multi-ply stitched preforms. *Composites Part A: Applied Science and Manufacturing*, **41**, 653-662, 2010.

[22] Parlevliet P.P, Bersee H.E.N. & Beukers A. Residual stresses in thermoplastic composites—A study of the literature—Part I: Formation of residual stresses. *Composites Part A: Applied Science and Manufacturing*, **37**, 1847-1857, 2006.

[23] Parlevliet P.P, Bersee H.E.N. & Beukers A. Residual stresses in thermoplastic composites—A study of the literature—Part II: Experimental techniques. *Composites Part A: Applied Science and Manufacturing*, **38**, 651-665, 2007.

[24] Parlevliet P.P, Bersee H.E.N. & Beukers A. Residual stresses in thermoplastic composites – a study of the literature. Part III: Effects of thermal residual stresses. *Composites Part A: Applied Science and Manufacturing*, **38**, 1581-1596, 2007.

[25] Jeronimidis G. & Parkyn A.T. Residual stresses in carbon fibre-thermoplastic matrix laminates. *Journal of Composite Materials*, **22**(5), 401-415, 1988.

[26] Chapman T.J., Gillespie J.W., Pipes R.B., Manson J.A.E. & Seferis J.C. Prediction of process-induced residual stresses in thermoplastic composites. *Journal of Composite Materials*, **24**(6), 616-643, 1990.

[27] Unger W.J. & Hansen J.S. The effect of thermal processing on residual strain development in unidirectional graphite fibre reinforced PEEK. *Journal of Composite Materials*, **27**(1), 59-82, 1993.

[28] Wang C. & Sun C.T. Thermoelastic behavior of PEEK thermoplastic composite during cooling from forming temperatures. *Journal of Composite Materials*, **31**(22), 2230-2248, 1997.

[29] Domb M.M. & Hansen J.S. The effect of cooling rate on free-edge stress development in semi-crystalline thermoplastic laminates. *Journal of Composite Materials*, **32**(4), 361-386, 1998.

[30] Bruno J.W. Micro-cracking evaluation of high modulus-graphite/epoxy (HM-Gr/Ep) under combined thermal and load cycling. *Proceedings of the 47th SAMPE International Symposium*, Long Beach, CA, USA, 222–235, 2002.

[31] Gillespie J.W. & Chapman T.J. The influence of residual stresses on Mode I interlaminar fracture of thermoplastic composites. *Journal of Thermoplastic Composites*, **6**(2), 160-174, 1993.

[32] Nairn J.A., Hu S. & Bark J.S. A critical evaluation of theories for predicting microcracking in composite laminates. *Journal of Material Science*, **28**, 5099-5111, 1993.

[33] Bechel V.T., Fredin M.B., Donaldson S.L., Kim R.Y. & Camping J.D. Effect of stacking sequence on micro-cracking in a cryogenically cycled carbon/bismaleimide composite. *Composites Part A: Applied Science and Manufacturing*, **34**, 663-672, 2003.

[34] Kellas S., Morton J. & Jackson K. Damage and failure mechanisms in scaled angle-ply laminates. *Composite Materials: Fatigue and Fracture*, **4**, 257-280, 1993.

[35] Parvizi A., Garrett K.W. & Bailey J.E. Constrained cracking in glass fiber-reinforced epoxy cross-ply laminates. *Journal of Materials Science*, **13**, 195-201, 1978.

[36] Flaggs D.L. & Kural M.H. Experimental determination of the in situ transverse lamina strength in graphite/epoxy laminates. *Journal of Composite Materials*, **16**(2), 103-116, 1982.

[37] Fukunaga H., Chou T., Peters P.W.M & Schulte K. Probabilistic failure strength analyses of graphite/epoxy cross-ply laminates. *Journal of Composite Materials*, **18**(4), 339-356, 1984.

[38] Peters P.W.M. The strength distribution of 90° plies in 0/90/0 graphite-epoxy laminates. *Journal of Composite Materials*, **18**(6), 545-556, 1984.

[39] Berthelot J.M. & Le Corre J.F. Statistical analysis of the progression of transverse cracking and delamination in cross-ply laminates. *Composites Science and Technology*, **60**, 2659-2669, 2000.

[40] Pagano N.J., Schoeppner G.A., Kim R. & Abrams F.L. Steady-state cracking and edge effects in thermo-mechanical transverse cracking of cross-ply laminates. *Composites Science and Technology*, **58**(11), 1811-1825, 1998.

[41] Johnson P. & Chang F.K. Characterization of matrix crack-induced laminate failure - Part II: Analysis and verifications. *Journal of Composite Materials*, **35**(22), 2037-2074, 2001.

[42] Berthelot J.M., Mahi A.E. & Le Corre J.F. Development of transverse cracking in cross-ply laminates during fatigue tests. *Composites Science and Technology*, **61**(12), 1711-1721, 2001.

[43] Yokozeki T., Aoki T. & Ishikawa T. Transverse crack propagation in the specimen width direction of CFRP laminates under static tensile loadings. *Journal of Composite Materials*, **36**(17), 2085-2099, 2002.

[44] Kessler S.S., Matuszeski T. & McManus H. Cryocycling and mechanical testing of CFRP for X-33 liquid H_2 fuel tank structure. *Proceedings of the 16th ASC Technical Conference*, Blacksburg, VA, USA, 2001.

[45] Bechel V.T. & Kim R.Y. Damage trends in cryogenically cycled carbon/polymer composites. *Composites Science and Technology*, **64**(12), 1773-1784, 2004.

[46] Henaff-Gardin C., Lafarie-Frenot M.C. & Gamby D. Doubly periodic matrix cracking in composite laminates Part 2: Thermal biaxial loading. *Composite Structures*, **36**, 131-140, 1997.

[47] Timmerman J.F., Hayes B.S. & Seferis J.C. Cure temperature effects on cryogenic microcracking of polymeric composite materials. *Polymer Composites*, **24**(1), 132-139, 2003.

[48] Park C.H. & McManus H.L. Thermally induced damage in composite laminates: Predictive methodology and experimental investigation. *Composites Science and Technology*, **56**, 1209-1219, 1996.

[49] Escoto J.I. Preliminary test method development and characterization of candidate composites for cryogenic tanks. *Thesis: Master of Science in Engineering.* Prairie View A&M University; USA, 2002.

[50] Kim R.Y. & Donaldson S.L. Experimental and analytical studies on the damage initiation in composite laminates at cryogenic temperatures. *Composite Structures*, **76**, 62-66, 2006.

[51] Shindo Y., Sato T., Narita F. & Sanada K. Mode II interlaminar fracture and damage evaluation of GFRP woven laminates at cryogenic temperatures using the 4ENF specimen. *Journal of Composite Materials*, **42**(11), 1089-1101, 2008.

[52] Melcher R.J. & Johnson W.S. Mode I fracture toughness of an adhesively bonded composite–composite joint in a cryogenic environment. *Composites Science and Technology*, **67**, 501-506, 2007.

[53] Timmerman J.F., Tillman M.S., Hayes B.S. & Seferis J.C. Matrix and fiber influences on the cryogenic microcracking of carbon fiber/epoxy composites. *Composites Part A: Applied Science and Manufacturing*, **33**, 323-329, 2002.

[54] Timmerman J.F., Hayes B.S. & Seferis J.C. Cryogenic microcracking of carbon fiber/epoxy composites: Influences of fiber-matrix adhesion. *Journal of Composite Materials*, **37**(21), 1939-1950, 2003.

[55] Carlile D.R., Leach D.C., Moore D.R. & Zahlan N. Mechanical properties of the carbon fibre/PEEK composite APC-2/AS-4 for structural applications. *Advances in Thermoplastic Matrix Composite Materials,* ASTM STP **1044**, 199-212, 1989.

[56] Aoki T., Ishikawa T., Kumazawa H. & Morino Y. Mechanical behaviour of CF/polymer composite laminates under cryogenic environment. *Proceedings of the 12th International Conference on Composite Materials*, Paris, France, 1999.

[57] Im K., Cha C., Kim S. & Yang I. Effects of temperature on impact damages in CFRP composite laminates. *Composites Part B: Engineering*, **32**(8), 669-682, 2001.

[58] Kobayashi S., Terada K., Ogihara S. & Takeda N. Damage-mechanics analysis of matrix cracking in cross-ply CFRP laminates under thermal fatigue. *Composites Science and Technology*, **61**, 1735–1742, 2001.

[59] Bechel V.T., Camping J.D. & Kim R.Y. Cryogenic/elevated temperature cycling induced leakage paths in PMCs. *Composites Part B: Engineering*, **36**, 171-182, 2005.

[60] Jamison R.D., Schulte K., Reifsnider K.L. & Stinchcomb W.W. Characterization and analysis of damage mechanisms in tension-tension fatigue of graphite/epoxy laminates. *Effect of Defects in Composite Materials*, ASTM STP **836**, 21-55, 1984.

[61] Lavoie J.A. & Adolfsson E. Stitch cracks in constraint plies adjacent to a cracked ply. *Journal of Composite Materials*, **35**(23), 2077-2097, 2001.

[62] Kumazawa H., Hayashi H., Susuki I. & Utsunomiya T. Damage and permeability evolution in CFRP cross-ply laminates. *Composite Structures*, **76**, 73-81, 2006.

[63] Kumazawa H., Aoki T. & Susuki I. Influence of stacking sequence on leakage characteristics through CFRP composite laminates. *Composites Science and Technology*, **66**(13), 2107–2115, 2006.

[64] Choi S. & Sankar B.V. Gas permeability of various graphite/epoxy composite laminates for cryogenic storage systems. *Composites Part B: Engineering*, **39**(5), 782-791, 2008.

[65] Bechel V.T, Negilski M. & James J. Limiting the permeability of composites for cryogenic applications. *Composites Science and Technology*, **66**, 2284–2295, 2006.

[66] Yokozeki T., Aoki T., Ogasawara T. & Ishikawa T. Effects of layup angle and ply thickness on matrix crack interaction in contiguous plies of composite laminates. *Composites Part A: Applied Science and Manufacturing*, **36**(9), 1229-1235, 2005.

[67] Yokozeki T., Ogasawara T. & Ishikawa T. Evaluation of gas leakage through composite laminates with multilayer matrix cracks: Cracking angle effects. *Composites Science and Technology*, **66**(15), 2815–2824, 2006.

[68] Yokozeki T., Ogasawara T., Aoki T. & Ishikawa T. Experimental evaluation of gas permeability through damaged composite laminates for cryogenic tank. *Composites Science and Technology*, **69**(9), 1334–1340, 2009.

[69] Grenoble R.W. & Gates T.S. Hydrogen permeability of polymer matrix composites at cryogenic temperatures. *Proceeding of 46th AIAA/ASME/ASCE/AHS/ASC Structures, Structural Dynamics and Materials Conference*, Autin, Texas, USA, 2005.

[70] Garg A.C. Delamination - A damage mode in composite structures. *Engineering Fracture Mechanics*, **29**(5), 557-584, 1988.

[71] Tay T.E. Characterization and analysis of delamination fracture in composites: An overview of developments from 1990 to 2001. *Applied Mechanics Reviews*, **56**(1), 1-32, 2003.

[72] Elder D.J., Thomson R.S., Nguyen M.Q. & Scott M.L. Review of delamination predictive methods for low speed impact of composite laminates. *Composite Structures*, **66**, 677-683, 2004.

[73] Orifici A.C., Herszberg I. & Thomson R.S. Review of methodologies for composite material modelling incorporating failure. *Composite Structures*, **86**(1-3), 194-210, 2008.

[74] Pascoe J.A., Alderliesten R.C. & Benedictus R. Methods for the prediction of fatigue delamination growth in composites and adhesive bonds − A critical review. *Engineering Fracture Mechanics*, **112-113**, 72-96, 2013.

[75] Griffith A.A. The phenomena of rupture and flow in solids. *Philosophical Transactions of the Royal Society of London. Series A, Containing papers of a Mathematical or Physical Character*, **221**, 163-198, 1922.

[76] Rybicki E.F. & Kanninen M.F. A finite element calculation of stress intensity factors by a modified crack closure integral. *Engineering Fracture Mechanics*, **9**(4), 931-938, 1977.

[77] Raju I.S. Calculation of strain-energy release rates with higher order and singular finite elements. *Engineering Fracture Mechanics*, **28**(3), 251-274, 1987.

[78] Kumar A., Gopalakrishnan S. & Chakraborty A. Modified Virtual Crack-Closure Technique using Spectral Element Method. *International Journal of Computational Methods*, **4**(1), 109-139, 2007.

[79] Wimmer G., Schuecker C. & Pettermann H.E. Numerical simulation of delamination onset and growth in laminated composites. Austrian Aeronautics Research, Network for Materials and Engineering, ILDSB, Vienna University of Technology, 2006.

[80] Krueger R. Virtual crack closure technique: History, approach, and applications. *ICASE Report No. 2002-10*. National Aeronautics and Space Administration Langley Research Center, Hampton, Virginia, USA, 2002.

[81] Krueger R. Development of a Benchmark Example for Delamination Fatigue Growth Prediction. *NIA Report No. 2010-04*. National Aeronautics and Space Administration Langley Research Center, Hampton, Virginia, USA, 2010.

[82] Schellekens J.C.J. & De Borst R. A non-linear finite element approach for the analysis of mode-I free edge delamination in composites. *International Journal of Solids and Structures*, **30**(9), 1239-1253, 1993.

[83] Allix O., Ladevéze P. & Corigliano A. Damage analysis of interlaminar fracture specimens. *Composite Structures*, **31**(1), 61-74, 1995.

[84] Allix O. & Corigliano A. Modeling and simulation of crack propagation in mixed-modes interlaminar fracture specimens. *International Journal of Fracture*, **77**(2), 111-140, 1996.

[85] Chaboche J.L., Girard R. & Schaff A. Numerical analysis of composite systems by using interphase/interface models. *Computational Mechanics*, **20**(1-2). 3-11, 1997.

[86] Alfano G. & Crisfield M.A. Finite element interface models for the delamination analysis of laminated composites: mechanical and computational issues. *International Journal for Numerical Methods in Engineering*, **50**(7), 1707-1736, 2001.

[87] Turon A., Camanho P.P., Costa J. & Dávila C.G. A damage model for the simulation of delamination in advanced composites under variable-mode loading. *Mechanics of Materials*, **38**(11), 1072-1089, 2006.

[88] Belytschko T. & Black T. Elastic crack growth in finite elements with minimal remeshing. *International Journal for Numerical Methods in Engineering*, **45**, 601-620, 1999.

[89] Melenk J. & Babuška I. The partition of unity finite element method. *Tech Rep Research Report No 1996-01*, Eidgenössische Technische Hochschule, Seminar für Angewandte Mathematik, Zurich, Switzerland, 1996.

[90] Hibbitt D., Karlsson B. & Sorensen P. *Inc. ABAQUS/Standard User's Manual, v. 6.11*. Pawtucket, Rhode Island, USA, 2011.

[91] Moës N. & Belytschko T. Extended finite element method for cohesive crack growth. *Engineering Fracture Mechanics*, **69**(7), 813-833, 2002.

[92] Sosa J.L.C. & Karapurath N. Delamination modelling of GLARE using the Extended Finite Element Method. *Composites Science and Technology*, **72**(7), 788-791, 2012.

[93] Ashari S.E. & Mohammadi S. Delamination analysis of composites by new orthotropic bimaterial extended finite element method. *International Journal for Numerical Methods in Engineering*, **86**(13), 1507-1543, 2011.

[94] Campilho R.D.S.G., Banea M.D., Chaves F.J.P. & Da Silva L.F.M. eXtended finite element method for fracture characterization of adhesive joints in pure mode I. *Computational Materials Science*, **50**(4), 1543-1549, 2011.

[95] Motamedi D. & Milani A.S. 3D nonlinear XFEM simulation of delamination in unidirectional composite laminates: A sensitivity analysis of modeling parameters. *Open Journal of Composite Materials*, **3**(4), 113-126, 2013.

[96] Motamedi D., Milani A.S., Komeili M., Bureau M.N., Thibault F., Trudel-Boucher D. A stochastic XFEM model to study delamination in PPS/Glass UD composites: Effect of uncertain fracture properties. *Applied Composite Materials*, **21**(2), 341-358, 2014.

[97] Bacarreza O. & Aliabadi M.H. A Novel Methodology for Fatigue Delamination Growth Analysis of Composites. *Key Engineering Materials*, **488-489**, 763-766, 2011.

[98] Bhattacharya S., Singh I.V., Mishra B.K. & Bui T.Q. Fatigue crack growth simulations of interfacial cracks in bi-layered FGMs using XFEM. *Computational Mechanics*, **52**(4), 799-814, 2013.

[99] Hashin Z. Failure criteria for unidirectional fiber composites. *Journal of Applied Mechanics*, **47**(2), 329-334, 1980.

[100] Tsai S.W. & Wu E.M. A general theory of strength for anisotropic materials. *Journal of Composite Materials*, **5**(1), 58-80, 1971.

[101] Puck A. & Schürmann H. Failure analysis of FRP laminates by means of physically based phenomenological models. *Composites Science and Technology*, **58**(7), 1045-1067, 1998.

[102] Liu C.J., Nijhof A.H.J., Ernst L.J. & Marissen R. Modeling failure interaction in notched cross-ply laminates. *Journal of Composite Materials*, **42**(20), 2175-2193, 2008.

[103] Maimi P., Mayugo J.A. & Camanho P.P. A three-dimensional damage model for transversely isotropic composite laminates. *Journal of Composite Materials*, **42**(25), 2717-2745, 2008.

[104] Crouch R.D., Clay S.B. & Oskay C. Experimental and computational investigation of progressive damage accumulation in CFRP composites. *Composites Part B: Engineering*, **48**, 59-67, 2013.

[105] De Moura M.F.S.F & Gonçalves J.P.M. Modelling the interaction between matrix cracking and delamination in carbon–epoxy laminates under low velocity impact. *Composites Science and Technology*, **64**(7-8), 1021-1027, 2004.

[106] Yang Q. & Cox B. Cohesive models for damage evolution in laminated composites. *International Journal of Fracture*, **133**(2), 107-137, 2005.

[107] Okabe T., Nishikawa M. & Takeda N. Numerical modeling of progressive damage in fiber reinforced plastic cross-ply laminates. *Composites Science and Technology*, **68**(10-11), 2282-2289, 2008.

[108] Wisnom M.R. Modelling discrete failures in composites with interface elements. *Composites Part A: Applied Science and Manufacturing*, **41**(7), 795-805, 2010.

[109] Moës N., Dolbow J. & Belytschko T. A finite element method for crack growth without remeshing. *International Journal for Numerical Methods in Engineering*, **46**(1), 131-150, 1999.

[110] Hettich T., Hund A. & Ramm E. Modeling of failure in composites by X-FEM and level sets within a multiscale framework. *Computer Methods in Applied Mechanics and Engineering*, **197**(5), 414-424, 2008.

[111] Van der Meer F.P. & Sluys L.J. Mesh-independent modeling of both distributed and discrete matrix cracking in interaction with delamination in composites. *Engineering Fracture Mechanics*, **77**(4), 719-735, 2010.

[112] Ahmed A. & Sluys L.J. A three-dimensional progressive failure model for laminated composite plates subjected to transverse loading. *Engineering Fracture Mechanics*, **114**, 69-91, 2013.

[113] Ahmed A. & Sluys L.J. A computational model for the simulation of dynamic fracture in laminated composite plates. *Journal of Composite Materials*, DOI: 10.1177/0021998314539777, 2014.

[114] Iarve E.V. Mesh independent modelling of cracks by using higher order shape functions. *International Journal for Numerical Methods in Engineering*, **56**(6), 869-882, 2003.

[115] Iarve E.V., Gurvich M.R., Mollenhauer D.H., Rose C.A. & Dávila C.G. Mesh-independent matrix cracking and delamination modeling in laminated composites. *International Journal for Numerical Methods in Engineering*, **88**(8), 749-773, 2011.

[116] Ju J., Pickle B.D., Morgan R.J. & Reddy J.N. An initial and progressive failure analysis for cryogenic composite fuel tank design. *Journal of Composite Materials*, **41**(21), 2545-2568, 2007.

[117] Roy S. & Benjamin M. Modeling of permeation and damage in graphite/epoxy laminates for cryogenic fuel storage. *Composites Science and Technology*, **64**(13-14), 2051-2065, 2004.

[118] Zhang J., Fan J. & Hermann K.P. Delaminations induced by constrained transverse cracking in symmetric composite laminates. *International Journal of Solids and Structures*, **36**(6), 813-846, 1999.

[119] Nair A. & Roy S. Modeling of permeation and damage in graphite/epoxy laminates for cryogenic tanks in the presence of delaminations and stitch cracks. *Composites Science and Technology*, **67**(11-12), 2592-2605, 2007.

[120] Xu J. Prediction of gas permeability in composite laminates using three-dimensional finite elements. PhD Thesis, University of Florida, USA, 2007.

[121] Noh J., Whitcomb J., Oh B., Lagoudas D.C., Maslov K., Ganpatye A. & Kinra V. Numerical modeling, thermomechanical testing, and NDE procedures for prediction of microcracking induced permeability of cryogenic composites. *Fifth Conference on Aerospace Materials, Processing, and Environmental Technology (AMPET)*, Huntsville, USA, 2002.

[122] Bois C., Malenfant J.C., Wahl J.C. & Danis M. A multiscale damage and crack opening model for the prediction of flow path in laminated composite. *Composites Science and Technology*, **97**, 81-89, 2014.

[123] Peddiraju P., Noh J., Whitcomb J. & Lagoudas D.C. Prediction of cryogen leak rate through damaged composite laminates. *Journal of Composite Materials*, **41**(1), 41-71, 2007.

[124] Kumazawa H. & Whitcomb J. Numerical modeling of gas leakage through damaged composite laminates. *Journal of Composite Materials*, **42**(16), 1619-1638, 2008.

3. A 2-D XFEM-based methodology for fatigue delamination and permeability of composites

Article overview

This work introduces the use of a mesh-independent XFEM crack growth technique for the prediction of fatigue delamination and permeability of composite laminates. As the first published work of this thesis, this study focuses on enhancing existing two-dimensional unit cell methods of permeability calculation through the use of a novel XFEM-based methodology. Previous studies have relied on the estimation of delamination length for a given unit cell, with subsequent DCOD and gas leakage simulations being dependent on this assumed length. In addition, any growth in the delamination due to repeated thermal cycles was unaccounted for, adversely affecting the accuracy of permeability predictions. The key novelty of this work is to remove the uncertainty of delamination length from permeability calculations. This is achieved through the use of a crack modelling methodology which does not require defining the delamination location a-priori and can simulate static and fatigue crack initiation and growth effectively with minimal computational expense.

Before detailed simulations of unit cell structures are presented, several test cases involving various modes of static and fatigue loading are described in order to validate the methodology. Although an XFEM approach to crack modelling offers

greater flexibility and efficiency over conventional techniques, due to its novelty it remains relatively under-studied in the literature. Simulations of standardised Mode I and Mode II fracture tests are conducted and compared directly to experimental results for a CF/PEEK material. More complex mixed-mode thermo-mechanical fatigue cases are also modelled and compared with published results. Finally, the technique is applied to established unit cell models, where fatigue delamination growth under cryogenic conditions representative of fuel tank loading is simulated. The resulting effect of delamination growth on DCOD and permeability is also predicted.

Abstract

Carbon fibre reinforced polymers (CFRP) are one of the prospective material families being investigated for use in the fuel tanks of future reusable space launch vehicles (RSLVs). The extreme thermo-mechanical loading that these structures experience can lead to damage build-up in the CFRP in the form of microcracking and delamination, which can lead to increased laminate permeability. This work presents a novel XFEM-based methodology for the combined simulation and prediction of thermal fatigue delamination for identification of delaminated crack opening displacement (DCOD) and, hence, composite laminate permeability. The methodology is validated through simulation of standardised static and fatigue delamination test methods, using low computational cost modelling techniques. Delamination growth in a quasi-isotropic laminate under cryogenic fatigue loading is used to examine the effects of initial interlaminar defects on subsequent crack growth, as well as the relationship between delamination length and material permeability based on DCOD values predicted by the new methodology.

3.1 Introduction

Fibre-reinforced composites are candidate materials for the next generation of reusable space launch vehicles (RSLVs). The drive to replace conventional metal alloys with alternative materials stems from the need to reduce the cost of

transporting a payload to orbit, which currently stands at around $20,000 per kg [1]. The high specific strength, specific stiffness, toughness and chemical resistance of composites such as carbon fibre reinforced polymers (CFRP) make them ideal for many structural components of RSLVs, in particular the fuel tanks which are used to store liquid hydrogen and liquid oxygen at cryogenic temperatures. Unlike current designs, the fuel tanks for RSLVs are anticipated to undergo numerous fuelling/refuelling and take-off/landing cycles, with the inner walls of the tank being exposed to temperatures as low as -250 °C. The extreme thermo-mechanical cycling resulting from such a regime can lead to severe damage accumulation in the CFRP in the form of microcracking and delamination, possibly resulting in permeation of the cryogen through the tank wall due to interaction between these damage modes as shown in Fig. 3.1.
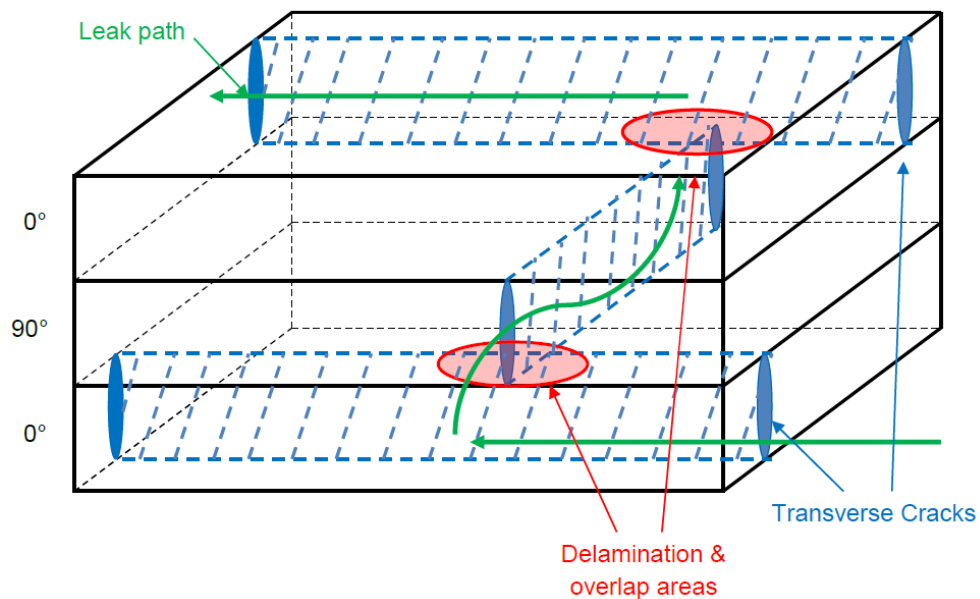
Figure 3.1 Schematic of a permeation path through a composite laminate resulting from the overlap area between adjacent transverse microcracks and delaminations.

The ability to model and predict the degradation of composites under thermal/mechanical fatigue loading is a key step in the design of efficient and safe cryogenic fuel tanks, as well as aerospace components in general. The effect of microcracking on the properties of composites, as well as its role in the development of other laminate failure modes, such as delamination, has been well documented

[2]. Zhang et al. [3] took a theoretical approach to investigating delaminations induced by transverse microcracking in composite laminates, using first-order shear laminate theory in their analysis. Roy and Benjamin [4, 5] built on this work to predict the opening displacement of transverse cracks, based on prescribed thermal and mechanical loads, as well as ply crack density and adjoining delamination length. They also predicted the through-thickness delaminated crack opening displacement (DCOD) distribution for a composite, subjected to thermal and mechanical loading, using both a mathematical model and a 2-D FE model of a composite laminate. These models were then used to predict laminate permeability based on the existence of overlap areas between transverse cracks and delaminations in the aforementioned leakage paths. Nair and Roy [6] went further and compared the permeability predicted by the FE models, which used crack densities taken from Bechel et al. [7] and an estimation of the variation of delamination length with thermal cycles as input, with experimental data from the same source with reasonable success.

The above studies rely on assuming a delamination length for a given number of thermal cycles. This is, in part, due to the difficulties in monitoring delamination growth in composite laminates [8, 9], where unlike transverse cracks, the delaminations are typically closed and difficult to locate and measure. However, the delamination length at the tips of transverse cracks has been shown to be an important factor in the determining the magnitude of DCOD and, hence, laminate permeability [4-6,10]. A method of predicting the growth of delaminations at overlap areas under thermal/mechanical loading will lead to more efficient modelling of damage progression in composite laminates, as well as greater accuracy in permeability predictions.

The area of composite failure simulation has been widely published on, and includes a number of delamination growth prediction models. The approach for the meso-level modelling of interlaminar failure has typically revolved around the development of analytical and numerical solutions involving a pre-defined interface [11-16], as well the use of specially devised constitutive equations and finite elements to simulate delamination growth and interaction between various damage modes [17-19]. This current work involves the meso-modelling of delamination growth in a CFRP laminate under cryogenic fatigue loading in order to predict the

DCOD of transverse microcracks and, hence, laminate permeability. The key novelty of this work centres on the use of the Virtual Crack Closure Technique (VCCT), in conjunction with the extended finite element method (XFEM), in order to predict the variation in DCOD with increasing delamination length, with minimal computational cost. This methodology is also used to predict the influence of existing interlaminar defects on subsequent fatigue delamination growth under cryogenic loading. Although XFEM is a relatively novel technique in the area of composite fracture mechanics, a number of studies [20, 21] into the use of this technique for static and fatigue delamination modelling, as well work on the development of bimaterial orthotropic enrichment functions for use with XFEM [22], have been conducted. However, it is understood that these studies rely on non-standard finite element platforms and do not cover the range of load cases nor the applications presented in this work. A globally applicable XFEM platform was a prerequisite for this study, due to the 3-D requirements for modelling large-scale fuel storage tanks and material defect distributions which will form the basis of future work.

The novel XFEM-based methodology for prediction of DCOD and delamination growth trends under thermal fatigue loading was validated using recognised test cases, involving thermal and mechanical loads, in both static and fatigue loading regimes. Static double cantilever beam (DCB) and end notch flexure (ENF) tests were used as a starting point for the study, with predicted crack growth from these models being compared with experimental test data for CF/PEEK specimens. Sub-critical loading scenarios, in the form of mechanical and thermal fatigue loading of composite laminates, were validated against analytical and experimental data from the literature. Subsequently, the modelling of delamination growth in a quasi-isotropic laminate under cryogenic fatigue loading was conducted in order to predict DCOD and, hence, composite laminate permeability.

3.2. Methodology

3.2.1 Delamination modelling methodology

The extended finite element method (XFEM) is an extension of the classical finite element method, based on the concept of partition of unity [23], which allows modelling of discontinuities through the use of special enrichment functions which are incorporated into the finite element approximation. XFEM was introduced by Belytschko and Black [24] as an alternative to modelling crack growth problems, but is useful in modelling material abstractions in general, such as voids, grain boundaries and dislocations [25, 26]. Conventional methods of analysing such discontinuities require that the finite element mesh conforms to the discontinuity. This becomes an issue when modelling crack growth, where the dimensions of the discontinuity may change considerably over the course of the analysis, meaning that constant re-meshing must be undertaken in order to represent the growing crack. With XFEM, the discontinuity is defined separately from the mesh, allowing a crack of arbitrary shape and location to be modelled effectively without re-meshing and without the usual extensive mesh refinement required to pre-define the discontinuity [27]. This gives XFEM a key advantage over alternative analysis methods where the computational expense of continuous re-meshing can add greatly to the model run time.

The enrichment functions for a general crack growth problem are contained in the finite element approximation of the displacement field and typically comprise of functions which capture the singularity at a crack tip and represent the displacement jump between crack faces. From the work of Moes et al. [28], the XFEM displacement vector function for a crack, $\boldsymbol{u}$, is given as

$$u = \sum_{i=1}^{N} N_i(x) \left\{ u_i + H(x)a_i + \sum_{k=1}^{4} F_k(x)b_i^k \right\} \tag{3.1}$$

where $N_i(x)$ are finite element nodal shape functions, $\boldsymbol{u}_i$ is the displacements of the nodes associated with the continuous part of the solution, $H(x)$ is the Heaviside function which deals with the discontinuous jump across crack faces, $\boldsymbol{a}_i$ and $\boldsymbol{b}_i^k$ are

nodal enriched degree of freedom vectors and $F_k(x)$ are the near-tip asymptotic functions for representing the singularity near the crack tip. A typical finite element mesh with a smooth crack introduced is shown in Fig. 3.2.
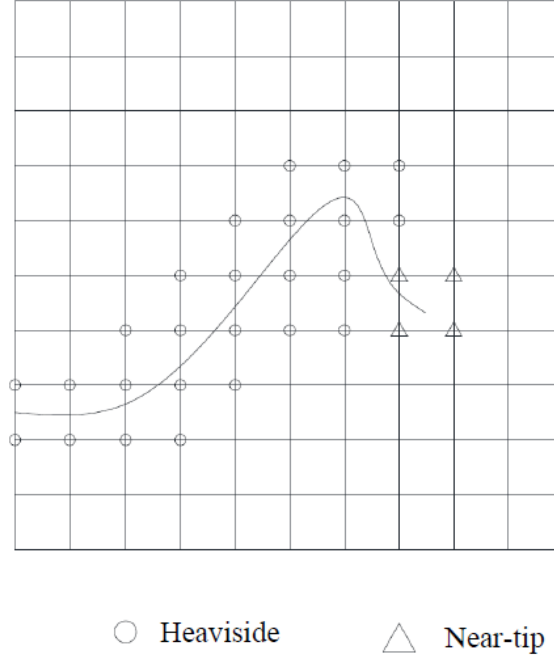

○ Heaviside   △ Near-tip

Figure 3.2 Schematic of a typical finite element mesh with a crack introduced, showing the enrichment functions relating to specific parts of the crack geometry.

The Heaviside enrichment function, which is used to represent the discontinuity present between separated crack surfaces, is described by Eq. 3.2 [29],

$$H(x) = \begin{cases} 1 & when \quad (x - x^*).n \geq 0 \\ -1 & otherwise \end{cases} \qquad (3.2)$$

where x is a Gauss point, x^* is the point on the crack nearest x and n is the unit normal to the crack at the position x^*. This function is used to describe areas of mesh cut by the main body of the crack. For 2-D areas cut by the tip of the crack, the enrichment functions shown in Eq. 3.3 are used,

$$F_k(x) = \left[\sqrt{r}\sin{\theta/2}, \sqrt{r}\cos{\theta/2}, \sqrt{r}\sin\theta\sin{\theta/2}, \sqrt{r}\sin\theta\cos{\theta/2}\right] \quad (3.3)$$

where (r, θ) are the polar coordinates of a system with its origin defined at the crack tip. This set of equations form the basis of a general 2-D crack analysis using XFEM.

In this work, the new fatigue delamination methodology is developed with the commercial finite element software, *Abaqus implicit v6.11* [29]. A globally applicable XFEM platform is essential due to the 3-D requirements for modelling large-scale fuel storage tanks and material defect distributions which will require crack propagation analysis to be undertaken via a user interface, without compromising the functionality of the basic finite element package.

The modelling of stationary cracks proceeds using the XFEM approach outlined above; however, for moving cracks a different approach is adopted. Keeping track of where the crack propagates is difficult, due to the degree of the crack singularity depending on the crack location for non-isotropic materials [29]. This approach relies on only considering the displacement jump across the crack faces, with the near tip enrichment functions not being used; hence, the stress singularity around the crack tip is not modelled. In real terms, this has the effect of the crack moving through a whole element at a time. To achieve this, phantom nodes are employed to represent the jump in crack surfaces, where real and corresponding phantom nodes separate when the prescribed fracture criterion has been satisfied. The phantom nodes are originally superimposed on the base element nodes and are fully constrained until damage initiation. The level set method is used to describe the crack geometry using two signed distance functions for the crack front and crack surface. This method is used to compute the interface motion of the crack between enriched elements. This approach is robust and exhibits minimal mesh dependence for adequately meshed models [29]. The degree of separation of the nodes is determined by the traction-separation cohesive behaviour, whereby the cohesive strength of an enriched element with a crack through it decreases to zero in accordance with the prescribed traction-separation law. The traction–separation model used is comprised of a linear elastic behaviour phase and a subsequent damage progression phase [29]. The constitutive matrix for the elastic phase, relating the stresses and separations in an enriched element are given by Eq. 3.4

3. A 2-D XFEM-based methodology for fatigue delamination and permeability of composites

$$\begin{Bmatrix} t_n \\ t_s \\ t_t \end{Bmatrix} = \begin{bmatrix} K_{nn} & 0 & 0 \\ 0 & K_{ss} & 0 \\ 0 & 0 & K_{tt} \end{bmatrix} \begin{Bmatrix} \delta_n \\ \delta_s \\ \delta_t \end{Bmatrix} \tag{3.4}$$

where t_n, t_s and t_t are the normal and shear components of the stress traction vector, K_{nn}, K_{ss} and K_{tt} are the stiffness components that relate the element stresses to separations and δ_n, δ_s and δ_t are the element separations related to the aforementioned normal and shear stresses.

The VCCT, using the principles of linear elastic fracture mechanics, is used for the damage progression analysis. This technique has been used to model delamination propagation along predefined surfaces successfully [30, 31] and is suitable for modelling quasi-brittle composites such as CF/PEEK. However, the version employed here does not require knowledge of the crack location or propagation path *a-priori*, allowing the user to forego costly mesh refinement and continual updating of the mesh in the area of interest. This feature is also critical to the ability of the methodology to predict crack growth due to random inherent material defects in composite laminates, which will form the basis of future work. The technique is based on the premise that the strain energy required to open a new crack surface by a certain length is the same as the energy required to close the crack by the same length. For XFEM crack growth, this new crack surface length corresponds to the enriched element length ahead of the crack front. The strain energy release rate at the crack tip is calculated as a function of the force at the tip and the COD. The relation for a Mode I crack growth situation is given by Eq. 3.5 [32],

$$G_I = \frac{1}{2\Delta a}(FV) \tag{3.5}$$

where G_I is the Mode I energy release rate, Δa is the crack extension, F is the vertical force between nodes i and i^*, and V is the vertical displacement between nodes $(i-1)$ and $(i-1)^*$ as shown in Fig. 3.3. Similar methods are used in determining Mode II and mixed-mode response with the VCCT (see A.1 for more detail).
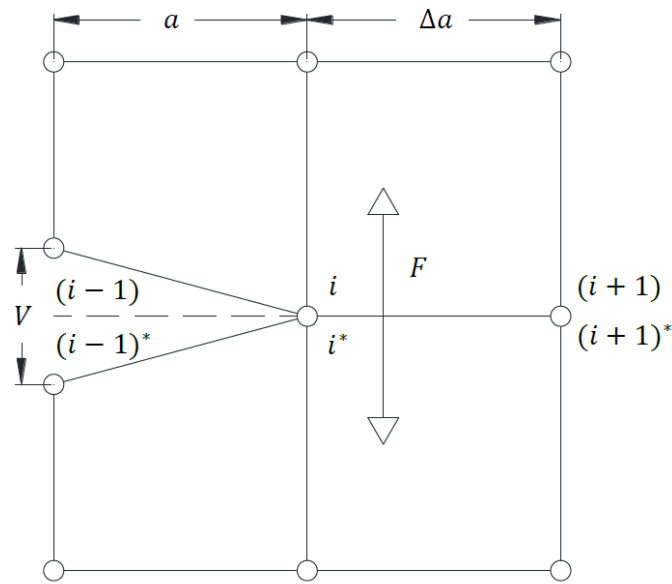
Figure 3.3 Finite element mesh showing the basis of the VCCT for a Mode I situation.

Once the strain energy release rate at the crack tip has been calculated, it is compared with the critical strain energy release rate required for crack propagation to occur. If the calculated value exceeds the prescribed critical value, then the real and phantom nodes of the enriched element will separate, with the traction between the two crack surfaces linearly decreasing as the strain energy necessary to cause fracture is dissipated [29], as illustrated in Fig. 3.4.
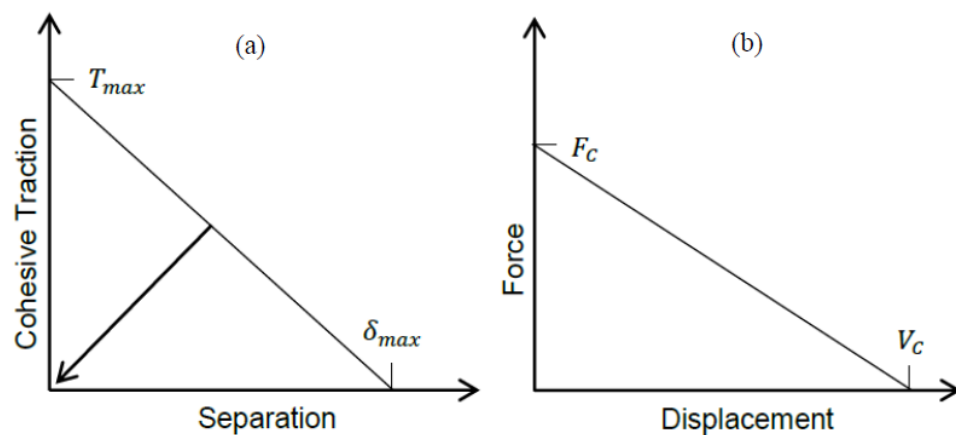
Figure 3.4 (a) General linear traction-separation behaviour for a crack element, where T_{max} is the maximum traction and δ_{max} is the maximum crack separation. (b) Force-displacement response at a cracked element using the VCCT. F_C and V_C are the critical force and displacement values respectively, relating to the critical strain

energy release rate required for full node separation. This criterion is given by Eq. 3.6 for a simple Mode I case,

$$f = {G_I}/{G_{IC}} \geq 1 \qquad (3.6)$$

where f is the fracture criterion and G_{IC} is the critical strain energy release rate for Mode I fracture (Mode I fracture toughness). Thus, for a simple crack growth model, the fracture criterion is the relevant critical strain energy release rate for the mode of loading.

3.2.2 Static delamination validation

3.2.2.1 DCB

The DCB test is a widely used method of determining the Mode I interlaminar fracture toughness of composite materials [33]. The test involves loading a pre-cracked specimen of composite laminate in a manner similar to that shown in Fig. 3.5.
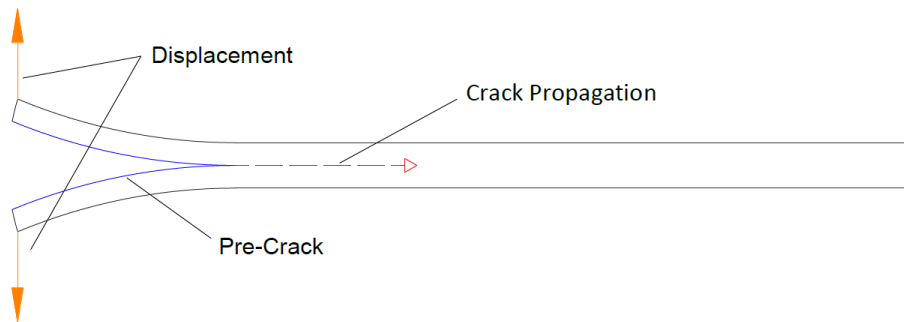
Figure 3.5 Schematic of a typical DCB specimen for determining the Mode I fracture toughness of a composite.

The pre-crack is introduced into the specimen by placement of a layer of release film into the mid-plane of the laminate during the manufacturing process. The edges of the specimen are then loaded via metallic hinges, which move apart with a constant cross head displacement. As the legs of the beam move apart, the load on the

specimen increases, resulting in a large deflection until a critical load is reached. At this point the crack begins to propagate from its initial position, with a corresponding drop in load occurring due to the increased crack length. This procedure is carried out until the desired crack length has been achieved, with the load and cross head displacement being recorded continuously. The Mode I fracture toughness energy, G_{IC}, is given by Eq. 3.7 [33],

$$G_{IC} = \frac{A}{aw} \times 10^6 \tag{3.7}$$

where A is the integrated area under the load-cross head displacement graph as per the AITM standard, a is the propagated crack length according to the AITM standard and w is the specimen width.

3.2.2.2 ENF

Although there is no standardised test for determining the Mode II interlaminar fracture toughness of composite materials, the ENF test is one of the more commonly used methods, partly due to its simplicity [34]. The test uses a pre-cracked specimen similar to that used in the DCB test, but is loaded in a 3-point bend configuration as shown in Fig. 3.6.
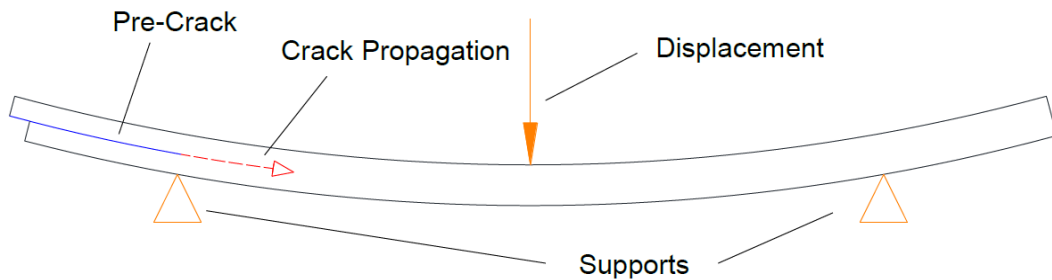

Figure 3.6 Schematic of a typical ENF specimen used for determining the Mode II fracture toughness of a composite.

The specimen is loaded under displacement control at a constant rate, with the load and cross head displacement being constantly recorded. For Mode II loading, the crack extends due to shear forces at the crack tip. Determining crack propagation

onset is a key aspect of this test method, due to the unstable crack growth arising from the loading configuration. The critical load at propagation onset is recorded and the test is stopped when a drop in load confirms this. The Mode II fracture toughness energy, G_{IIC}, is given by Eq. 3.8 [35],

$$G_{IIC} = \frac{9Pa^2d}{2w\left(L_S^3/4 + 3a^3\right)} \times 1000 \tag{3.8}$$

where P is the load at crack propagation onset, a is the initial length of the pre-crack as per the AITM standard [35], d is the cross head displacement at crack propagation onset, w is the specimen width and L_S is the span length.

Both the DCB and ENF tests were carried out by ÉireComposites Teo using autoclaved Gurit Suprem/AS4C CF/PEEK specimens [36]. The mechanical properties of the material and test parameters are given in Tables 3.1 and 3.2 respectively. See A.2 for more details on the fracture toughness tests carried out by ÉireComposites.

Table 3.1 Mechanical properties of CF/PEEK material used in DCB and ENF tests.

Material	E_1 (GPa)	E_2 (GPa)	G_{12} (GPa)	v_{12}
Suprem/AS4C	142	8.9	5.1	0.34

Table 3.2 Specimen dimensions and experimental parameters for DCB and ENF tests. A 20-ply lay-up is used for each specimen.

Test	DCB	ENF
Length (mm)	250	160
Span (mm)	N/A	100
Pre-crack (mm)	35	35
Width (mm)	25	25
Thickness (mm)	2.5	2.5
Cross head speed (mm/min)	10	1

3. A 2-D XFEM-based methodology for fatigue delamination and permeability of composites

The finite element models for both test cases were created in accordance with the properties and dimensions given in Tables 3.1 and Tables 3.2. The test cases were modelled in 2-D using CPE4R plane strain, reduced integration elements, with the loads being applied in the form of displacement boundary conditions. See A.3 for more details on the element type. It should be noted that 2-D models of these fracture tests are unable to deal with the free-edge effects that can lead to non-uniform energy release rate distributions across the specimen widths and associated uneven crack fronts [37]. However, these effects are confined to a relatively small region at the specimen edges [38], with the resulting increase in accuracy of crack growth prediction deemed insufficient to warrant a full 3-D analysis for the present application. Another issue which could introduce inaccuracies into the simulation is that the XFEM model does not take into account the effects of fibre-bridging that is known to occur during DCB tests [39].

The pre-crack for each specimen was introduced through appropriate partitioning of the part at the mid-plane of the specimen. This pre-crack represents the initial starter crack required for the DCB and ENF tests, with the subsequent crack growth occurring along an undefined path, as is the case with XFEM. Due to the existence of a pre-crack in the model, a damage initiation criterion was not required. Damage evolution, or crack propagation, was dictated by the fracture criterion assigned for each test. This criterion was prescribed in the form of the relevant fracture toughness for the mode of loading, which was 1062 Jm^{-2} for Mode I and 999 Jm^{-2} for Mode II [36]. The crack propagation direction was assigned to be parallel to the element local 1-direction, which corresponds to the fibre direction of the laminate. A structured mesh was used for the analyses and consisted of 10,000 elements for the DCB test and 7,200 elements for the ENF test. In order to ensure convergence of the solution, a small time incrementation was used and appropriate alterations were made to the general solutions controls of the model, including making the analysis discontinuous. Further details on the general type of time incrementation and solution controls used can be found in Section 3.3.2. See A.3 for more details on the mesh density and convergence controls used for the simulations.

3.2.3 Mechanical fatigue validation

The DCB specimen under cyclic mechanical loading is the standard test case for delamination of composites [40] and is key to validating the fatigue prediction capabilities of this methodology. The test case investigated is based on the work of Krueger [41], who worked on the development of a benchmark for delamination fatigue growth prediction. A 2-D finite element model of the DCB specimen is created and the resulting crack growth over a given number of fatigue cycles is compared with output from Krueger, who relies on a conventional finite element model, requiring a pre-defined crack path and associated levels of mesh refinement. The primary difference between the fatigue and static cases is that the specimen is sub-critically loaded in the fatigue case. The specimen is cyclically loaded under constant amplitude displacement control, with a load ratio of R = 0.1 and a maximum displacement which corresponds to an energy release rate of 80% of the specimen G_{IC} at the crack front, in accordance with a draft of the ASTM standard for Mode I fatigue delamination in polymer matrix composites [40]. The variation of applied displacement, $\frac{\delta}{2}$, with time, t, for the cyclic loading is given by Eqn. 3.9 [41]

$$\frac{\delta}{2} = \frac{\delta_{max}}{2}\{a_0 + b_1 \sin \omega(t - t_0)\} \tag{3.9}$$

where $\frac{\delta_{max}}{2}$ is the maximum displacement, a_0 and b_1 are constants, ω is the circular frequency and t_0 is the start time.

For the stable growth phase observed in this method of fatigue loading, the increasing delamination length leads to a drop in load for each constant amplitude displacement cycle. This growth region is defined by the change in energy release rate for a given number of cycles. Below the energy release rate threshold, G_{thresh}, no crack growth occurs, while above the energy release rate upper limit, G_{pl}, the crack grows at an accelerated rate. Between these limits, the well-known Paris equation is used to model the fatigue crack growth, and is given in Eq. 3.10,

$$\frac{da}{dN} = c\Delta G^n \tag{3.10}$$

where $\frac{da}{dN}$ is the crack growth per cycle, c and n are material constants and ΔG is the relative fracture energy release rate. The issue of delamination onset for fatigue crack growth is dealt with by defining a fracture criterion, f, as shown in Eq. 3.11 [29],

$$f = \frac{N}{c_1 \Delta G^{c_2}} \geq 1 \tag{3.11}$$

where N is the cycle number and c_1 and c_2 are material constants. Crack propagation will not commence until this relation is satisfied. A graphical representation of the growth regime used is shown in Fig. 3.7.
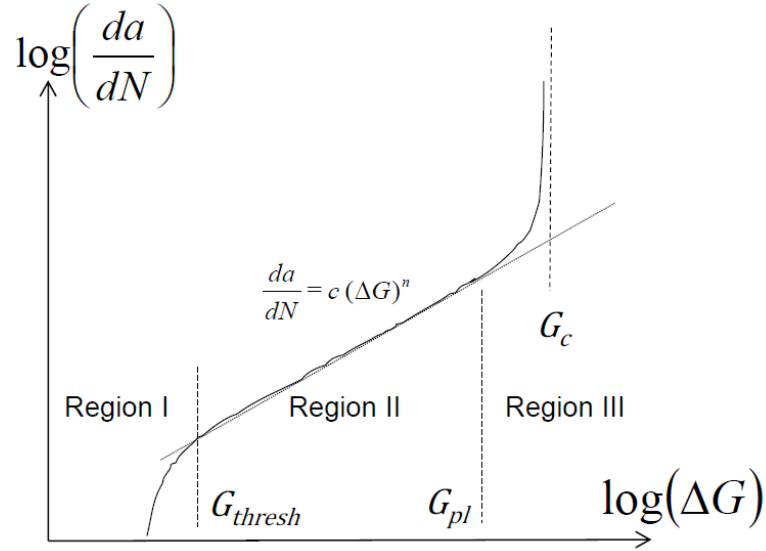
Figure 3.7 Fatigue crack growth regime. The Paris equation growth region is bounded by the energy release rate threshold, G_{thresh}, and the energy release rate upper limit, G_{pl}.

Due to the high computational cost associated with fatigue loading, the present methodology implements a low-cycle fatigue analysis using the direct cyclic approach to model the damage progression in the specimen. This method involves

computing the material fatigue response at a number of distinct points over the course of the loading, with the spacing of these points representing a particular span of loading cycles. In this way, the predicted damage progression at a particular point and time increment can be used to calculate the change in material properties for the next increment, based on a prescribed damage evolution law. Such an approach allows modelling of damage progression over the entire load history through the extrapolation of a relatively small number of load points, leading to significantly reduced solution times. The various parameters relating to the Paris equation, onset fracture criterion, threshold and upper limit energy release rates and Fourier terms relating to the low-cycle fatigue approach are defined as input to the analysis. Appropriate values for these parameters as used in the test case can be found in [41]. Properties of unidirectional CF/epoxy were used for the test, with the cyclic loading being applied via displacement boundary conditions in the same manner as the static DCB test.

The test case was modelled using CPE4R plane strain, reduced integration elements, with 1,800 elements used in the mesh (See A.3 for more detail on mesh density). Comparisons between 2-D and 3-D simulations for fatigue delamination can be found in [41]. The computational expense associated with a full 3-D model was found to be several orders of magnitude higher than for an equivalent 2-D model, with the run-times spanning days as opposed to minutes, achieving only marginal improvements in accuracy. This is in keeping with the preliminary 3-D static analysis reported in Section 3.3.1.1.

3.2.4 Thermal fatigue validation

The final test case studied in this work is the delamination of a cross-ply laminate under thermal fatigue loading. The cross-ply case compares predicted delamination growth with existing experimental data from the literature for a $[0^{\circ}/90^{\circ}]$ CF/Epoxy laminate. Unlike the previous cases, interlaminar delamination of the composite is driven by the mismatch in coefficients of thermal expansion (CTE) between adjacent plies. This mismatch arises from the difference between the fibre-dominated properties of the 0° ply and the matrix dominated properties of the 90° ply. This case

involves modelling the thermal fatigue delamination growth of the laminate and comparing the delamination growth with experimental data from Ramanujam et al. [42], whose work uses a similar cross-ply layup. In [42], unsymmetrical $[0^°/90^°]$ CF/Epoxy test specimens were subjected to thermal cycling consisting of a ΔT of 140 °C, representing a change in temperature from 20 °C to 160 °C with a total cycle length of 110 minutes. Much in the same way as the aforementioned static DCB and ENF tests, the specimens were manufactured with pre-existing interlaminar delaminations, with the initial crack subsequently growing due to the thermal loading. The crack length was measured by visual detection methods after every 20 cycles. The specimen layup and loading configuration is shown in Fig. 3.8.
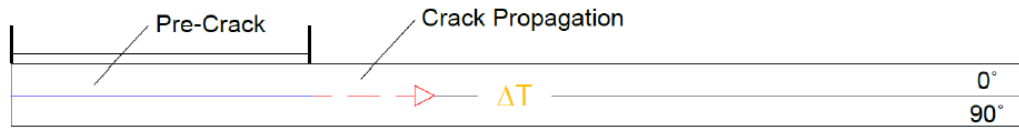
Figure 3.8 Schematic of the cross-ply layup showing the direction of crack propagation.

The thermal fatigue analysis requires additional material properties in the form of CTE values. Unlike the DCB case, which deals with Mode I fracture, the thermal fatigue case results in a more complex, mixed-mode fracture, behaviour. Mixed-mode fracture is dictated by an equivalent energy release rate [29], G_{equivC}, which combines energy release rates in all three fracture modes into a single fracture criterion. A number of mode-mix formulae for computing equivalent energy release rates are available. The BK law model, suggested by Benzeggagh and Kenane [43], was chosen for this study due to its previous successful implementation in studying delamination growth [44]. The BK law is given by Eq. 3.12,

$$G_{equivC} = G_{IC} + (G_{IIC} - G_{IC})\left(\frac{G_{II} + G_{III}}{G_I + G_{II} + G_{III}}\right)^{\eta} \qquad (3.12)$$

where G_{III} is the Mode III energy release rate and η is a curve fit parameter. Paris equation fatigue constants and material properties used in the model are similar to those employed by Ramanujam et al. for their 2-D model. The test case was modelled using CPE4R plane strain, reduced integration elements, with 2,240 elements used in the mesh (See A.3). The cyclic thermal loading was applied directly to the element nodes using the same cyclic loading described in Eq. 3.9, with a thermal load replacing the direct mechanical displacements and the frequency of loading adjusted to the experimental cycle time.

3.2.5 DCOD and permeability predictions

The quasi-isotropic laminate used for predicting the variation of DCOD with cryogenic fatigue loading is based on the five layer model (FLM) outlined in Nair and Roy [6], who used analytical methods and 2-D finite element models to predict DCOD for predefined delamination lengths. There are 90°, ±45° and 0° ply groups. The FLM is represented by a quarter repeating interval as shown in Fig. 3.9, with the method of measurement for DCOD also included. The lines of symmetry are through the central 0° ply group and on the right hand side of the laminate.
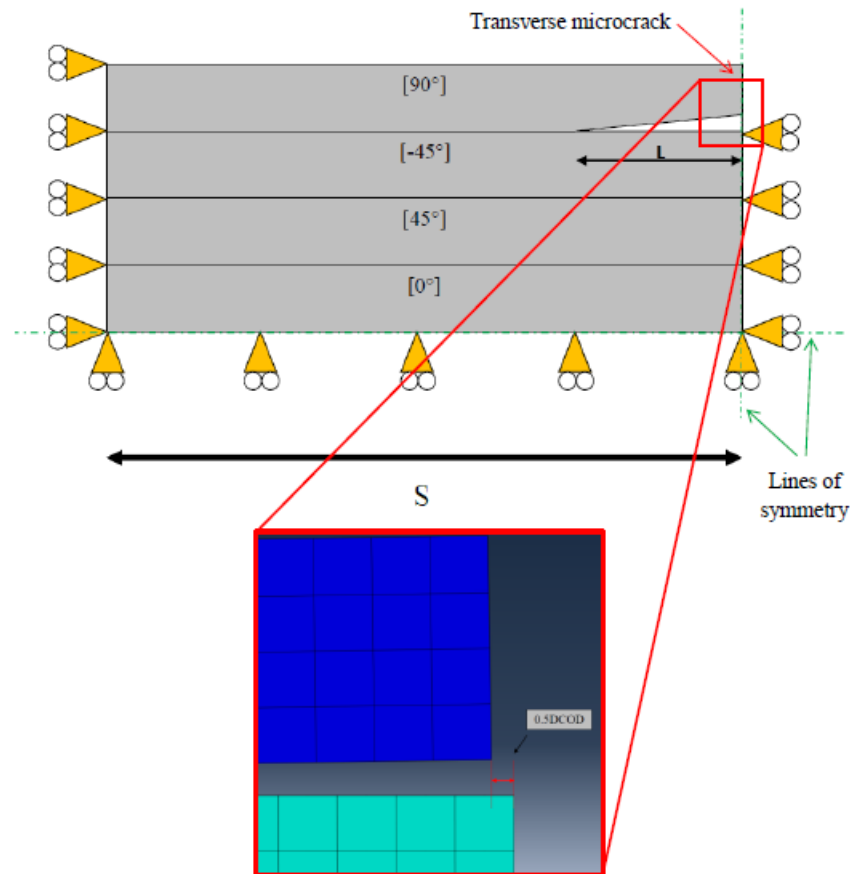
Figure 3.9 Schematic of FLM test case repeating interval [6] including a close-up view of how the DCOD is measured from a finite element model.

The dimensions of this interval are related to the crack density of the material specimen which it represents, where S is the inverse of the crack density for this quarter FLM. This model assumes an existing transverse micro-crack is present in the 90° ply of the laminate, which is adjacent to a delamination of length L. The purpose of this repeating interval model is to determine the DCOD of the transverse micro-crack under loading, based on a given crack density and delamination length. The magnitude of the DCOD value is directly related to the area of the leakage path through the laminate and, therefore, affects laminate permeability. Following [6], an expression for material permeability for a composite laminate, B_0, is given in Eqn. 3.13

$$B_0 = C \left[\sum_{K=1}^{N} \left(\sin \theta \big/ N_K N_{K+1} \Delta_K \Delta_{K+1} \right) \right]^{-1} \tag{3.13}$$

where C is the material conductance, θ is the ply angle, N_K and N_{K+1} are the crack densities of adjacent plies and Δ_K and Δ_{K+1} are the DCOD of adjacent plies. It has been shown that the DCOD of the transverse crack is directly related to the adjacent delamination length, L [6]. Thus, with knowledge of the how the delamination length varies with fatigue loading, it becomes possible to predict the laminate permeability after an arbitrary number of load cycles.

The modelling of the quasi-isotropic lay-up proceeds in a manner similar to that outlined in Section 3.2.4, including the use of a similar crack growth regime. The test case was modelled using CPE4R plane strain, reduced integration elements, with a relatively dense mesh of 16,256 elements used, reflecting the increased complexity of the model (See A.3). The cyclic cryogenic loading was applied directly to the element nodes. Table 3.3 provides details of the test parameters.

Table 3.3 Test parameters for quasi-isotropic lay-up model. ΔT corresponds to range of -252 °C to 224 °C.

Material	CF/Epoxy
Lay-up	[90°/-45°/+45°/0°]s
S	5.08 mm
Ply thickness	0.0762 mm
Thermal cycle	ΔT = -476 °C

Once again, a 2-D model was deemed sufficient to track delamination growth with good accuracy based on previous test cases and due to the relatively wide section associated with this type of composite structure.

3.3 Results and discussion

3.3.1 Static results

The output from the experimental tests was in the form of load-displacement plots and Mode I and Mode II fracture toughness values. Due to the fact that the mean fracture toughness from each test was used as input for the models, the load-displacement graphs were used to compare the performance of the finite element models with the experimental results from ÉireComposites. See A.2 for more details.

3.3.1.1 DCB

A contour plot of the cracked mesh and load-displacement curves for the experimental and predictions are shown in Fig. 3.10.
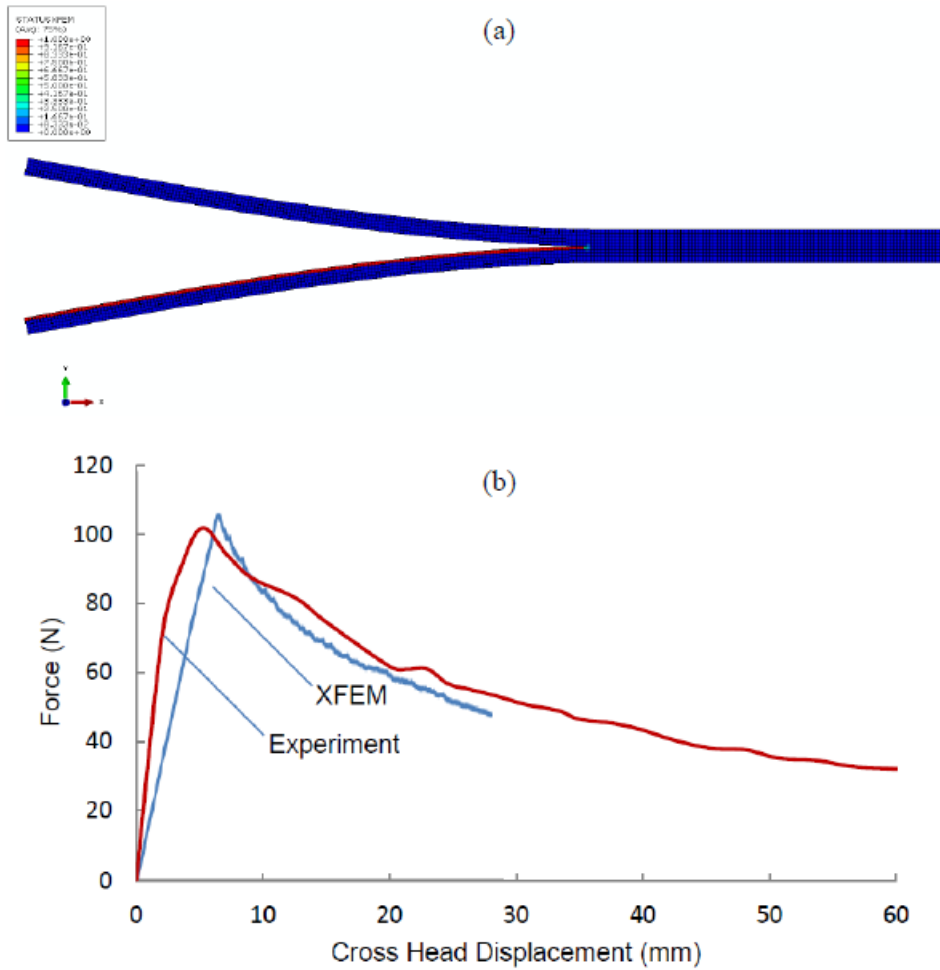
Figure 3.10 (a) Contour plot of cracked DCB mesh. (b) Load-displacement curves for both experimental (ÉireComposites [36]) and DCB tests.

Both curves exhibit an initial linear variation of force with cross head displacement, representing the elastic response of the material. The slopes of the linear-elastic sections of the tests are not co-incident. This difference can be attributed to the variation in material properties and dimensions of the experimental test specimens (six in total), with the model relying on taking the mean value of the material properties and test specimen dimensions. Another factor affecting the linear response section is the pre-crack length, where differences in pre-crack length could result in differences in initial slope. The point of initial crack propagation for both cases matches closely, with the critical load registered for the model being just 4 N higher than the average of the experimental data, which represent a deviation of less than 5%. The model also manages to track the crack growth accurately, with the load-

displacement curves for both methods following similar paths. Note that due to a convergence issue, the steady crack propagation phase of the XFEM DCB test terminates before the experimental test curve. See A.2 for more details on the DCB experimental testing and the experimental data variance.

A convergence study was conducted to determine the effect of mesh density on the predicted critical load for the 2-D model. The 10,000 element mesh used in this analysis output a load value within 3% of the converged value obtained with 113,000 elements, with a significantly reduced model run-time. It was also observed that a relatively coarse mesh of 1,000 elements proved capable of predicting critical loads within 9% of the converged solution, highlighting the robustness of the technique.

Preliminary studies using a 3-D model of the DCB test specimen were also conducted. Free-edge effects were observed at the specimen edges, in the form of crack surface variation, as shown in Fig. 3.11.
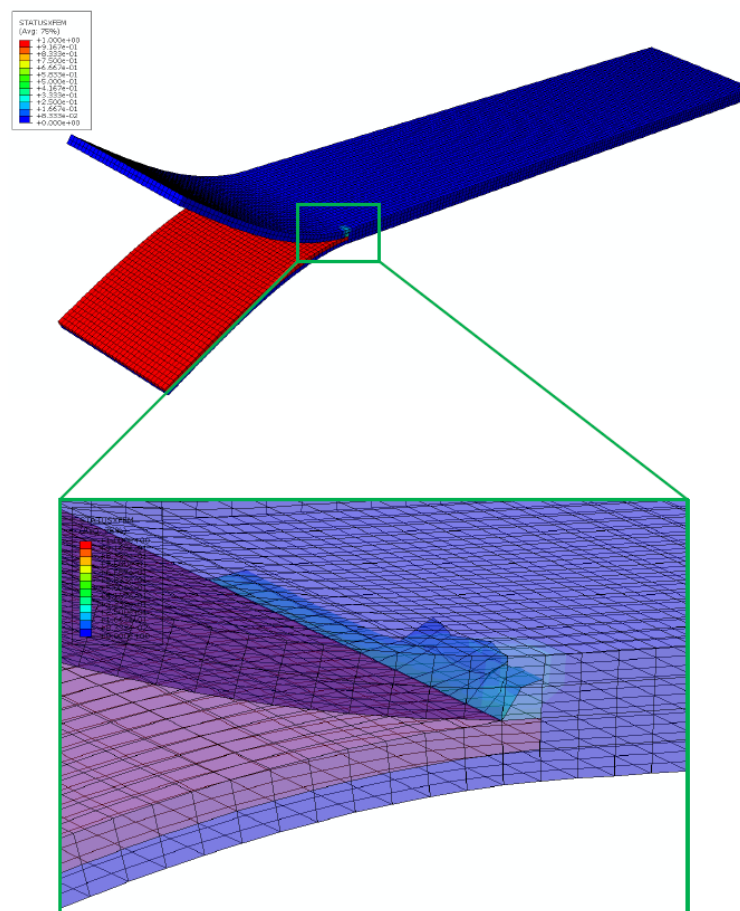
Figure 3.11 Crack surface variation in a 3-D DCB model with intralaminar and interlaminar cracking.

However, the move to a 3-D modelling space brought an associated order-of-magnitude increase in run-time, as well as additional convergence issues, even when using a coarse mesh. Given the good accuracy of the 2-D model in comparison with the experimental results, the need for a full 3-D model was not apparent.

3.3.1.2 ENF

The load-displacement curves for the experimental and simulated ENF tests are shown in Fig. 3.12.
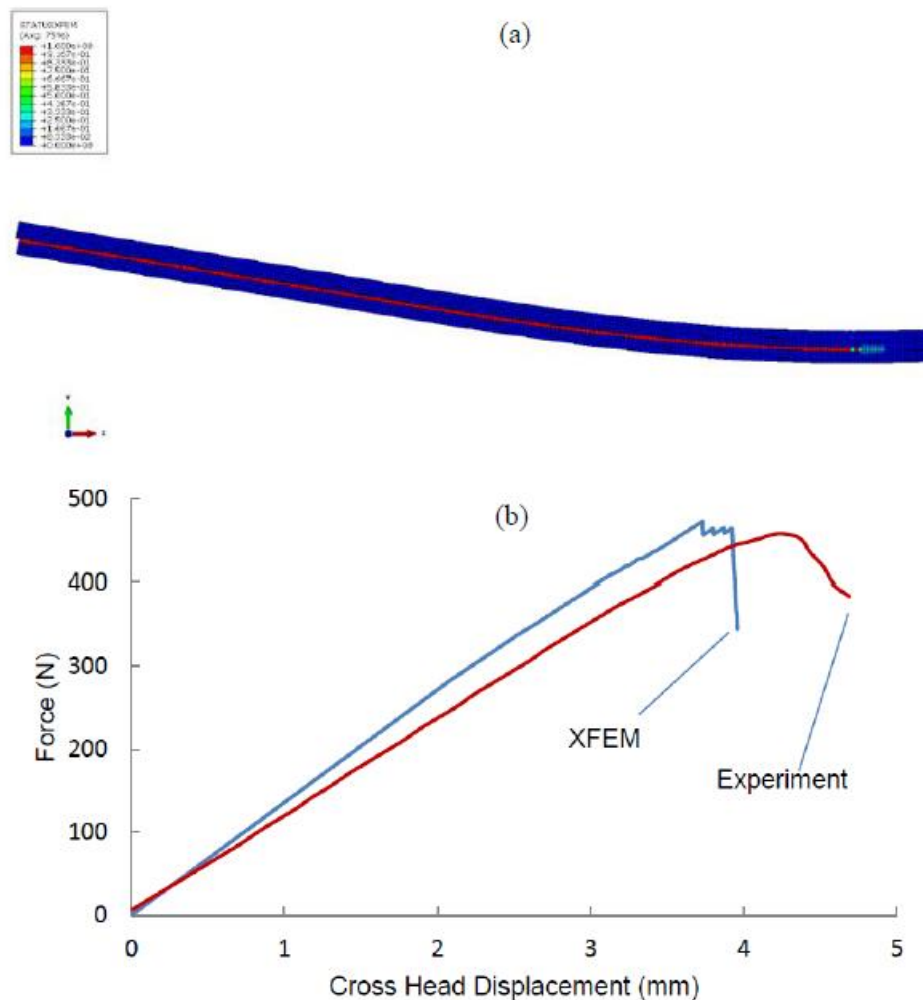

Figure 3.12 (a) Contour plot of cracked ENF mesh. (b) Load-displacement curves for both experimental (ÉireComposites [36]) and ENF tests.

Again, the difference in the linear portion of the load-displacement curves can be partly attributed to the variation in material properties and test specimen dimensions between experimental test specimens and the properties and dimensions used for the model. The critical aspect of this test, the point of crack propagation onset, is represented well by the model. The critical load at onset differs by less than 20 N from the average experimental data, representing a deviation of less than 5%, whilst the cross head displacement at onset differs by less than 0.5 mm. After the onset of propagation, crack growth for the ENF test is unstable, leading to convergence issues for the model and the subsequent sharp drop off in load, with a similar trend being observed in the experimental data curve. See A.2 for more details on the ENF experimental testing and the experimental data variance. Due to the similarity in dimensions between the ENF and DCB specimens, 7,200 elements were used in the mesh, representing approximately the same level of refinement that produced good results for the DCB test.

3.3.2 Mechanical fatigue results

Output from the DCB fatigue case in the form of total delamination length against loading cycles is used for comparison with [41], which used analytical and conventional finite element models relying on predefined the crack paths, to track the delamination growth. The main aim of this test case was to investigate the capability of VCCT based XFEM methodology to model delamination growth under fatigue loading, including the correct implementation of the Paris equation for fatigue crack growth. Krueger's work contains a detailed sensitivity analysis of the effects of various input parameters such as the time increments used and the element size and type on the overall delamination growth. In order to make a meaningful comparison with the published work, a test case with similar crack tip element size was chosen. The crack growth curves for both models are plotted in Fig. 3.13.
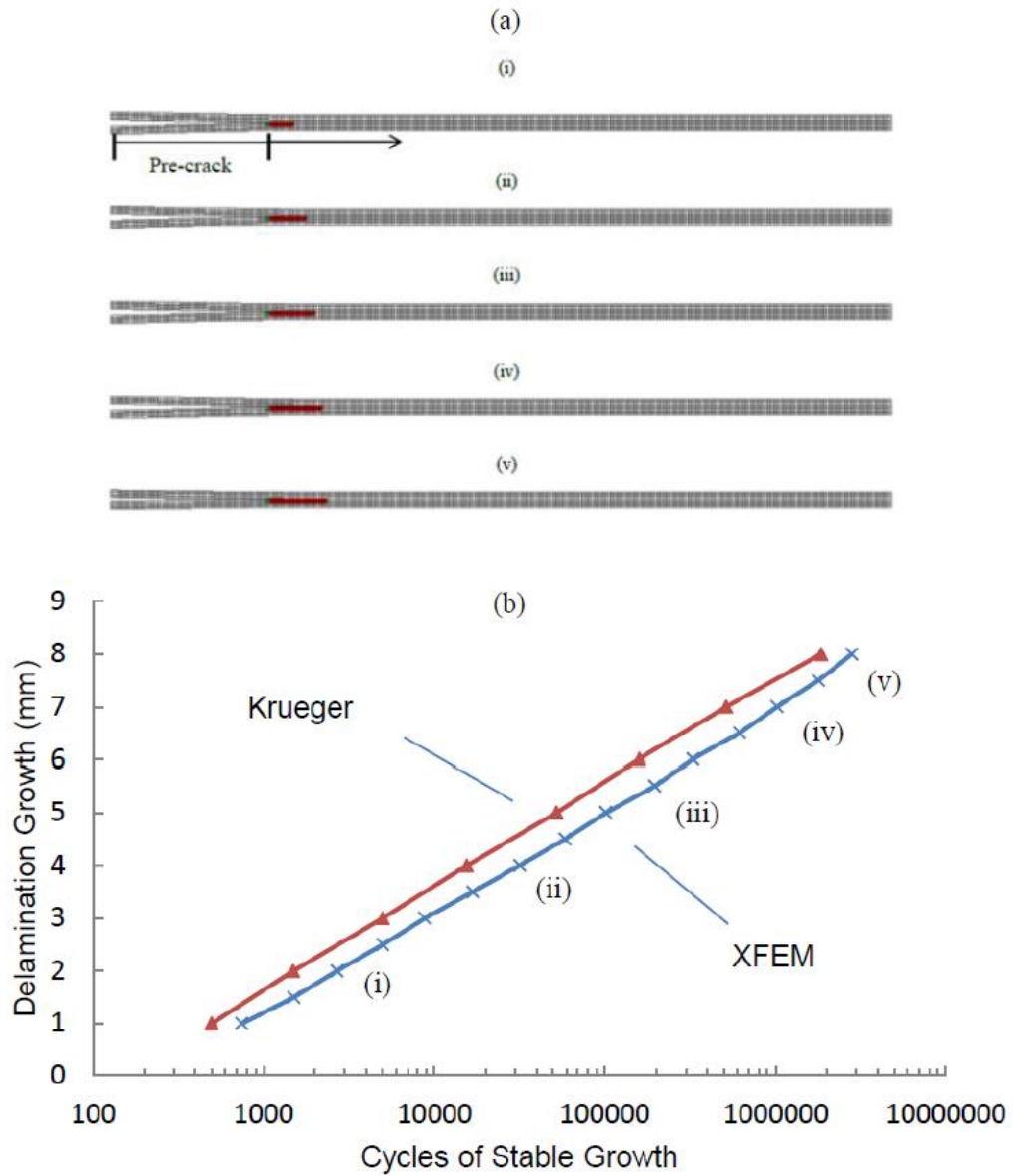
Figure 3.13 (a) Snapshots of delaminaion growth from the model at various cycles (i)-(v). (b) Comparison of delamination growth behaviour between model and [41].

Both curves in Fig. 3.13 (b) exhibit the characteristic linear increase in delamination length expected of the Paris equation when plotted on a log scale. The matching slopes of the growth curves and similar overall delamination length indicate successful implementation of the Paris equation for fatigue crack growth in the model. This was achieved without the need to predefine the crack propagation path or bonded surface regions as was required in [41].

As mentioned previously, a number of factors could account for the slight offset between curves, meaning careful consideration of appropriate time incrementation and element size amongst other parameters is essential to the accuracy of the model. Decreasing the time increment used in the analysis was found to lead to more accurate prediction of crack propagation, in keeping with Krueger's findings. The downside to this is vastly increased computation time, requiring a trade-off between accuracy and model run-time. As a result, a time increment of 0.001, or one hundredth of a loading cycle, was used, based on the accuracy of preliminary simulations.

Specialised general solution controls were also required to achieve convergence within a reasonable time frame, due to the discontinuous nature of the analysis. These solution control parameters can be used to change the convergence control algorithm and the time incrementation used by the finite element code. By using a discontinuous analysis, the default time incrementation parameters I_0 and I_R were changed to 8 and 10 respectively, with the effect of increasing the number of equilibrium iterations before convergence checks were conducted. The default value of I_A, the maximum number of cutbacks allowed for an increment, was increased from 5 to 20. Cutbacks occur during crack propagation, with dynamic reductions in time increment being used to ensure convergence of the solution. Although changing the default solution controls is not recommended for most analyses, the complexity of crack propagation simulations requires this fine-tuning in order to achieve solution convergence within an acceptable run-time, or in some cases, to converge at all. These changes did not impact the accuracy of the delamination growth prediction for the converged solutions. See A.3 for more details on the convergence controls used in this chapter. The reader is referred to [45-47] for more detailed studies on error control for quasi-static analyses and XFEM in general.

3.3.3 Thermal fatigue results

The thermal fatigue delamination test case represents an important step in determining the applicability of using the VCCT based XFEM methodology to predict delamination length for cryogenically cycled laminates. Experimental data

relating to delamination growth under cryogenic cycling for CFRP is not widely available in the literature at this time. The output from the thermal fatigue model was therefore compared with experimental data from the work of Ramanujam et al. [42]. In this work, data relating to the crack growth which occurs in a cross ply CFRP laminate subjected to 500 thermal cycles is presented. A comparison between this crack growth data and the current predicted data is shown in Fig. 3.14.
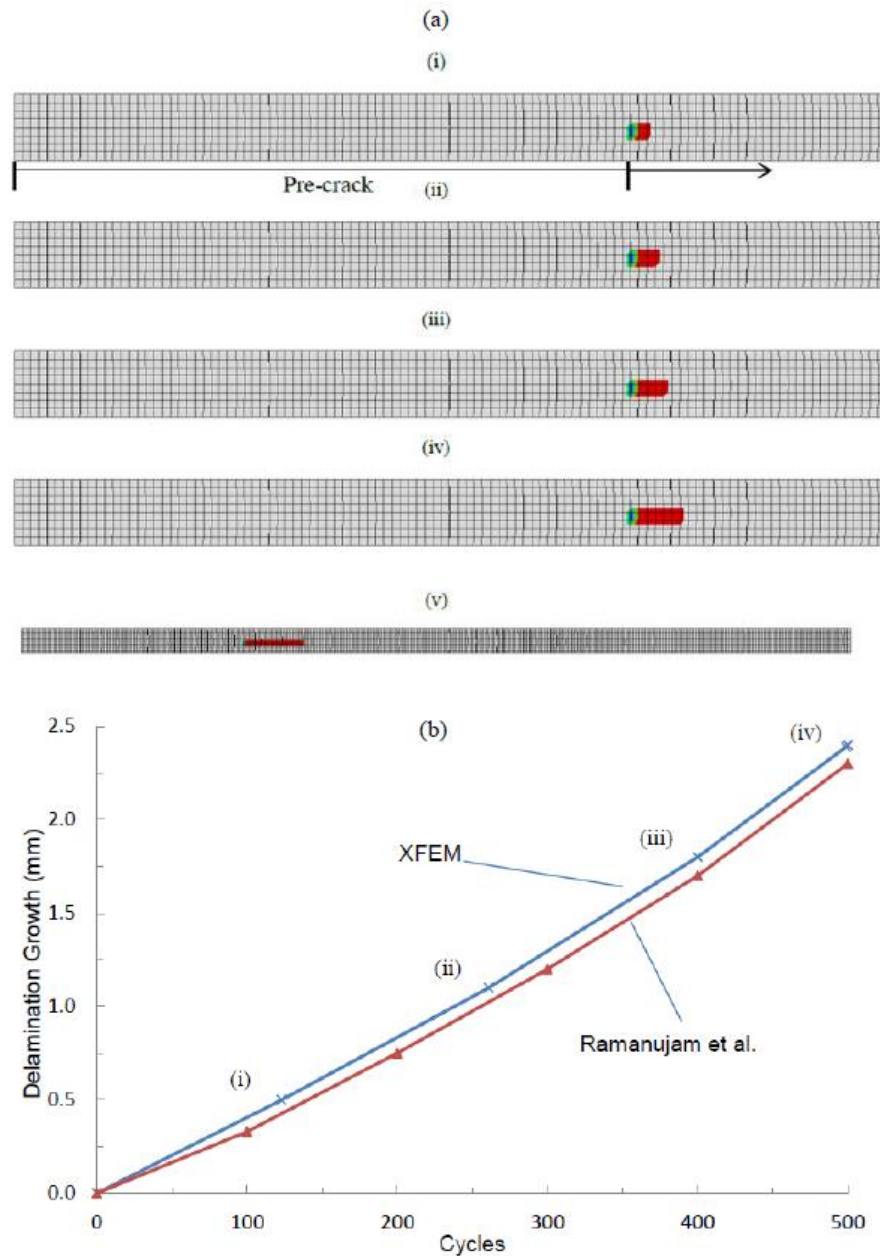

Figure 3.14 (a) Snapshots of delaminaion growth from the model at various cycles (i) – (v), where (v) shows delamination growth of 9.5 mm at 2000 cycles. (b) Comparison between crack growth output from the model and experimental data from [42].

The crack growth predicted is shown to closely match the experimental data, with the propagated length differing by only 0.2 mm after 500 loading cycles. This is in keeping with the tendency of 2-D models to provide a conservative estimate of total crack propagation length, as well as illustrating accuracy of this technique in modelling thermal fatigue crack growth. Similar modifications to the model solution controls as outlined in Section 3.3.2 were also applied to this case.

It should be noted that the crack lengths from the experimental data were taken from surface of the laminate and may not reflect the crack lengths through the specimen thickness [42]. A 3-D model would be required to investigate possible differences in crack propagation through the entire laminate, relating to the aforementioned free edge effects. However, the 2-D model tracks the delamination growth with good accuracy and with over an order of magnitude reduction in the computational expense of a full 3-D model of the laminate, such as the 60,000 solid element model used by Ramanujam et al.

3.3.4 DCOD and permeability results

The model of the quasi-isotropic FLM described in Section 3.2.5 was subjected to 75 cryogenic loading cycles, consisting of a ΔT of -476 °C. An initial delamination length, a_0, of 0.75 mm was chosen as a test case to ensure proper implementation of the Paris equation in the model. Fig. 3.15 shows the delamination growth in the FLM for this case.

(a)

(i)

(ii)
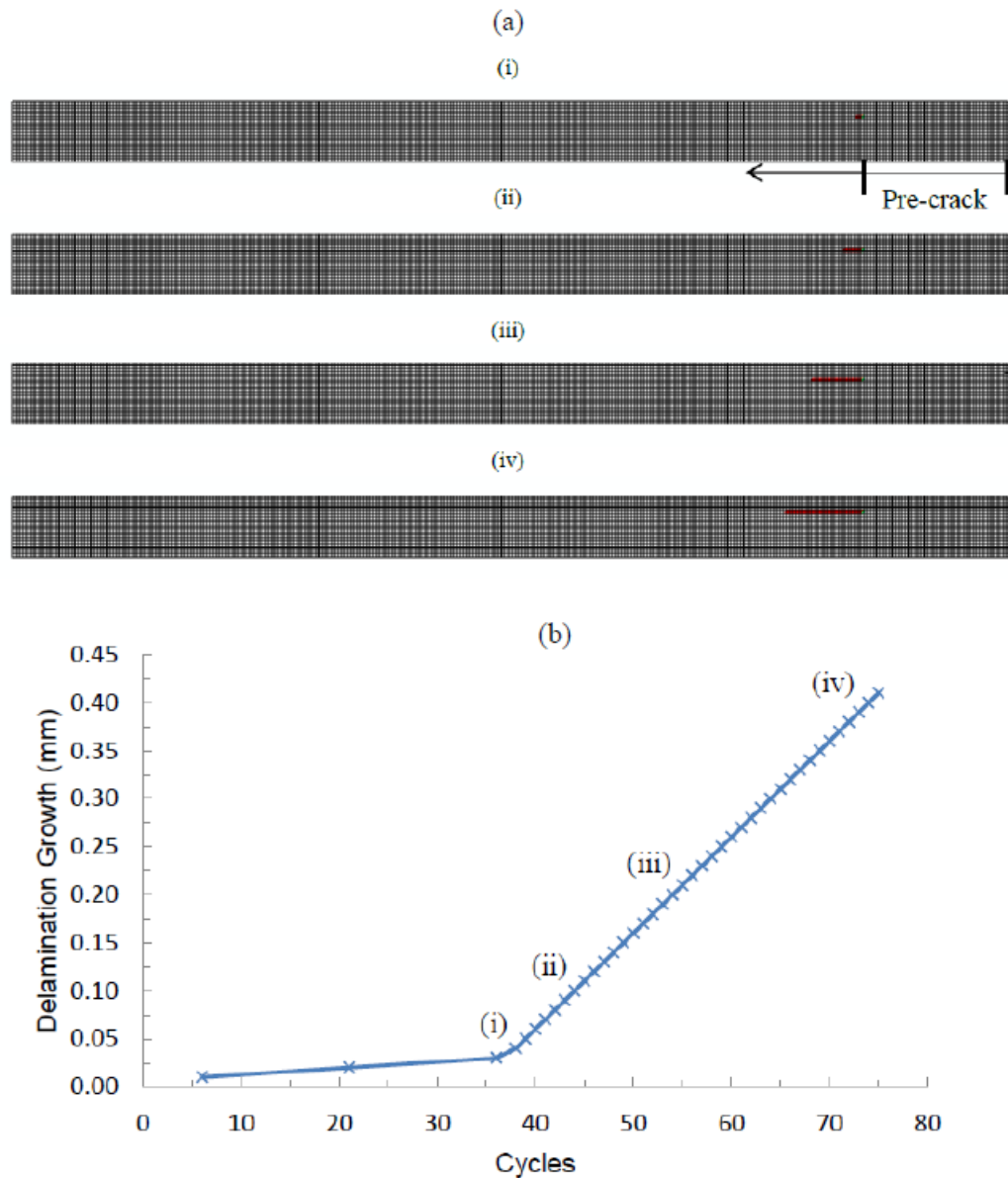

(iii)

(iv)

(b)

Figure 3.15 (a) Snapshots of delaminaion growth from the model at various cycles (i) − (iv). (b) Plot of the delamination growth for the 0.75 mm initial delamination case after 75 cycles.

Successful implementation of the Paris equation for the FLM is observed in Fig. 3.15 (b), with the characteristic steady growth phase commencing at cycle 36 and continuing until the analysis was stopped at cycle 75. The bulk of the delamination growth occurs during this phase, with the initiation phase below cycle 35 contributing little to the total overall delamination length.

3. A 2-D XFEM-based methodology for fatigue delamination and permeability of composites

The effect of varying the initial delamination length on the total delamination growth for 75 loading cycles was subsequently investigated. Although no initial crack is required for the analysis, in order to reduce the model run-time an initial delamination length was included in this study to ensure prompt propagation. These initial delamination lengths were selected to be on generally the same size scale as the laminate thickness, making their dimensions comparable to common manufacturing defects which could be present in the composite. As in the previous test cases, the subsequent crack propagation path was not defined in the model. Fig. 3.16 (a) shows the change in total delamination length observed for the various intial crack lengths with which the FLM was seeded.
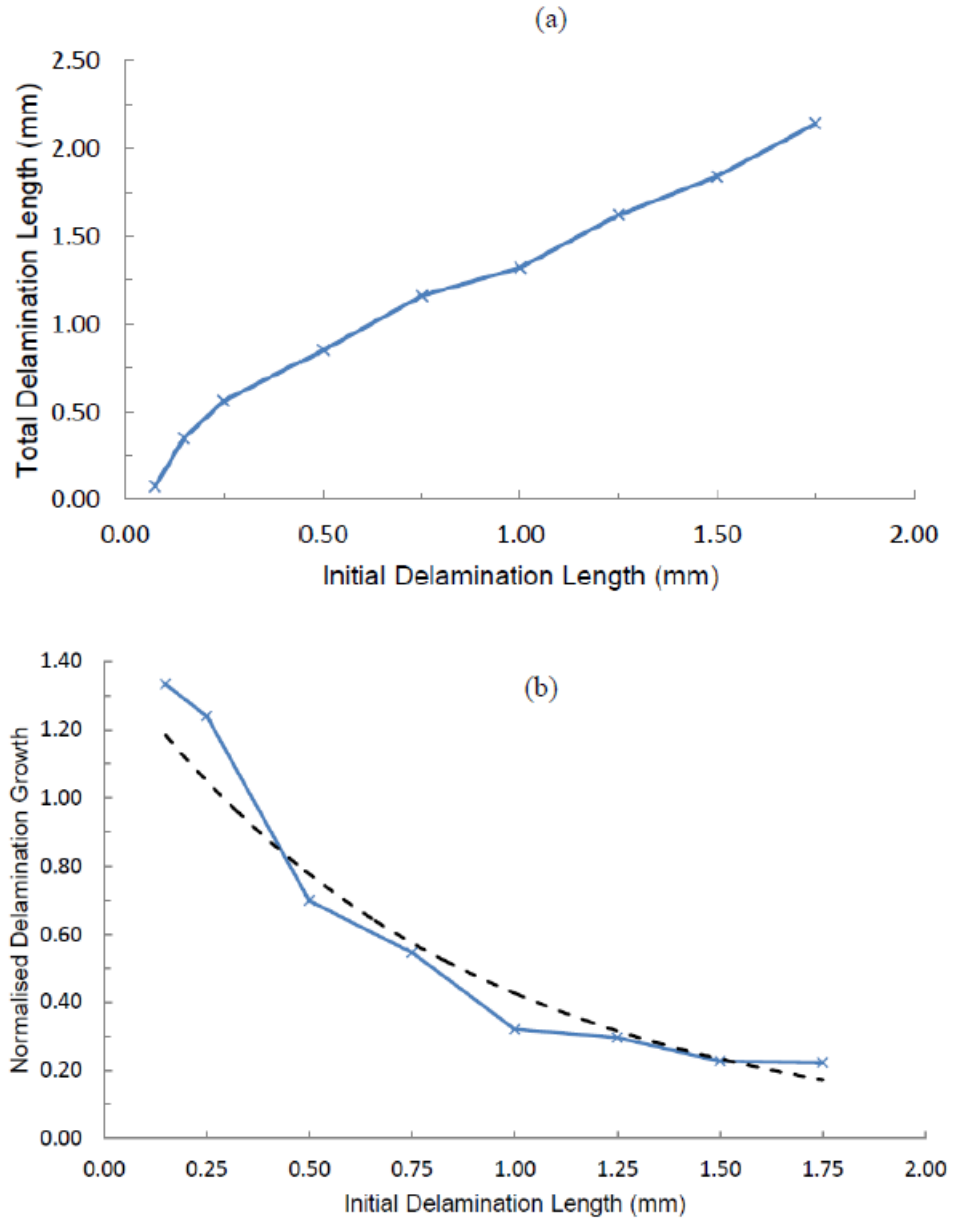
Figure 3.16 (a) Plot of total delamination length, which combines initial and growth lengths, against initial delamination length for 75 load cycles. (b) Plot of normalised delamination growth against initial delamination length for 75 load cycle with exponential trend line superimposed.

The total delamination length in this case is defined as the sum of the initial seeded length and the subsequent growth length. The first crack length chosen was 0.0762 mm, which corresponds to the ply thickness of the laminate. For the given load and cycling conditions chosen, no delamination growth was recorded for this delamination length. Upon increasing the initial crack to a length between the ply thickness and approximately 0.25 mm, high relative growth occurs before levelling

off to a near linear relationship for longer initial delamination lengths. A possible reason for the lack of growth of cracks shorter than the ply thickness is the magnitude of the energy release rate at these lengths. It has been observed [48] that, under displacement control, J-integrals reach their maximum value when the delamination length equals the ply thickness, so that steady delamination growth can be expected after the delamination length has exceeded ply thickness.

Fig. 3.16 (b) plots normalised delamination growth against the initial delamination length, where the y-axis is normalised with respect to the initial delamination length. For initial crack lengths close to the ply thickness, high relative growth rates are observed, while a distinct levelling off in relative growth is noticeable for the longer initial delamination lengths. Physically, this can be attributed, in part, due to the increasingly large crack length requiring greater load amplitude to achieve consistent crack growth rates. For mixed-mode loading at a constant amplitude this implies that after a certain delamination length has been attained, delamination growth rate will eventually reduce to a point wherby an increased load amplitude is required to further propagate the crack. The graph appears to follow an exponential trend, shown by the dotted line in Fig. 3.16 (b), of the form given in Eqn. 3.14

$$\frac{a_{tot} - a_0}{a_0} = \beta e^{-\alpha a_0} \tag{3.14}$$

where a_{tot} is the total delamination length after 75 cycles and β and α are constants with values 1.42 and 1.20, respectively. These graphs highlight the influence of the initial delamination length on subsequent crack growth for the FLM. This trend suggests the presence of interlaminar defects, with similar dimensions to the laminate ply thickness, could represent areas of greater concern with regard to crack growth rates for relatively low cycle applications.

The relationship between DCOD and delamination length for the FLM is shown in Fig. 3.17, which uses some of the delamination lengths from the previous crack growth models. The values for DCOD for each delamination length were measured as per the method outlined in Fig. 3.9, based on the relative displacement of nodes in the finite element mesh. A linear relationship between the delamination length and

the DCOD was predicted by [6], using estimated delamination lengths based on the number of thermal cycles applied to the lamiante. Fig. 3.17 illustrates a similar linear trend for the FLM, wherby the longer the delamination present, the greater the resulting transverse crack opening displacement for a given ply thickness.
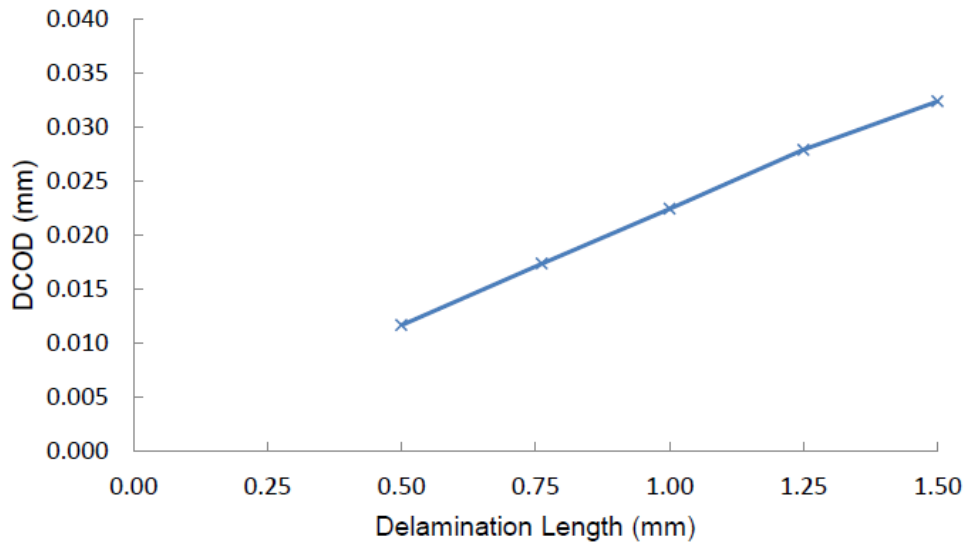

Figure 3.17 Plot of DCOD against delamination length for the FLM under thermal loading.

However, in this case, the different delamination lengths were not based on an estimation, but were predicted for a given number of cryogenic cycles, using the previously outlined methodology.

This direct relationship highlights the importance of accurate prediction of delamination length when modelling and designing composite structures in which permeability is an issue, with the magnitude of the DCOD being related to permeability by Eqn. 3.13. For completeness, the effect of crack density (CD) and delamination length, as predicted by the FLM, on laminate permeability are shown in Fig. 3.18. It should be noted that the permeability calculations for the laminate were based on preliminary material conductance values obtained from [6]. As predicted by Eqn. 3.13, both delamination length and crack density are found to strongly influence laminate permeability. Longer delamination lengths, through the relationship with DCOD shown in Fig. 3.17, lead to larger overlap areas and hence wider leakage paths for fluid to permeate through. A greater crack density means the

existence of more transverse micro-cracks per length of laminate, thereby increasing the quantity of available leakage paths.
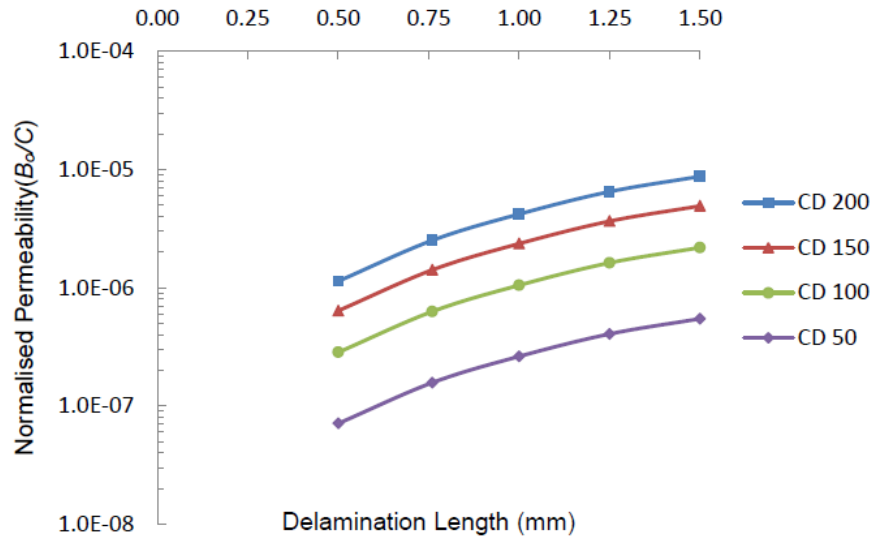

Figure 3.18 Plot of normalised permeability against delamination length for varying laminate crack densities for the FLM.

3.4. Conclusions and future work

This study has presented a novel XFEM-based methodology for the combined simulation and prediction of thermal fatigue delamination for identification of DCOD and, hence, composite laminate permeability. The methodology was validated through simulation of standardised static fracture toughness tests and fatigue delamination test methods from the literature.

Mode I DCB and Mode II ENF models were used to compare the static delamination prediction capability with experimental test data for CF/PEEK. The 2-D models proved capable of predicting crack propagation onset for both test cases, with a critical load deviation of less than 5%, as well as accurately tracking the subsequent crack propagation phase. Preliminary studies using a 3-D model of the DCB test specimen were also conducted, with the move to a 3-D modelling space bringing an associated order-of-magnitude increase in run-time, even when using a coarse mesh.

3. A 2-D XFEM-based methodology for fatigue delamination and permeability of composites

The accuracy of the low computational cost 2-D model in comparison with the experimental results highlights the robustness of this approach.

Sub-critical loading scenarios, in the form of mechanical and thermal fatigue of composite laminates, were validated against analytical and experimental data from the literature. The DCB fatigue delamination model predictions closely matched benchmark studies based on the ASTM standard, which were carried out using conventional finite element analysis. Crucially, the predictions were carried out at a significantly reduced computational cost and without the need to define a crack path, *a-priori*. Modelling of mixed-mode delamination growth in a thermally cycled cross-ply laminate was also conducted, with the results being compared with experimental data from the literature. The delamination growth length predicted after 500 thermal cycles was found to be within approximately 5% of the experimental measurements, with the 2-D model providing slightly conservative results.

Delamination growth in a quasi-isotropic laminate under cryogenic fatigue loading was used to examine the effects of initial interlaminar defects on subsequent crack growth, as well as the relationship between delamination length and material permeability based on varying DCOD values. For initial defect lengths close to the ply thickness, high relative growth rates were predicted, while a distinct levelling off in relative growth is noticeable for the longer initial delamination lengths. This suggests the presence of interlaminar defects, with similar dimensions to the laminate ply thickness, could represent areas of greater concern with regard to crack growth rates for relatively low cycle applications.

The model also predicted a linear relationship between the delamination length and the DCOD, as suggested by the literature. However, where previous DCOD calculations were based on estimated delamination lengths related to the number of thermal cycles applied to the lamiante, the new methodology allows accurate prediction of the delamination length for an arbitray number of cryogenic cycles. The relationship between the DCOD and delamination was such that the longer the delamination present, the greater the resulting transverse crack opening displacement for a given ply thickness. The applicability of these DCOD values in providing a preliminary prediction of cryogenically cycled laminate permeability was also illustrated.

Future work will include a 3-D implementation of the methodology outlined in this work in order to predict intralaminar and interlaminar crack initiation and propagation within large scale structures such as cryogenic fuel tanks. To achieve this, a dual approach of introducing imperfections into the material is proposed. The first approach will involve developing a multi-phase model by randomly distributing voids and inclusions of a suitable size range throughout the 3-D material space. Upon application of thermo-mechanical loads, these defects are predicted to lead to stress concentrations within the laminate, which, using the novel XFEM-based methodology outlined, will cause crack nucleation at loads below the fracture strength of the bulk material. The second approach will be based on a stochastic characterisation on the materials fracture strength to represent the inherent flaws within the material. The fracture strength distributions associated with the material and loading type will be assigned randomly to enriched elements in the finite element mesh of the structure to be modelled. Under loading, cracks are predicted to initiate and propagate from and through areas of lower strength.

3.5 References

[1] Grimsley B.W., Cano R.J., Norman J.J., Loos A.C., McMahon W.M. Hybrid Composites for LH2 Fuel Tank Structure. NASA Langley Research Center, Hampton, Virginia, 2001.

[2] Nairn J.A. Matrix Microcracking in Composites. *Polymer Matrix Composites*, Pergamon, Ch.13, 2001.

[3] Zhang J., Fan J., Herrmann K.P. Delaminations induced by constrained transverse cracking in symmetric composite laminates. *International Journal of Solids and Structures*, **36**, 813-846, 1997.

[4] Roy S. & Benjamin M. Modelling of opening displacement of transverse cracks in graphite-epoxy laminates using shear lag analysis. American Society for Composites, Lafayette, Indiana, Paper 023, 2002.

[5] Roy S. & Benjamin M. Modelling of permeation and damage ingraphite/epoxy laminates for cryogenic fuel storage. *Composites Science and Technology*, **64**, 2051-2065, 2004.

[6] Nair A. & Roy S. Modelling of permeation and damage in graphite/epoxy laminates for cryogenic tanks in the presence of delaminations and stitch cracks. *Composites Science and Technology*, **67**(11–12), 2592-2605, 2007.

[7] Bechel V.T., Negilski M. & James J. Limiting the permeability of composites for cryogenic applications. *Composites Science and Technology*, **66**(13), 2284-2295, 2006.

[8] Todoroki A., Tanaka Y. & Shimamura Y. Delamination monitoring of graphite/epoxy laminated composite plate of electric resistance change method. *Composites Science and* Technology, **62**(9), 1151-1160, 2002.

[9] Bois C. & Hochard C. Monitoring of laminated composites delamination based on electro-mechanical impedance measurement. *Journal of Intelligent Material Systems and Structures*, **15**(1), 59-67, 2004.

[10] Peddiraju P., Noh J., Whitcomb J. & Lagoudas D.C. Prediction of cryogen leak rate through damaged composite laminates. *Journal of Composite Materials*, **41**(1), 41-71, 2007.

[11] Allix O. & Ladevèze P. Interlaminar interface modelling for the prediction of delamination. *Composite Structures*, **22**(4), 235-242, 1992.

[12] Allix O. & Ladevèze P. Damage analysis of interlaminar fracture specimens. *Composite Structures*, **31**(1), 61-74, 1995.

[13] Allix O. & Corigliano A. Modeling and simulation of crack propagation in mixed-modes interlaminar fracture specimens. *International Journal of Fracture*, **77**, 111-140, 1995.

[14] Ladevèze P., Allix O, Deü J. & Lévêque D. A mesomodel for localisation and damage computation in laminates. *Computer Methods in Applied Mechanics and Engineering*, **183** (1–2), 105-122, 2000.

[15] Allix O. & Corigliano A. Geometrical and interfacial non-linearities in the analysis of delamination in composites. *International Journal of Solids & Structures*, **36**(15), 2189-2216, 1999.

[16] Kerfriden P., Allix O. & Gosselet P. A three-scale domain decomposition method for the 3D analysis of debonding in laminates. *Computational Mechanics*, **44**(3), 343-362, 2009.

[17] Turon A., Camanho P.P., Costa J. & Dávila C.G. A damage model for the simulation of delamination in advanced composites under variable-mode loading. *Mechanics of Materials*, **38**(11), 1072-1089, 2006.

[18] Van der Meer F.P. & Sluys L.J. Mesh-independent modeling of both distributed and discrete matrix cracking in interaction with delamination in composites. *Engineering Fracture Mechanics*, **77**(4), 719-735, 2010.

[19] Van der Meer F.P., Moës N. & Sluys L.J. A level set model for delamination – Modeling crack growth without cohesive zone or stress singularity. *Engineering Fracture Mechanics*, **79**, 191-212, 2012.

[20] Curiel Sosa J.L. & Karapurath N. Delamination modelling of GLARE using the extended finite element method. *Composites Science and Technology*, **72**(7), 788-791, 2012.

[21] Bacarreza O. & Aliabadi M.H. A novel methodology for fatigue delamination growth analysis of composites. *Key Engineering Materials*, **488-489**, 763-766, 2011.

[22] Esna Ashari S. & Mohammadi S. Delamination analysis of composites by new orthotropic bimaterial extended finite element method. *International Journal of Numerical Methods in Engineering*, **86**(13), 1507-1543, 2011.

[23] Melenk J.M. & Babuska I. The partition of unity finite element method: Basic theory and applications. *Computer Methods in Applied Mechanics and Engineering*, **139**, 289–314, 1996.

[24] Belytschko T. & Black T. Elastic crack growth in finite elements with minimal remeshing. *International Journal of Numerical Methods in Engineering*, **45**, 601-620, 1999.

[25] Abdelaziz Y. & Hamouine A. A survey of the extended finite element. *Computers and Structures*, **86**(11–12), 1141-1151, 2008.

[26] Belytschko T., Gracie R. & Ventura G. A review of extended/generalized finite element methods for material modelling. *Modelling and Simulation in Materials Science and Engineering*, **17**(4), 1-24, 2009.

[27] Shi J., Chopp D., Lua D., Sukumar N. & Belytschko T. Abaqus implementation of extended finite element method using a level set representation for three-dimensional fatigue crack growth and life predictions. *Engineering Fracture Mechanics*, **77**, 2840-2863, 2010.

[28] Moes N., Dolbow J. & Belytschko T. A finite element method for crack growth without remeshing. *International Journal of Numerical Methods in Engineering,* **46**(1), 131-150, 1999.

[29] Hibbitt, Karlsson & Sorensen. *Inc. ABAQUS/Standard User's Manual, v. 6.11.* Pawtucket, Rhode Island, 2011.

[30] Wimmer G., Schuecker C. & Pettermann H.E. Numerical simulation of delamination onset and growth in laminated composites. Austrian Aeronautics Research, Network for Materials and Engineering, ILDSB, Vienna University of Technology, 2006.

[31] Krueger R. Virtual crack closure technique: History, approach, and applications. ICASE Report No. 2002-10. National Aeronautics and Space Administration Langley Research Center, Hampton, Virginia, 2002.

[32] Kumar A., Gopalakrishnan S. & Chakraborty A. Modified virtual crack-closure technique using spectral element method. *International Journal of Computational Methods*, **4**(1), 109-139, 2007.

[33] Airbus industrie test method for determination of interlaminar fracture toughness energy of carbon fiber reinforced plastics, Mode I AITM 1.0005, Issue 2. Airbus Industrie, Blagnac Cedex, France, 1994.

[34] O'Brien T.K. Interlaminar fracture toughness: the long and winding road to standardization. *Composites Part B: Engineering*, **29**(1), 57-62, 1998.

[35] Airbus industrie test method for determination of interlaminar fracture toughness energy of carbon fiber reinforced plastics, Mode II. AITM 1.0006, Isuue 2. Airbus Industrie, Blagnac Cedex, France, 1994.

[36] Kilroy J. New carbon fibre/PEEK composites for space applications final test report. Doc. No. 02/025. CTL Tástáil Teo, Indreabhán, Co. Galway, Ireland, 2006.

[37] Kruger R. Three dimensional finite element analysis of multidirectional composite DCB, SLB and ENF specimens. ISD-Report No. 94/2, 1994.

[38] Olsson R. On improper foundation models for the DCB specimen. ICCM 16, Kyoto, **2**, paper SP223247, 2007.

[39] Huang X.N. & Hull D. Effects of fibre bridging on G_{IC} of a unidirectional glass/epoxy composite. *Composites Science and Technology*, **35**(3), 283-299, 1989.

[40] Standard test method for Mode I fatigue delamination propagation of unidirectional fiber-reinforced polymer matrix composites. Draft standard, ASTM International, Committee D30 on Composites, 2009.

[41] Krueger R. Development of a benchmark example for delamination fatigue growth prediction. NIA Report No. 2010-04. National Institute of Aerospace, Hampton, Virginia, 2010.

[42] Ramanujam N., Vaddadi P., Nakamura T. & Singh R.P. Interlaminar fatigue crack growth of cross-ply composites under thermal cycles. *Composite Structures*, **85**(2), 175-187, 2008.

[43] Benzeggagh M.L. & Kenane M. Measurement of mixed-mode delamination fracture toughness of unidirectional glass/epoxy composites with mixed-mode bending apparatus. *Composites Science and Technology*, **56**(4), 439-449, 2006.

[44] Reeder J.R. 3D mixed-mode delamination fracture criteria–An experimentalist's perspective. National Aeronautics and Space Administration Langley Research Center, Hampton, Virginia, 2006.

[45] Allix O., Kerfriden P. & Gosselet P. On the control of the load increments for a proper description of multiple delamination in a domain decomposition framework. *International Journal of Numerical Methods in Engineering*, **83**(11), 1518-1540, 2010.

[46] González-Estrada O.A, Ródenas J.J., Bordas S.P.A., Duflot M., Kerfriden P. & Giner E. On the role of enrichment and statical admissibility of recovered fields in a-posteriori error estimation for enriched finite element methods. *Engineering Computations*, **29**(8), 2012.

[47] Loehnert S., Prange C. & Wriggers P. Error controlled adaptive multiscale XFEM simulation of cracks. *International Journal of Fracture*, **178**(1-2), 1-10, 2012.

[48] Sankar B., Xu J. & Van Pelt J. Lightweight Composite Tanks for Liquid Hydrogen Storage. Nasa/CR − 2008-215440/Part 3, Department of Mechanical & Aerospace Engineering, University of Florida, Gainesville, 2008.

4. Damage characterisation of cryogenically cycled carbon fibre/PEEK laminates

Article overview

This work describes the experimental testing undertaken in order to characterise the damage formation in CF/PEEK laminates under cryogenic loading. The primary motivation for this study was the lack of published data relating to the cryogenic cycling of CF/PEEK as well as to investigate the interaction between the two main sub-critical damage modes: microcracking and delamination. It marks the first stage in a shift away from the conventional 2-D unit cell approach outlined in **Chapter** 3, where the location of transverse microcracks were pre-defined in order to simplify predictions. The unique combination of optical microscopy and 3-D X-ray CT employed in this work allows the complete characterisation of through-thickness crack networks, and hence gas leak paths, throughout the 3-D material space. DCOD and crack density values measured from cycled laminates allow the development and validation of future models based on the response of the material to the relevant cryogenic loading. Furthermore, these techniques are used to investigate the role of inherent material defects on crack initiation and morphology in general, laying the foundations for a realistic random microcrack initiation modelling methodology.

4. Damage characterisation of cryogenically cycled carbon fibre/PEEK laminates

Aside from characterising the fundamental interaction between damage modes, the influence of laminate thickness, material type, residual stress and stacking sequence on damage formation are also examined. Resulting trends in through-thickness microcacking, the magnitude of DCOD and the relative importance of fatigue loading provide insight into how to design for minimal laminate permeability; lessons which can be applied to larger composite structures such as cryogenic fuel tanks.

Abstract

A unique insight into damage formation in CF/PEEK laminates before, during and after cryogenic cycling, using optical microscopy and 3-D X-ray computed tomography (CT), is presented. Thicker laminates were found to exhibit significantly greater microcrack density and delamination when compared to thinner laminates, with lay-up and material type also being important contributing factors. Thermal residual stress induced microcracking was also found in thicker laminates post-processing. 3-D rendering software was used to prove the presence of through thickness crack networks within the laminates, as well as the extent of cracking through the specimen width. Crack opening in inner and off-axis ply groups was found to be significantly less than outer plies, implying the importance of these plies in limiting laminate permeability. The presence of voids was found to influence crack nucleation and growth paths within the laminates, with full void volume characterisation presented.

4.1 Introduction

Due to their favourable mechanical and physical properties, carbon-fibre reinforced polymers (CFRP) are seen as candidate materials for the fuel tanks of next generation reusable space launch vehicles (RSLVs) and expendable space launch vehicles [1]. With the RSLVs undergoing numerous fuelling/refuelling cycles, the tank walls will be repeatedly exposed to cryogenic temperatures as low as -250 °C. This thermal cycling can lead to microcracking and delamination formation within

4. Damage characterisation of cryogenically cycled carbon fibre/PEEK laminates

the CFRP, which, in severe cases, can result in permeation of the cryogen through the fuel tank walls. Therefore, a precise understanding of the methods of damage accumulation and how the various damage modes interact within thermally cycled composite laminates underpins the potential use of CFRP for RSLVs. Transverse microcracking in off-axis plies is typically the first noticeable damage mode encountered in composite laminates. Due to the multiaxial nature of thermal loading, cracks may form in both the outer and inner ply groups [2, 3] and may occur below the failure strength of the bulk material [4]. Overlapping microcracks in adjacent plies contribute to the formation of leakage paths through a damaged laminate, with factors such as stacking sequence, laminate thickness, and edge effects all affecting crack density and permeability [5-10]. With subsequent thermal cycles or increased amplitude of loading, delaminations may initiate from existing transverse cracks or from free edges. These delaminations can connect staggered microcracks in adjacent plies, leading to the formation of leakage paths that might not have developed through microcracking alone. The presence of delaminations can also lead to increased transverse crack opening at ply interfaces [11-14]. Delamination growth in laminates with existing transverse cracks under thermal fatigue loading has been modelled, showing a direct correlation between delaminated crack opening displacement and laminate permeability [15, 16]. This paper seeks to characterise the internal structure and damage present in pre- and post-cryogenically cycled CF/PEEK laminates of varying thickness and lay-up. Previous research into thermally induced microcracking has been limited to cryogenically cycling specimens of similar thicknesses [17-19], sometimes leading to ambiguous results due to the unknown role of thermal gradients and laminate thickness for the same material. However, the effects of varying centre-ply group thickness on microcracking has been studied and is well summarised in [2], which notes that the strain to initiate microcracking in the centre plies of cross-ply laminates decreases with increasing ply thickness. In this work, a comprehensive experimental study involving laminates made from unidirectional CF/PEEK tape sourced from three suppliers, in three different thicknesses (8-ply, 16-ply and 32-ply) and in two lay-up configurations ($[0°/90°]_{2S}$ and $[0°/45°/135°/90°]_S$) is undertaken. Two non-destructive testing (NDT) techniques are used to monitor damage progression before and during cycling: 2-D optical microscopy and 3-D X-ray computed tomography (CT). X-ray CT is increasingly becoming a viable testing technique due to

technological advances and reduction in equipment costs. This technique allows a full 3-D characterisation of the damage modes within a specimen [20-22], as well as allowing for void identification [22-25]. The majority of work in the area to date has focused on the scanning of small, representative volumes, with relatively few published works on damage characterisation in full specimens [26], particularly for thermally cycled laminates. This work offers insight into the defects present and damage formation in cryogenically cycled laminates by combining the detail of high magnification optical microscopy with the global outlook offered by 3-D X-ray CT. Void contents for each laminate type are compared and the effect of voids on crack initiation and crack growth paths are investigated. Crack density and crack opening displacement (COD) measurements taken from each specimen are used to show the significant influence of laminate thickness, lay-up and material type on subsequent damage. The importance of inner ply cracking for overall laminate permeability is also shown, with off-axis cracking observed to be more extensive than previously thought.

4.2 Methodology

4.2.1 Materials

CF/PEEK is a high-performance thermoplastic carbon-composite material. Thermoplastic composites offer a number of advantages over thermosetting composites in terms of the improved range of properties and processing techniques available. Crucially, CF/PEEK exhibits significantly higher toughness values, particularly Mode I fracture toughness, when compared to CF/epoxy materials, which translates to increased resistance to damage propagation [27-29]. Thermoplastics also allow the use of out-of-autoclave processing techniques such as automated tape placement (ATP), facilitating the manufacturing of large structures like cryo-tanks without the capital investment required for an autoclave several metres in diameter. Three types of CF/PEEK were used in testing: (i) Suprem T/60%/IM7/PEEK/150, (ii) Cytec APC-2 IM7 and (iii) Tencate CF/PEEK CETEX TC1200 AS4. Two lay-ups were also used for each material type: $[0°/90°]_{2S}$ cross-ply and $[0°/45°/135°/90°]_S$ quasi-isotropic configurations. Table 4.1 summarises the

4. Damage characterisation of cryogenically cycled carbon fibre/PEEK laminates

mechanical properties of a range of common CF/PEEK materials. (See A.4 for more material and processing information).

Table 4.1 Summary of mechanical properties of various types of commercially available CF/PEEK from manufacturers' datasheets.

Property	Cytec APC-2/AS4 (60%) [31]	Cytec APC-2/IM7 (60%) [31]	Tencate AS4 (59%) [32]	Tencate IM7 (59%) [32]	Suprem AS4 (55%) [33,34*]	Suprem IM7 (60%) [34]
0° Tensile Modulus GPa (°C)	138 (-55°C), 138 (24°C)	172 (-55°C), 172 (24°C)	130	172	141(196°C), 126 (70°C), 144 (20°C) 130*	165
90° Tensile Strength MPa (°C)	99 (-55°C), 86 (24°C)	63 (-55°C), 60 (24°C)	76	86	51 (196°C), 62 (-70°C), 54 (20°C) 90*	65
90° Tensile Modulus GPa (°C)	10.3 (-55°C), 10.3 (24°C)	11 (-55°C), 10 (24°C)	10	10.3	9.4 (70°C), 8.9 (20°C) 10*	10
GIC J/m^2 (°C)	1500 (55°C), 1700(24°C)	1600 (55°C), 2300(24°C)	1510(20°C)	N/A	1062 (20°C)	1515(20°C)
GIIC J/m^2 (°C)	1800 (55°C), 2000 (24°C)	2100 (55°C), 1900 (24°C)	1910(20°C)	N/A	1000 (20°C)	1355(20°C)

In order to determine the effect of laminate thickness on microcracking, three different thicknesses were used for each lay-up configuration. These laminate thicknesses corresponded to ply counts of 8, 16 and 32, with the plies being approximately 0.14 mm thick for all materials. Ply-level scaling was used to vary the laminate thickness. The rationale here is that this method can provide a more accurate view of the role of thickness in damage formation during processing and cryogenic cycling when compared to the sub-laminate scaling method, due to the consistent mechanical [30] and thermal response of the laminate with increasing thickness. An interlaced stacking sequence, based on scaling at a sub-laminate level, would be more effective for the design of cryo-tanks against microcracking. However, the present testing was not devised to limit microcracking, but to allow a direct comparison between damage formation in laminates of varying thickness.

Using an interlaced stacking sequence would potentially mask the full extent of this thickness effect in terms of damage formation. Fig. 4.1 summarises the test specimen materials and lay-ups.
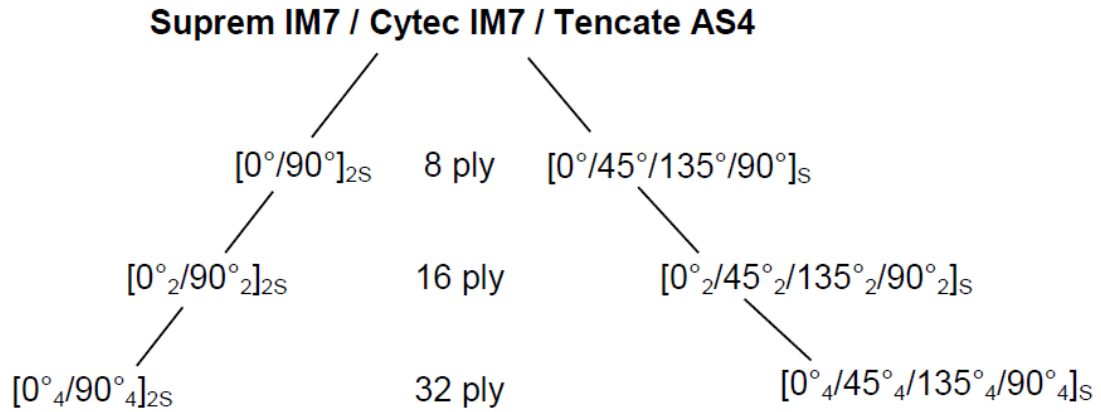
Suprem IM7 / Cytec IM7 / Tencate AS4

$[0°/90°]_{2S}$ 8 ply $[0°/45°/135°/90°]_S$

$[0°_2/90°_2]_{2S}$ 16 ply $[0°_2/45°_2/135°_2/90°_2]_S$

$[0°_4/90°_4]_{2S}$ 32 ply $[0°_4/45°_4/135°_4/90°_4]_S$

Figure 4.1 Summary of the materials, lay-ups and thicknesses used for the test specimens.

The laminates were hand laid-up and autoclaved. The Cytec and Tencate material had a processing temperature of 385 °C, with the Suprem material being processed at 375 °C, as per manufacturers' instructions. The temperature and pressure traces during autoclaving are plotted in Fig. 4.2. (See A.4 for further material processing details).
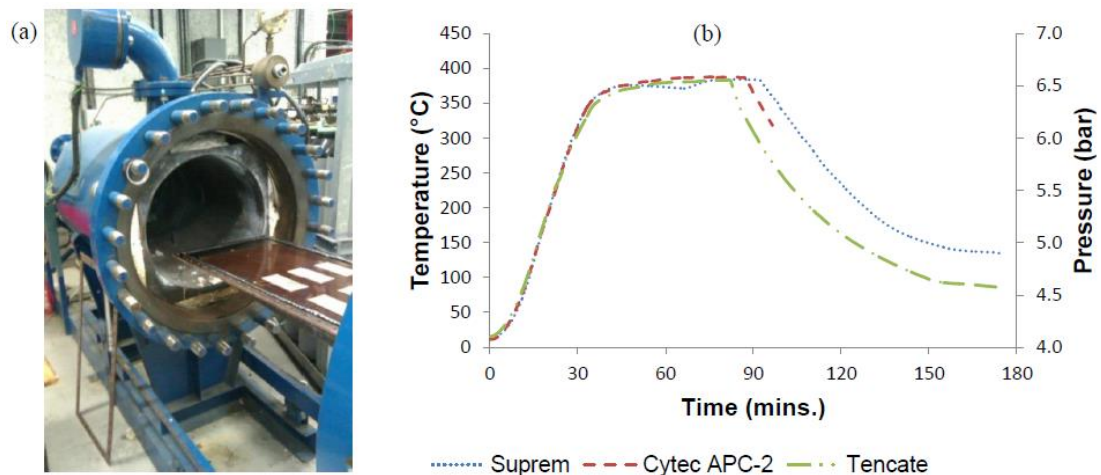
Figure 4.2 (a) Autoclave in ÉireComposites used for consolidating laminates (b) Temperature and pressure traces for the laminates during autoclaving.

The average cooling rate and peak cooling rate were 3.8 °C/min and 4.9 °C/min respectively. Each laminate measured approximately 150 mm x 70 mm as manufactured, with three identical test specimens, measuring 27 mm x 34 mm, being extracted using a water-jet cutting machine in order to minimise damage to the free edges. The specimen dimensions were chosen as a compromise between having a side length which was sufficient to display negligible edge effects at its mid-point and being compact enough to allow a comprehensive X-ray CT scan of the entire specimen.

4.2.2 Specimen preparation

Prior to thermal cycling, the specimens were prepared for optical microscopy through grinding, polishing and cleaning of the specimen edges. The objective of this was to achieve a sufficiently reflective surface to allow for material characterisation and crack detection on a given cross-section. Two specimens from each laminate were polished, one on the 0° side (aligned with fibres) and one on the 90° side (with the 0° fibre ends visible). This allowed the viewing of transverse cracks through each ply in the laminates. Prior to polishing, the specimens were mounted in quick-set epoxy resin holders. The specimens were hand ground using successively finer grit paper ranging from P180 to P2400, before being machine polished on cloth using diamond solutions ranging from 6 μm to 0.25 μm. The specimens were thoroughly cleaned with water, soap solution and isopropyl alcohol between each grinding and polishing stage (See A.1).

4.2.3 Thermal cycling

Liquid Hydrogen (LH$_2$) is often used as fuel for space launch vehicles, with liquid Oxygen (LOX) being used as the oxidiser. Due to cost and safety concerns associated with using open containers of these cryogens, liquid Nitrogen (LN), which has a boiling point between that of LH$_2$ and LOX at -196 °C, was used for cycling the laminates. The thermal cycle consisted of immersing a batch of the

4. Damage characterisation of cryogenically cycled carbon fibre/PEEK laminates

specimens directly into an open Dewar of LN$_2$ (Fig. 4.3 (a)), before placing them in warm air flow at 40 °C from a fan (Fig. 4.3 (b)).
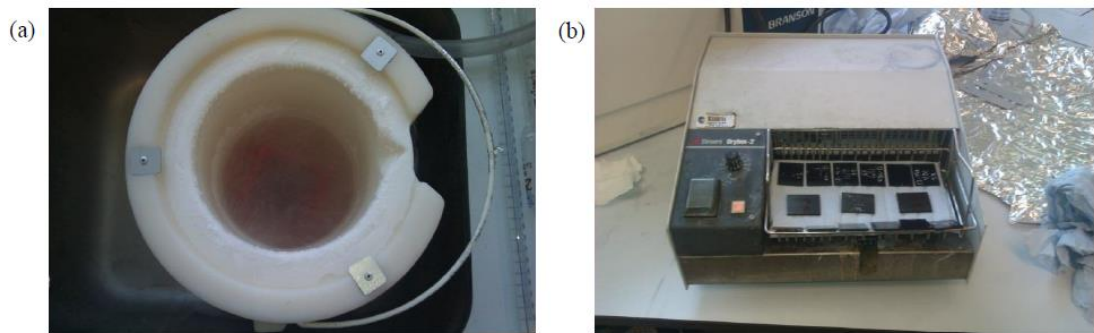

Figure 4.3 (a) Open Dewar of LN2 with immersed specimens (b) Specimen dryer used for warming

In order to ensure the specimens reached thermal equilibrium during the cooling and warming stages, a thermocouple was embedded within an initial 8-ply test specimen to track temperature change at its centre. The temperature trace is shown in Fig. 4.4.
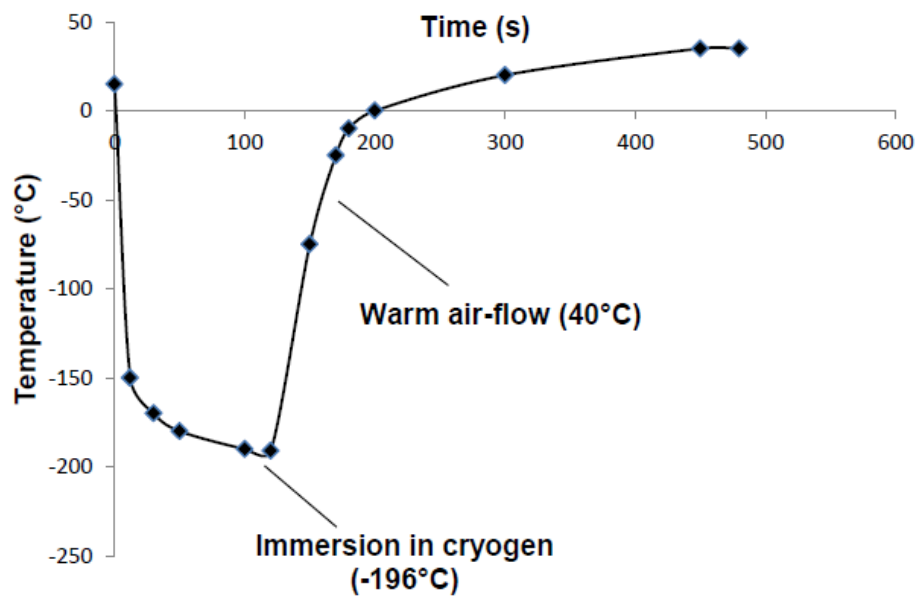
Figure 4.4 Temperature trace for an 8 ply specimen immersed in cryogen and warmed in air flow.

4. Damage characterisation of cryogenically cycled carbon fibre/PEEK laminates

The centre of the specimen was found to reach -196 °C within 2 minutes following immersion in the LN_2, while the centre of the specimen reached 40 °C 6 minutes after removal of the specimen from the Dewar, giving a total cycle time of 8 minutes. In order to account for any margin-of-error in the temperature measurements, the standard cycle time for an 8-ply laminate was increased to 11 minutes, consisting of a 3 minute cool down period followed by an 8 minute warming period. In order to estimate the required cycle times for the thicker 16-ply and 32-ply specimens, 3-D finite element (FE) heat transfer simulations were conducted. These models predicted that a doubling of specimen thickness would also lead to an approximate doubling in cycling time, as well as showing the magnitude of thermal gradients with the specimens themselves. Fig. 4.5 plots the maximum variation in temperature between the surface of a specimen and its centre for multiple ply thicknesses using a surface convective heat transfer coefficient of 75 $Wm^{-2}K^{-1}$. This value represents the lower end of the transfer coefficient range based on predictions from the temperature trace in Fig. 4.4.
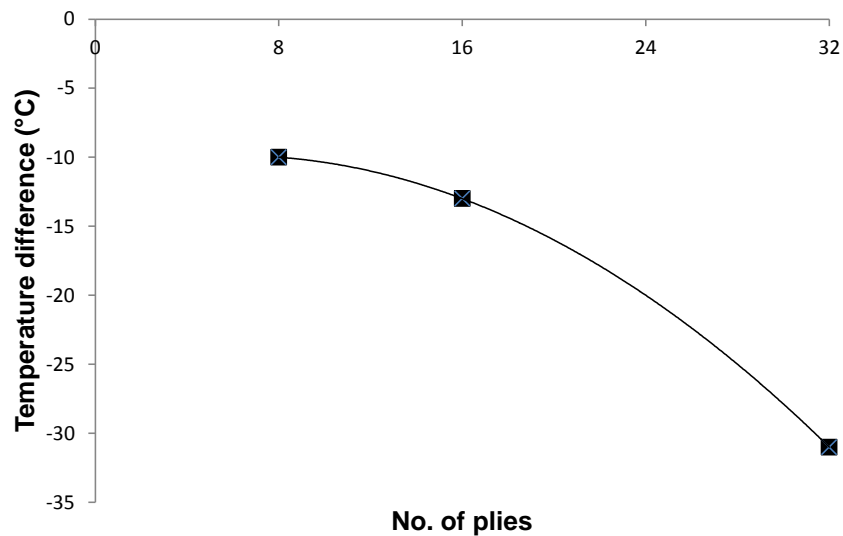

Figure 4.5 Comparison of FE predicted maximum temperature differences between the outer surface and centre point of specimens for a range of ply thicknesses.

The longitudinal and transverse thermal conductivities used in the simulation were 6.0 and 1.2 $Wm^{-1}K^{-1}$ [35] respectively while the density and specific heat capacity were 1550 kgm^{-3} and 950 $Jkg^{-1}K^{-1}$ [35]. Based on the temperature trace for the 8-ply

laminate and predictions from the FE simulations, the cycle times for the 16-ply and 32-ply laminates were chosen as twice (22 mins.) and four times (44 mins.) the 8-ply time, respectively. The specimens were exposed to 50 cryogenic cycles, which is representative of at least 10 launches of a RSLV, albeit without consideration of the additional mechanical loading acting on the cryo-tank (See A.5 for further detail on cryogenic cycling).

4.2.4 Material and damage characterisation

Characterisation of the internal structure of the laminates and subsequent crack growth monitoring was carried out using optical microscopy and X-ray CT. As mentioned previously, three identical specimens were extracted from each master laminate. Two of these specimens were polished in accordance with the protocol outlined in Section 4.2.2. The cross-sections on the polished 0° and 90° sides of these specimens were examined under an optical microscope at the following magnifications: 12.5×, 50×, 100× and 200×. The sides were viewed before and during cycling in order to characterise the internal structure of the laminates and to observe subsequent crack growth. The remaining specimen from each batch was left unpolished in order to ensure that the preparation process was not damaging the specimens prior to cycling. An additional benefit of X-ray CT, is that it does not require any specific specimen preparation. The scans were carried out before and after cycling using a *Phoenix M nano/microtom* [36]. The X-ray gun was rated at 180 kV, with scans being carried out at 160 kV and 28 μA, giving a scan power of 4.5 W. A total of 1,000 images were generated for each scan over a 360° field of view, for a total scan time of 67 minutes. The tomographical reconstruction was carried out using *Davos* software, whilst volume rendering was completed using *VGStudio MAX 2.2*. Two primary scan resolutions were used in this study: 15 μm and 33 μm. A central portion of each specimen was scanned at the higher 15 μm resolution before cycling in order to provide a detailed characterisation of the general structure of the laminates. The upper scan resolution limit for the specimens was 11 μm using the *Phoenix M*; however, due to the proximity between the specimen edge and the gun with specimen rotation, this was reduced to 15 μm. The diameter of a typical carbon-fibre in high performance composites ranges from 5 μm to 7 μm;

hence individual fibres were not discernible for the specimen dimensions of this study, even at the highest scan resolution. The specimens were also scanned at 33 μm before and after thermal cycling. This resolution was the highest available for which the entire specimen could be contained within the region of interest on the detector, allowing identification of all cracks and defects within the sample (See A.6 for further detail).

4.3 Results

4.3.1 Initial characterisation

General structure

Optical micrographs of each specimen were taken prior to cycling in order to determine any distinguishable structural features which may influence future damage build-up. Fig. 4.6 shows typical cross-sections for 16-ply Suprem (a), 16-ply Cytec APC-2 (b) and 8-ply Tencate (c) specimens.
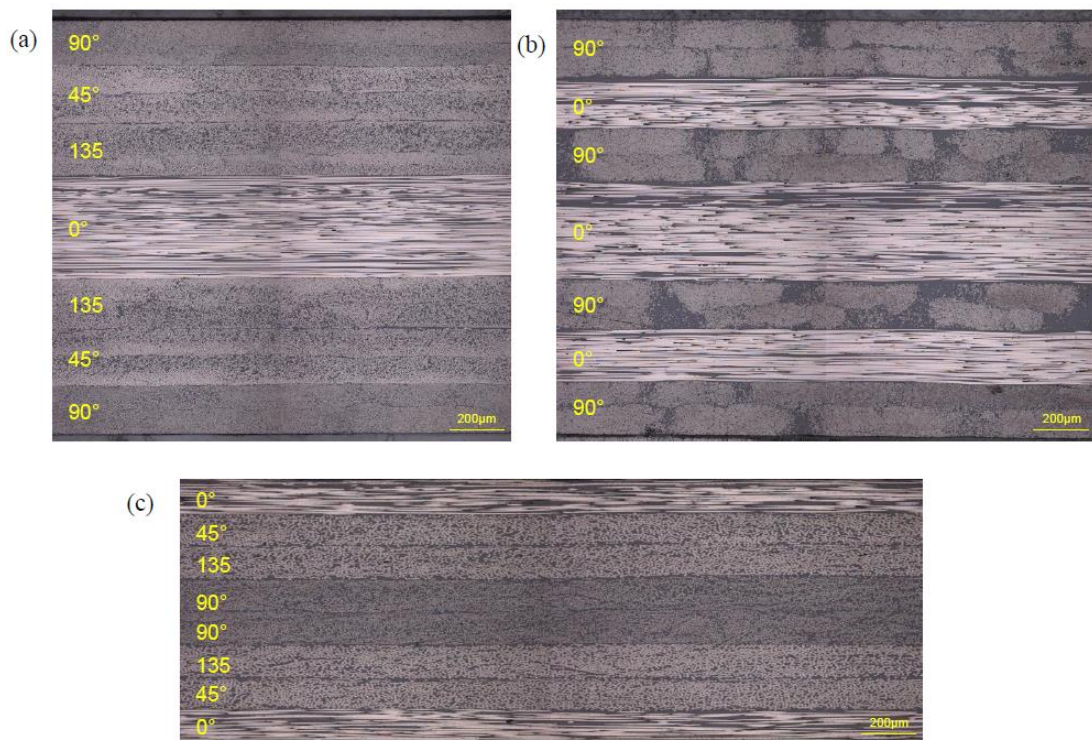
Figure 4.6 Optical micrographs of (a) 16-ply QI Suprem (b) 16-ply cross-ply Cytec APC-2 (c) 8-ply QI Tencate.

The micrographs were selected to represent the general, defect-free structure for each material. Both the Suprem and Tencate materials were found to have a relatively homogenous structure, with an even distribution of fibres within each ply. Although the ply boundaries are distinguishable by narrow resin bands (visible in (c)), the laminates were generally well consolidated. The Cytec APC-2 material differed considerably, with the fibres appearing to remain clustered in tows, leaving large resin-rich areas throughout the laminate. This inhomogeneous structure was observed in Cytec APC-2 specimens of all thicknesses and lay-ups. The resin-rich areas were also visible in X-ray CT scans of the laminates, as shown by the darker areas in Fig.4.7 (b). These scans illustrate the increased resin-rich area content of the Cytec APC-2 material with respect to Suprem and Tencate. Thresholding of the scan gray-level was used to isolate the resin areas from the carbon fibres, based on the difference in density between PEEK and carbon fibre. Large resin bands are visible along ply boundaries as well as the more isolated, through-thickness resin areas.
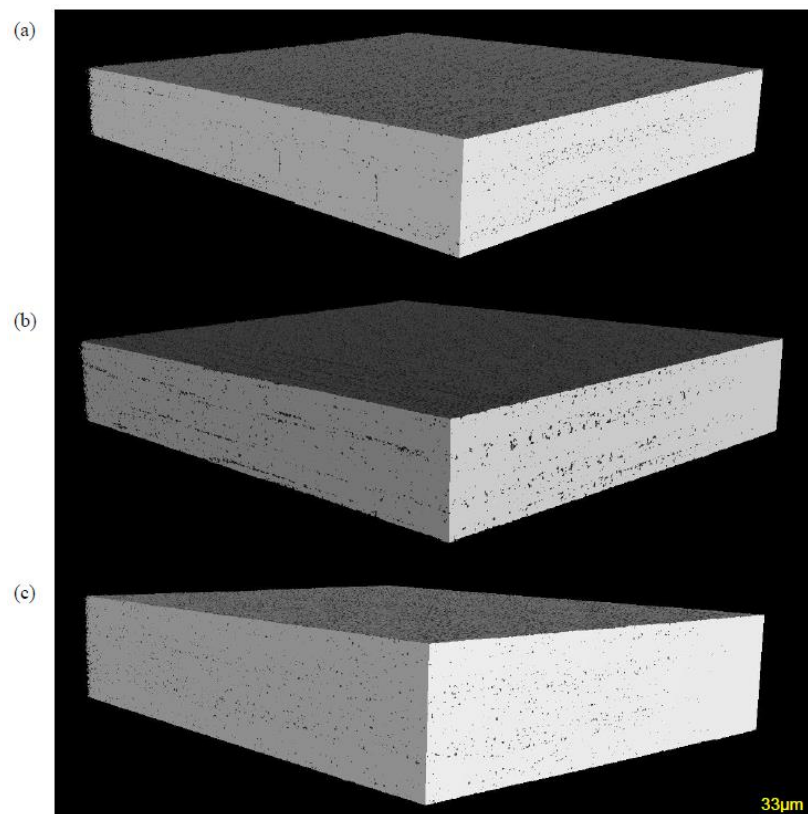

Figure 4.7 Rendered X-ray CT scans of 32-ply cross-ply (a) Suprem (b) Cytec APC-2 and (c) Tencate laminates, with the darker areas showing resin-rich bands and pockets.

Defects from processing

Each laminate was examined for common defects which typically arise from the processing of the composite material. Void formation can occur due to the presence of trapped air between the plies and/or volatiles within the material, which are released during the curing cycle. These voids can act as crack nucleation points within the laminate, as well as increasing laminate permeability. Optical micrographs (Fig. 4.8) and X-ray CT scans were used to determine the extent of void formation within the specimens.
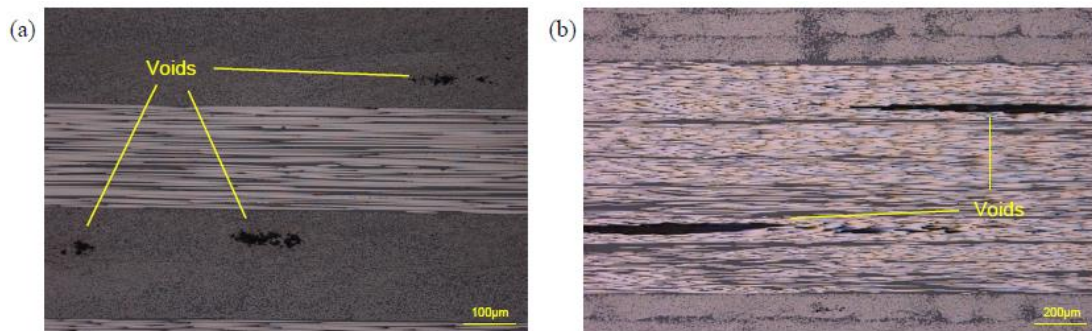
Figure 4.8 (a) Small and medium sized voids in a Suprem laminate (b) Large, elongated voids in a Cytec APC-2 laminate. These large, inter-ply voids were not common in the examined specimens.

In keeping with findings from [22, 37, 38], smaller voids tended to take on a spherical shape, whilst larger voids had a notably more elongated appearance. Characterisation of the void content of the specimens through X-ray CT was dependant on the resolution of the scan and the thresholding limits used to isolate the voids from the surrounding material. For the resolution of 33 μm applicable here, only voids with a dimension greater than 66 μm were distinguishable (See A.6). Void volume content analyses were carried out on all laminate types using a defect detection algorithm from the rendering software. In general, voids were found to be evenly dispersed throughout the specimen thickness and width. Fig. 4.9 shows the results of this void detection.

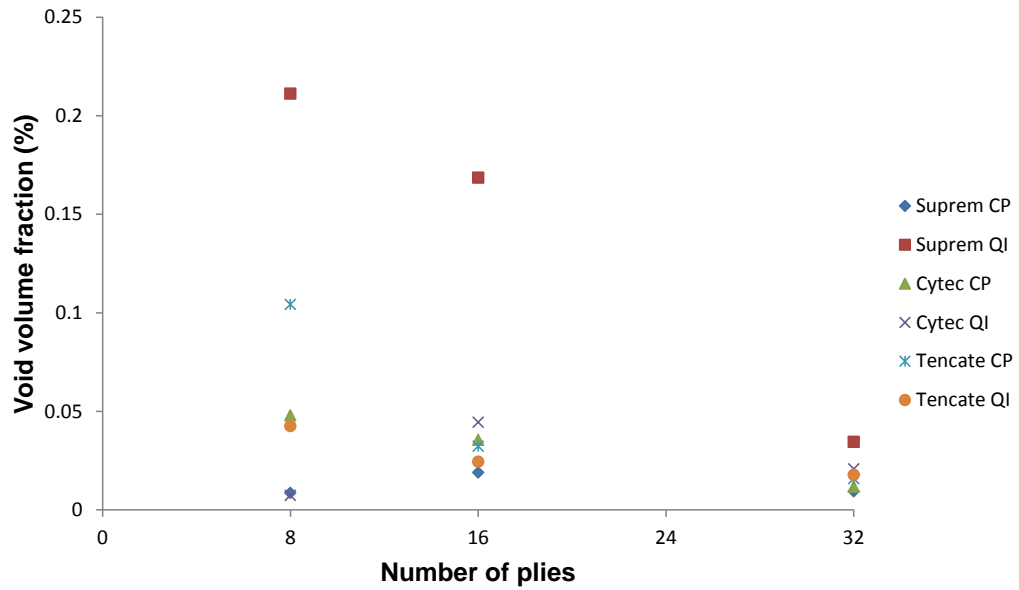4. Damage characterisation of cryogenically cycled carbon fibre/PEEK laminates

Figure 4.9 Void volume fraction results for all laminate types obtained using X-ray CT analysis software (QI = Quasi-Isotropic; CP = Cross-Ply).

These results are summarised in Table 4.2 in terms of material type, lay-up and thickness.

Table 4.2 Summary of void volume content of the laminates.

Material	Average void volume fraction (%)
Suprem	0.075
Cytec	0.028
Tencate	0.039
Lay-up	**Average void volume fraction (%)**
Cross-ply	0.031
Quasi-isotropic	0.063
No. of plies	**Average void volume fraction (%)**
8	0.070
16	0.054
32	0.018

All specimens examined were found to have a void volume fraction below 0.25%, with the majority being below 0.05%. Given that a 1% void volume fraction is generally held as the upper acceptable limit for aerospace grade composites, the

laminates were deemed to have a very low void content. This low relative void content also means that statistical variance in measurements can contribute, in-part, to trends in void volume contents for specimens of various CF/PEEK materials, lay-ups and thicknesses. As shown in Table 4.2, noticeable differences in void content were found between laminates of differing lay-up and thickness, with thinner, quasi-isotropic laminates generally having higher void contents. Fig 4.10 shows a rendered X-ray CT scan of a 32-ply Tencate specimen, with a threshold applied to isolate voids from the surrounding material.
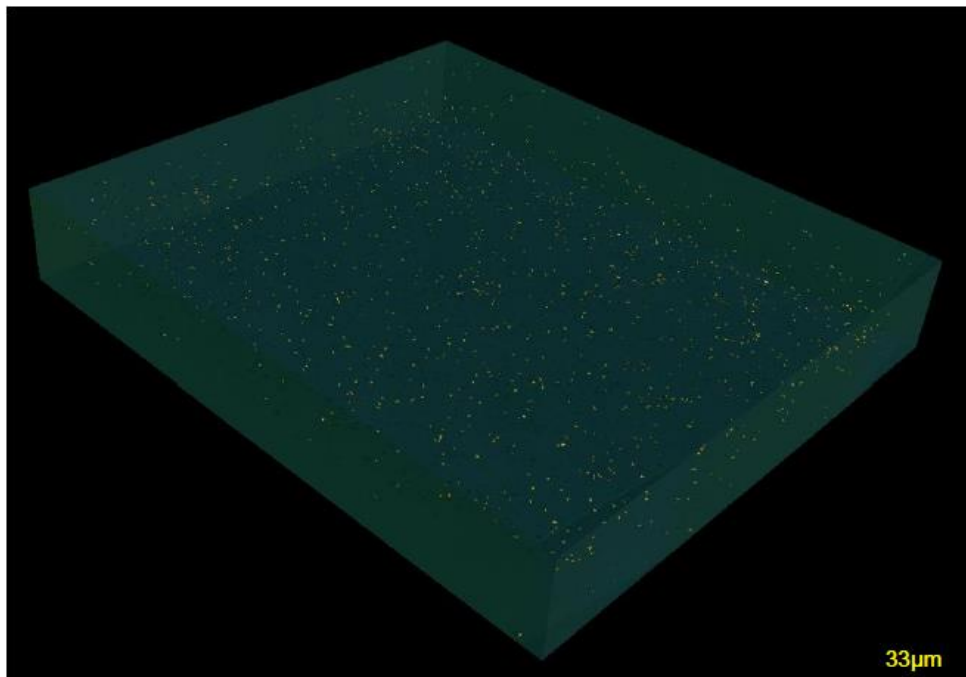
Figure 4.10 Rendered X-ray CT scan of a 32-ply cross-ply Tencate specimen with a threshold applied to reveal voids.

The scan revealed an abundance of small to medium sized voids dispersed evenly throughout the specimen. Larger voids, on the order of several mm^3 in volume, were also found clustered together, though in fewer numbers. Analysis of void morphology based on the X-ray scans corroborated the qualitative analysis of the optical micrographs in that there exists a direct relationship between void sphericity and void radius as shown in Fig. 4.11, where sphericity is defined as the ratio between the surface of a sphere with the same volume as the defect and the surface of the defect [39].
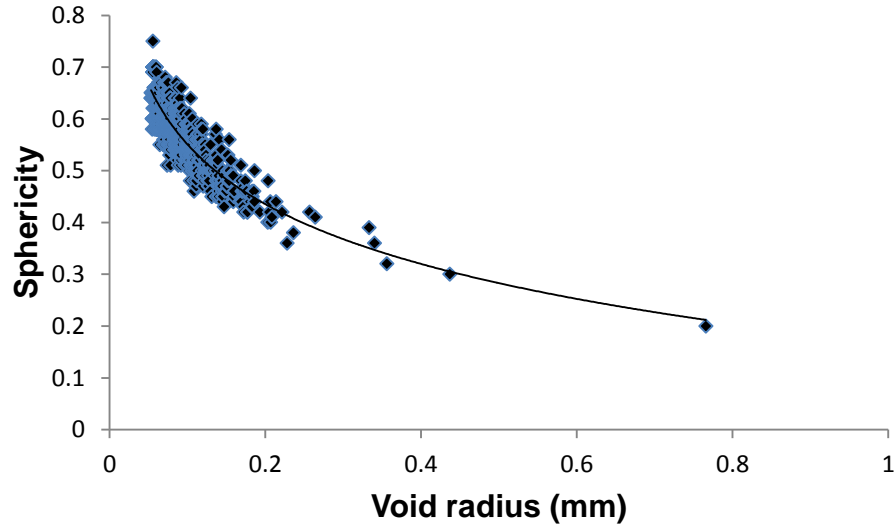
Figure 4.11 Comparison of void sphericity with void radius for all 1,143 detectable voids in a 32-ply Cytec quasi-isotropic laminate. Larger voids were found to be less spherical than smaller voids.

Post-processing cracking

Due to the high processing temperature required for CF/PEEK (375 °C to 385 °C), thermal residual stresses are well known to be present in laminates immediately after processing and cooling to room temperature. The origin of these stresses are generally categorised as follows [40]:

- Micromechanical level – Due to mismatch between thermal expansion coefficients between fibres and the matrix
- Macro-mechanical level – Due to mismatch in expansion between plies of varying orientation
- Global level – Due to thermal gradients within the laminate as a whole arising during cooling

Common defects caused by these residual stresses include microcracking and delamination [41]. Upon examination under an optical microscope a number of the laminates were found to have residual stress-induced microcracks, before any cryogenic cycling commenced. Fig. 4.12 summarises the post-processing microcracking in all laminates, where the severity of microcracking is represented on a scale from I to V in order of increasing number of cracks.
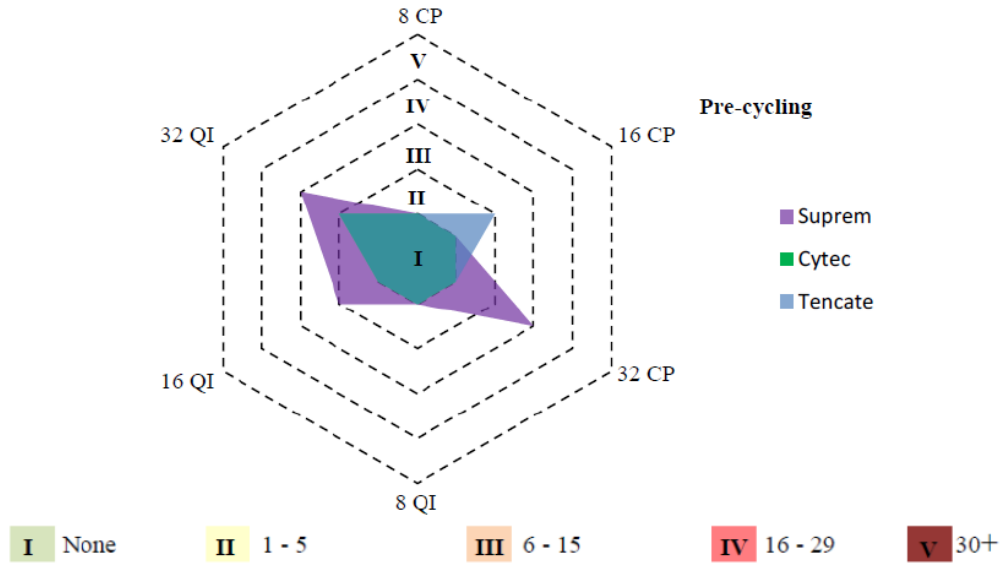
Figure 4.12 Summary of microcracking in all laminates pre - cycling. The laminates are classified in terms of the number of microcracks per polished specimen side. (QI = Quasi-Isotropic; CP = Cross-Ply).

The scale represents the average number of microcracks in the most severely damaged ply group for each laminate type. Microcrack counts in subsequent figures are based on the microcrack fully extending through at least one ply in a given ply group. Delaminations are not counted. Fig 4.13 (a) shows microcracking present in the 45° plies of 32-ply QI Suprem laminate before thermal cycling.
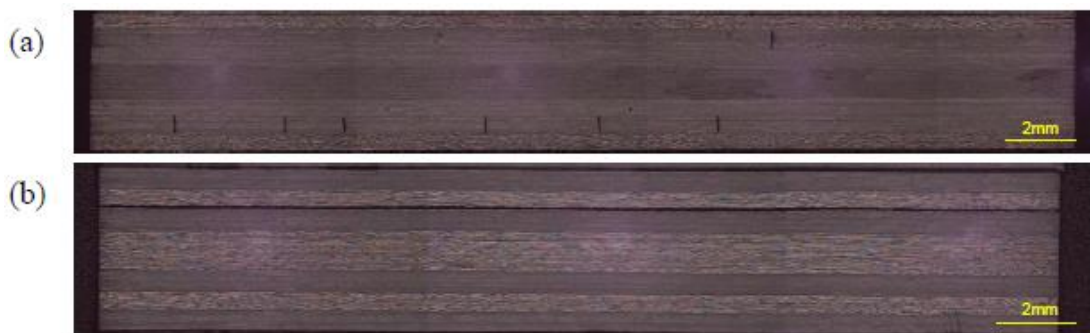

Figure 4.13 (a) Residual stress induced microcracking in the 45° plies of a 32-ply QI Suprem laminate, before thermal cycling (b) Residual stress induced delamination in a 32-ply cross-ply Suprem laminate, before thermal cycling.

All 32-ply QI laminates for each material contained transverse microcracks due to residual stresses. The 16-ply QI Suprem specimens also contained microcracks. This trend indicates that both macro-mechanical and global level stresses are responsible, given (i) the predominance of microcracks in the thickest QI laminates, and (ii) the absence of cracks in cross-ply or thinner QI laminates. A notable exception to this trend was the 32-ply cross-ply Suprem specimens. While containing little microcracking, large-scale delamination between 0° and 90° ply groups was observed. Fig. 4.13 (b) shows one such delamination which extends the entire length of the examined cross-section. It is likely that this delamination arose due to the large mismatch in thermal expansion coefficient between the ply groups, leading to stresses sufficiently high to exceed the mixed-mode fracture energy of the composite. Fig. 4.14 shows a rendered X-ray CT scan of residual stress induced microcracking in a 32-ply QI Suprem laminate.
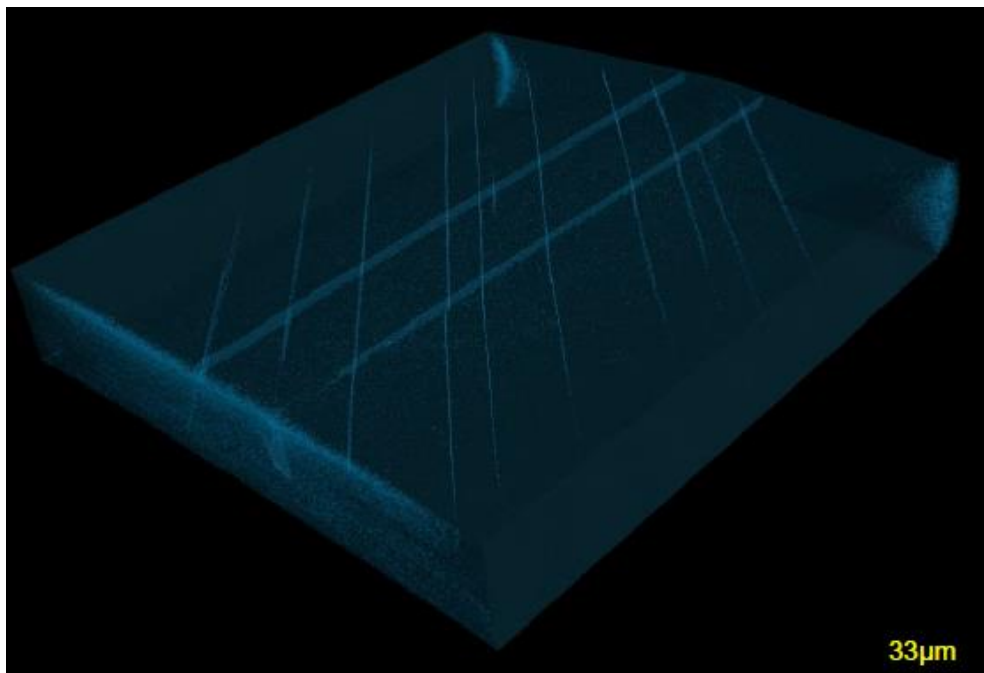

Figure 4.14 Rendered X-ray CT scan of residual stress induced microcracking in a 32-ply QI Suprem laminate. The cracks were found to extend across the full width of the specimen.

111

4.3.2 Damage characterisation due to thermal cycling

Global damage trends

All test specimens were subjected to 50 cryogenic load cycles (as shown in Fig. 4.4), with the exception of the 32-ply Suprem laminates, which were subjected to 30 cycles. The specimens were examined under an optical microscope after cycles 1, 2, 3, 5, 10, 15, 20, 30 and 50, with snapshots of the laminates and X-ray CT scans taken after cycles 1 and 50. After 1 cycle, substantial microcracking and delamintation was observed in most of the 32-ply laminates, with more moderate levels of damage present in 16-ply laminates and little or no cracking present in the 8-ply specimens. No further damage accumulation occurred in any of the laminates, even after 50 cycles, with the exception of the Cytec APC-2 32-ply cross-ply specimens. Here, one extra crack developed in each of the test specimens after cycle 10. The lack of damage accumulation subsequent to the first cycle suggests that substantial relaxation of residual stresses occurred with the first exposure to cryogenic temperatures. The formation of microcracks and delaminations in certain ply groups would have reduced the constraint placed upon adjacent, uncracked plies, leading to a reduction in stress in these plies for a given temperature drop. The general thermal history for the laminates is shown in Fig.4.15.
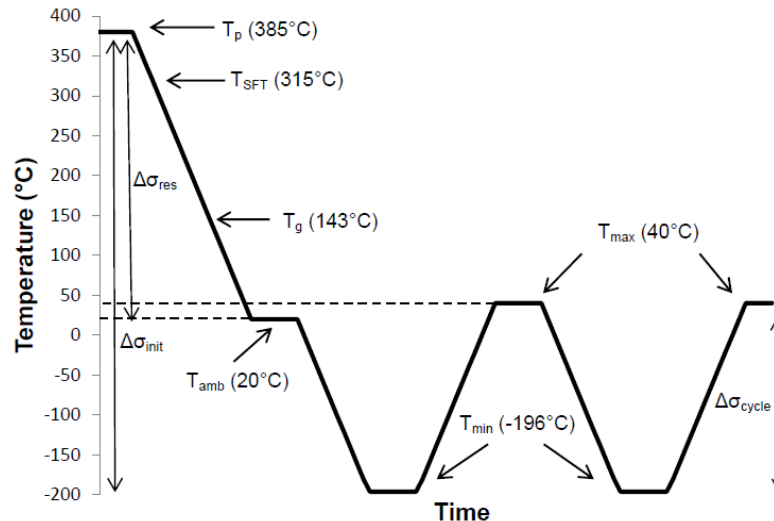

Figure 4.15 Thermal history for the laminates from processing to cryogenic cycling. The processing temperatures given are for a typical CF/PEEK material.

4. Damage characterisation of cryogenically cycled carbon fibre/PEEK laminates

The drop in temperature from T_p (processing) through T_{SFT} (stress free temperature) and T_g (glass transition) to T_{amb} (ambient) gives rise to a change in residual stress of $\Delta\sigma_{res}$. The Stress Free Temperature (SFT) for semi-crystalline polymer matrices is found near the peak crystallisation temperature due to the load-bearing capability of the newly formed crystalline phase below this point. The exact value of the SFT of a given material varies with cooling rate. The value of 315 °C given here is taken as an average of the values presented by [42, 43], which lay in the range of 310 °C to 32 8°C. For some laminates, particularly the Suprem material, these residual stresses were sufficient to cause damage initiation. Upon immersion in the cryogen at T_{min}, the total change in stress in the laminates is given as $\Delta\sigma_{init}$. The magnitude of this stress change was sufficient to increase damage levels in previously cracked laminates as well as initiating damage in some previously uncracked specimens. Subsequent thermal cycling from T_{min} to T_{max} leads to a stress change of $\Delta\sigma_{cycle}$. For the majority of specimens, this stress change was insufficient to cause damage initiation or further damage propagation. Additional work on the magnitude of the thermal stresses, following on from [16] and to be published elsewhere, corroborates that cracking occurs on the first cryogenic cycle for certain laminates. Fig. 4.16 summarises the general damage trends for the specimens in terms of the number of microcracks per specimen side.
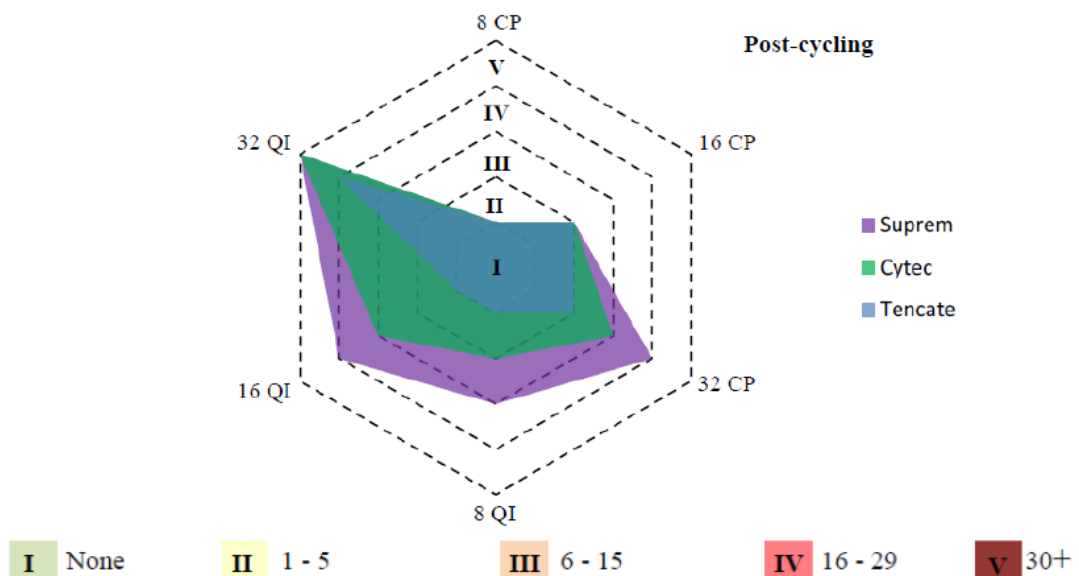

Figure 4.16 Summary of microcracking in all laminates post - cycling. The laminates are classified in terms of the number of microcracks per polished specimen side. (QI = Quasi-Isotropic; CP = Cross-Ply).

4. Damage characterisation of cryogenically cycled carbon fibre/PEEK laminates

Three primary trends in damage formation were observed in the specimens based on:

- Laminate thickness
- Lay-up
- Material type

The major difference in crack densities between 8-, 16- and 32- ply specimens is indicative of the role played by laminate thickness in microcrack formation. Most of the 8-ply laminates were found to be crack-free or, at worst, contain a small number of cracks after either 1 or 50 cycles. A larger number of microcracks, up to 15 per specimen, were present in the 16-ply laminates, with only the Tencate quasi-isotropic laminates remaining crack-free. A substantial increase in damage was detected in the 32-ply laminates, with all specimens registering at least moderate microcracking. High crack densities were observed in most of these specimens, with some containing large-scale delaminations, comprising up to 50% of the specimen width. The lay-up of the specimens was also found to influence the extent and mode of damage in the laminates. Quasi-isotropic laminates generally exhibited higher crack densities than cross-ply laminates. However, the tendency to delaminate along ply group boundaries was observed in the thicker cross-ply laminates. Fig. 4.17 compares the extent of microcracking and the damage modes in 32-ply cross-ply and quasi-isotropic Suprem laminates.
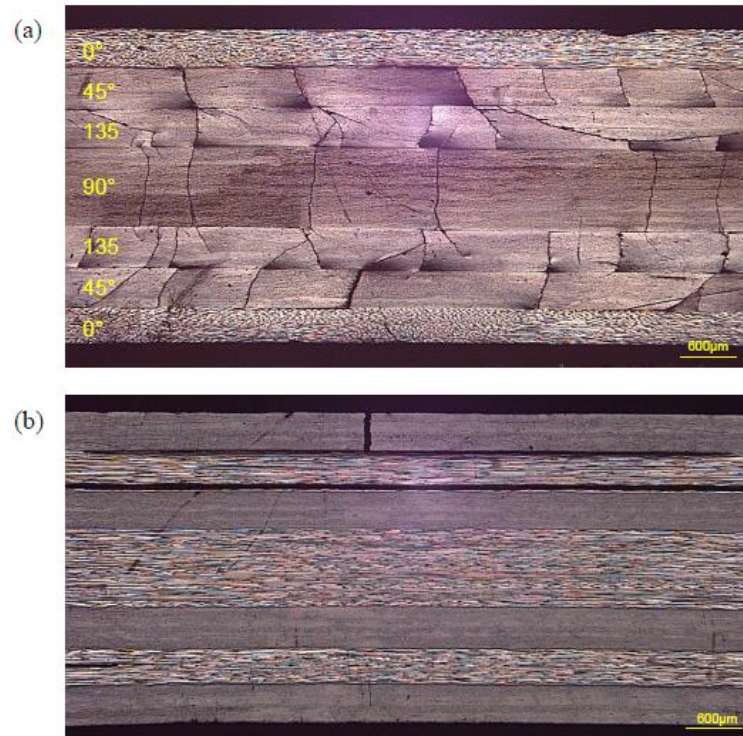
Figure 4.17 (a) Cryogenically induced high density microcracking and delaminations in a 32-ply Suprem quasi-isotropic laminate (b) Cryogenically induced large-scale delamination and single microcrack in a 32-ply Suprem cross-ply laminate.

The micrographs of Fig. 4.17 illustrate widespread damage formation for the Suprem laminates, with the quasi-isotropic laminates containing extensive microcracking and short delaminations and the cross-ply laminates displaying a number of extensive inter-ply delaminations, accompanied by relatively few microcracks with large crack opening displacements. This trend was also observed in X-ray CT scans of the specimens. Fig. 4.18 shows high density microcracking, with multiple families of 0°/90° and 45° transverse cracks visible and extending across the entire width of the quasi-isotropic specimens (a), (c) and (e).
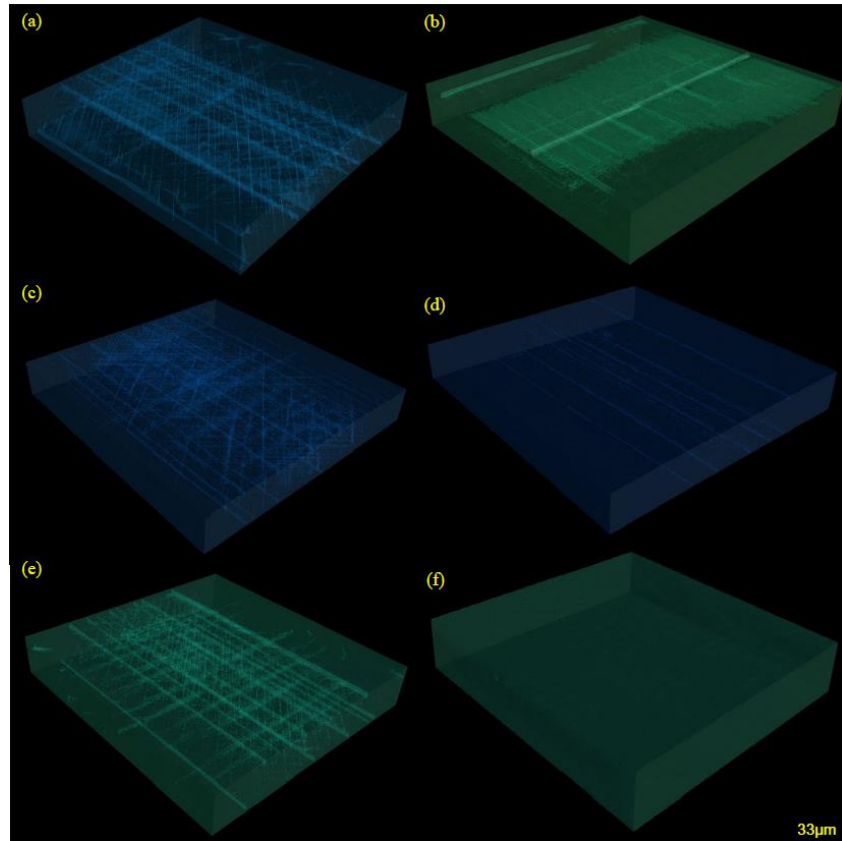
Figure 4.18 X-ray CT scans of post-cycled damage in full specimens for Suprem QI and CP (a-b), Cytec APC-2 QI and CP (c-d) and Tencate QI and CP (e-f) 32-ply laminates after 50 thermal cycles.

Damage in cross-ply specimens (b), (d) and (f) is characterised by wide transverse cracks in the outer plies and extensive delamination between ply groups. Fig. 4.19 compares the average crack densities for cross-ply and quasi-isotropic 32-ply laminates.
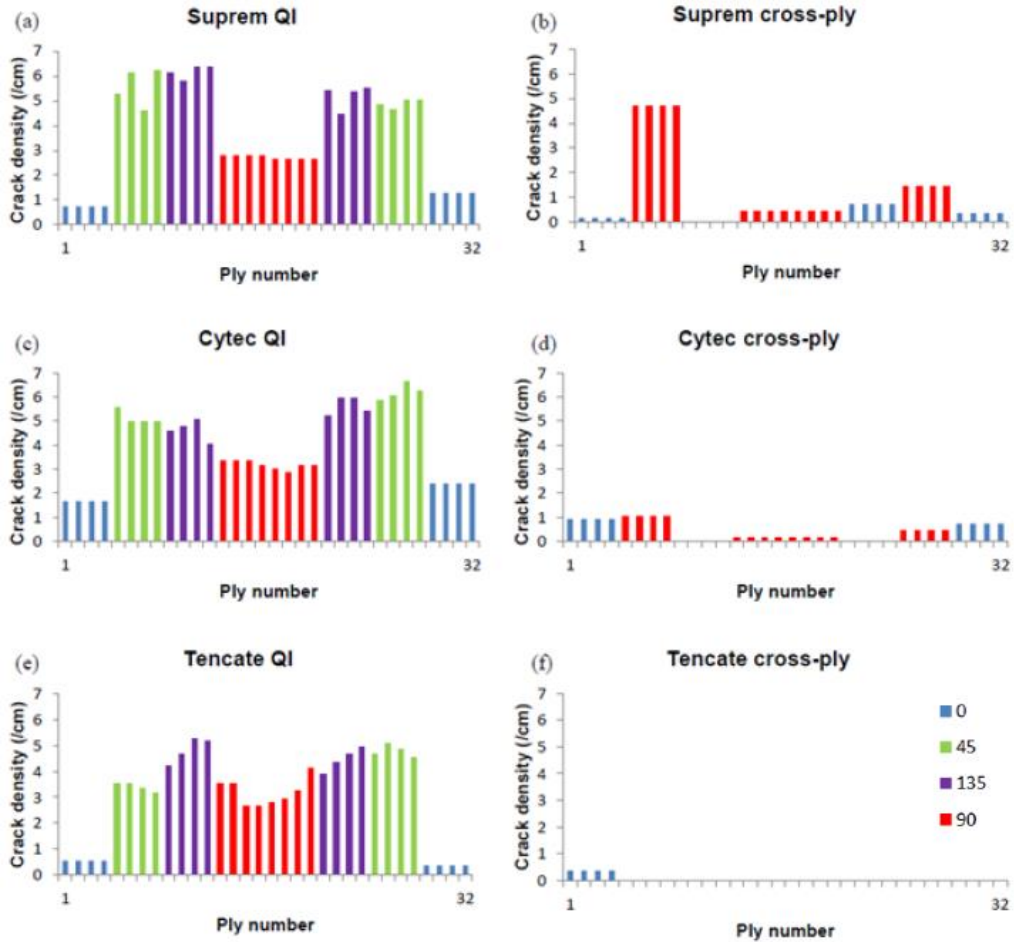
Figure 4.19 Summary of microcrack densities in Suprem, Cytec APC-2 and Tencate 32-ply laminates after 50 thermal cycles. The graphs are arranged to display the crack density for the four plies in each ply group through the laminate thickness.

There is a clear trend towards higher crack densities in quasi-isotropic laminates, particularly in the inner, off-axis ply groups. This trend was corroborated by 3-D finite element analyses of the stresses induced in 32-ply quasi-isotropic and cross-ply laminates due to a change in temperature from 40 °C to -196 °C, as shown in Fig. 4.20.
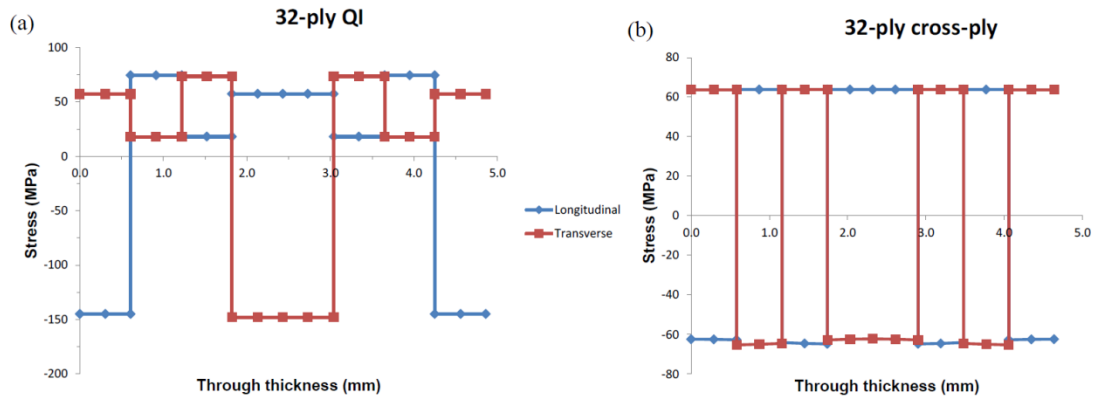
Figure 4.20 3-D FE predicted through thickness stress variation due to a ΔT = -236 °C for 32-ply CF/PEEK (a) quasi-isotropic (edge) and (b) cross-ply (centre) laminates. Longitudinal and transverse refer to global directions.

The CF/PEEK was modelled as a linear thermoelastic material, with transversely-isotropic properties taken as an average of those presented in Table 4.1. The thermal properties used in the analyses were those presented in Section 4.2.3. Fig. 20(a) shows the through-thickness stress variation for a 32-ply quasi-isotropic laminate at -196 °C, measured at the edge of the laminate. The peak tensile stress of 74.2 MPa is observed to occur in the inner off-axis plies, which were also observed to have the highest crack density after physical testing. This tensile stress was also found to be higher than the 63.7 MPa predicted for the cross-ply laminates in Fig. 4.20 (b), although stress through the thickness for both lay-ups at centre points are identical. These peak stress values are also in the region of the average transverse tensile strength of both the Cytec and Suprem materials. It is also worth noting the high compressive stresses, on the order of 150 MPa, present in the outer and centre ply groups at the specimen edges. A transient thermal stress analysis, using a convection coefficient of 500 $Wm^{-2}K^{-1}$, was also carried out for the cross-ply laminates. This convection coefficient represents a value closer to the upper bound of the estimated transfer coefficient range. Fig. 4.21 plots the transient thermal tensile stress variation at a number of points, from the outer plies through to the centre plies of 8, 16 and 32-ply laminates.
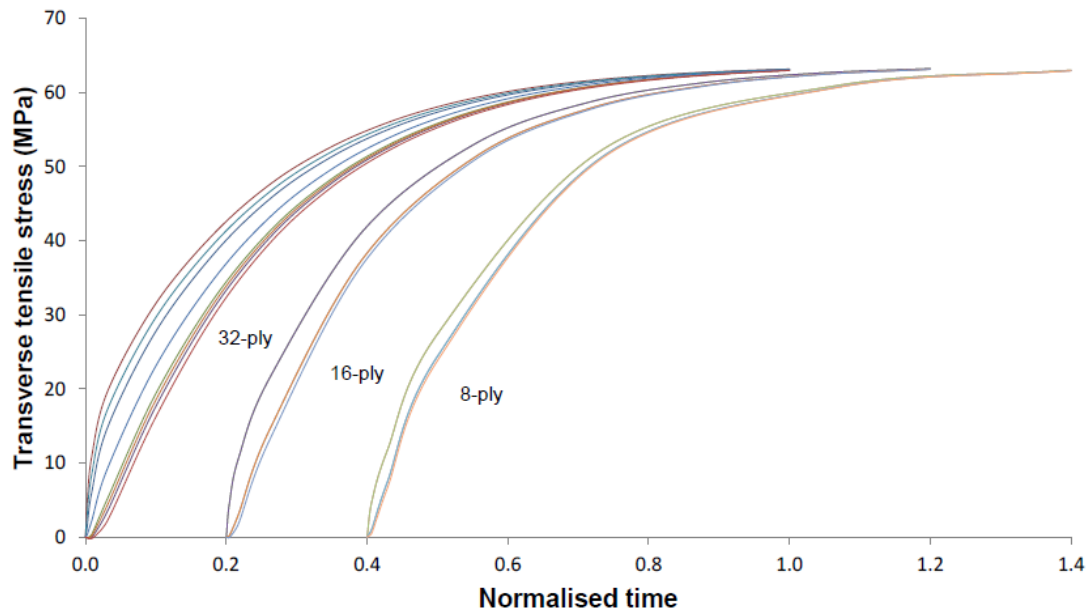
Figure 4.21 3-D FE transient thermal stress analysis for a CF/PEEK laminate showing through-thickness transverse tensile stress variation for 8, 16 and 32-ply laminates. The time is normalised with respect to the total time required for each laminate to reach thermal equilibrium with the liquid nitrogen. Note the origin of time has been shifted by 0.2 for the 16-ply model and 0.4 for the 8-ply model for clarity.

This plot illustrates the skin-core effect for laminates, whereby unevenly cooled specimens exhibit noticeably higher tensile stresses in their outer ply groups, due to thermal self-equilibration effects. This effect is more pronounced for thicker laminates, with the 32-ply model predicting a highly inhomogeneous stress state, characterised by a difference of over 20 MPa between the transverse tensile stresses in the outer and inner plies. During the early stages of cooling, the peak transverse tensile stress observed in the outer plies of the 32-ply laminate is almost double that of the 8-ply laminate. This additional self-equilibration of stress, which is more prominent in thicker laminates, contributes to the damage behaviour observed. At the end of the cooling, the final stress state within the laminates is identical, regardless of thickness, as shown in Fig 4.21. It should be noted that the difference in damage formation between the thicker and thinner laminates could also be partly attributed to the increased influence of edge effects for thicker laminates, as well as the size effect, which is related to the probability of there being a crack-initiating defect in a given volume of material [44-46]. It is clear from Fig. 4.16 that certain material

types were more susceptible to microcracking than others, with the Suprem CF/PEEK material exhibiting the most damage before and after cycling and the Tencate material the least. The material properties shown in Table 4.1 can go some way to explaining these differences. The Tencate material, which uses the less stiff AS4 fibres, is quoted as having a transverse tensile strength approximately 15% higher than the Suprem or Cytec materials. Although microcracking cannot be explained in terms of transverse tensile strength alone [2], the lower strength values for the Cytec and Suprem materials would lead to, on average, earlier onset of damage when compared to a similar Tencate laminate for the same cryogenic cycle. Available fracture toughness data for Suprem and Tencate show both materials as having a similar GIC fracture toughness. However the GIIC value for Suprem is significantly lower, which may contribute to the extensive delamination observed in the thicker cross-ply Suprem laminates and to the level of damage observed in the Suprem laminates in general. The specific fibre surface treatments used for each prepreg are not available and may also contribute to differences in damage formation between material types. It is also possible that void content may influence the level of damage observed in certain specimens. As Table 4.2 shows, the Suprem material, and quasi-isotropic laminates in general, were found to have higher void contents, in keeping with the higher crack densities found in these laminates. However, the heavily damaged 32-ply laminates were also found to have the lowest void content by volume, indicating that the thickness effect is likely a more dominant driver of damage formation in thermally cycled laminates.

Crack morphology

Microcrack shape and location was found to be influenced by crack density and lay-up. Straight transverse cracks were predominant in low crack density laminates for cross-ply lay-ups and, for the most part, in quasi-isotropic (Fig. 4.13 (a)) lay-ups too. For quasi-isotropic lay-ups, the cracks tended to arrest or initiate slight delaminations at ply group interfaces, while cross-ply cracks tended to lead to larger delaminations, ranging in size from one ply thickness to greater than half the specimen width. This typically caused the formation of larger crack opening displacements in the cross-ply laminates, up to 120 μm width as shown in Fig. 4.22 (b).
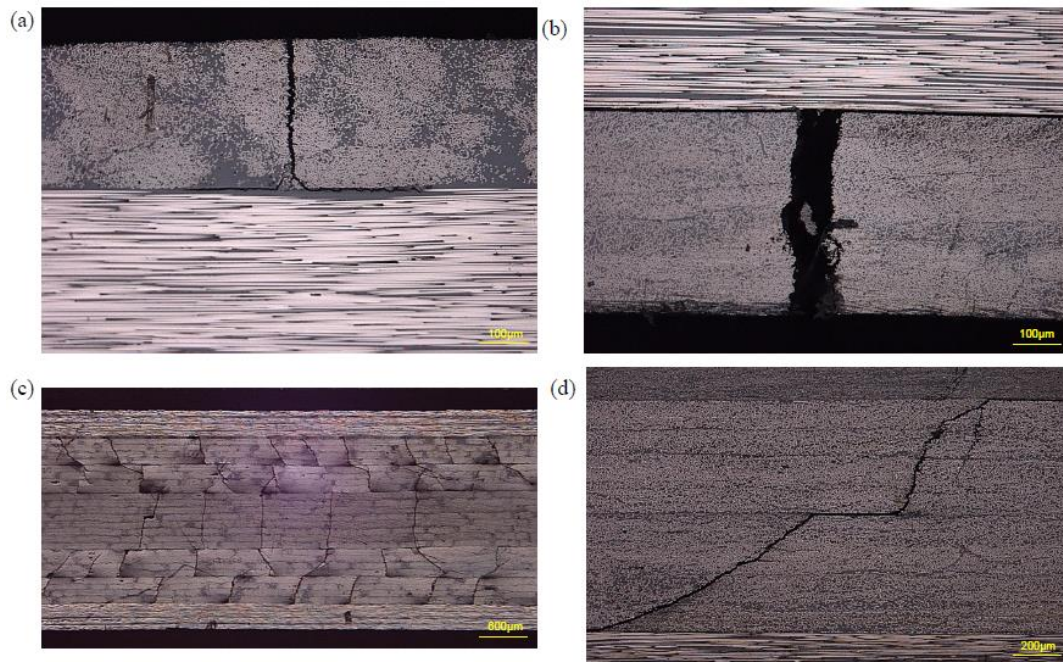
Figure 4.22 (a) Transverse microcrack and associated delamination in a moderately damaged Cytec APC-2 cross-ply 32-ply laminate (b) Significant delaminated crack opening displacement in a cross-ply 32- ply Suprem laminate (c) Microcrack networks in a Cytec APC-2 32-ply quasi-isotropic laminate (d) Cracks in adjacent ply groups joined by a delamination.

In general for low damage levels, the cracks were not seen to influence the shape or location of other cracks. In high crack density quasi-isotropic laminates, angled cracks were observed in the off-axis plies. These cracks typically propagated through the 45°, 135° and 90° plies, being angled in the off-axis plies and generally perpendicular to the horizontal in 90° plies. At ply group interfaces, some cracks were found to grow straight through while others initiated a short delamination, before propagating into the next ply group, as shown in Fig. 4.22(c), (d). Due to the widespread interaction between adjacent cracks, through-thickness networks were found to be commonplace. Microcracks in the outer ply groups of laminates were consistently found to be wider than those in inner ply groups. This is likely due to the constraining effects of adjacent plies on inner ply groups. It was also found that COD (crack opening displacement) in thicker laminates were greater than in thinner laminates. Fig. 4.23 displays COD measurements obtained from optical micrographs and image processing software.
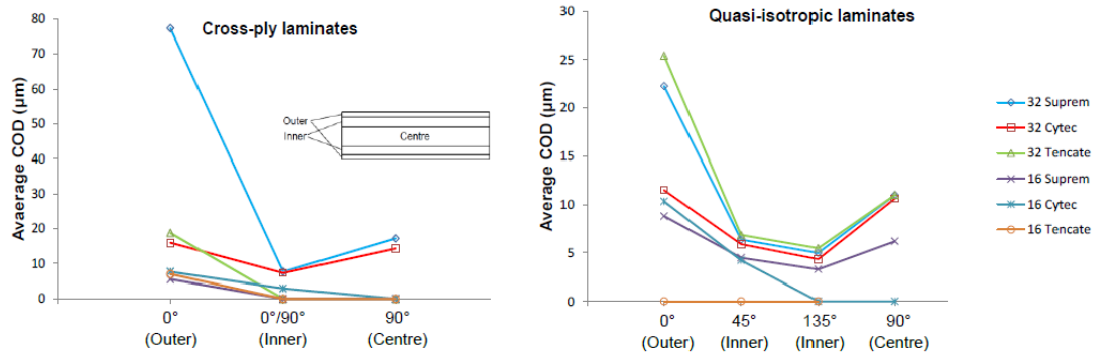
Figure 4.23 Variation of average COD values through the specimen thickness for (a) cross-ply laminates and (b) quasi-isotropic laminates.

These COD values also show that for a given crack network through a laminate thickness, the permeability of the laminate would be restricted by the relatively narrow crack openings found in the inner and off-axis plies. Some specimens were also found to have only have microcracks present in the outer layers, meaning the uncracked inner and centre plies would effectively block cryogen leakage. A large proportion of cracks in all plies tended to propagate through the entire width of the specimen. This is in contrast to the short 'stitch' cracks which were found to develop in ±45° plies in previous work [8, 47, 48] and only propagated through the length of a few ply thicknesses. Fig. 4.24 presents a top-down view of a damaged 32-ply laminate, showing overlapping crack families in the 0°/90° and off-axis plies as well as the large proportion of microcracks which have extended fully though the specimen width. Fig. 4.24 also shows off-axis ply cracks extended through the specimen width.
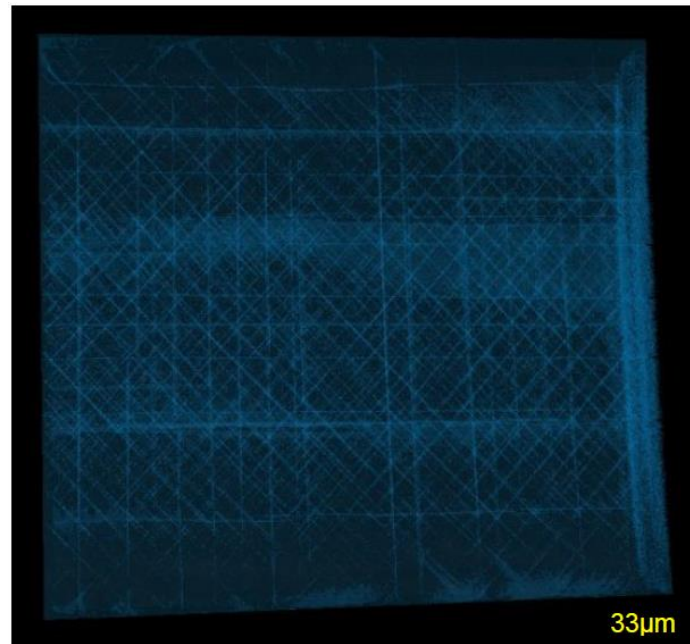
Figure 4.24 X-ray CT scan of microcracking and delamination in a Suprem 32-ply quasi-isotropic laminate. Off-axis cracks can be clearly seen running through the width of the specimen.

Crack initiation

Crack initiation in composite materials can occur below the failure strength of the bulk constituent materials. As mentioned in Section 4.3.1, defects present in the laminate can act as crack nucleation points as well as influencing crack growth paths. Crack paths in laminates with high void contents were found to be significantly influenced by the presence of these defects, as shown by the micrographs in Fig. 4.25.
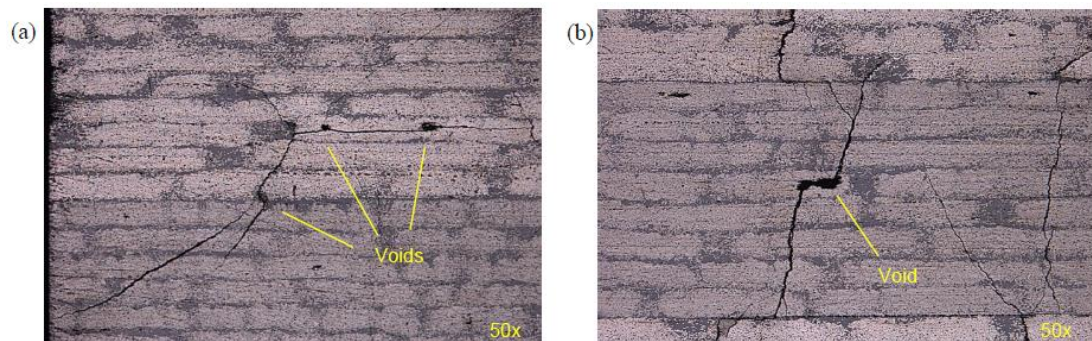

Figure 4.25 (a) Micrograph of a crack path influenced by the presence of voids in a Cytec APC-2 32-ply quasi-isotropic laminate (b) Crack spanning central 90° ply group and passing through a large void in the same Cytec APC-2 laminate.

Fig. 4.25 (a) shows a network of microcracks which appear to have initiated near a cluster of voids and propagated towards the centre and edge of the laminate simultaneously. Fig. 4.25 (b) shows the influence of a large void on crack formation at the centre of the same laminate. No significant difference in microcrack density was observed at the specimen edges compared to the centre. However, cracks within a few ply thicknesses of the edge were found to grow towards the edge, as seen in Fig. 4.25 (a). The most noticeable edge effect was the initiation of free-edge delaminations and their propagation towards the specimen centre. It should be noted that even after 50 cycles, these delaminations remained confined to the outer corners and edges, usually arresting after propagation to a length of approximately 1 to 2 mm. Fig. 4.26 shows several examples of edge delaminations in 32-ply laminates.
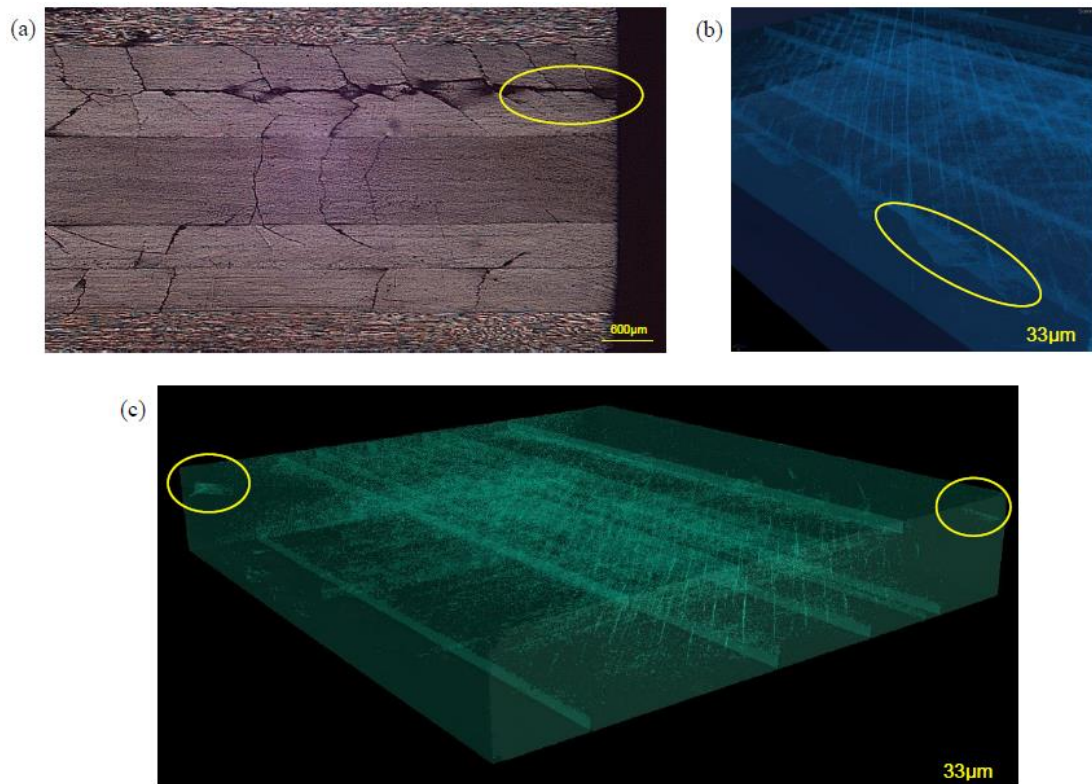

Figure 4.26 (a) Edge delamination and microcracking in a Tencate 32-ply quasi-isotropic laminate (b) Edge delamination and microcracking in a Suprem 32-ply quasi-isotropic laminate (c) Delamination initiation at opposing corners of a Tencate 32-ply quasi-isotropic laminate.

4.4 Conclusions and future work

Optical microscopy and 3-D X-ray CT have been used to characterise the internal structure and damage formation in cryogenically cycled CF/PEEK laminates of multiple thickness, lay-up and material type. Combining these techniques facilitates a complete 3-D characterisation of damage for entire specimens, whilst also allowing detailed investigation of single cracks or defects. A thickness effect was observed with respect to damage formation in the laminates. Extensive microcracking and delamination was observed in 32-ply specimens, compared to moderate microcracking in 16-ply specimens and little or no damage in 8-ply laminates for the same number of cryogenic cycles. This effect is attributed to more severe thermal gradients during cycling and larger residual stresses for thicker specimens. Lay-up and material type were found to affect damage formation, with quasi-isotropic laminates performing worse than cross-ply laminates, particularly in relation to microcrack density. Through-thickness microcrack networks were found to occur more readily in quasi-isotropic laminates, implying poorer permeability characteristics. After cycling, the Suprem IM7 material contained the most microcracking, followed by the Cytec IM7 and Tencate AS4. Available material property data from the manufactures and previous testing showed that the Suprem material had a lower GIC and GIIC fracture toughness than the Cytec material, while the Tencate material had the highest 90° tensile strength. Microcracking was detected in some specimens pre-cycling, which can be attributed to residual thermal stresses arising from processing. For most laminates, no further damage accumulation occurred after the 1st cryogenic cycle. Using 3-D X-ray CT, the majority of cracks, including those in off-axis plies, were found to extend fully through the specimen width. Voids were found to significantly influence the location of microcracks and the path of subsequent crack growth. Delaminations were found to initiate at the free edges of the more heavily damaged 32 ply laminates, but only extended a short distance towards the specimen centre after 50 cycles. Microcrack density was not greatly influenced by proximity to free edges. Crack opening displacement of transverse cracks was found to generally increase with the length of adjacent inter-ply delaminations. Large crack openings were observed in thicker laminates, particularly in the outer plies. Crack opening in inner and off-axis ply

groups was found to be significantly less than outer plies, implying the importance of these plies in limiting laminate permeability. Future work will include further cycling of the laminates until failure of all specimens. This is envisaged to require several hundred cycles for the thinner laminates and will be carried out using an automated cycling system. Modelling work will focus on prediction of crack densities and COD observed in experimental work using XFEM and statistical methods, with an aim to calculating laminate permeability.

Acknowledgements

4.5 References

[1] Grimsley B.W., Cano R.J., Norman J.J., Loos A.C. & McMahon W.M. Hybrid Composites for LH2 Fuel Tank Structure, NASA Langley Research Center, Hampton,Virginia, 2001.

[2] Nairn J.A. Matrix microcracking in composites. *Polymer matrix composites*, Ch. 13, Pergamon, 2001.

[3] Henaff-Gardin C., LaFarie-Frenot M.C. & Gamby D. Doubly periodic matrix cracking in composite laminates Part 2: Thermal biaxial loading. *Composite Structures*, **36**(1-2), 131-140, 1996.

[4] Berthelot J.M. & LeCorre J.F. Statistical analysis of the progression of transverse cracking and delamination in cross-ply laminates. *Composites Science and Technology*, **60**, 2659-2669, 2000.

[5] Kumazawa H., Aoki T. & Susuki I. Influence of stacking sequence on leakage characteristics through CFRP composite laminates. *Composites Science and Technology*, **66**, 2107-2115, 2006.

[6] Xu J. & Sankar B.V. Prediction of stitch crack evolution and gas permeability in multidirectional composite laminates. *Composites Part A: Applied Science and Manufacturing*, **39**, 1625-1631, 2008.

[7] Yokozeki T., Ogasawara T. & Ishikawa T. Evaluation of gas leakage through composite laminates with multilayer matrix cracks: Cracking angle effects. *Composites Science and Technology*, **66**, 2815-2824, 2006.

[8] Bechel V.T., Camping J.D. & Kim R.Y. Cryogenic/elevated temperature cycling induced leakage paths in PMCs. *Composites Part B: Engineering*, **36**, 171-182, 2005.

[9] Bechel V.T. & Kim R.Y. Damage trends in cryogenically cycled carbon/polymer composites. *Composites Science and Technology*, **64**, 1773-1784, 2004.

[10] Park C.H. & McManus H.L. Thermally induced damage in composite laminates: Predictive methodology and experimental investigation. *Composites Science and Technology,* **56**, 1209-1219, 1996.

[11] Roy S. & Benjamin M. Modelling of opening displacement of transverse cracks in graphite-epoxy laminates using shear lag analysis. American Society for Composites, Lafayette, Indiana, paper 023, 2002.

[12] Roy S. & Benjamin M. Modelling of permeation and damage in graphite/epoxy laminates for cryogenic fuel storage. *Composite Science and Technology*, **64**, 2051-2065, 2004.

[13] Nair A. & Roy S. Modelling of permeation and damage in graphite/epoxy laminates for cryogenic tanks in the presence of delaminations and stitch cracks. *Composite Science and Technology*, **67**(11-12), 2592–605, 2007.

[14] Peddiraju P., Noh J., Whitcomb J. & Lagoudas DC. Prediction of cryogen leak rate through damaged composite laminates. *Composite Materials*, **41**(1), 41–71, 2007.

[15] Grogan D.M., Leen S.B., Semprimoschnig C.O.A & Ó Brádaigh C.M. Modelling of thermal and mechanical fatigue delamination growth in composites using XFEM. Proceedings of the 12th International Symposium on Materials in the Space Environment, Noordwijk, The Netherlands, September 24th – 28th, 2012.

[16] Grogan D.M., Leen S.B. & Ó Brádaigh C.M. An XFEM-based methodology for fatigue delamination and permeability of composites. *Composite Structures*, **107**, 205-218, 2014.

[17] Bechel V.T., Fredin M.B., Donaldson S.L., Kim R.Y. & Camping J.D. Effect of stacking sequence on micro-cracking in a cryogenically cycled carbon/bismaleimide composite. *Composites Part A: Applied Science and Manufacturing*, **34**, 663-672, 2003.

[18] Escoto J.I. Preliminary test method development and characterization of candidate composites for cryogenic tanks. Master of Science in Engineering Thesis. Prairie View A&M University; December 2002.

[19] Bechel V.T., Negilski M. & James J. Limiting the permeability of composites for cryogenic applications. *Composites Science and Technology*, **66**(13), 2284-2295, 2006

[20] Schilling P.J, Karedla B.R., Tatiparthi A.K., Verges M.A. & Herrington P.D. X-ray computed microtomography of internal damage in fiber reinforced polymer matrix composites. *Composites Science and Technology*, **65**, 2071-2078, 2005.

[21] Wright P., Fu X., Sinclair I. & Spearing S.M. Ultra high resolution computed tomography of damage in notched carbon fiber – epoxy composites. *Journal of Composite Materials*, **42**(19), 1993-2002, 2008.

[22] Lambert J., Chambers A.R., Sinclair I. & Spearing S.M. 3D damage characterisation and the role of voids in the fatigue of wind turbine blade materials. *Composites Science and Technology*, **72**, 337-343, 2012.

[23] Kastner J., Plank B., Salaberger D. & Heinzl C. Advanced X-ray tomographic methods for quantitative characterisation of carbon fibre reinforced polymers. 4th International Symposium on NDT in Aerospace, Augsburg, Germany, November 13th – 15th, 2012.

[24] Kastner J., Plank B., Kottler C. & Revol V. Comparison of phase contrast X-ray computed tomography methods for non-destructive testing of materials. World Conference on Non – Destructive Testing, Durban, South Africa, April 16th – 20th, 2012.

[25] Little J.E., Yuan X.W. & Jones M.I. Voids characterisation in carbon fibre/epoxy composite laminates. 18th International Conference on Composite Materials, Edinburgh, Scotland, July 27th - 31st, 2009.

[26] Crouch R.D., Clay S.B. & Oskay. C. Experimental and computational investigation of progressive damage accumulation in CFRP composites. *Composites Part B: Engineering*, **48**, 59-67, 2013.

[27] Aoki T., Ishikawa T., Kumazawa H. & Morino Y. Mechanical behaviour of CF/polymer composite laminates under cryogenic environment. Proceedings of the 12th International Conference on Composite Materials, Paris, 1997.

[28] Yoon H. & Takahashi K. Mode I interlaminar fracture toughness of commingled carbon fibre/PEEK composites. *Journal of Materials Science*, **28**, 1849-1855, 1993.

[29] Crick R. A., Leach D. C., Meakin P. J. & Moore D. R. Interlaminar fracture morphology of carbon fibre/PEEK composites. *Journal of Materials Science*, **22**, 2094-2104, 1987.

[30] Kellas S., Morton J. & Jackson K. Damage and failure mechanisms in scaled angle-ply laminates. *Composite Materials: Fatigue and Fracture*, **4**, 257-280, 1993.

[31] Cytec Engineered Materials. APC-2 PEEK Thermoplastic Polymer Technical Data Sheet. www.cytec.com, 2012.

[32] Tencate Advanced Composites. TenCate Cetex TC1200/1220 Technical Data. www.tencate.com, 2013.

[33] Kilroy J. New carbon fibre/PEEK composites for space applications final test report. Doc. No. 02/025. CTL Tástáil Teo, Indreabhán, Co. Galway, Ireland, 2006.

[34] Suprem SA. Suprem T-narrow. www.suprem.ch.

[35] Material database for CF/PEEK IM7 from CES EDUPack 2012. Granta's CES EduPack, Granta Material Intelligence, Granta Design Limited, 2012.

[36] www.ge-mcs.com/en/phoenix-xray, Accessed 2014.

[37] Chambers A.R., Earl J.S., Squires C.A. & Suhot M.A. The effect of voids on the flexural fatigue performance of unidirectional carbon fibre composites developed for wind turbine applications. *International Journal of Fatigue*, **28**, 1389–1398, 2006.

[38] Mandell J.F. & Tsai J.Y. Effect of porosity on delamination of resin-matrix composites. WRDC-TR-89-3932. Final report for period; June-1984–June 1987.

[39] VG Studio MAX 2.2 Reference Manual, 2012.

[40] Parlevliet P.P, Bersee H.E.N. & Beukers A. Residual stresses in thermoplastic composites − A study of the literature − Part I: Formation of residual stresses. *Composites Part A: Applied Science and Manufacturing,* **37**, 1847-1857, 2006.

[41] Parlevliet P.P, Bersee H.E.N. & Beukers A. Residual stresses in thermoplastic composites − A study of the literature − Part III: Effect of thermal residual stresses. *Composites Part A: Applied Science and Manufacturing*, **38**, 1581-1596, 2007.

[42] Jeronimidis G. & Parkyn A.T. Residual stresses in carbon fibre-thermoplastic matrix laminates. *Journal of Composite Materials*, **22**, 401-415, 1988.

[43] Schulte K.J. & Hahn H.T. Prediction and control of processing-induced residual stresses in composites part II: AS4/PEEK composite. Final Technical Report for Air Force Office of Scientific Research (Grant 87-0242), 1989.

[44] Lu C., Danzer R. & Fischer F.D. Fracture statistics of brittle materials: Weibull or normal distribution. *Physical Review E*, **65**, 067102, 2002.

[45] Gurvich M.R. Strength/size effect for anisotropic brittle materials under a random stress state. *Composites Science and Technology*, **59**, 1701-1711, 1999.

[46] Curtin W.A. & Ibnabdeljalil M. Strength and reliability of fibre reinforced composites: localised load sharing and associated size effects. *International Journal of Solids and Structures*, **34**(21), 2649-2668, 1997.

[47] Lavoie J.A. & Adolfsson E. Stitch cracks in constraint plies adjacent to a cracked ply. *Journal of Composite Materials*, **35**, 2077–2097, 2001.

[48] Yokozeki T., Aoki T., Ogasawara T. & Takashi I. Effects of layup angle and ply thickness on matrix crack interaction in contiguous plies of composite laminates. *Composites Part A: Applied Science and Manufacturing*, **36**(9), 1229–1235, 2005.

5. A combined 3-D XFEM and cohesive zone model for composite laminate microcracking and permeability

Article overview

This work presents a novel computational methodology for predicting three-dimensional microcracking, delamination and permeability in composite laminates. Based on the complex 3-D crack networks observed in the experimental testing in **Chapter** 4, the need to expand permeability prediction beyond the pre-defined 2-D unit cell models of **Chapter** 3 is apparent. This methodology combines the use of XFEM for random microcrack initiation with a cohesive zone model for delamination, allowing discrete damage modelling of multi-ply composite laminates. The method is developed so as to avoid pre-defining the position of transverse microcracks or initial delamination lengths, leading to more realistic crack growth simulations. The three key contributing factors to laminate permeability, namely DCOD, crack density and overlapping crack networks, can all be predicted using the method for direct comparison with measured experimental values.

Central to the flexibility and novelty of the method is the simulation of random microcrack initiation and growth in the absence of geometrical or load-based stress

concentrations by XFEM. This is achieved through the use of two alternative methods: the first is based on a volume-adjusted Weibull distribution of fracture strengths and the second is based on incorporating the presence on defects into the material based on the 3-D X-ray CT scans presented in **Chapter** 4. From experimental observations of delamination growth paths, a defined cohesive fracture plane for inter-ply failure is used in conjunction with the intra-ply XFEM. This helps to significantly reduce the computational cost of damage models, allowing each ply to be modelled using a single element through the thickness. If XFEM was used to model inter-ply failure, special purpose interface elements would have to be included at each ply interface. This would effectively double the number of elements, and associated computational time, required for damage simulations. Also, XFEM currently allows only a single crack, or damage mode, to be modelled in a given element. This limits the ability to capture coincident inter- and intra-ply cracking. Thus, a combined XFEM-SCZM is essential to the scalability of the approach with respect to large laminate structures as well as the ability to accurately predict crack opening at ply interfaces. The method is validated against experimental work by comparison of DCOD values for rectangular coupons. Permeability calculations are also presented and the results are compared with measurements from leak testing of similar materials.

Abstract

A novel computational methodology for predicting three-dimensional microcracking and permeability in composite laminates is presented. The methodology simulates microcrack initiation and propagation using the extended finite element method (XFEM) and delamination using a mixed-mode cohesive zone model. Random microcrack initiation is modelled using a random (Weibull) distribution of fracture strengths. The Weibull distribution is adjusted to account for specimen volume, allowing mesh independent crack density predictions. An alternate method is also investigated, based on an elemental representation of defects using measured void geometry. The predicted microcracking and damage distributions are shown to correlate closely with 3-D X-ray CT (computed tomography) scans of cryogenically cycled specimens. Crack opening displacements are consistent with laminate test

measurements. Permeabilities, based on the dimensions of the leak paths, were found to be within the measured range for various CF (carbon fibre)/PEEK materials.

5.1 Introduction

Due to their high specific strength and stiffness, composite materials are ideal for use in industries such as aerospace, automotive and renewable energy, amongst others. However, a major issue with using composite materials for such applications is their propensity to microcrack and delaminate under thermal and mechanical loads. Taken by themselves, these damage modes do not typically constitute full structural failure, with the early growth of microcracks and delaminations being difficult to detect [1-3]. However, this sub-critical damage build-up leads to a number of undesirable effects such as a multi-directional reduction in strength and stiffness, increased susceptibility to attack from solvents and the formation of gas leakage paths through the material [4-11]. Understanding the mechanisms of damage accumulation and how the various damage modes interact is particularly important for pressure vessel applications, including cryogenic fuel tanks for the next generation of re-useable space launch vehicles (RSLVs). The formation of through-thickness crack networks in such structures can allow cryogen leakage to occur, with catastrophic results [12].

Intra-laminar failure, in the form of transverse microcracking in off-axis plies, is usually the first noticeable damage mode encountered in composite laminates. Due to the multi-axial nature of thermal loading, cracks may form in multiple ply groups simultaneously and below the failure strength of the material [13-15]. Overlapping microcrack families in adjacent plies allow the formation of leakage paths through a damaged laminate, with factors such as stacking sequence and laminate thickness being known to influence crack density and permeability [16-19]. With more severe loading, inter-laminar damage in the form of delamination may develop, which can link microcracks in adjacent plies, leading to the formation of leakage paths that might not have developed through microcracking alone. The interaction between delaminations and microcracks has been found to affect transverse crack opening at ply interfaces [20, 21]. Delamination growth in laminates with existing transverse cracks under thermal fatigue loading has previously been modelled by the authors,

showing a direct correlation between delaminated crack opening displacement and laminate permeability [22, 23].

The complexity of multiple failure modes acting simultaneously within a composite, in addition to random crack initiation due to variations in material properties, lay-up, loading and the presence of manufacturing defects, calls for a sophisticated and flexible modelling methodology. Attempts at developing finite element models capable of predicting both intra-laminar and inter-laminar failure in composites have used a partition of unity approach for microcracks and a cohesive approach for delaminations [24, 25]. However, previous studies have not been able to model or predict the formation of random 3-D crack networks in laminates. The ability to predict this sub-critical damage build-up in a single model is of prime importance to understanding composite structure failure. Existing permeability models have been based on repeating 2-D and 3-D geometries, with pre-existing cracks defined [20, 21, 26-28]. This study, through meso-level modelling of laminates, presents a novel methodology to predict random (Weibull and defect based) crack initiation and growth in composites laminates. The 3-D models developed allow mesh independent prediction of crack density, the direct measurement of crack opening displacement and crack overlap areas, and, hence, laminate permeability. The methodology is developed on a globally applicable platform allowing the potential of up-scaling the approach to deal with large structures, including cryo-tanks. A parallel programme of experimental work on cryogenic cycling of CF/PEEK laminates has been conducted and some of these results are presented here for comparison and calibration purposes. 3-D X-ray CT (computed tomography) scans of pristine and damaged laminates have been used to provide input in terms of defect distributions and as a means of comparing resulting damage accumulation. The permeability of modelled laminates is also compared to previously measured leak rates from test specimens.

5.2 Methodology

The methodology developed in this work is based on a combined XFEM (extended finite element method) and SCZM (surface cohesive zone model) approach to

damage modelling in composite laminates. XFEM is used for microcrack initiation and propagation (intra-laminar failure), with a Weibull strength distribution being used to account for the random nature of the distribution of matrix microcracking. This approach is predicated on the random distribution of laminate strength within the finite element model of the laminate. An alternate method, based on using an experimental defect distribution to represent material discontinuities, is also presented. Here, a distribution of a-priori micro-voids (ellipsoidal) is defined within the finite element mesh, based on measured distributions of these micro-voids. Delamination growth between plies (inter-laminar failure) is based on a mixed-mode SCZM. A globally applicable XFEM platform is essential due to the 3-D requirements for future modelling of large-scale fuel storage tanks and material defect distributions which will require crack propagation analysis to be undertaken via a user interface. Fig. 5.1 gives a general overview of the method.
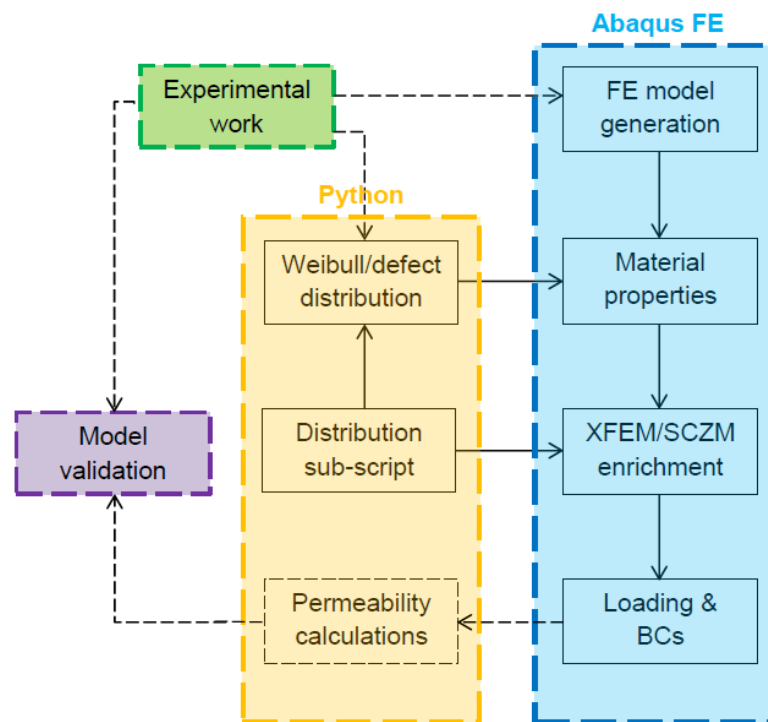

Figure 5.1 Flowchart showing the general overview of the method.

5.2.1 Experimental work

In order to develop accurate models of crack growth behaviour, an extensive programme of material and damage characterisation was undertaken, as described in

[29]. Optical microscopy and 3-D X-ray CT were used to determine the void contents of a range of CF/PEEK materials of varying thickness (8-ply, 16-ply and 32-ply) and lay-up. Subsequently these laminates were cryogenically cycled in liquid nitrogen (+40 °C to -196 °C), with damage progression monitored, also using optical microscopy and 3-D X-ray CT. The thicker laminates were found to crack extensively after one cycle, with no subsequent crack growth observed after 50 cycles. The resulting crack patterns and dimensions measured from this experimental work, as well as the defect distributions obtained, are employed directly in this present work to define the inputs to the micro-void models and to compare the predicted microcrack distributions against, i.e. for both calibration and independent validation of the models.

5.2.2 Intra-ply microcracking XFEM model

The extended finite element method is an extension of the classical finite element method, based on the concept of partition of unity [30], which allows modelling of discontinuities through the use of special enrichment functions which are incorporated into the finite element approximation. XFEM is effective and efficient for modelling material discontinuities in general, such as voids, grain boundaries, dislocations and crack growth problems [31, 32]. Conventional methods of analysing such discontinuities require that the finite element mesh conforms to the discontinuity. This becomes an issue when modelling crack growth, where the dimensions of the discontinuity may change considerably over the course of the analysis, so that constant re-meshing is required in order to represent crack growth. With XFEM, the discontinuity is defined separately from the mesh, allowing a crack of arbitrary shape and location to be modelled effectively without the need for re-meshing and without the usual extensive mesh refinement required [33]. Knowledge of the crack location or propagation path is not required a-priori, allowing the user to forego costly mesh refinement and continual updating of the mesh in the area of interest. This feature is critical to the ability of the methodology to predict microcrack growth due to random inherent material defects in composite laminates, which forms the basis of this work.

5. A combined 3-D XFEM and cohesive zone model for composite laminate microcracking and permeability

The proposed methodology is implemented here within the general purpose, non-linear finite element code, Abaqus [34]. This has significant benefits due to the widespread use of Abaqus in both academic and industrial applications. Phantom nodes are defined within enriched elements to represent the jump in crack surfaces, where real and corresponding phantom nodes separate when the prescribed fracture criterion has been satisfied. The degree of separation of the nodes is defined via a traction-separation cohesive behaviour, whereby the cohesive strength of an enriched cracked element decays to zero. The traction–separation model used here comprises a linear elastic behaviour phase and a subsequent damage progression phase. The constitutive matrix for the elastic phase, relating the stresses and separations in an enriched element are given by Eq. (5.1) [34],

$$
\begin{Bmatrix} t_n \\ t_s \\ t_t \end{Bmatrix} = \begin{bmatrix} K_{nn} & 0 & 0 \\ 0 & K_{ss} & 0 \\ 0 & 0 & K_{tt} \end{bmatrix} \begin{Bmatrix} \delta_n \\ \delta_s \\ \delta_t \end{Bmatrix} \tag{5.1}
$$

where t_n is the normal component of the stress traction vector and t_s and t_t are the two shear tractions along the local 1- and 2-directions, respectively. K_{nn}, K_{ss} and K_{tt} are the stiffness components that relate the element stresses to separations and δ_n, δ_s and δ_t are the element separations related to the aforementioned normal and shear stresses.

XFEM can be used to model inter-laminar failure. However, in order to accurately capture the transition between inter-ply and intra-ply failure modes using XFEM, it is necessary to use an increased mesh density at the ply interfaces, due to the constraint of one crack surface per element in XFEM. A computationally inexpensive alternative proposed here is to combine an XFEM-based microcracking prediction methodology with a SCZM methodology for inter-laminar failure. This method allows a relatively straightforward interaction between adjacent plies and cracks using pre-defined delamination surfaces. This combined approach is necessary to facilitate large-scale structural damage modelling, e.g. for cryogenic fuel tank structure models, and for subsequent associated permeability predictions. Fig. 5.2 illustrates the significant difference in mesh densities required for combined

microcack and delamination prediction using (a) a pure XFEM approach and (b) the proposed XFEM-SCZM approach.
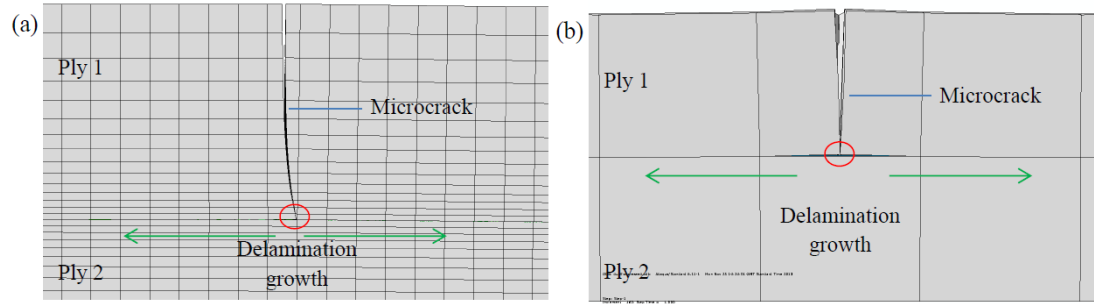

Figure 5.2 Comparison of the level of mesh refinement required for (a) a pure XFEM based approach and (b) the novel, proposed XFEM-SCZM approach, for modelling the transition between a transverse crack and resulting delamination at a ply interface.

5.2.3 Delamination SCZM model

The SCZM simulates the decohesion of initially-bonded delamination surfaces which correspond to the outer layers of adjacent ply groups in a laminate. The interfaces between such adjacent ply groups are assumed to be of negligible thickness. A generalized traction-separation behaviour is implemented for the surface decohesion, similar to the XFEM cohesive behaviour. This method allows the modelling of delamination at interfaces, with failure of the cohesive bond characterized by progressive degradation of the cohesive stiffness in direct proportion to the critical energy release rate. The traction-separation model used here assumes initially linear elastic behaviour followed by the initiation and evolution of damage based on mixed-mode fracture. The elastic behaviour is based on a constitutive matrix similar to that of Eq. (5.1). Due to the complex multi-axial loading during cryogenic cycling, damage evolution is described by the Benzeggagh and Kenane criteria [35] for mixed-mode fracture, which defines an equivalent critical energy release rate, G_{equivC}, combining energy release rates from all three fracture modes (G_I, G_{II} and G_{III}) as follows:

$$G_{equivC} = G_{IC} + (G_{IIC} - G_{IC}) \left(\frac{G_{II} + G_{III}}{G_I + G_{II} + G_{III}} \right)^{\eta} \tag{5.2}$$

where η is a curve fitting parameter.

5.2.4 Microcrack initiation

Being an intra-ply failure mode, microcracking is modelled using XFEM. A crack is assumed to initiate when the relevant fracture criterion, f, is exceeded. In this work, the maximum nominal stress criterion is used, whereby a crack initiates when the value of f exceeds a pre-defined tolerance as follows:

$$f = max\left\{\frac{\langle t_n \rangle}{t_n^o}, \frac{t_s}{t_s^o}, \frac{t_t}{t_t^o}\right\} \tag{5.3}$$

where t_n^o, t_s^o and t_t^o define the peak values of the nominal stress in the normal direction and local 1- and 2- (shear) directions. The surface of newly formed cracks is orthogonal to the normal component of the stress traction vector, which depends on the local material orientation assigned to the enriched element. The X-ray CT scans of the cryogenically cycled CF/PEEK laminates show that transverse microcracks align with the fibre direction in each ply of a damaged laminate, as shown in Fig. 5.3.
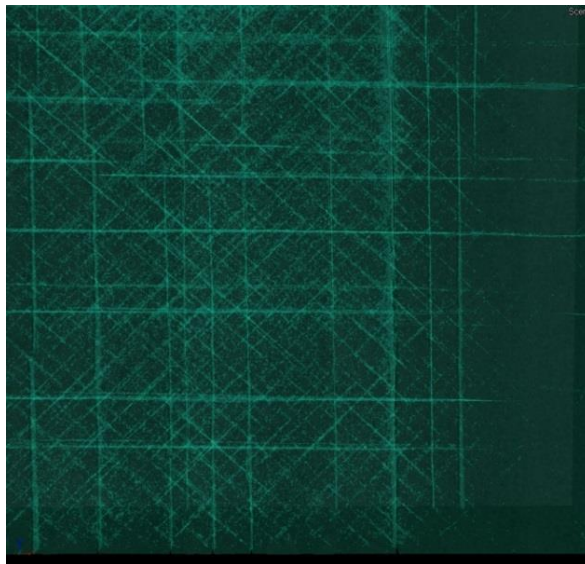

Figure 5.3 X-ray CT scan of a cryogenically cycled quasi-isotropic CF/PEEK laminate with transverse microcracks aligned with the fibre directions (0°, 45°, 135° and 90°).

This dependence of crack-growth direction on the local fibre orientation allows for a simplified modelling methodology, whereby a single set of material properties and fracture parameters is defined for the 0° ply. Material property definitions can then be applied to off-axis plies by transformation via local co-ordinate systems relative to the base 0° definition (Fig. 5.4).
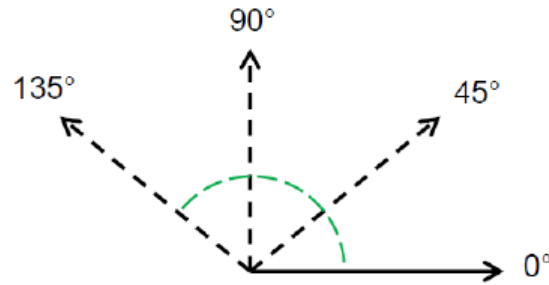

Figure 5.4 Transformation of material properties for off-axis plies are carried out relative to the base 0° definition.

In order to develop a realistic random damage model, manufacturing defects and discontinuities need to be integrated into the simulation. Optical microscopy has shown that voids, inclusions, resin-rich areas and other defects within the plies are possible crack nucleation points, whereby initiation may occur locally at stress levels below the fracture strength of the bulk material. The presence of these discontinuities was found to have a direct correlation to crack formation in the cryogenically cycled laminates [29]. The principle method of representing these defects and discontinuities within the material space is based on a Weibull strength distribution. An alternative method, based on an elemental representation of defects, is also presented. These methods are discussed below.

The first approach is based on the inherent random distribution of the material fracture strength, to simulate microcrack initiation [15, 25, 36]. A continuous probability Weibull distribution is used to represent this distribution of fracture strength [37, 38]. For a given load, σ, the strength distribution is given by:

$$F(\sigma) = 1 - exp\left[-\left(\frac{\sigma - \sigma_{th}}{\sigma_0}\right)^m\right] \qquad (5.4)$$

where σ_{th} is the threshold stress below which failure does not occur, σ_0 is the normalised material strength and m is the Weibull modulus. The distribution associated with the material is assigned randomly to all enriched elements in the finite element mesh (See A.7 for details). Under loading, cracks are predicted using XFEM to initiate and propagate from and through areas of lower strength, specifically below the fracture strength of the bulk material. Fig. 5.5 shows a Weibull distribution of random fracture strengths assigned to a 1,000 element mesh, generated using Python code for a carbon-fibre composite material with a mean transverse tensile strength of 85 MPa and a Weibull modulus of 12 [25].
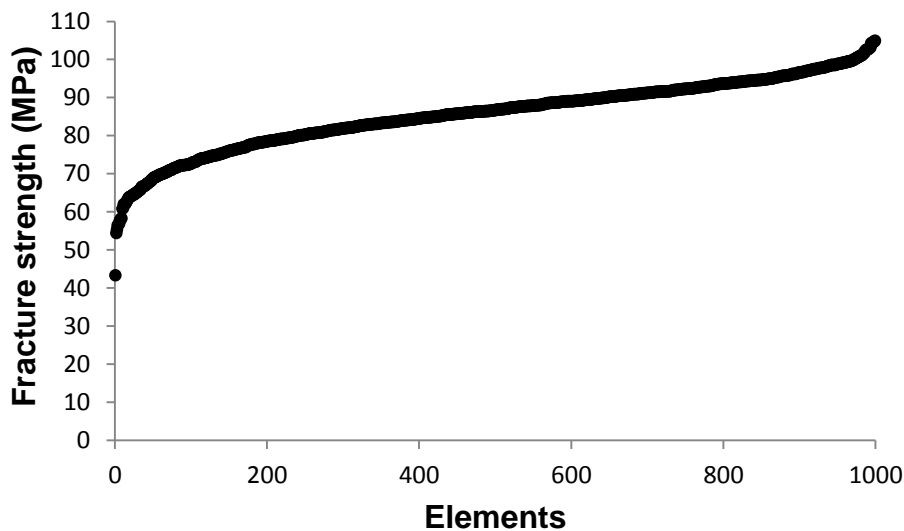
Figure 5.5 Weibull distribution of random strengths for 1000 element mesh with: $\boldsymbol{\sigma_0}$ = 85 MPa, $\boldsymbol{m}$ = 12.

Python is a multi-paradigm, open source programming language [39] which is used here to generate random distributions such as the Weibull distribution, through built-in functions. It was chosen here as a scripting language due to its compatibility for use with Abaqus FE analyses.

5. A combined 3-D XFEM and cohesive zone model for composite laminate microcracking and permeability

The second approach for capturing material defects and discontinuities is based on an elemental representation of defects. A customised Python code was written to randomly vary the elastic properties in a finite element mesh of the composite lay-up according to the measured Gaussian distribution of voids, inclusions and resin-rich areas [29] (Chapter 4).

Voids can be represented by ellipsoids within an element volume. Knowing the size range of voids within a given laminate, it is possible to randomly distribute voids within this size range throughout the laminate. The effect of voids is to degrade various material properties [40-43], including stiffness, of the surrounding material in an element in proportion to the maximum cross-sectional area of the void as viewed from orthogonal reference planes. To this end, it is assumed that the major and minor axes of the ellipsoids align with the primary directions (x, y, z), corresponding to the fibre and transverse directions, as shown in Fig. 5.6.
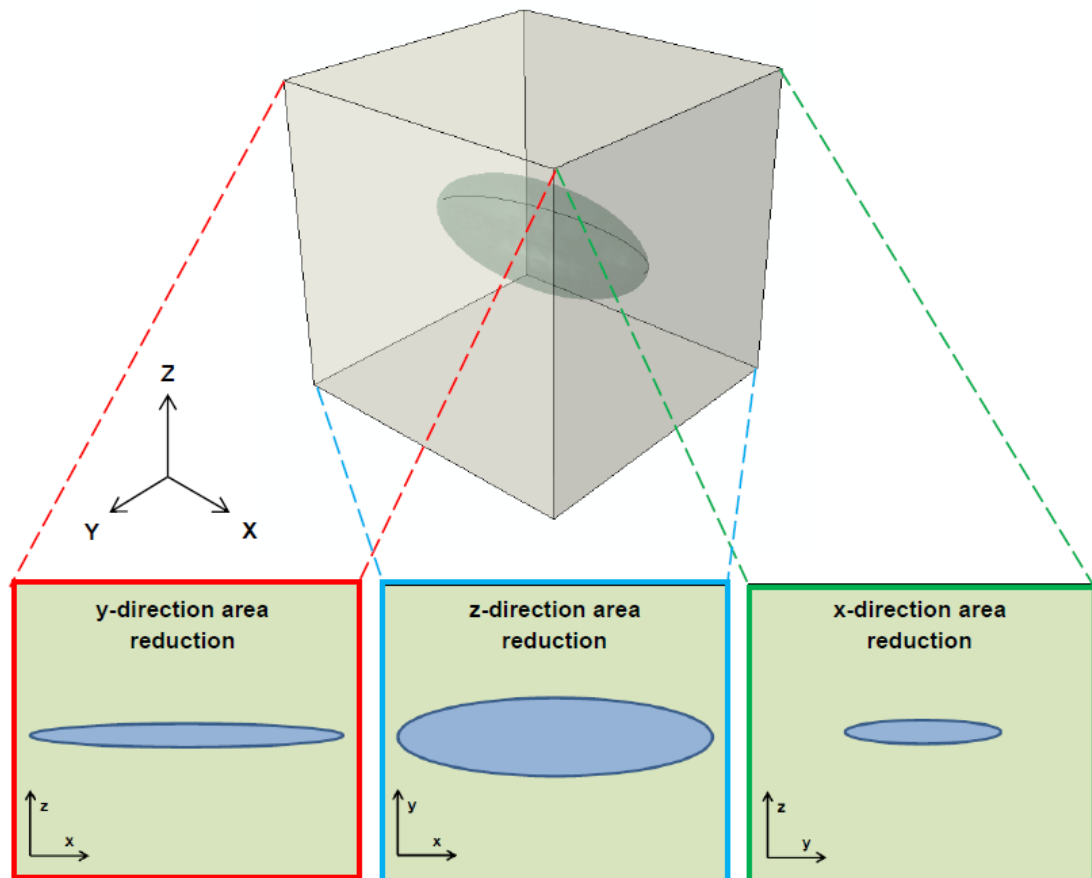

Figure 5.6 y, z, and x-direction area reduction in a 3-D element due to the presence of an ellipsoidal void.

Based on the measured size ranges of voids from X-ray CT scans of the CF/PEEK laminates [29], Gaussian distributions are used to assign appropriate random x (length), y (width) and z (height) values for each ellipsoid. These distributions can be expressed in terms of the following probability density function for a variate x:

$$P(x) = \frac{1}{\sigma\sqrt{2\pi}} e^{-\frac{(x-\mu)^2}{2\sigma^2}} \tag{5.5}$$

where μ is the mean and σ is the standard deviation. Expressing the reduction in stiffness of a material element as a proportion of the element occupied by a void, the corresponding reduced element stiffnesses (E_i^*) are thus calculated as follows: (see Section 6.3.3 for further details)

$$E_1^* = (1 - \pi yz)E_1 \tag{5.6}$$

$$E_2^* = (1 - \pi xz)E_2 \tag{5.7}$$

$$E_3^* = (1 - \pi xy)E_3 \tag{5.8}$$

where E_1 is the fibre direction modulus and E_2, E_3 are the transverse moduli. Fig. 5.7 shows the trend in void morphology in terms of the relationship between sphericity, S, and void radius, r_{void}, from the measured data, where sphericity is defined as the ratio between the surface area of a sphere with the same volume as a defect and the surface area of the defect. The decreasing sphericity of voids with increasing void volume is a commonly observed trend in composite materials.
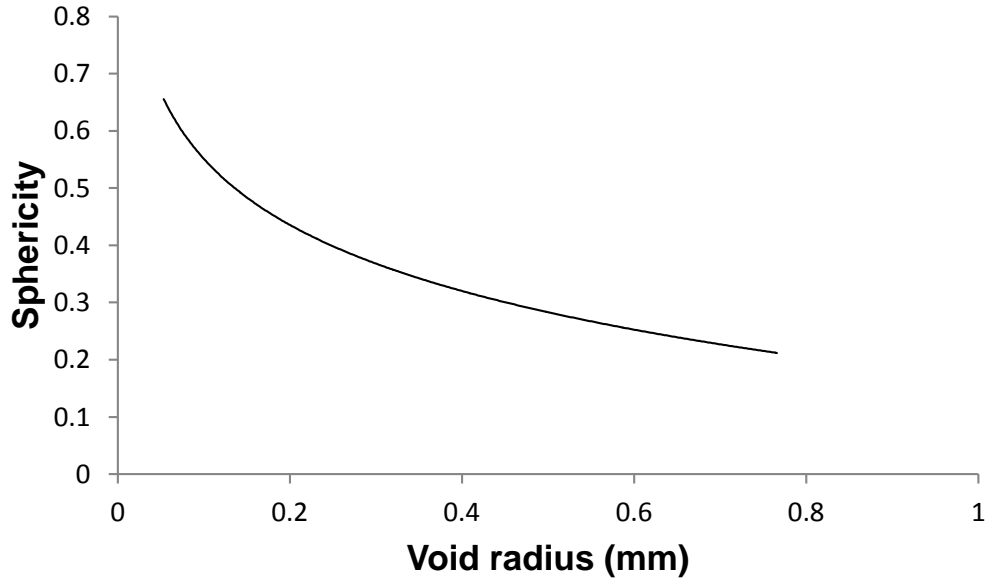
Figure 5.7 Relationship between sphericity and void radius from test data [29] for a CF/PEEK laminate for $a = b = 0.167$.

This relationship can be expressed as:

$$S = -a \ln r_{void} + b \qquad (5.9)$$

where a and b are constants. In general, the greater the void volume, the more elongated the void.

The effect of inclusions and resin-rich regions within the material is dealt with in the same way as voids. However, instead of reducing the stiffness of an element based on the presence of a void, the properties of the element are altered to represent those of the discontinuity. In the case of large resin-rich areas in composites, as shown by the dark regions in Fig. 5.8, the properties of entire elements are replaced by those of the polymer.
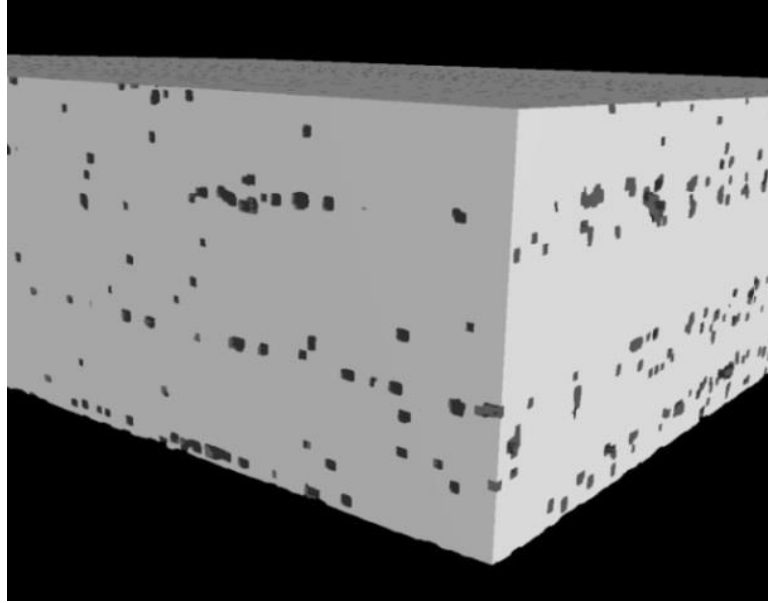
Figure 5.8 Filtered X-ray CT scan of a CF/PEEK laminate with resin-rich regions shown as dark cuboids within the bulk material.

5.2.5 Size effect and mesh dependence

The effect of specimen size on strength is a well-known physical phenomenon [37, 44, 45], arising from the higher probability of occurrence of a critical flaw in larger specimens than in smaller specimens of the same material. Consider the FE analysis of composite laminates with the specimen discretised into a number of individual elements, based on the assigned mesh density. If size effects are not taken into account, the same strength distribution would be applied to the elements in meshes of different densities, resulting in mesh-dependent crack density predictions. Fig. 5.9 further explains this effect.
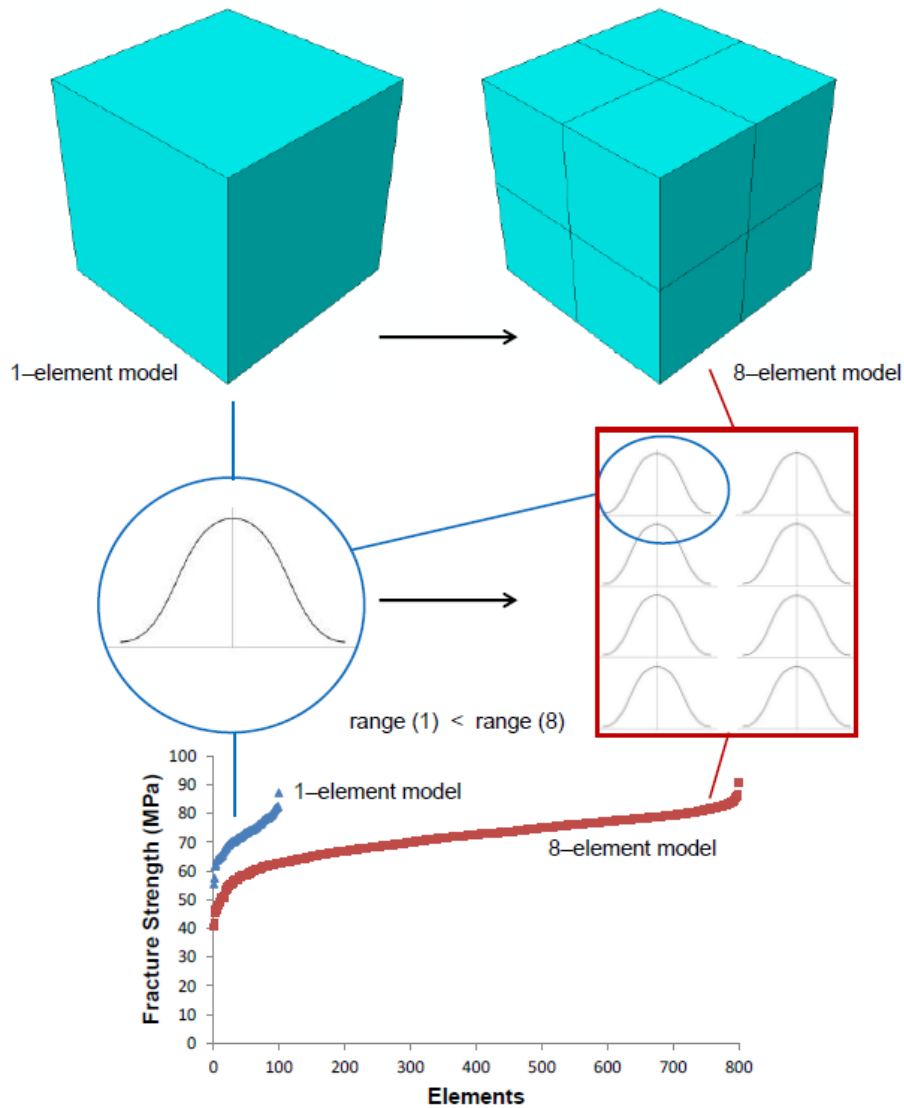
Figure 5.9 The effect of mesh density on the strength of an element. The probability of failure in the 8-element model is greater than for the 1-element model, for equal fracture strength distributions applied to each constituent element. This is shown by the difference in fracture strength ranges between the 1-element and the 8-element distributions.

On average, a larger volume should contain more defects than a smaller volume. The two meshes in Fig. 5.9 have equal volumes but different mesh densities. Given that the total meshed volume is the same, the probability of failure for both meshes should be equal. However, during material property assignment, if the same strength distribution is assigned to the single large element as to each of the 8 smaller elements, the probability of there being a defect in the denser mesh increases relative

to the coarse mesh. This is due to the statistical effect whereby there is likely to be a larger variance in 8 distributions than in a single distribution. This means the likelihood of failure of one or more elements in the equivalent 8 element mesh is greater, leading to a direct correlation between crack density and mesh density. In order to correct for this effect, a single large element should, therefore, have a higher probability of failure than a single small element from the equivalent 8-element mesh. To account for size effect and mesh dependency in crack density predictions here, the Weibull distribution is normalised with respect to the reference element volume. The volume adjusted mean strength, $\bar{\sigma}_s$, for the distribution is therefore given as:

$$\bar{\sigma}_s = \bar{\sigma}_0 \left(\frac{v}{V_0}\right)^{-1/m} \tag{5.10}$$

where v is the element volume and V_0 is the reference element volume. Fig. 5.10 shows this theoretical variation of Weibull mean strength parameter, $\bar{\sigma}_s$, against element volume for a carbon composite material with a mean fracture strength, $\bar{\sigma}_0$, of 75 MPa and a Weibull modulus, m, of 12, based on Eq. (5.10) for a reference element volume of 1 mm^3.
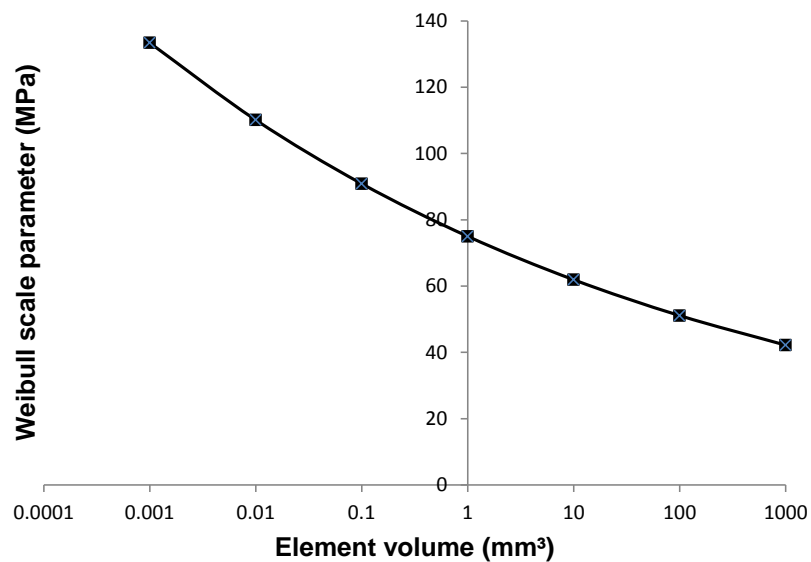
Figure 5.10 Variation of mean strength with volume for a carbon composite material. $\bar{\sigma}_0 = 75$ MPa, $m = 12$.

In order to demonstrate the mesh independence of this approach, a sensitivity study was carried out to determine the number of elements, in a given finite element mesh, with fracture strengths below the mean fracture strength of the material. A number of Weibull distributions were generated for meshes of different densities, giving different element volumes, as shown in Table 5.1.

Table 5.1 Relationship between element volume and the number of elements in a FE mesh for a specimen size of 100 mm^3.

Number of elements	Element volume v (mm^3)
100	1
200	0.5
1000	0.1
2000	0.05
10000	0.01
20000	0.005
100000	0.001

The mean fracture strength was defined to vary with element volume v, as defined by Eq. (5.10). The results of the sensitivity study are shown in Fig. 5.11.
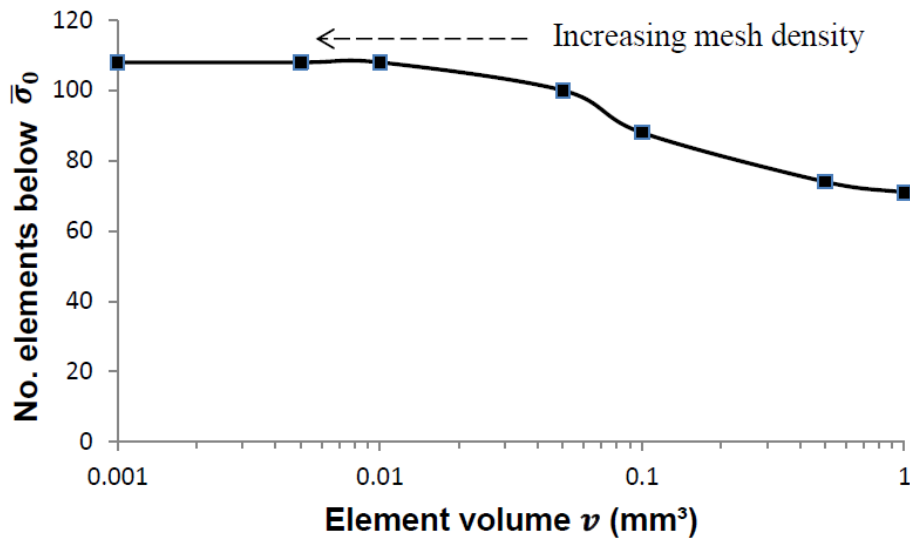
Figure 5.11 A case study showing the effect of element volume on the number of elements below a specified mean fracture strength. The plateau below an element volume of 0.01 mm^3 indicates that the number of defects is independent of the mesh density for this particular fracture strength distribution and threshold level.

The effect of mesh density on the number of elements below the mean fracture strength is shown to be invariant for this particular distribution case, within the bounds of normal statistical scatter, for element volumes below 0.01 mm^3. Predicted microcrack density is directly controlled by the total number of elements below the mean fracture strength, i.e. a larger number of weaker elements leads to a higher crack density at a given load. Fig. 5.11 shows that the number of low-strength elements remains constant for high mesh densities (element volume < 0.01 mm^3), i.e. that the methodology is capable of capturing the effect of element volume on mean element fracture strength. Above a certain threshold (element volume < 0.01 mm^3, number of elements $< 10,000$), mesh independency is achieved. Hence, mesh independent prediction of crack density is only possible for a specific range of mesh densities. It is necessary, therefore, to establish mesh convergence for reliable results for a given fracture strength distribution and threshold level (See A.7).

5.2.6 Permeability prediction

The extreme thermal stresses arising from cryogenic cycling are sufficient to cause extensive through-thickness microcracking and delamination in composite laminates. Overlapping crack networks in adjacent plies can lead to permeation of the cryogen though the laminate thickness. Fig. 5.12 shows an X-ray CT scan of these crack networks present in a cryogenically cycled CF/PEEK laminate [29].
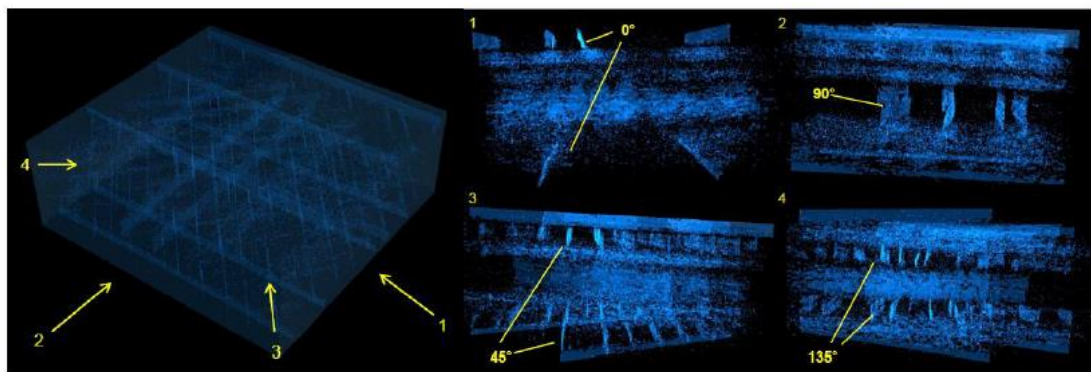
Figure 5.12 Through-thickness crack network in a quasi-isotropic $[0°/45°/135°/90°]_S$ CF/PEEK laminate showing 4 distinct overlapping crack families.

5. A combined 3-D XFEM and cohesive zone model for composite laminate microcracking and permeability

Due to the prevalence of these crack networks in damaged laminates, permeability predictions are typically focused on determining the magnitude of crack openings and the overlap area between adjacent damaged plies [20, 21, 26, 27]. Following [21], an expression for material permeability for an N-ply composite laminate, β_0, is given as:

$$\beta_0 = C \left[\sum_{K=1}^{N} \left(\frac{\sin \theta}{CD_K CD_{K+1} DCOD_K DCOD_{K+1}} \right) \right]^{-1} \qquad (5.11)$$

where C is the material conductance, θ is the ply angle, CD_K and CD_{K+1} are the crack densities of adjacent plies and $DCOD_K$ and $DCOD_{K+1}$ are the delaminated crack opening displacements (DCOD) of adjacent plies. Fig. 5.13 illustrates the overlap area formed by two adjacent microcracks.
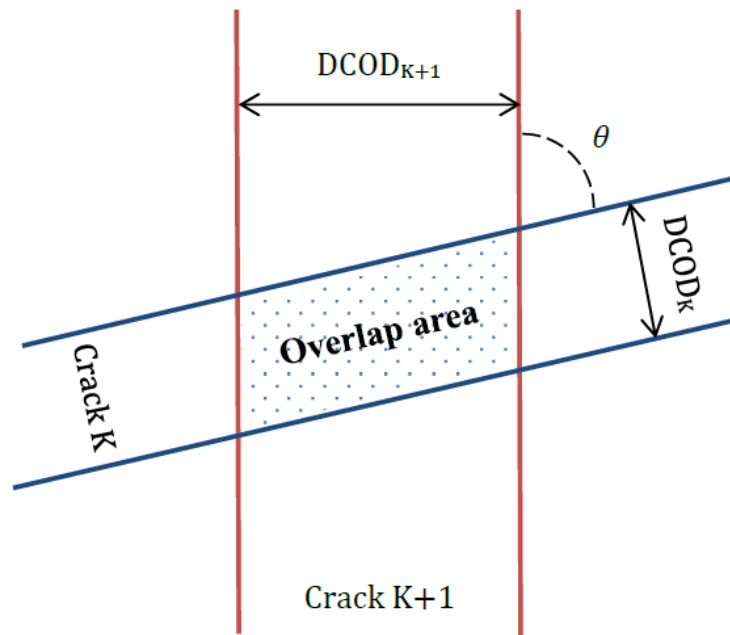
Figure 5.13 Overlap area formed by the DCOD of two adjacent microcracks, crack K and crack K+1, at an angle θ to each other.

Modelling the following three key damage characteristics, as well as the interaction between them, is crucial to developing a methodology capable of predicting laminate permeability:

5. A combined 3-D XFEM and cohesive zone model for composite laminate microcracking and permeability

- Crack density - CD_K, CD_{K+1}
- Delaminated crack opening displacement - $DCOD_K$, $DCOD_{K+1}$
- Overlapping crack families $- \theta$

5.2.7 Finite element implementation

In order to implement the above methodology combining XFEM and SCZM, the Abaqus FE code is employed along with customised Python code. A flowchart of the modelling process is shown in Fig. 5.14
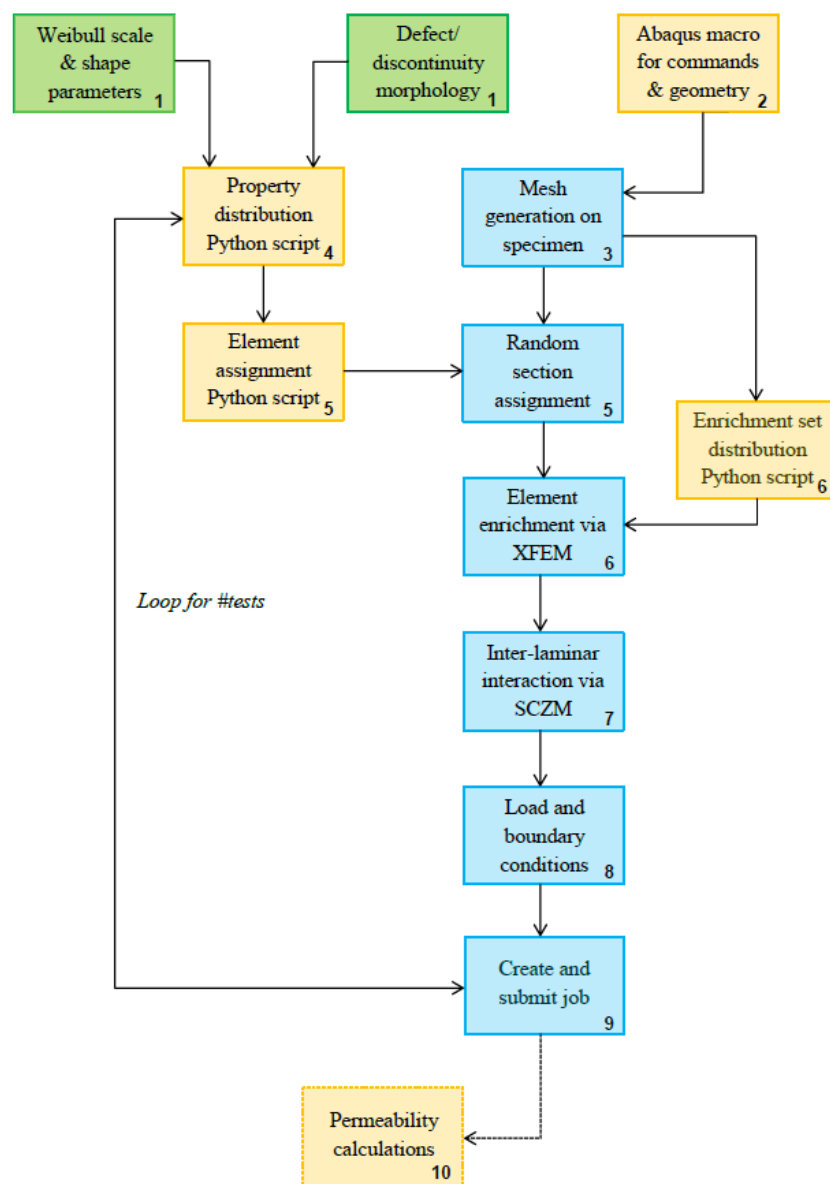
Figure 5.14 Flowchart showing the implementation of the combined XFEM-SCZM methodology within Abaqus and Python.

5. A combined 3-D XFEM and cohesive zone model for composite laminate microcracking and permeability

- Step 1: Weibull parameters or defect distributions are obtained from the literature/experimental work

- Step 2: An Abaqus macro is developed in Python script containing relevant commands and the model geometry

- Step 3: The geometry and mesh are generated within the FE programme, with the model being partitioned into individual plies or ply groups

- Step 4: Separate Python scripts are then used to define a volume-adjusted Weibull fracture strength distribution (See A.7) or a defect/discontinuity distribution

- Step 5: The relevant material/fracture properties of the composite are then updated on an element-by-element basis, based on whichever distribution will be used in the analysis and are then randomly assigned to each element in the previously generated FE mesh

- Step 6: A number of XFEM assignment sets are used to automatically enrich all elements in the mesh (Fig. 5.15)

Geometry generation and ply partition

Random element assignment & XFEM enrichment

SCZM interaction definition
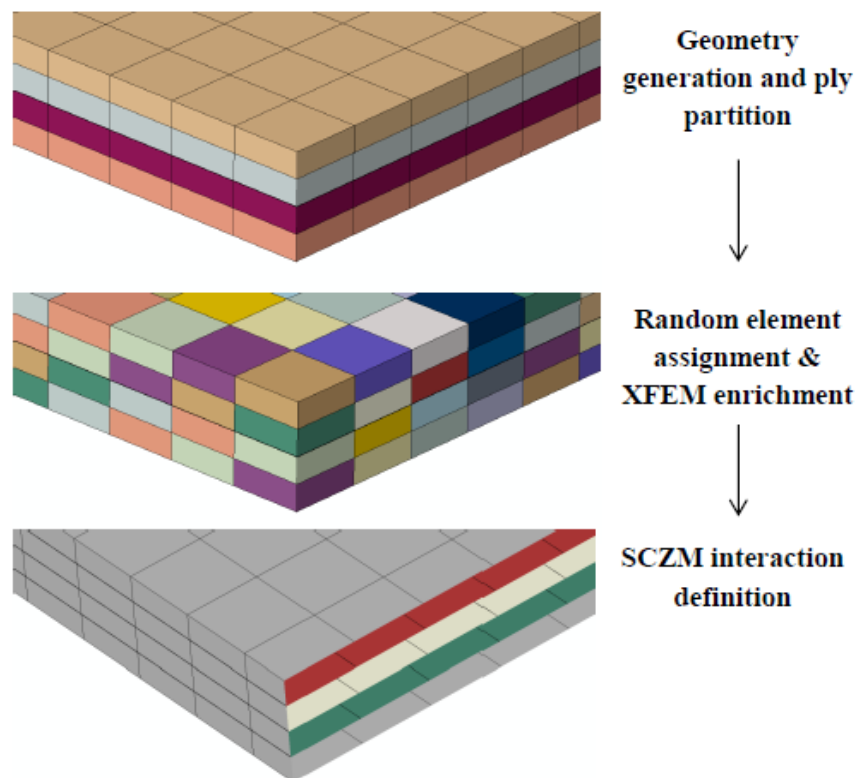
Figure 5.15 Main steps in the FE implementation of the methodology.

- Step 7: The SCZM interactions are defined between each ply group (Fig. 5.15)
- Step 8: Loading and boundary conditions are defined within the FE software and the model is then run
- Step 9: A Python macro can also be included to run multiple iterations of the model using different random distributions for use in Monte Carlo simulations

In step 10, permeability calculations are carried out based on Eq. (5.11), using the calculated DCOD and overlap areas from the FE model using an integrated Python code:

- Read nodal connectivity from mesh
- Read x,y,z nodal displacements from output database
- Cross reference connectivity with cracked XFEM elements
- DCOD calculation based on relative x,y,z displacements of adjacent nodes in crack elements
- Calculation of crack-overlap area for individual crack networks
- Sum over the entire laminate and calculate permeability

The Python code calculates laminate permeability based on co-incident crack networks. For more complex crack networks, the process is augmented by direct identification and measurement of leakage path dimensions.

5.3 Test cases

5.3.1 Transverse tension test

The transverse tension test for composites was used as a general method for verifying the mesh independent microcrack initiation aspect of the methodology. In this test, a CF/PEEK coupon 2.5 mm thick, 25 mm wide and with a 150 mm gauge length, is loaded in tension. The uni-directional composite lay-up is such that the fibres are aligned perpendicular to the direction of extension. A volume-adjusted

Weibull strength distribution was assigned to the elements in a number of similar specimens with mesh densities varying from 4,000 to 36,000 elements, to give element volumes between approximately 2.34 mm^3 and 0.26 mm^3, respectively. A limit was placed on the distributions such that no element could be assigned a fracture strength greater than 110 MPa, which was assumed to be the upper limit of the transverse strength of the material, based on the strength of pure PEEK. 3-D solid reduced integration elements were used in the analysis, with displacement-control. A uniform mesh density was used throughout each specimen. The base case CF/PEEK properties used in this and subsequent analyses are given in Table 5.2. The analysis results for two different mesh densities are shown in Fig. 5.16.

Table 5.2 Main properties of CF/PEEK used in analyses.

Property	Suprem IM7 (60%)
0° Tensile Modulus (GPa)	165
Poisson's ratio	0.3
90° Tensile Strength ($\bar{\sigma}_0$) (MPa)	65
90° Tensile Modulus (GPa)	10
Shear Modulus (GPa)	5.5
GIC (J/m^2)	1515
GIIC (J/m^2)	1355
Weibull modulus ($\boldsymbol{m}$)	12

In Fig. 5.16, fully open transverse cracks can be seen extending partially or fully across the specimens, as signified by the presence of red elements.

4.000 elements   21.000 elements
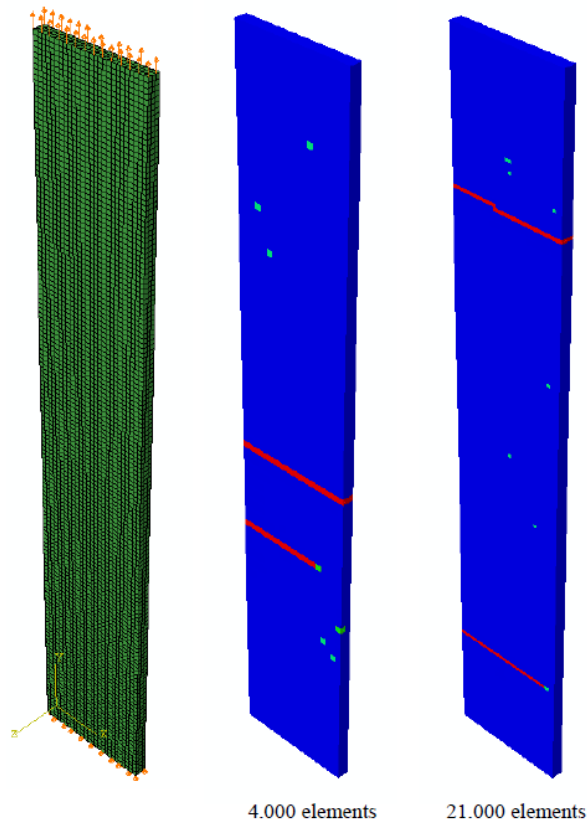
Figure 5.16 Results of the transverse tension tests on uni-directional laminae for the 4,000 element and 21,000 element specimen models. The specimens are shown at failure, with the horizontal red rows of elements signifying fully open cracks.

Numerous partially cracked cyan-coloured elements are also visible in each specimen, representing the extent of local damage formation, prior to failure. Fig. 5.17 (a) shows the result of the size-effect adjustment made to the fracture Weibull distributions for each mesh density.
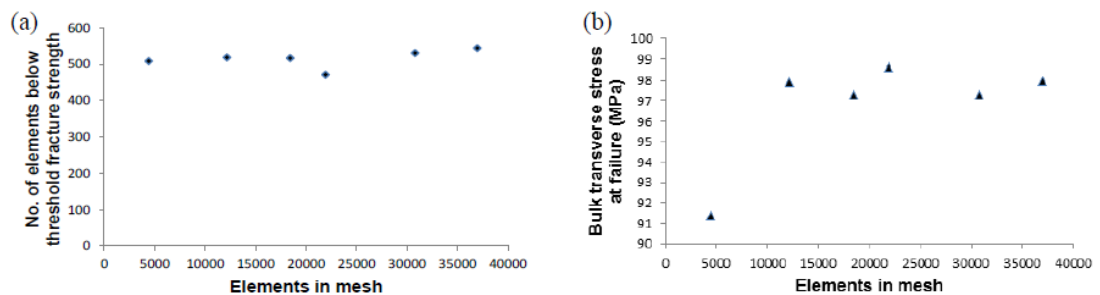
Figure 5.17 (a) Number of elements below the threshold fracture strength limit, set at 110 MPa, for each mesh. (b) Bulk transverse stress at failure for each mesh density.

All distributions yield approximately 500 elements with a fracture strength below the pre-assigned threshold of 110 MPa. Fig. 5.17 (b) shows that apart from the specimen with the lowest mesh density of 4,000 elements, all other meshes produced results consistent with a bulk transverse stress at failure of approximately 98 MPa. This result indicates that above a certain density limit (4,000 elements), mesh independence is achieved for this specific fracture strength distribution and applied threshold level, with specimen failure occurring at a similar, but statistically-varying, load point for all models.

5.3.2 Cryogenic permeability prediction

5.3.2.1 Overview

The specimens investigated for this case are similar to the rectangular (34 mm× 27 mm) CF/PEEK laminates tested in [29] (Chapter 4). Of the 8-ply, 16-ply and 32-ply laminates which were tested, the thickest 32-ply specimens were found to crack after a single cryogenic cycle (ΔT = -236 °C) in liquid nitrogen, leading to the formation of extensive through-thickness crack networks and associated crack overlap areas. This result was observed through the use of 3-D X-ray CT. At sufficient scan resolution (15 μm), it was possible to examine overlapping crack groups in damaged specimens, and to directly measure individual crack opening displacements and crack overlap areas, as shown in Fig. 5.18.
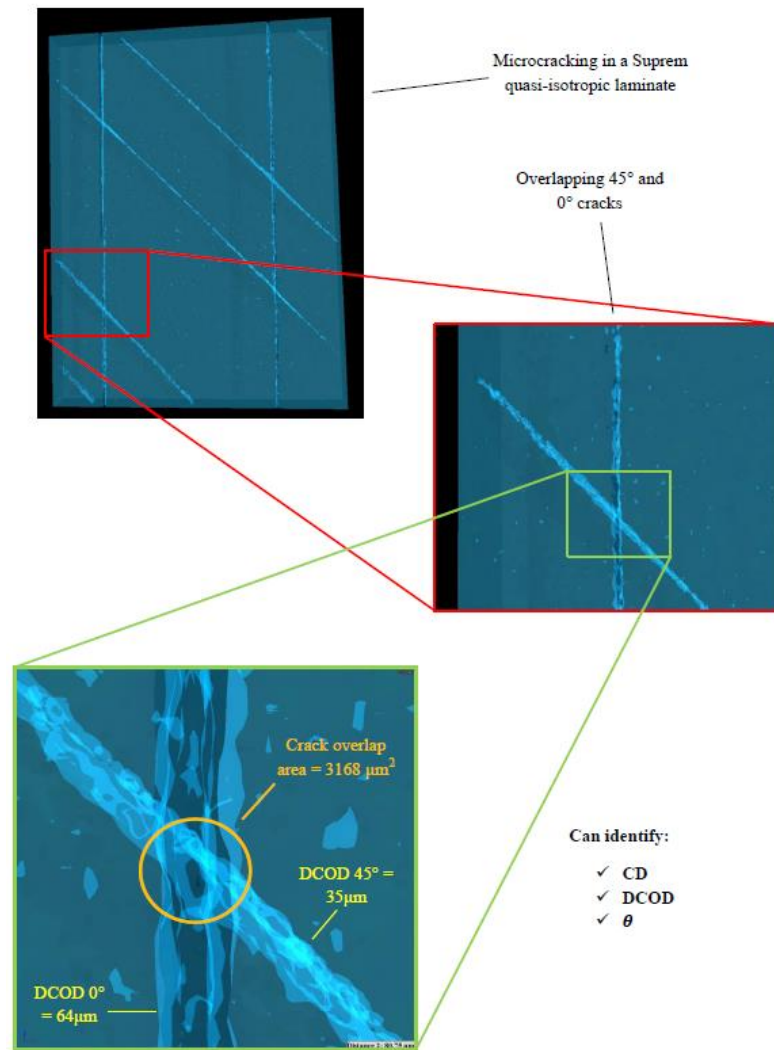
Figure 5.18 3-D X-ray CT scan of a cryogenically cycled CF/PEEK laminate. The scan resolution (15 μm) allows the direct measurement of DCOD and crack overlap area for individual cracks.

The proposed modelling methodology allows the prediction of laminate permeability based on the physical opening of 3-D XFEM cracks in adjacent plies, similar to the method by which the overlap area is calculated in Fig. 5.18. The technique is illustrated in Fig. 5.19, where a single crack network has been modelled using the combined XFEM-SCZM approach, with the DCOD values being directly measured at the overlap area.
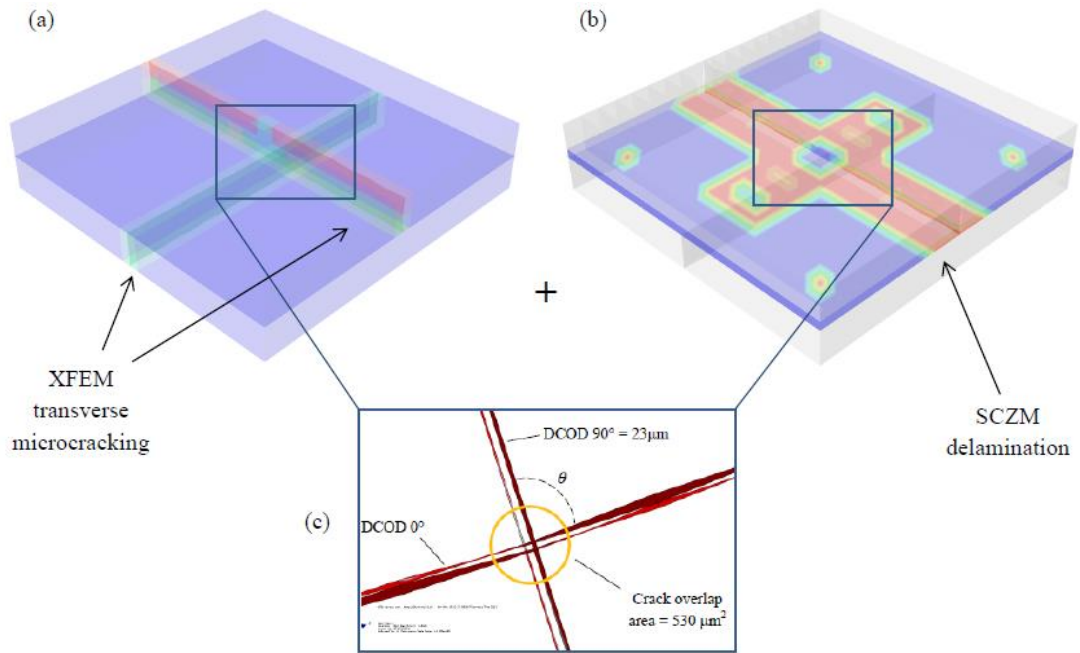
Figure 5.19 A combined XFEM- SCZM model of a single crack network. The XFEM-predicted transverse cracking is shown in (a), while the SCZM-predicted delamination is shown in (b). The resulting leak path and the method of calculating the crack overlap area, based on measurement of DCOD, is illustrated in (c).

5.3.2.2 Weibull distribution method

The first test case uses a Weibull distribution of fracture strengths to simulate random microcrack initiation. The distribution is size dependent and is based on the transverse tensile strength of Suprem IM7, given in Table 5.2, for a specimen volume of approximately 9375 mm^3. Two 32-ply lay-up configurations were modelled: $[0°_4/90°_4/0°_4/90°_4]_S$ and $[0°_4/45°_4/135°_4/90°_4]_S$, each with a volume of 4112 mm^3. The part geometries were uniformly meshed with 120,000 3-D elements, for an element volume of 0.034 mm^3, with a surface interaction defined between each of the ply groups. A thermal load, ΔT = -339 °C, based on the difference between the glass transition temperature of the material (143 °C) and the temperature of liquid nitrogen (-196 °C), was applied directly to the mesh. Note that a transient thermal history applied to the mesh, as described in Chapter 6, would more accurately capture the thermal loading experienced by the experimental test

specimens. This range was chosen to simulate the drop in temperature experienced by laminates on the first cryogenic exposure after processing. In addition, symmetry conditions were applied to the specimen edges to mitigate against computationally expensive edge effects.

The simulations were performed on 24 2.4GHz Intel Ivy Bridge cores on an SGI ICE X system at the Irish Centre for High Performance Computing (ICHEC), with each simulation typically requiring 1,150 CPU hours. Extremely small time increments, on the order of 10^{-16} units, were required in order to ensure solution convergence, due to the rapid growth of multiple cracks simultaneously. Specialised general solution controls were also required, including increased number of allowable increment cutbacks in line with the discontinuous nature of the analyses. Figs. 5.20 and 5.21 shows the results of the simulations in terms of the resulting surface cohesive forces and the XFEM crack surfaces.
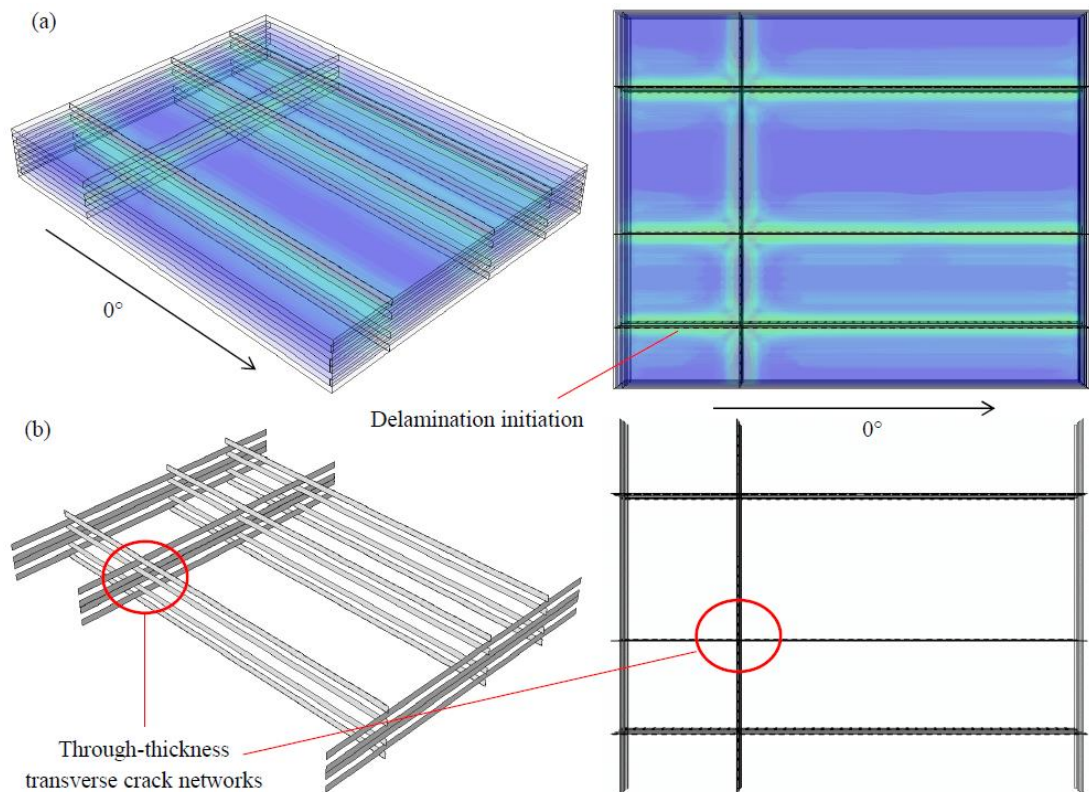
Figure 5.20 Predicted (a) SCZM normal force magnitude and (b) XFEM crack surface output for the cross-ply laminate using the Weibull distribution method, ΔT = -339 °C.
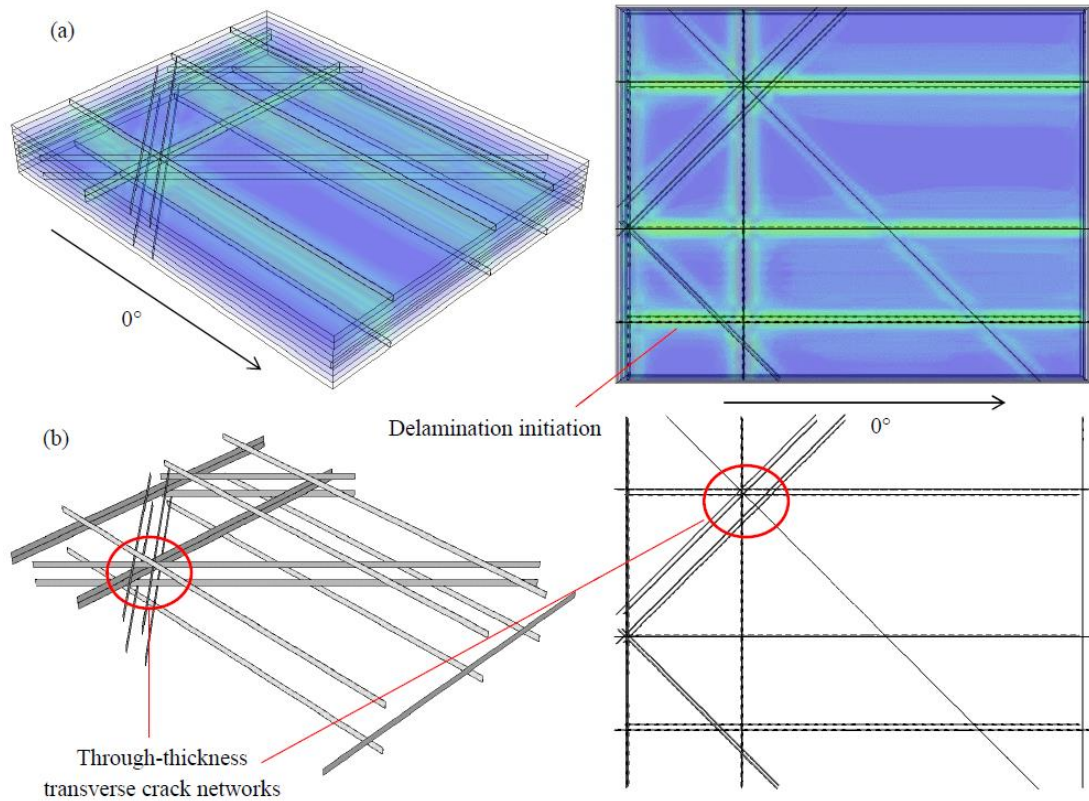
Figure 5.21 Predicted (a) SCZM normal force magnitude and (b) XFEM crack surface output for the quasi-isotropic laminate using the Weibull distribution method, $\Delta T = -339$ °C.

As expected, crack nucleation occurred in low-strength elements first. The degradation in stiffness of cracked elements was found to cause an altered stress field in the vicinity of the initial crack, leading to an increased likelihood of crack initiation and propagation in adjacent elements and ply groups. In the case of the cross-ply laminate (Fig. 5.20), the initial nucleation sites subsequently developed into the hubs of through-thickness crack networks. As observed in cryogenic experiments, transverse microcracks were able to propagate across the entire specimen. The majority of cracks grew simultaneously within an extremely small time increment ($<10^{-10}$), with the exception of some cracks in the inner 0° plies, which took slightly longer to grow across the entire specimen width. This action suggests near-instantaneous crack formation on an experimental time-frame. Interfacial damage was non-existent, except for relatively minor delaminations along crack paths and overlap areas.

The quasi-isotropic laminate (Fig. 5.21) was found to exhibit more complex crack network formation. Like the cross-ply laminate, initial nucleation sites influenced crack formation in adjacent plies; however, not all of these sites resulted in co-incident through-thickness cracking. Several inter-connected leakage paths were predicted, comprised of spatially disparate cracks throughout the laminate. Other cracks, particularly in the 90° plies, were predicted to form in isolation, not connected to any crack network. Again, the majority of the crack growth was predicted to occur simultaneously and near-instantaneously, with the exception of the slightly slower growth of cracks in the outer 0° plies. Minor delamination was also predicted at crack overlap areas. Fig. 5.22 compares COD values from experimental work with the above simulations.
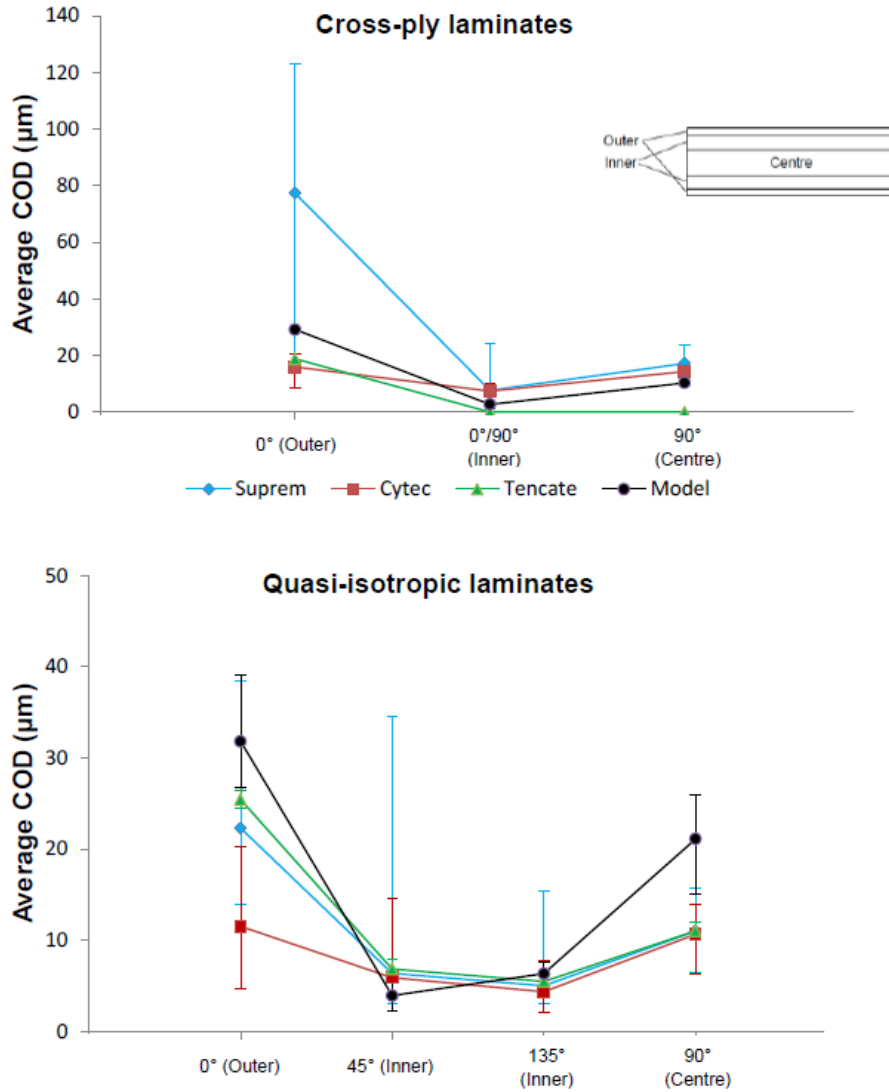
Figure 5.22 Comparison of average crack opening displacements through the thickness of 32-ply laminates for experimental (Suprem, Cytec and Tencate CF/PEEK laminates [29]) and models (Suprem laminates). The error bars refer to the range (maximum and minimum) of measured COD values in each ply group.

The crack openings calculated from the models were found to follow the same general trend measured in the test specimens, where the microcracks in the outer ply groups of laminates were consistently found to be wider than those in inner ply groups. This trend also shows, with regards to co-incident crack networks, that permeability of the laminate would be restricted by the relatively narrow crack openings found in the inner and off-axis plies. Permeability output for the laminates using the Weibull strength distribution method is given in Section 5.3.2.3.

5.3.2.2 Defect distribution method

The input data for the defect distribution method is based on the void content analyses from [29] for 32-ply CF/PEEK laminates, which provide the range and variation in void dimensions in terms of x-y-z coordinates. As described in the previous section, full cross-ply and quasi-isotropic laminates were modelled using the same thermal load. However, a reduced mesh of approximately 46,000 elements, for an element volume of 0.088 mm^3, was used for these simulations. In order to reduce computational expense, the void range was subject to a lower bound, below which the smaller voids (< 0.025 mm^3 in volume) were assumed to have a negligible effect on the surrounding material properties. Due to the lower mesh density, input processing was generally completed in less than 0.5 hours, with the simulations being run over the same system described in Section 5.3.2.2. Difficulty in achieving solution convergence within the 48 hour processing window for this method required using a reduced toughness Suprem IM7 material model, with the fracture toughness values being reduced by an order of magnitude. Figs. 5.23 and 5.24 shows the results of the simulations in terms of the resulting surface cohesive forces and the XFEM crack surfaces.
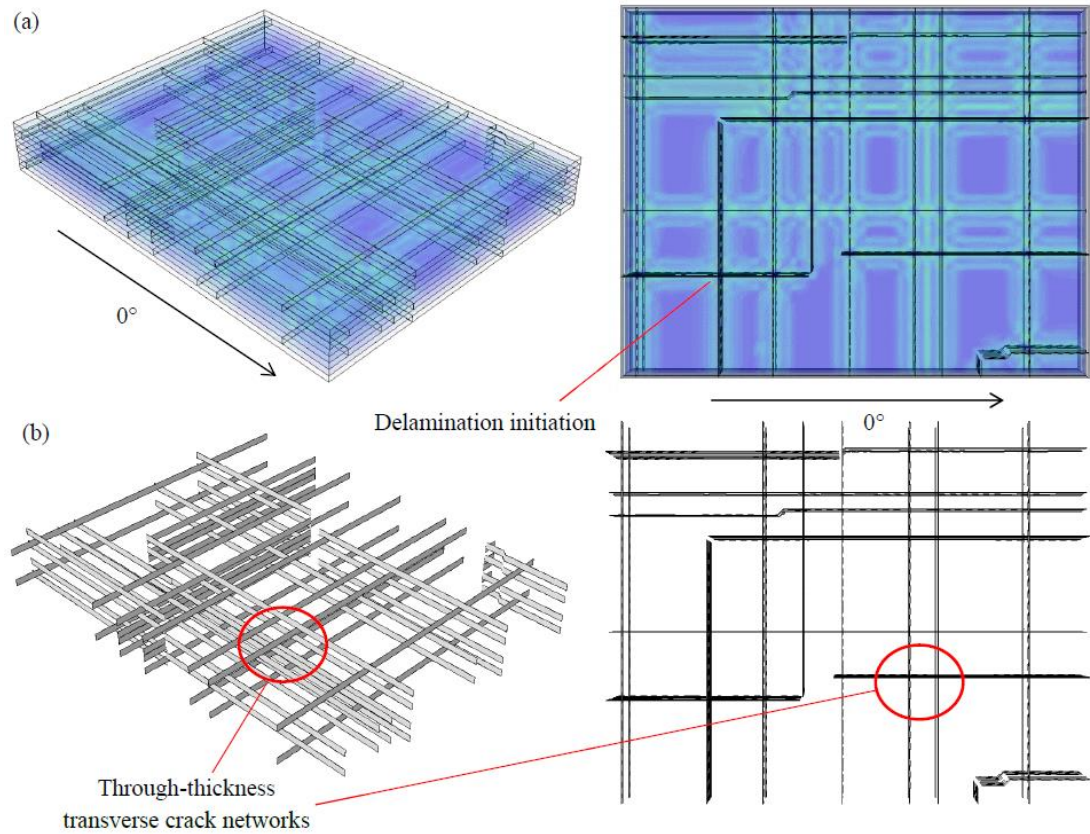
Figure 5.23 Predicted (a) SCZM normal force magnitude and (b) XFEM crack surface output for the cross-ply laminate using the defect distribution method, $\Delta T = -339 \,°C$.
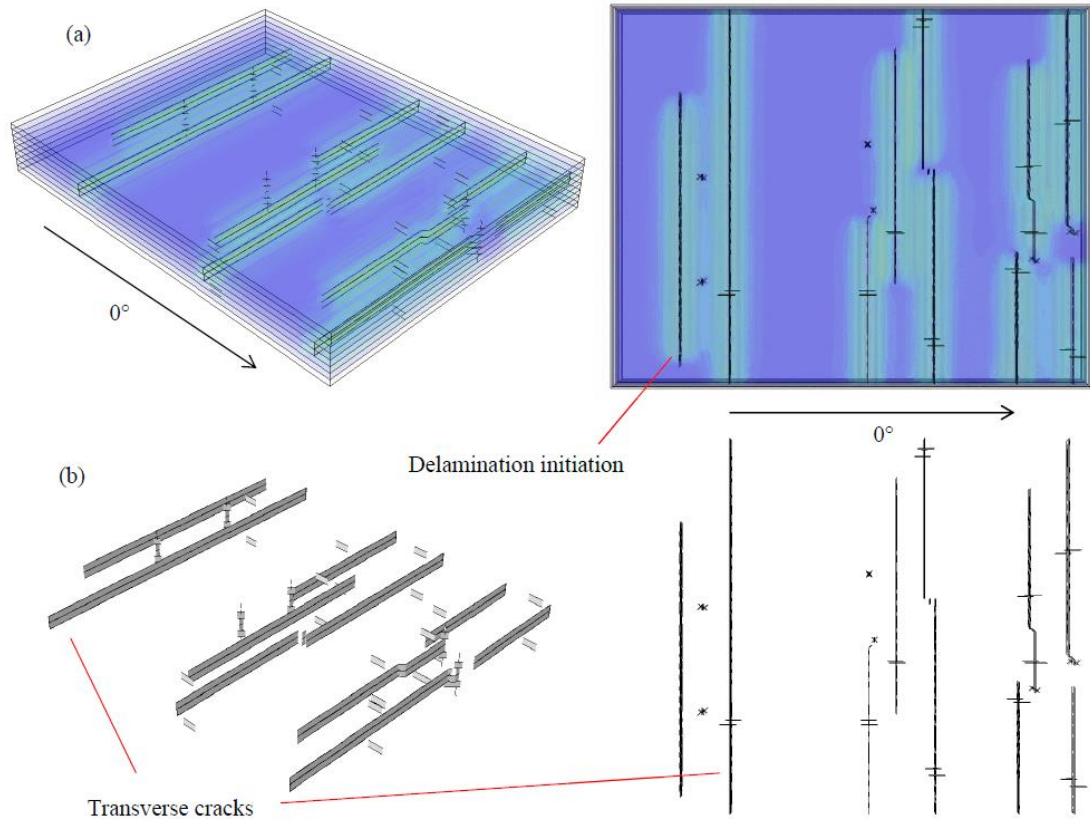
Figure 5.24 Predicted (a) SCZM normal force magnitude and (b) XFEM crack surface output for the quasi-isotropic laminate using the defect distribution method, $\Delta T = -339$ °C.

Crack nucleation for this method was found to occur in the region surrounding high void content elements. This is the result of the low stiffness of high void content elements, which leads to the formation of local stress concentrations. Elements in the direct vicinity of these voids are therefore subjected to stress levels above those present in the bulk material. As mentioned previously, achieving full crack propagation using this method proved computationally more expensive than for the Weibull method. In order to ensure prompt crack growth in this case, with a focus on qualitative trends in terms of distributions and orientations of microcracking, the material toughness was artificially reduced by a factor of 10. Fig. 5.23 shows the extensive microcrack formation for the 32-ply cross-ply laminate. As with the Weibull method, crack growth is predicted across the laminate within an extremely small time increment. However, a small number of cracks were predicted to not

propagate fully across the specimen width prior to the simulation terminating. This trend was more noticeable for the quasi-isotropic laminate shown in Fig. 5.24, where only cracks in the centre plies were predicted to undergo significant growth within the simulation run-time. Crack nucleation was predicted in off-axis and outer ply groups, but these cracks were not predicted to grow through more than a few elements

5.3.2.3 Permeability calculations

Permeability calculation was implemented though the customised Python code discussed in Section 5.2.7 and by direct computation of crack opening displacements from the simulation deformed geometry, depending on the complexity of the resulting leak paths. Predictions for the Weibull and defect distribution simulation methods were compared with leak rates for available CF/PEEK 8-ply laminates exposed to a single cryogenic cycle (Table 5.3). Note, no through thickness networks were observed in 8-ply Suprem specimens tested in this work (Chapter 4). No relevant experimental test data was available for the thicker 16- and 32-ply laminates.

Table 5.3 Measured (experiment – ÉireComposites Teo) and predicted (simulation) leak rates for a range of CF/PEEK 8-ply laminates exposed to a single cryogenic cycle. QI = quasi-isotropic, CP = cross-ply, * = reduced toughness material.

Material	Type	Leak rate (ssc/s/m^2)
Cytec AS4 (8-ply QI)	Experiment	8.50×10^{-5}
Tencate AS4 (8-ply QI)	Experiment	1.00×10^{-4}
Suprem IM7 (8-ply QI)	Experiment	2.50×10^{-1}
Suprem IM7 (32-ply CP)	Weibull simulation	8.42×10^{-3}
Suprem IM7 (32-ply QI)	Weibull simulation	3.60×10^{-3}
Suprem IM7* (32-ply CP)	Defect simulation	1.18×10^{-2}
Suprem IM7* (32-ply QI)	Defect simulation	-

The predicted leak rates for the simulations were found to lie between the bounds of the most and least permeable test specimens. For the Weibull simulations, the cross-

ply laminate was predicted to have a slightly higher permeability, based on a predicted general trend of wider adjacent overlapping cracks. Although the cross-ply defect simulations had a significantly greater crack density compared to the cross-ply Weibull simulations, the leak rates for the laminates were quite similar. This is due to a 'bottleneck' effect, whereby the centre ply group of the defect laminate has a relatively low crack density, thus limiting the potential for leakage as a function of these crack dimensions, in spite of higher crack densities in the outer ply groups. Given the limiting effect of low crack density plies on leak rates for laminates, identification of these low-damage ply groups is of prime importance for the design of composite cryogenic storage vessels. While the quasi-isotropic defect simulation laminate predicted fully propagated microcracks, no through-thickness crack networks were predicted, resulting in zero leak rate.

5.4 Conclusions

A combined XFEM and cohesive zone methodology for predicting composite laminate microcracking distributions and permeability is presented. The method uses XFEM for random microcrack initiation and propagation (intra-laminar failure) and SCZM for the delamination between plies (inter-laminar failure). The methodology allows for complex 3-D crack networks to be modelled and enables direct computation of DCOD values and crack overlap areas for permeability prediction.

Given the inherently random nature of the potential microcracking features in composite materials, two distinct methods of predicting random microcrack initiation were investigated. In the first method, a Weibull distribution, for stochastic characterisation of the fracture strength of a material was used to represent the presence of defects within the material. Based on the strength distribution, a random fracture strength, adjusted to account for size effects, was assigned to each element in the FE mesh. Mesh independence was established via a series of transverse tensile test simulations using a range of mesh densities. The second approach was based on an elemental representation of defects. This involved the reduction in a given element stiffness based on the dimensions of defects, specifically voids, within its

bounds. The size range of voids was taken from measurements via 3-D X-ray CT characterisation of CF/PEEK laminates.

Full 3-D simulations of 32-ply cross-ply and quasi-isotropic laminates, subjected to a cryogenic load history, using both methods of defect representation, predicted extensive through-thickness crack networks consistent with X-ray CT scans of similar tested specimens. Average COD values taken from the models were found to follow the same trends as those measured experimentally, with inner ply groups having consistently narrower crack openings than outer ply groups. Permeability calculations for the damaged laminates fell within the range of measured leak rates from tested CF/PEEK specimens, indicating the applicability of the methodology to complex damage accumulation prediction for composite materials.

Future work will include modelling of realistic cryogenic pressure vessel structures to determine the optimum composite lay-up for minimal gas leakage. The models will incorporate transient heat transfer to examine the effects of tank wall thickness on damage formation.

5.5 References

[1] Todoroki A., Tanaka Y. & Shimamura Y. Delamination monitoring of graphite/epoxy laminated composite plate of electric resistance change method. *Composites Science and Technology*, **62**(9), 1151–60, 2002.

[2] Bois C. & Hochard C. Monitoring of laminated composites delamination based on electro mechanical impedance measurement. *Journal of Intelligent Material Systems and Structures*, **15**(1), 59–67, 2004.

[3] Boccaccini A.R., Ponton C.B. & Chawla K.K. Development and healing of matrix microcracks in fibre reinforced glass matrix composites: assessment by internal friction. *Materials Science and Engineering: A*, **241**(1-2), 141-150, 1998.

[4] Herakovich C.T. Damage-induced property changes in composites subjected to cyclic thermal loading. *Engineering Fracture Mechanics*, **25**(5-6), 779-791, 1986.

[5] Meraghni F., Blakeman C.J. & Benzeggah M.L. Effect of interfacial decohesion on stiffness reduction in a random discontinuous-fibre composite containing matrix microcracks. *Composites Science and Technology*, **56**(5), 541-555, 1996.

[6] Lim S.G. & Hong C.S. Effect of transverse cracks on the thermomechanical properties of cross-ply laminated composites. *Composites Science and Technology*, **34**(2), 145-162, 1989.

[7] Kashtalyan M.Y. & Soutis C. Mechanisms of internal damage and their effect on the behaviour and properties of cross-ply composite laminates. *International Applied Mechanics*, **38**(6), 3-22, 2002.

[8] Joseph P.V., Rabello M.S, Mattoso L.H.C., Joseph K. & Thomas S. Environmental effects on the degradation behaviour of sisal fibre reinforced polypropylene composites. *Composites Science and Technology*, **62**(10-11), 1357-1372, 2002.

[9] Davies P., MazEas F. & Casari P. Seawater aging of glass reinforced composites: shear behaviour and damage modelling. *Journal of Composite Materials*, **35**(15), 1343-1372, 2001.

[10] Murthy H.N.N., Sreejith M., Krishna M., Sharma S.C. & Sheshadri T.S. Seawater durability of epoxy/vinyl ester reinforced with glass/carbon composites. *Journal of Reinforced Plastics and Composites*, **29**(10), 1491-1499, 2010.

[11] Segovia F., Salvador M., Sahuquillo O. & Vincente A. Effects of long-term exposure on E-glass composite material subjected to stress corrosion in a saline medium. *Journal of Composite Materials*, **41**, 2119-2128, 2007.

[12] Final Report of the X-33 Liquid Hydrogen Tank Test Investigation Team, Marshall Space Flight Center, Huntsville, Alabama, 2000.

[13] Nairn J.A. Matrix microcracking in composites. *Polymer matrix composites*, Ch. 13, Pergamon, 2001.

[14] Henaff-Gardin C., LaFarie-Frenot M.C. & Gamby D. Doubly periodic matrix cracking in composite laminates Part 2: Thermal biaxial loading. *Composite Structures*, **36**(1-2), 131-140, 1996.

[15] Berthelot J.M. & LeCorre J.F. Statistical analysis of the progression of transverse cracking and delamination in cross-ply laminates. *Composites Science and Technology*, **60**, 2659-2669, 2000.

[16] Kumazawa H., Aoki T. & Susuki I. Influence of stacking sequence on leakage characteristics through CFRP composite laminates. *Composites Science and Technology*, **66**, 2107-2115, 2006.

[17] Yokozeki T., Ogasawara T. & Ishikawa T. Evaluation of gas leakage through composite laminates with multilayer matrix cracks: Cracking angle effects. *Composites Science and Technology*, **66**, 2815-2824, 2006.

[18] Bechel V.T., Camping, J.D. & Kim R.Y. Cryogenic/elevated temperature cycling induced leakage paths in PMCs. *Composites Part B: Engineering*, **36**, 171-182, 2005.

[19] Park C.H. & McManus H.L. Thermally induced damage in composite laminates: predictive methodology and experimental investigation. *Composites Science and Technology*, **56**, 1209-1219, 1996.

[20] Roy S. & Benjamin M. Modelling of permeation and damage in graphite/epoxy laminates for cryogenic fuel storage. *Composite Science and Technology*, **64**, 2051-2065, 2004.

[21] Nair A. & Roy S. Modelling of permeation and damage in graphite/epoxy laminates for cryogenic tanks in the presence of delaminations and stitch cracks. *Composite Science and Technology*, **67**(11-12), 2592–2605, 2007.

[22] Grogan D.M., Leen S.B., Semprimoschnig C.O.A & Ó Brádaigh C.M. Modelling of thermal and mechanical fatigue delamination growth in composites

using XFEM. Proceedings of the 12th International Symposium on Materials in the Space Environment, Noordwijk, The Netherlands, September 24th – 28th, 2012.

[23] Grogan D.M., Leen S.B. & Ó Brádaigh C.M. An XFEM-based methodology for fatigue delamination and permeability of composites. *Composite Structures*, **107**, 205-218, 2014.

[24] Van der Meer F.P. & Sluys L.J. Mesh-independent modeling of both distributed and discrete matrix cracking in interaction with delamination in composites. *Engineering Fracture Mechanics*, **77**, 719–735, 2010.

[25] Iarve E.V., Gurvich M.R. & Mollenhauer D.H. Mesh-independent matrix cracking and delamination modelling in laminated composites. *International Journal for Numerical Methods in Engineering*, **88**, 749-773, 2011.

[26] Kumazawa H. & Whitcomb J. Numerical modelling of gas leakage through damaged composite laminates. *Journal of Composite Materials*, **42**, 1619-1638, 2008.

[27] Xu J., Sankar B.V. & Bapanapalli S. Finite Element Based Method to Predict Gas Permeability in Cross-ply Laminates. *Journal of Composite Materials*, **42**(9), 849-864, 2008.

[28] Bois C., Malenfant J.C., Wahl J.C. & Danis M. A multiscale damage and crack opening model for the prediction of flow path in laminated composite. *Composites Science and Technology*, **97**, 81-89, 2014.

[29] Grogan D.M., Leen S.B., Semprimoschnig C.O.A. & Ó Brádaigh C.M. Damage characterisation of cryogenically cycled carbon fibre/PEEK laminates. *Composites Part A: Applied Science and Manufacturing*, **66**, 237-250, 2014.

[30] Melenk J.M. & Babuska I. The partition of unity finite element method: basic theory and applications. *Computer Methods in Applied Mechanics and Engineering*, **139**, 289–314, 1996.

[31] Abdelaziz Y. & Hamouine A. A survey of the extended finite element. *Computers and Structures*, **86**(11–12), 1141–51, 2008.

[32] Belytschko T., Gracie R. & Ventura G. A review of extended/generalized finite element methods for material modelling. *Modelling and Simulation in Materials Science and Engineering*, **17**(4), 24, 2009.

[33] Shi J., Chopp D., Lua D., Sukumar N. & Belytschko T. Abaqus implementation of extended finite element method using a level set representation for three-dimensional fatigue crack growth and life predictions. *Engineering Fracture Mechanics*, **77**, 2840–63, 2010.

[34] Hibbitt, Karlsson & Sorensen. Inc. ABAQUS/Standard User's Manual, v. 6.11. Pawtucket, Rhode Island, 2011.

[35] Benzeggagh M.L. & Kenane M. Measurement of mixed-mode delamination fracture toughness of unidirectional glass/epoxy composites with mixed-mode bending apparatus. *Composites Science and Technology*, **56**(4), 439-449, 1996.

[36] Zhou F. & Molinari F. Dynamic crack propagation with cohesive elements: a methodology to address mesh dependency. *International Journal for Numerical Methods in Engineering*, **59**, 1-24, 2004.

[37] Lu C., Danzer R. & Fischer F.D. Fracture statistics of brittle materials: Weibull or normal distribution. *Physical Review E*, **65**, 067102, 2002.

[38] Dirikolu M.H., Aktas A. & Birgoren B. Statistical analysis of fracture strength of composite materials using Weibull distribution. *Turkish Journal of Engineering and Environmental Sciences*, **26**, 45-48, 2002.

[39] Available at www.python.org, 2014.

[40] Madsen B. & Lilholt H. Physical and mechanical properties of unidirectional plant fibre composites - An evaluation of the influence of porosity. *Composites Science and Technology*, **63**, 1265-1272, 2003.

[41] Zhu H., Wu B., Li D., Zhang D. & Chen Y. Influence of voids on the tensile performance of carbon/epoxy fabric laminates. *Journal of Materials Science and Technology*, **27**(1), 69-73, 2011.

[42] Huang H. & Talreja R. Effects of void geometry on elastic properties of unidirectional fiber reinforced composites. *Composites Science and Technology*, **65**, 1964-1981, 2005.

[43] Chao L. & Huang J.H. Prediction of elastic moduli of porous materials with equivalent inclusion method. *Journal of Reinforced Plastics and Composites*, **18**(7), 592-602, 1999.

[44] Gurvich M.R. Strength/size effect for anisotropic brittle materials under a random stress state. *Composites Science and Technology*, **59**, 1701-1711, 1999.

[45] Curtin W.A. & Ibnabdeljalil M. Strength and reliability of fibre reinforced composites: localised load sharing and associated size effects. *International Journal of Solids and Structures*, **34**(21), 2649-2668, 1997.

6. Damage and permeability in tape-laid thermoplastic composite cryogenic tanks

Article overview

This work presents a combined experimental and numerical approach to the design and analysis of tape-laid composite cryogenic tanks. The experimental techniques outlined in **Chapter** 4 are applied to characterising a new tape-laid CF/PEEK material in the form of flat laminate and cylindrical sections. Due to the nature of the tape laying process, the quality of the laminates and defects present can differ significantly from autoclaved specimens. Also, given the novelty of the process, relatively little data on testing and characterisation for thermoplastic materials has been published to date. The numerical methodology outlined in **Chapter** 5 is expanded upon and scaled to account for the larger model size and geometry required for cryogenic tanks. An iterative design process for the tank is described, with the aim of minimising transverse microcrack initiation and growth. Several provisional tank lay-ups are subsequently selected for damage analysis, using a cylindrical sub-model. This sub-model brings together relevant input data from previous chapters in the form of temperature-dependant material properties ranging from processing to cryogenic temperatures, transient thermo-mechanical load profiles and defect distributions to simulate random microcrack initiation. Additional simulations of the best performing tank design are then conducted in order to ensure

6. Damage and permeability in tape-laid thermoplastic composite cryogenic tanks

the absence of through-thickness leak paths over multiple defect permutations. In contrast to the 2-D pre-defined unit cell model outlined in **Chapter** 3, this model showcases the ability of the methodology to complete a fully 3-D meso-scale permeability prediction of a large-scale structure, representing a significant step forward in permeability and damage simulation capability for composites.

Abstract

This work presents a combined experimental and numerical approach to the design and analysis of tape-laid thermoplastic composite cryogenic tanks. A detailed material and defect characterisation of automated tape-laid CF/PEEK is undertaken using optical micrography and 3-D X-ray CT (computed tomography) as well as cryogenic testing to investigate damage formation. Resulting material data is used as input for a novel XFEM (extended finite element method)-cohesive zone methodology which is used to predict intra- and inter-ply damage in an internally pressurised cryogenic tank. An optimised tank lay-up is presented and analysed using the numerical method to ensure resistance to microcrack formation and fuel leakage through the tanks walls under operating loads.

Abbreviations

SFT   Stress Free Temperature

TTS   Transverse Tensile Strength

TCS   Transverse Compressive Strength

IPSS   In-Plane Shear Strength

ILSS   Inter-Laminar Shear Strength

SHC   Specific Heat Capacity

UD   UniDirectional specimen

QI   Quasi-Isotropic specimen

COD   Crack Opening Displacement

6.1 Introduction

Due to their high specific strength and stiffness amongst other properties, carbon-fibre reinforced polymers (CFRP) are seen as candidate materials for the fuel tanks of next generation reusable launch vehicles (RLVs). These fuel tanks will be exposed to cryogenic temperatures as low as -250 °C and to internal pressurisation as high as 1 MPa. This extreme thermo-mechanical loading can lead to microcracking and delamination formation within the CFRP, which, in severe cases, can result in permeation of the cryogen through the fuel tank walls. A precise understanding, therefore, of the methods of damage accumulation in the material and how the various damage modes interact underpins the potential use of CFRP for RLVs.

While numerous works have been published on the design and testing of composite overwrapped pressure vessels (COPVs) [1-4], the unique challenges posed by cryogenic fuel storage have yet to be fully addressed. Work on the design and analysis of composite cryo-tanks has intensified since the failure of the NASA/Lockheed X-33 RLV fuel tank [5], where fuel leakage occurred due to cryogenically induced damage in the composite tank wall. Subsequent experimental and theoretical analyses of cryo-tanks [6, 7] have found that, unlike traditional COPVs, the thermal stresses induced by cryogenic loading are the main design consideration and play a critical role in damage formation. In addition, the role of material quality and processing conditions on damage initiation remain understudied [8, 9], particularly for advanced thermoplastic composites such as CF/PEEK, which are increasingly used in conjunction with novel processing techniques such as automated tape laying (ATL) for the manufacturing of large structures.

Thermoplastic composites offer several advantages over thermosets in terms of their improved range of properties and processing techniques available. CF/PEEK is a high-performance thermoplastic carbon-composite material, which is increasingly being used in the aerospace industry for weight sensitive designs and is also known to offer increased resistance to damage propagation compared to epoxy based materials [10, 11]. Importantly, thermoplastics allow the use of out-of-autoclave processing techniques such as automated tape laying (ATL), a relatively new processing method based on the in-situ consolidation of plies. This is carried out by a computer controlled robot which typically applies pre-preg tape to a heated mould

placed on a revolving mandrel, using a heat source such as a laser which is focused on the ply lay-down area. Unlike autoclave processing, consolidation occurs at the point where the robotic head first heats, then melts and finally consolidates and cools the incoming tape, as opposed to processing the entire laminate simultaneously. This facilitates the manufacture of large structures without the investment required for a large autoclave of several metres diameter. Thus the technique is well suited to producing components such as cryo-tanks. The main drawbacks of this technique include the potential for poor ply adhesion due to insufficient melting and adhesion and the presence of significant residual stress gradients due to non-uniform cooling [8, 12, 13]. The tape- laying process itself can also result in gaps due to overlapping plies which can result in high void contents. These issues can often lead to composite laminates of a lower general quality than those produced in an autoclave [9, 14].

CF/PEEK, due to its high processing temperature and semi-crystalline nature, exhibits significant property variation with temperature. Residual stress build-up for CF/PEEK laminates begins below the stress free temperature (SFT), which is approximately 315 °C [15]. This is far above the glass transition temperature of 143 °C, which usually marks the point of residual stress formation for amorphous polymeric composites. Thus, using this material for cryogenic applications can involve having to design for thermal residual stresses due to temperature changes in excess of 500 °C. The difficulty in accurately characterising material properties, including fracture strength and toughness, over such a wide temperature range means that little experimental data is available from the literature, particularly for relatively novel materials such as tape-laid CF/PEEK.

This work aims to advance the design and analysis of linerless composite cryo-tanks by combining the extensive material characterisation of a tape-laid composite with a novel numerical methodology capable of predicting composite laminate damage and permeability. This approach represents a significant departure from existing analysis methods such as unit cell, first-ply-failure and continuum analyses [6, 16-21] by allowing the discrete damage modelling of large structures using detailed material data inputs. An optimised cryo-tank design is also presented, which accounts for the thermo-mechanical stresses resulting from processing, fuelling and internal pressurisation. A sub-model meso-scale damage analysis shows that the optimised

tank design is capable of preventing fuel leakage after exposure to cryogenic temperatures and internal pressurisation.

6.2 Material characterisation

6.2.1 Overview of material properties

Measurements of temperature-dependant mechanical, thermal and fracture properties of CF/PEEK materials have been collated from several sources in Tables 6.1 and 6.2. Using the properties of the tape laid Suprem IM7 [22] at 25 °C from Table 6.1 as a base, temperature-dependant data is generated by interpolation and normalisation using fitting functions across a range of temperatures for available material data. Table 6.3 presents the resulting interpolated temperature dependant data which is used in subsequent modelling work, described in Section 6.3. Linear interpolation has been used to complete the material data set where possible. Material strength and fracture toughness data are not available above the glass transition temperature of the material.

Table 6.1 Measured temperature-dependant mechanical and fracture properties of CF/PEEK materials. E and G are the elastic and shear moduli, TTS and TCS are the transverse tensile and compressive strengths, IPSS and ILSS are the in-plane and inter-laminar shear strengths, G_{IC} and G_{IIC} are Mode I and Mode II fracture toughness. The subscripts 1 and 2 refer to the longitudinal and transverse directions. [1]Suprem Victrex AS4 [23], [2]Cytec APC-2/IM7 [24], [3]Suprem Victrex IM7 [22], [4]Suprem Victrex IM7 [23].

Temp. (°C)	E_1 (GPa)	E_2 (GPa)	G_{12} (GPa)	TTS (MPa)	TCS (MPa)	IPSS (MPa)	ILSS (MPa)	G_{IC} (J/m^2)	G_{IIC} (J/m^2)
-196	[1]141	-	-	[1]51	-	[1]81	[1]106	-	-
-70	-	-	-	[1]63	-	[1]104	[1]116	-	-
-55	[2]172	[2]11	[2]5.9	-	-	-	-	[2]1600	[2]2100
25	[3]155.0	[3]8.6	[3]4.00	[3]41	[3]163	[3]80	[3]98	[3]1910	[4]1355
125	-	-	-	[1]48	-	[1]75	-	-	-

Table 6.2 Measured temperature-dependant mechanical and thermal properties of CF/PEEK materials. E and G are the elastic and shear moduli, ν is Poisson's ratio, ρ is density, SHC is the specific heat capacity, α and k are the thermal expansion coefficients and conductivities. The subscripts 1 and 2 refer to the longitudinal and transverse directions. [1]APC-2/AS4 adapted from [25], [2]PEEK/IM7 adapted from [26], [3]APC-2/AS4 adapted from [27].

Temp. (°C)	[1]E_1 (GPa)	[1]E_2 (GPa)	[1]G_{12} (GPa)	[2]ν_{12}	[3]ρ (kg/m³)	[3]SHC (j/kg.K)	[3]α_1 (10^{-6}/K)	[3]α_2 (10^{-6}/K)	[3]k_1 (W/m.K)	[3]k_2 (W/m.K)[3]
25	134	10.3	6.00	0.32	1598	930	0.2	28.8	3.5	0.4
50	134	10.3	6.00	0.32	1598	930	0.2	29.4	4.6	0.5
75	134	9.6	5.43	0.34	1598	930	0.3	30.0	4.9	0.6
100	134	9.6	5.43	0.35	1593	1040	0.3	31.0	5.1	0.6
125	134	8.3	4.86	0.36	1593	1040	0.4	32.4	5.5	0.6
150	131	8.3	4.86	0.37	1586	1260	0.4	40.0	5.9	0.7
175	131	4.5	2.51	-	1586	1260	0.5	47.7	5.9	0.7
200	130	4.3	2.16	-	1575	1300	0.5	50.0	5.9	0.7
225	130	4.3	2.16	-	1575	1300	0.6	60.0	6.0	0.7
250	129	3.6	0.95	-	1563	1400	0.7	70.0	6.1	0.7
275	130	3.6	0.95	-	1563	1400	0.8	80.0	6.4	0.7
300	130	1.7	0.53	-	1551	1550	0.9	90.0	6.7	0.8
315	128	0.6	0.23	-	1551	1550	1.0	108.0	6.7	0.8

Table 6.3 Interpolated temperature-dependant material properties for tape-laid Suprem IM7 based on the measured properties in Tables 6.1 and 6.2.This data is used as input for subsequent numerical simulations. Data in italics has been linearly interpolated where possible. Material strength and toughness data are not available beyond the glass transition temperature of the material (143 °C).

Temp. (°C)	E_1 (GPa)	E_2 (GPa)	G_{12} (GPa)	ν_{12}	ρ (kg/m³)	SHC (J/kg.K)	α_1 (10⁻⁶/K)	α_2 (10⁻⁶/K)	k_1 (W/m.K)	k_2 (W/m.K)	TTS (MPa)	TCS (MPa)	IPSS (MPa)	ILSS (MPa)	G_{Ic} (J/m²)	G_{IIc} (J/m²)
-196	152.0	9.5	4.40	0.32	1598	930	0.0	24.7	3.5	0.4	39	163	74	121	1340	1890
-70	154.7	9.5	4.40	0.32	1598	930	0.0	24.7	3.5	0.4	47	163	95	133	1340	1890
-55	155.0	9.5	4.40	0.32	1598	930	0.1	25.4	3.5	0.4	46	163	93	127	1340	1890
25	155.0	8.6	4.00	0.32	1598	930	0.2	28.8	3.5	0.4	41	163	80	98	1910	1710
50	155.0	8.6	4.00	0.32	1598	930	0.2	29.4	4.6	0.5	40	163	77	92	1910	1710
75	155.0	8.6	3.62	0.34	1598	930	0.3	30.0	4.9	0.6	39	163	75	86	1910	1710
100	155.0	8.0	3.62	0.35	1593	1040	0.3	31.0	5.1	0.6	37	163	72	80	1910	1710
125	155.0	6.9	3.24	0.36	1593	1040	0.4	32.4	5.5	0.6	36	163	69	74	1910	1710
150	151.5	6.9	3.24	0.37	1586	1260	0.4	40.0	5.9	0.7	N/A	N/A	N/A	N/A	N/A	N/A
175	151.5	3.8	1.67	0.37	1586	1260	0.5	47.7	5.9	0.7	N/A	N/A	N/A	N/A	N/A	N/A
200	150.4	3.6	1.44	0.37	1575	1300	0.5	50.0	5.9	0.7	N/A	N/A	N/A	N/A	N/A	N/A
225	150.4	3.6	1.44	0.37	1575	1300	0.6	60.0	6.0	0.7	N/A	N/A	N/A	N/A	N/A	N/A
250	149.2	3.0	0.63	0.37	1563	1400	0.7	70.0	6.1	0.7	N/A	N/A	N/A	N/A	N/A	N/A
275	150.4	3.0	0.63	0.37	1563	1400	0.8	80.0	6.4	0.7	N/A	N/A	N/A	N/A	N/A	N/A
300	150.4	1.4	0.35	0.37	1551	1550	0.9	90.0	6.7	0.8	N/A	N/A	N/A	N/A	N/A	N/A
315	148.0	0.5	0.16	0.37	1551	1550	1.0	108.0	6.7	0.8	N/A	N/A	N/A	N/A	N/A	N/A

When compared with previously published material data for a similar grade of CF/PEEK processed using an autoclave [26], the tape-laid material exhibits lower strength values, particularly in the matrix-dominated directions. Transverse tensile strength alone was found to reduce by a third for the tape laid material. The increased presence of manufacturing defects resulting from the tape-laying process contributes to this property degradation.

6.2.2 Defect characterisation

The void and inclusion content for several types of tape-laid CF/PEEK laminates were measured using 3-D X-ray computed tomography (CT). This non-destructive testing technique allows full internal characterisation of a specimen based on the varying densities of its constitutive material phases. The specimens (see Table 6.4) were manufactured from a Suprem T/60%/IM7/PEEK/150 material with 0.14 mm ply thickness and included:

- Two unidirectional coupons, named UD1 and UD2 from a flat plate (16-ply, 34 mm $\times$ 27 mm)
- Two [45°/-45°/90°/0°/90°/0°/90°/0°/90°]$_S$ coupons QI1 and QI2, from a flat plate (18-ply, 34 mm $\times$ 27 mm)
- One unidirectional hoop wound section (16-ply, 100 mm wide, 500 mm diameter)

A KUKA KR 180 R2900 robot with a laser-line diode laser module (LDM) 3000W system operated by the Irish Centre for Composites Research (ICOMP) and based at the University of Limerick [14], Ireland, was used to manufacture the specimens. The nominal process parameters included a lay-down speed of 6m/min, a target temperature of 420 °C, a tool temperature of 280 °C, a roller pressure supply of 4.5 bar. and a laser power of 500 W. Due to the nature of the ply-by-ply lay-up process, material inhomogeneity in the form of through-thickness crystallinity gradients is expected in the specimens. While there was no specific thermal post-treatment applied to the specimens, a relatively high tool temperature of 280 °C was used. This would help to offset the high cooling rates typically associated with the lay-up of the initial plies, with the effect of bringing their crystallinity levels closer to those in the

centre of the laminate [28]. In addition, given that the lay-up process for the samples spanned several hours, the majority of the laminate would be kept above the glass transition temperature of the material. This would facilitate relatively uniform cool rates and thus crystallisation levels, at least for a portion of the thermal profile. Although it was not possible to measure the exact crystallinity gradient through the samples, work from collaborators has shown that the average crystallinity of samples increased from 17% to an optimal 35%, when using a 280 °C heated tool compared to an unheated tool [14, 29]. For this reason, using a heated tool can be described as a form of thermal treatment, with the effect of increasing sample crystallinity and with the expected effect of reducing the magnitude of crystallinity gradients. Further work is required in order to precisely quantify the crystallinity gradients within tape-laid CF/PEEK laminates.

The CT scans were carried out using a Phoenix M nano/microtom at a scan resolution of 33 μm. The X-ray gun was rated at 180 kV, with scans being carried out at 160 kV and 28 μA, giving a scan power of 4.5 W. A total of 1,000 images were generated for each scan over a 360° field of view, for a total scan time of 67 minutes. The tomographical reconstruction was carried out using Davos software, whilst volume rendering was completed using VGStudio MAX 2.2. Fig. 6.1 shows a rendered CT scan of voids in the UD1 specimen and a 34 mm × 27 mm section of the hoop specimen.
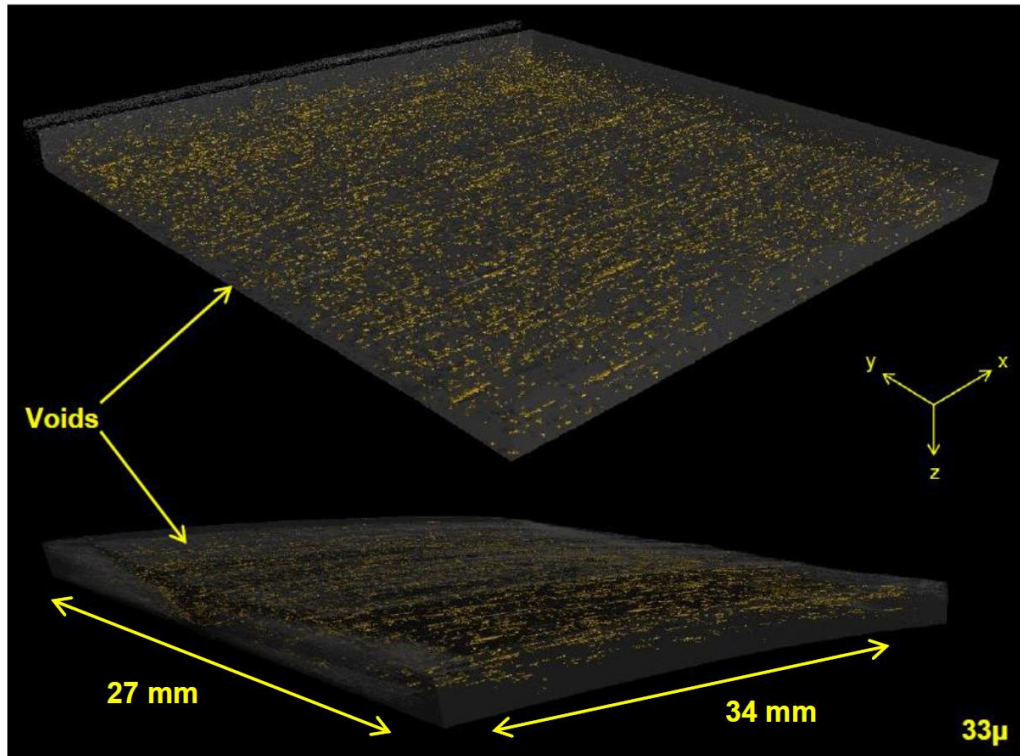
Figure 6.1 3-D X-ray-CT scan of voids present in tape-laid UD1 (top) and hoop CF/PEEK specimens (bottom). (Where the x direction is the fibre direction, y is transverse to the fibre direction and z is the thickness direction).

Complete characterisation of individual void morphology and total void volume content within the scan area is possible using this technique. Table 6.4 provides details of the average x, y and z dimensions of the voids ($\bar{x}$, $\bar{y}$, $\bar{z}$) and their respective standard deviations ($\sigma(x)$, $\sigma(y)$, $\sigma(z)$) for each specimen type as measured using the volume-rendering software. The total void volume as a percentage of the specimen volume is also provided.

Table 6.4 Mean and standard deviation of the x, y and z dimensions of voids in unidirectional (UD1, UD2), hoop and quasi-isotropic (QI1, QI2) tape-laid CF/PEEK specimens measured using 3-D X-ray CT. Void volume content is also provided, where possible. *Indicates gaps included in void content.

Specimen	$\bar{x}$ (mm)	σ(x) (mm)	$\bar{y}$ (mm)	σ(y) (mm)	$\bar{z}$ (mm)	σ(z) (mm)	Void (%)
UD1	0.265	0.169	0.168	0.073	0.087	0.045	0.26
UD2	0.280	0.183	0.171	0.075	0.093	0.041	0.33
Hoop	0.244	0.185	0.193	0.131	0.098	0.066	0.22
QI1	0.281	0.208	0.196	0.161	0.083	0.039	0.69
QI2	0.264	0.143	0.190	0.150	0.086	0.079	N/A
QI2*	0.526	1.117	0.333	1.418	0.106	0.135	1.45

Although all specimens were found to have a void volume content below the 1.5% considered generally acceptable for aerospace components, they compared relatively poorly with similar autoclaved specimens which were found to have an order of magnitude lower void contents [30]. The unidirectional and hoop specimens were found to have lower void contents, likely due to the absence of air gaps, which are discussed in Section 6.2.3. As expected, the void geometry was found to be related to the laminate lay-up, with the largest dimension of the voids being aligned with the fibre direction (x) and the smallest dimension being in the thickness direction (z). This trend also carried through to the computed standard deviations of the void dimensions. The specimen QI2 was found to have a particularily high void content due to a large number of gaps being present, which in turn skewed the measured void morphology. A more detailed overview of void morphology for the UD1 and QI1 specimens is provided in Fig. 6.2. Fig. 6.2 (a) and (b), which show the distribution of void volumes within the specimens. The vast majority of voids have a volume of less than 0.05 mm^3, although a large proportion of the total void volume is contained within a minority of large voids. This is particularily true for the QI1 specimen, where less than 10% of voids account for 64% of the total void volume. Fig. 6.2 (c) shows the relationship between void sphericity and void radius, where sphericity is defined as the ratio between the surface of a sphere with the same volume as the defect and the surface of the defect. Smaller voids tend to be more spherical while

larger voids are more elongated and elliptical. It should be noted that inclusion content for all specimens was found to be negligible.
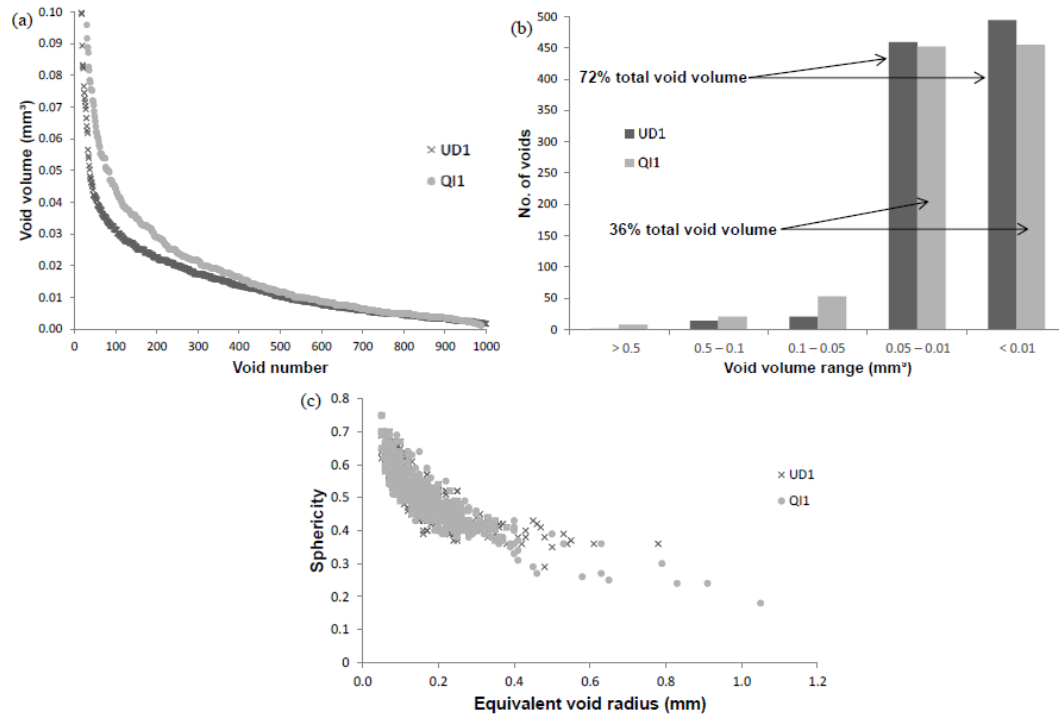

Figure 6.2 (a) Distribution of void volumes below 0.1 mm³ arranged from highest to lowest measured using 3-D X-ray CT for tape-laid unidirectional (UD1) and quasi-isotropic CF/PEEK specimens (QI1). (b) Bar chart showing the frequency of voids within a given volume range. (c) Relationship between the sphericity and the equivalent radius of voids from specimens UD1 and QI1.

6.2.3 Microcracking and gaps

The specimens were also examined for the presence of microcracks and gaps, which can arise due to processing. One side of each of the UD and QI specimens was polished to facilitate optical examination under a microscope. No microcracks or gaps were observed in the UD specimens. In total, three surface microcracks were detected in the quasi-isotropic specimens: one in QI1 and two in QI2. Although the presence of microcracking post-processing is undesirable for cryo-tank applications, given the minor level of damage present and its location on the surface of the specimens, the effect on the structural integrity of a tank would be negligible.

6. Damage and permeability in tape-laid thermoplastic composite cryogenic tanks

However, due to the novelty of the tape-laying process and material, further refinement of the processing technique is required in order to produce aero-space quality components. Six gaps were detected in the QI1 specimen and seven in the QI2 specimen, with QI2 containing several notably wide gaps, as can be seen in Fig. 6.3. The QI1 and QI2 specimens were also exposed to a single cryogenic cycle via immersion in liquid nitrogen (LN2) from -196 °C to 40 °C in order to examine the resulting damage formation and its implications for laminate permeability.
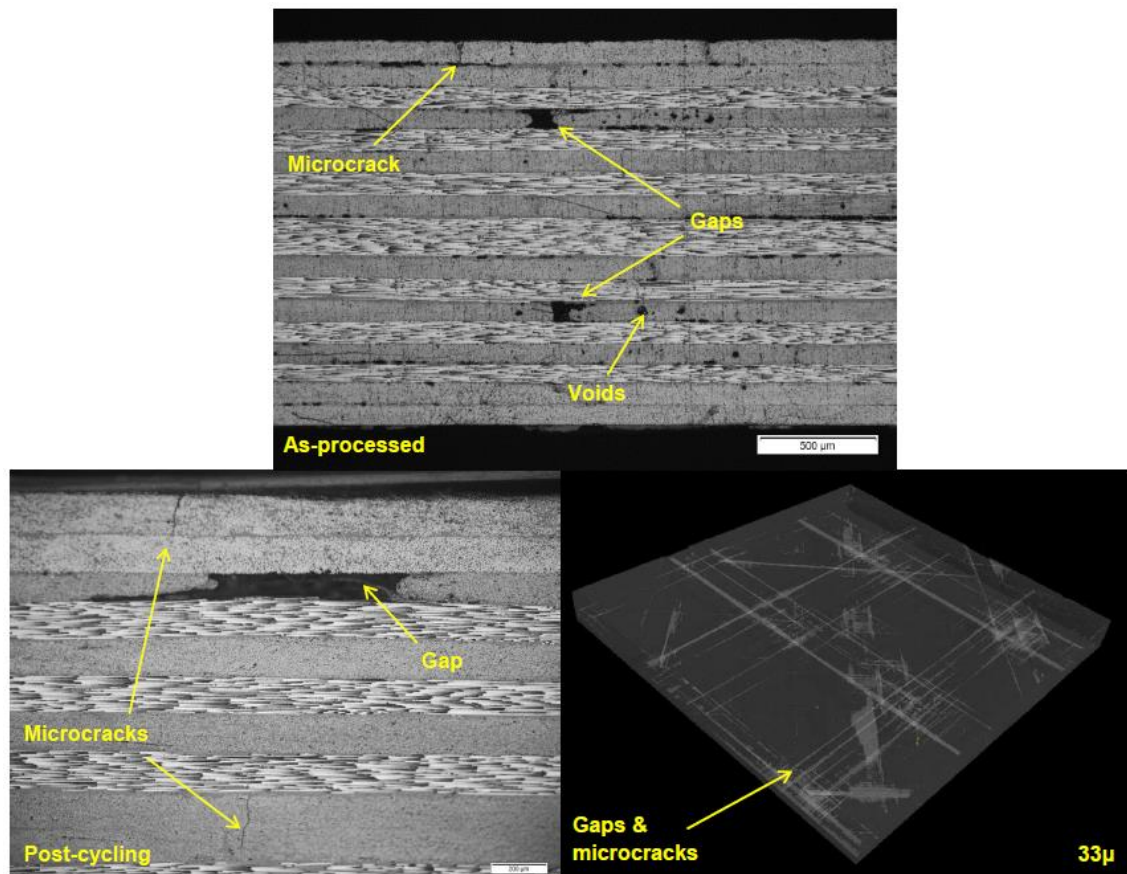
Figure 6.3 An optical micrograph of gaps, a surface microcrack and voids in the tape-laid CF/PEEK specimen QI2, as processed (top), a micrograph of a gap and two transverse microcracks present in specimen QI2 after exposure to a single cryogenic cycle (left) and rendered 3-D X-ray CT scan of microcracking and gaps in the same specimen (right).

Moderate damage accumulation was observed post-cycling with transverse microcracks forming in the outer and central plies as shown in Fig. 6.4 (a), although the presence of through-thickness crack networks was not obvious. However, the

location of gaps in otherwise un-damaged plies led to a reduction in the number of pristine barrier plies, with the consequence of decreased resistance to leakage if the material was used for a cryo-tank. The average crack opening displacement (COD) of transverse microcracks is shown in Fig. 6.4 (b). The COD measurements were made from optical micrographs of the specimens by taking the distance between the surfaces of an open microcrack. As such, COD is a measure of the degree of opening of a microcrack, with the implication that microcracks with larger COD values would permit greater fluid leak rates through a damaged ply and laminate. The COD values were found to be relatively low when compared to previous work [30]. This is due to the constantly varying ply orientation and lack of ply blocking. Although the likelihood of through-thickness crack networks forming in the laminates is greatly increased by the presence of gaps, which themselves can be over 100 times the width of microcracks, their presence can be significantly reduced by appropriate adjustment of the tape placement width. It should be noted that no gaps were observed in the unidirectional specimens. The constantly varying ply angle in the quasi-isotropic specimens likely contributed to the gaps remaining unfilled during processing, due to the fibres acting as a bridge across the gaps.
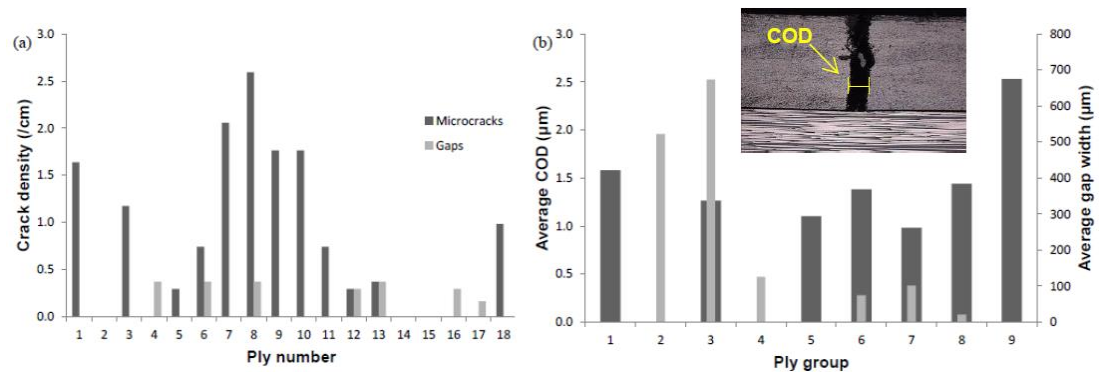

Figure 6.4 (a) Ply level microcracking detected using micrographs of QI1 and QI2 after cryogenic cycling. Gaps are also included. (b) Crack opening displacement and gap width measurement from cycled specimens. Ply groups 1 - 9 refer to symmetric ply pairs i.e. ply group 1 comprises the outer 45° plies.

6.3 Cryo-tank modelling

6.3.1 Tank design

Aside from external launch and structural loads, the primary design considerations for cryo-tanks for space applications are temperature and pressure based. Unlike conventional composite overwrapped pressure vessels (COPVs), which require a liner to prevent fluid leakage [31], linerless composite tanks must remain impermeable without the presence of additional barrier materials. Additionally, due to the large temperature difference between processing temperatures and the cryogenic fuel, thermal loading is the dominant load form. Internal tank pressure is generally far below the levels that typical COPV designs can tolerate. For this reason, mitigation of thermal stress is seen as a key design requirement for linerless cryo-tanks.

In this work, a design for a scaled-down version of a cryo-tank for a RLV is presented. The tank has a 500 mm diameter and holds approximately 90 litres of cryogen. A symmetric 20-ply lay-up, giving a wall thickness of 2.8 mm, is used. This is in order to ensure structural integrity at a maximum expected operating pressure of 10 bar. Both material processing and tank fuelling are represented by a two-stage thermal load as shown in Fig. 6.5, with an internal pressure ramp load being applied from the start of the fuelling profile. The processing profile is included due to the residual stress formation which can occur in thermoplastic laminates from the SFT to ambient temperature. The temperature dependant material properties shown in Table 6.3 are used in conjunction with the full thermo-mechanical load profile described in Fig. 6.5 as inputs for subsequent numerical simulations. For damage simulations, material strength and toughness data are not available above the glass transition temperature of CF/PEEK. No notable damage formation is expected above this temperature.

Different convection coefficients (h) are used to simulate the rate of cooling for each stage. It should be noted that the thermal boundary conditions applied for the numerical simulations do not account for the ply-by-ply lay-up process. Convective heat transfer is assumed to occur from both the outer and inner surfaces of the tank simultaneously for the processing portion of the profile, from the stress free

temperature to ambient temperature, as shown in Fig. 6.5. This approach is justified by the following points:

- An applicable, comprehensive thermal profile for the ply-by-ply lay-up process for the cryo-tank is not available. Given the myriad contributing factors of the process including the lay-down speed, roller pressure, laser power, tool temperature and target temperature, formulating an accurate thermal profile remains a highly complex task [12, 32] and beyond the scope of this work.

- A complete set of temperature dependant thermo-mechanical properties for the tape-laid CF/PEEK material, ranging from the stress free temperature to ambient temperature, is not available at present. The absence of this data further compounds uncertainties relating to the processing conditions in determining an accurate thermal profile for the lay-up process.

- The use of a relatively high tool temperature of 280 °C will contribute to a more uniform thermal profile within the laminate during processing and cool-down. This means that a significant proportion of the processing temperature profile will comprise a steady cooling phase, similar to that of autoclave processing to an extent.

- While using a simplified thermal profile for the processing portion of the loading can alter the detail of damage formation within the tank, its effect is deemed negligible for this application. As observed in experimental test specimens and predicted by numerical simulations, the bulk of damage formation occurs within the fuelling (i.e. cryogenic) thermal profile.

For these reasons, a simplified thermal profile, resembling autoclave processing, was used in numerical simulations. For the cryogenic portion of the load profile, convective heat transfer is assumed to occur from the inner surface of the tank wall, leading to thermal gradients within the structure.
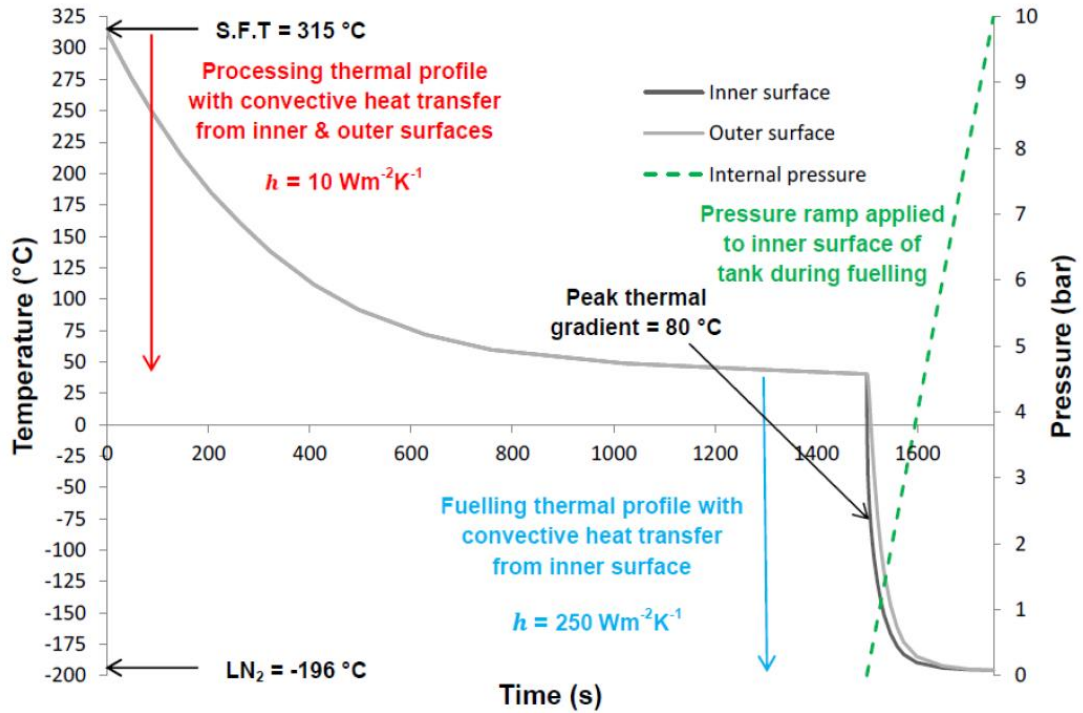
Figure 6.5 The thermo-mechanical load profile used as input for numerical simulations. A two-stage thermal load is applied, accounting for both the processing and fuelling of the tank. An internal pressure ramp load is applied to the inner surface of the tank during the fuelling profile.

The design of the tank lay-up is key to preventing damage formation and leakage. Assuming a leak-before-burst criterion focused on the cylindrical portion of the tank (Fig. 6.6), the following steps were adopted in designing the general stacking sequence:

1. Limiting of thermal stress is prioritised due to the large temperature change. Therefore ply-angle variation is minimised throughout the lay-up. A unidirectional lay-up is most suited for the reduction of laminate level thermal stress, but is not practical for resisting internal pressurisation loads.

2. For an internally-pressurised tank with closed ends, the nominal hoop stress is twice the axial stress. Therefore an optimal unidirectional lay-up should have the fibres orientated in the hoop direction.

3. The axial stress due to internal pressure then becomes the limiting design failure issue due to the possibility of transverse failure of the hoop-orientated plies.

4. This axial stress is reduced by rotating the angles of specific hoop plies towards the axial direction. This must be designed to also balance with increasing thermal stresses due to the increasing ply-angle variation.
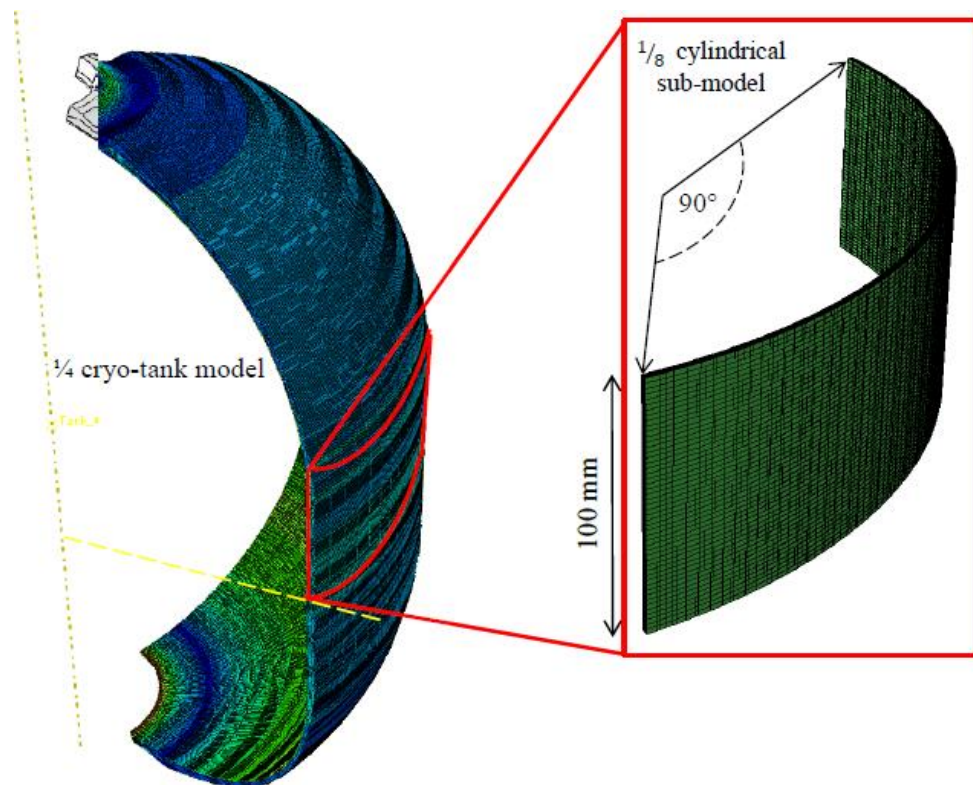

Figure 6.6 Schematic showing the location of the cylindrical sub-model in relation to the full cryo-tank. Tank design is focused on this sub-region.

6. Damage and permeability in tape-laid thermoplastic composite cryogenic tanks

The wound composite modeller (WCM) [33], a plugin for Abaqus FEA software, was used to rapidly test prospective lay-ups based on the latter design steps. As is the case with conventional filament winding methods, plies were grouped in opposing pairs according to the following general lay-up: $[90°_2/\pm\theta°/\pm\theta°/90°_2/\pm\theta°_2]_S$. Fig. 6.7 shows the predicted stress distributions transverse to the fibre direction through the cylindrical portion of the tank wall for several lay-up iterations at maximum expected operating loads.
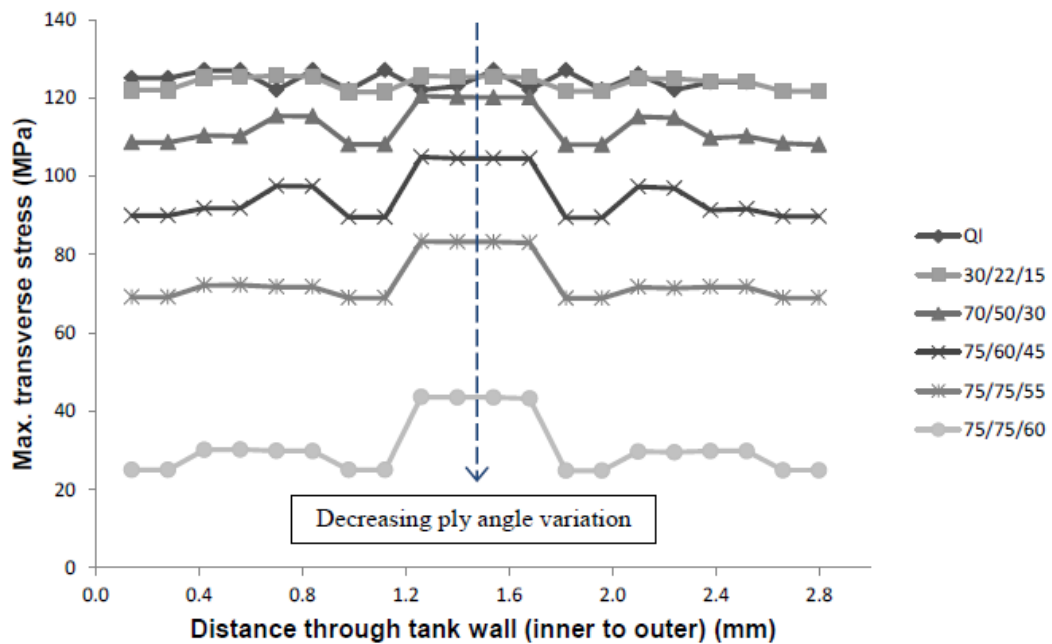
Figure 6.7 Transverse stress distributions through the cylindrical portion of the tank wall for several lay-up variations under the loading described in Fig. 6.5. The numbers in the legend refer to the angles $\pm\,\boldsymbol{\theta}°$ in the general 20-ply lay-up $[90°_2/\pm\theta°/\pm\theta°/90°_2/\pm\theta°_2]_S$. QI refers to the test specimen lay-up $[45°/-45°/90°/0°/90°/0°/90°/0°/90°]_S$.

Ensuring that the transverse tensile strength of the composite is not exceeded is an important factor in limiting matrix microcracking and hence leakage. Fig. 6.7 shows a clear trend in the relationship between decreasing ply angle variation and decreasing peak transverse stress. Conventional COPV lay-ups using a mixture of hoop and low-angle helical plies (plies between 5° and 30°) are shown to be unsuitable for the unique demands of cryogenic fuel storage, where the minimisation of thermal stress is critical. As the $[90°_2/\pm75°/\pm75°/90°_2/\pm60°_2]_S$ lay-up was the only stacking sequence in which the transverse strength of the composite was not

193

exceeded in every ply, it was selected for more in-depth analysis via the damage sub-model outlined below in Section 6.3.2. It should be noted that for certain conventional filament winding methods, such a high-angle helical lay-up would not enable full coverage of the polar boss regions around the ends of the tank. Additional reinforcement in the form of pre-fabricated doilies [1, 34] would be required at the polar bosses in order to ensure continuation of the desired lay-up from the cylindrical section to the dome section of the tank.

6.3.2 Combined XFEM-SCZM damage method

A combined XFEM (extended finite element method) and SCZM (surface cohesive zone model) approach to damage modelling in composite laminates is developed here. Modelling is focused on the meso-scale, with XFEM being used for microcrack initiation and propagation (intra-laminar failure) and SCZM for mixed-mode delamination growth between plies (inter-laminar failure). This methodology allows the discrete modelling of microcracks and hence prediction of laminate permeability. It is also applicable to relatively large-scale structures such as cryo-tanks (Fig. 6.8). The general XFEM-SCZM approach is implemented within an adapted form of the general purpose, non-linear finite element code, *Abaqus v6.14*, as is described in detail in previous work [35, 36].

Damage sub-model
$^1/_8$ cylindrical section
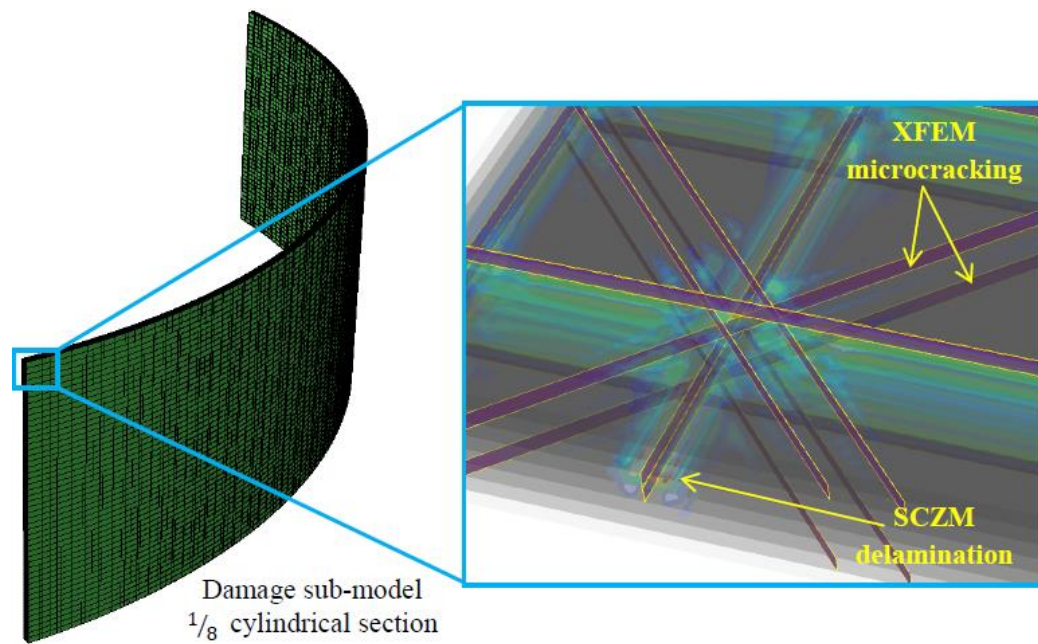
Figure 6.8 The combined XFEM-SCZM method facilitates prediction of microcracking and delamination in large scale structures such as the cylindrical sub-model of the cryo-tank shown above.

However, due to the complex thermo-mechanical load state present in the cryo-tank, the original method [36] has been improved here to incorporate a more sophisticated mixed-mode compression-shear matrix failure criterion. Oblique fracture planes aligned with the fibre angle are now permitted, along with the usual transverse microcracking perpendicular to the ply interface. However, transverse microcracking remains the dominant damage mode for these loading conditions and the main contributor to laminate permeability given the tendency of these cracks to open due to tensile loading. Fig. 6.9 illustrates the main matrix failure modes modelled using XFEM for an assumed two-element model.
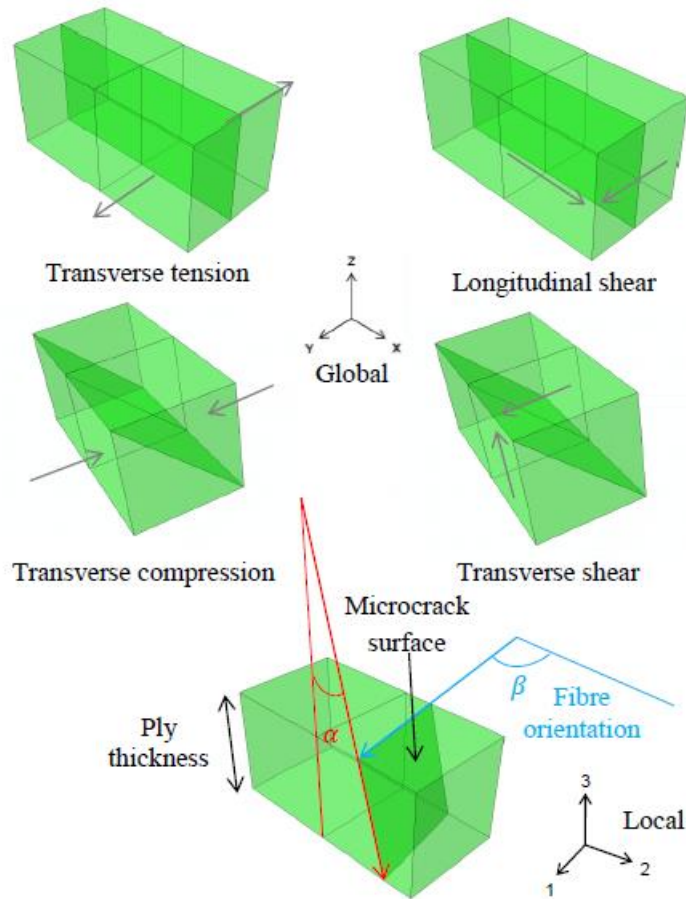
Figure 6.9 Schematic showing the microcrack morphology related to tensile, compressive and shear loading in a two-element model. Oblique fracture planes are orientated at a prescribed angle **α** (i.e 54° for transverse compression) and are parallel to the ply fibre angle **β**.

This enhancement is implemented through a user defined damage initiation sub-routine (UDMGINI) [37] within the general XFEM framework. A crack is assumed to initiate when the relevant fracture criterion, f, is exceeded, where f_t is the tensile failure criterion and f_c is the compressive failure criterion. This criterion is based on the Hashin failure criteria [38] for matrix failure:

- For tensile matrix failure ($\sigma_{22} + \sigma_{33} > 0$), $f_t \geq 1 =$ failure

$$f_t = \frac{(\sigma_{22} + \sigma_{33})^2}{Y_T^2} + \frac{\sigma_{23}^2 - \sigma_{22}\sigma_{33}}{S_{23}^2} + \frac{\sigma_{12}^2 + \sigma_{13}^2}{S_{12}^2} \qquad (6.1)$$

- For compressive matrix failure ($\sigma_{22} + \sigma_{33} < 0$), $f_c \geq 1 = $ failure

$$f_c = \left[\left(\frac{Y_C}{2S_{23}}\right)^2 - 1\right]\left(\frac{\sigma_{22} + \sigma_{33}}{Y_C}\right) + \frac{(\sigma_{22} + \sigma_{33})^2}{4S_{23}^2} + \frac{\sigma_{23}^2 - \sigma_{22}\sigma_{33}}{S_{23}^2} + \frac{\sigma_{12}^2 + \sigma_{13}^2}{S_{12}^2}$$

(6.2)

where σ and associated subscripts refer to conventional transverse tensile, compressive or shear stress in the local coordinate system. Y_T and Y_c are the tensile and compressive strengths of the matrix and S and associated subscripts are the shear strengths of the matrix. Depending on the failure mode, the angle of the fracture plane, denoted as α in Fig. 6.9, can also be pre-defined and will align parallel to the local '1' or fibre direction, which is at an angle β to the global 'x' direction. This capability has been included in order to capture the general trends in crack morphology observed for different load combinations. The temperature dependent material data shown in Table 6.3 are used as inputs for the combined XFEM-SCZM damage models. The TTS and TCS values in Table 6.3 correspond to the Y_T and Y_c values, respectively, in the Hashin criteria. The IPSS values in Table 6.3 are used to account for each of the shear strengths of the matrix, S in the Hashin criteria. This generalisation was made due to a lack of detailed multi-directional strength data for tape-laid CF/PEEK. The ILSS value is used for inter-laminar damage initiation in the SCZM portion of the damage simulations.

6.3.3 Microcrack initiation

Two distinct methods of simulating random microcrack initiation within the cryo-tank, based on methods outlined in [36], are used. These methods have been adapted for use with the tape-laid CF/PEEK material described in Section 6.2. The first approach is based on the inherent random distribution of the material fracture strength in the form of a continuous probability Weibull distribution, which is volume-adjusted to account for the size effects associated with mesh density of the FE damage models. The two properties required to generate a fracture strength distribution for a given material using this method are the mean fracture strength of the material, $\bar{\sigma}_0$, and a Weibull modulus, m. The transverse tensile strength of the

tape-laid CF/PEEK was taken here as the mean fracture strength, which is identified as 41 MPa at ambient temperature. Due to the lack of experimental data in the literature on the material, an inverse identification procedure was adopted to estimate the Weibull modulus of the material. Based on the tensile test geometry described in [36], successive tensile test simulations were performed, iteratively adjusting the Weibull modulus for a prescribed strength distribution until the predicted average bulk transverse stress at failure matched the measured value of 41 MPa. Fig. 6.10 (a) shows the resulting Weibull fracture strength distribution based on the identified m value of 3.5 for 5,000 elements in an FE mesh. Note that a limited distribution is used in simulations in order to prevent any element from having a transverse strength above 100 MPa, taken as the upper limit of physically realistic values.
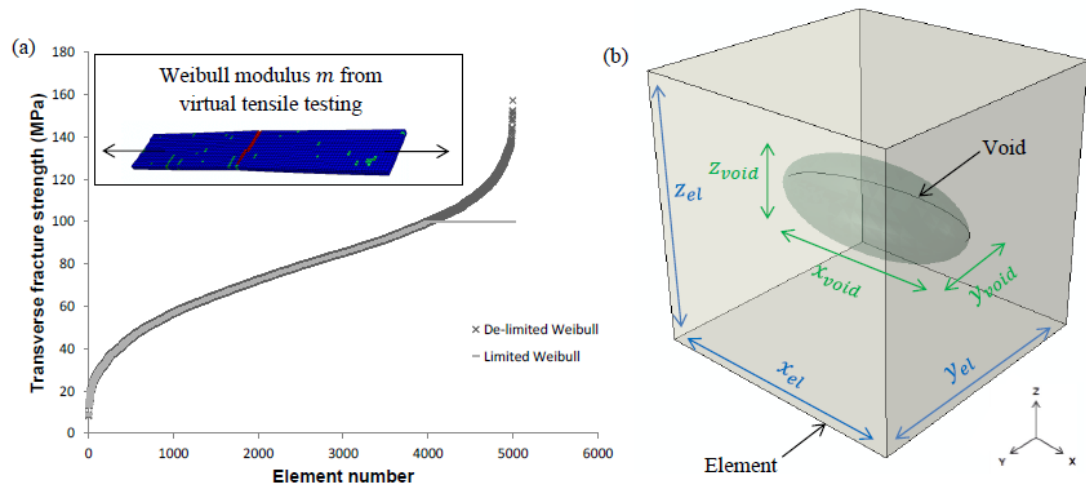
Figure 6.10 (a) De-limited and limited Weibull distributions used in modelling. The element fracture strengths are ordered smallest to largest. (b) Schematic of an air void within an element. The reduction in element stiffness is based on the dimensions of the void as measured using 3-D X-ray CT and forms the basis of the direct defect method.

The second approach is based on a general elemental representation of defects whereby voids are represented via reduced element stiffness throughout the finite element mesh [36]. The purpose of this is to simulate the local inhomogeneity in stiffness within the composite material due to the presence of randomly distributed defects. Voids can be idealised as ellipsoids within an element volume (Fig. 6.10 (b)), whose x_{void}, y_{void}, and z_{void} dimensions are based on a random Gaussian

distribution around the average measured void dimensions $\bar{x}$, $\bar{y}$ and $\bar{z}$ of Table 6.4. The voids are randomly distributed throughout the mesh in the finite element model, with one void being assigned to each element. The void dimensions are normalised with respect to the element dimensions x_{el}, y_{el} and z_{el} as follows:

$$x = \frac{x_{void}}{x_{el}} \tag{6.3}$$

$$y = \frac{y_{void}}{y_{el}} \tag{6.4}$$

$$z = \frac{z_{void}}{z_{el}} \tag{6.5}$$

with appropriate element dimensions being selected for the model mesh to ensure that each of x, y, and z are < 1. The voids act to reduce element stiffness in accordance with the following:

$$E_1^* = \left(1 - \frac{\pi y z}{4}\right) E_1 \tag{6.6}$$

$$E_2^* = \left(1 - \frac{\pi x z}{4}\right) E_2 \tag{6.7}$$

$$E_3^* = \left(1 - \frac{\pi x y}{4}\right) E_3 \tag{6.8}$$

where E_i^* is the reduced element stiffness, E_1 is the fibre direction modulus and E_2, E_3 are the transverse moduli. The reduction in stiffness in a given direction is therefore proportional to the maximum cross-sectional area of the void as viewed from that direction [36] i.e. the 2-D ellipse area. The shear moduli are set to be reduced as follows: G_{12} is reduced in proportion to E_3^*, G_{13} in proportion to E_1^* and G_{23} in proportion to E_2^*. This simplified approach is intended to simulate, with minimal computational expense, the general effects of void geometry on composite material stiffness [39], using experimentally measured data as input. The reader is directed to [39, 40] for more detailed and precise studies which attempt to predict the exact effects of void geometry on the elastic constants of composite materials.

6.3.4 Tank damage and permeability

The damage sub-model consists of $^{1}/_{8}$ th of the cylindrical portion of the cryo-tank, which corresponds to a section 100 mm wide as shown in Fig. 6.6. Symmetry boundary conditions are used to constrain the sub-model and to ensure accurate response in relation to the full cryo-tank. The temperature dependant material properties shown in Table 6.3 along with the full thermo-mechanical load profile described in Fig. 6.5 are used as inputs for the simulations. Although the lay-up consists of 20 plies, only 15 distinct plies are required due to ply pairing e.g. combining two adjacent 90° plies to form one thicker ply. A SCZM is defined between each ply. The mesh density for each ply was chosen to allow up to 5 microcracks per cm of cylinder width or circumference. This crack density corresponds to the maximum crack density observed in heavily damaged cryogenically cycled CF/PEEK laminates in [30]. Each model comprises 150,000 3-D solid elements, with simulations being performed on twenty-four 2.4GHz cores on a cluster based at the Irish Centre for High Performance Computing (ICHEC). Model run-times varied between 36 and 72 hours depending on the level of damage formation. Sequential thermo-mechanical analyses were required in order to model the transient thermal behaviour shown in Fig. 6.5.

Simulations were performed using the two different microcrack initiation methods described in Section 6.3.3. Volume-adjusted Weibull fracture strengths, generated using the Weibull modulus of 3.5, were randomly assigned to each element in the FE mesh. A number of the lay-ups of Fig. 6.7 were modelled using this method, as shown in Fig. 6.11.
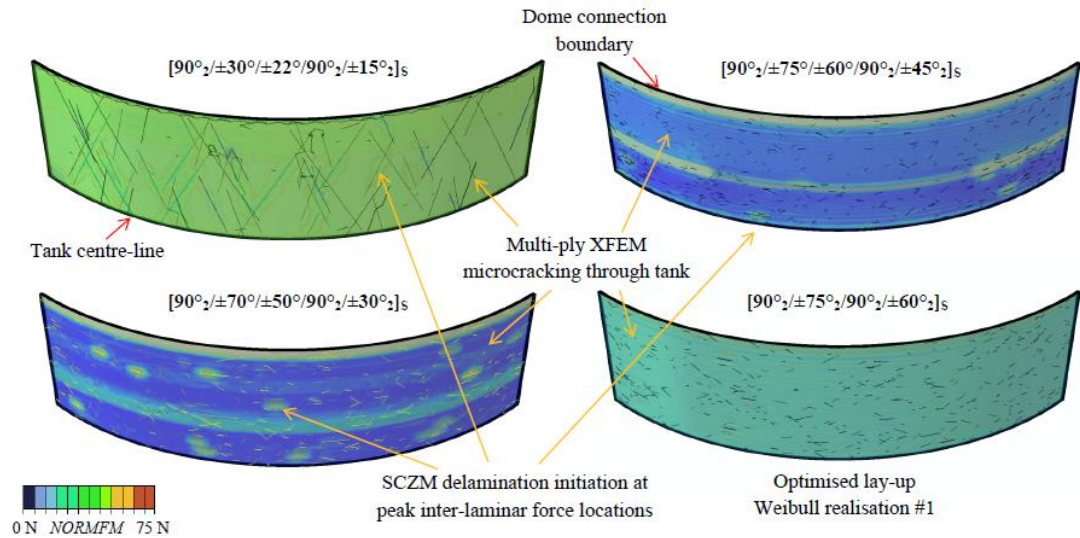
Figure 6.11 Comparison of through-thickness damage formation for all plies from the outer to the inner surface of the tank for several lay-ups showing XFEM microcracking and intensity of SCZM inter-laminar normal force magnitude (NORMFM).

In accordance with the transverse stress profiles in Fig. 6.7, significant microcracking was observed in the $[90°_2/\pm30°/\pm22°/90°_2/\pm15°_2]_S$ lay-up, with damage accumulation reaching such a level that the simulation was halted due to the estimated convergence time. The $[90°_2/\pm75°/\pm60°/90°_2/\pm45°_2]_S$ and $[90°_2/\pm70°/\pm50°/90°_2/\pm30°_2]_S$ lay-ups performed better, with less microcracking at equivalent loading. However damage reached an unacceptable level before the load step was complete. Delamination initiation areas can be seen in Fig. 6.11 for these simulations, at locations of peak inter-laminar forces, as predicted by the surface cohesive model. The $[90°_2/\pm75°_2/90°_2/\pm60°_2]_S$ lay-up achieved convergence promptly, with moderate levels of microcracking visible through the tank wall. In order to investigate damage formation in this lay-up, an additional four simulations were undertaken using the Weibull method (Fig. 6.12) and three using the direct defect method (i.e. for more random distributions of fracture strengths) (Fig. 6.13). The void dimensions from Table 6.4 for the QI2 specimen were used for the direct defect simulation, giving an average void content of between 1.45%, the highest measured by the 3-D X-ray CT analysis.
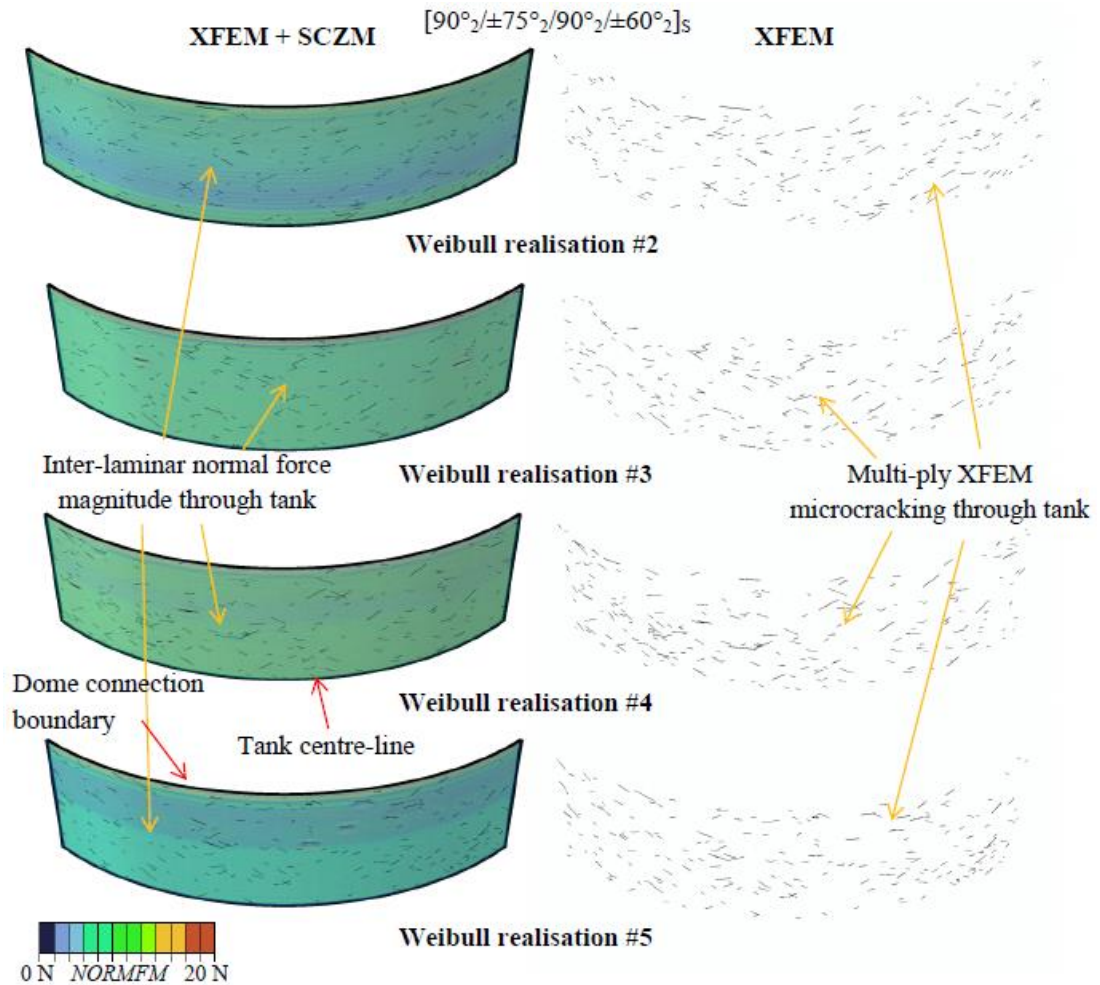
Figure 6.12 Through-thickness damage formation in all plies from the outer to the inner surface of the tank for the remaining realisations of the Weibull damage models for the optimised [90°₂/±75°₂/90°₂/±60°₂]s lay-up. The magnitude of the SCZM inter-laminar normal forces (NORMFM) and the discrete XFEM microcracking in isolation are shown for each realisation.
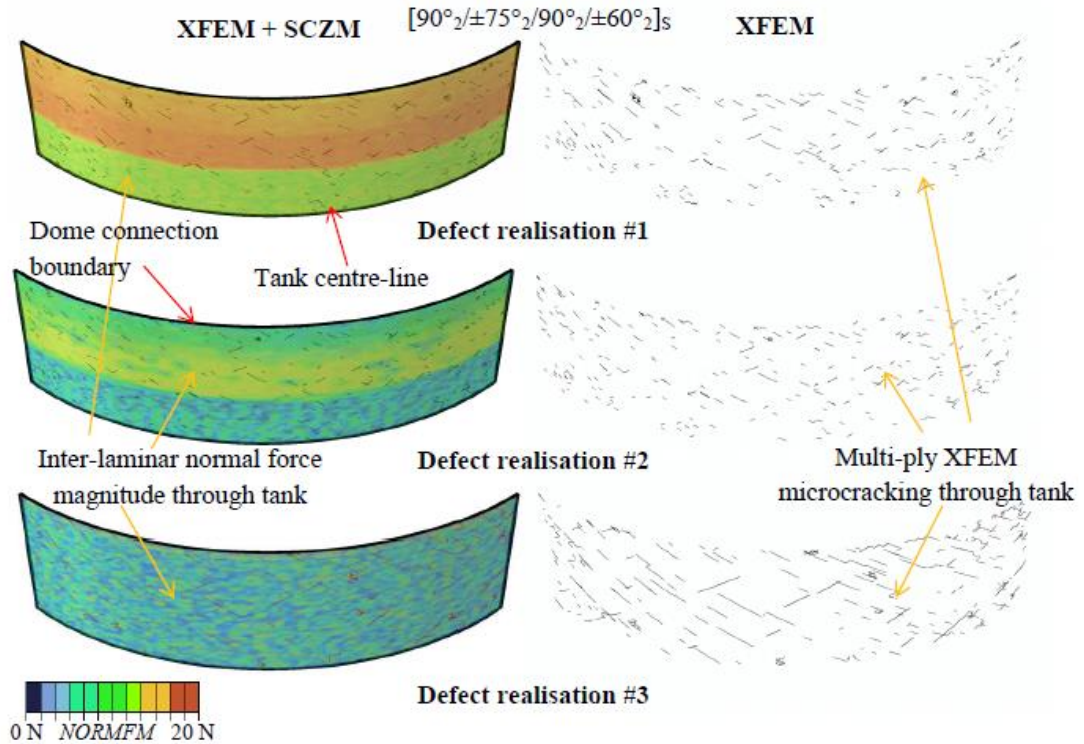
Figure 6.13 Through-thickness damage formation in all plies from the outer to the inner surface of the tank for the three realisations of the direct defect damage method, using the $[90°_2/\pm75°_2/90°_2/\pm60°_2]_s$ lay-up, each with an average void content of approximately 1.45%. The magnitude of the SCZM inter-laminar normal forces (NORMFM) and the discrete XFEM microcracking in isolation are shown for each realisation.

A qualitative analysis of the damage formation shown in Figs. 6.12 and 6.13 indicates consistent microcracking for each method within their respective sample set, with low-to-moderate damage levels visible in most plies. These figures show microcracking in all 20 plies through the thickness of the tank, from the outer surface to the inner surface. The accompanying contour plots provide a general overview of the resulting inter-laminar normal forces through the tank, given that it is not practical to display the individual plots for each ply interface. The range of these normal forces (0 N to 20 N) is significantly below those predicted for the alternate lay-ups (0 N to 75 N) in Fig. 6.11. This is due in part to the lower level of microcracking present in the optimised lay-up and the prevalence of large, open microcracks in the alternate lay-ups which can influence the inter-laminar cohesive zone. This leads to relatively uniform contour plots when compared with those in Fig. 6.11, with the exception of boundary effects at the dome connection area which

can induce minor inter-laminar force gradients. This effect can be seen in direct defect realisation #1 in Fig. 6.13. 3-D manipulation of these damage models allows a quantitative analysis of the average ply-by-ply crack density for each method, as given in Fig. 6.14. The variation in crack density for the Weibull method mirrors the transverse stress distribution for the lay-up shown in Fig. 6.7, with the centre $\pm 60°$ plies exhibiting the highest number of microcracks. It is also worth noting that the average crack densities of the plies on the inner surface of the tank were higher than their corresponding plies on the outer surface. Although microcracks initiated in every ply throughout the tank wall, the low crack density of the outer plies meant that no through-thickness crack networks were detected for any of the five Weibull simulations, implying negligible permeability for the design. Crack density values taken from the direct defect simulations show the same microcracking trend for the centre plies. However no microcracks were observed in the hoop or $\pm 75°$ plies. This was due to the void induced stress concentrations being of insufficient magnitude to initiate cracking in these plies, despite the maximum measured void content being used in the simulations. In this case, the Weibull method can be considered a more thorough approach to damage and permeability prediction.
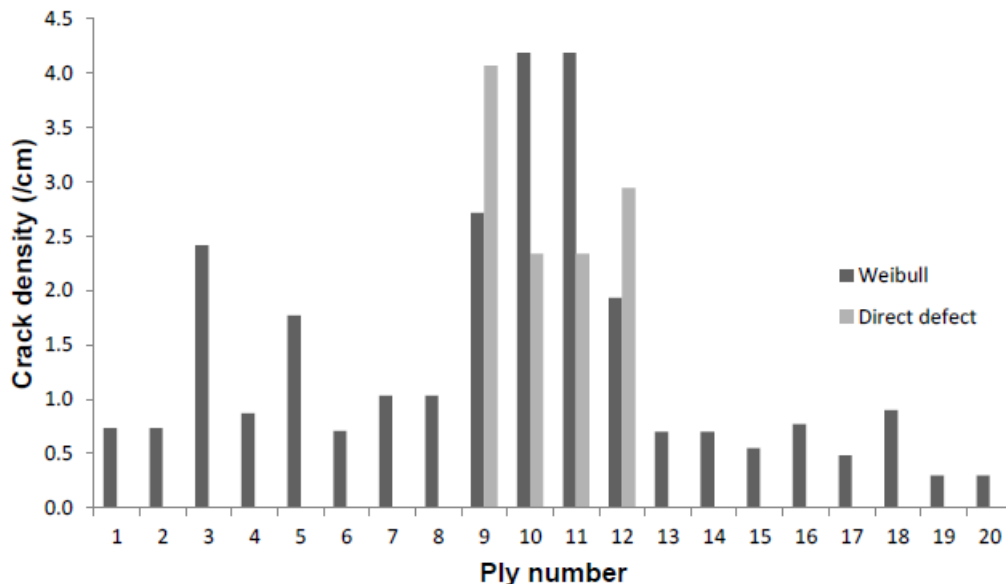

Figure 6.14 Comparison of average crack densities for each ply of the $[90°_2/\pm 75°_2/90°_2/\pm 60°_2]_S$ cryo-tank predicted by the Weibull and direct defects modelling methods. Ply 1 is on the inner surface of the tank.

6.4. Conclusions

A combined experimental and numerical method for the prediction of damage and permeability in internally pressurised linerless cryogenic tape-laid tanks is presented. A detailed characterisation of a tape–laid CF/PEEK material is presented, with temperature-dependant material properties covering the range from processing to cryogenic temperatures. Optical micrography and 3-D X-ray CT were used to investigate the defect content of the material as well as damage due to cryogenic cycling. Void content of the tape-laid material was found to be an order of magnitude higher than for comparable autoclave processed material, although similar trends in void morphology were observed. Transverse microcracks were also present throughout the test specimens post-cycling.

A detailed tank design, based on reducing the transverse stress throughout the tank wall, was developed. Unlike lay-ups typically used for COPVs, a combination of hoop and high-angle helical plies were found to be most efficient at reducing transverse stress levels due to combined thermo-mechanical loading. A sub-model of the cryo-tank was developed to predict intra- and inter-ply damage formation based on a novel XFEM-SCZM methodology. The material properties and defect distributions of the tape-laid material were used as inputs for the model. Two methods of modelling microcrack initiation were employed: a Weibull distribution of fracture strengths method and a void-based stiffness reduction method. Several lay-up variations were tested using the modelling technique. The optimised high-angle helical tank was shown to be least susceptible to through-thickness microcrack formation and hence cryogen leakage.

6.5 References

[1] Madhavi M., Rao K.V.J. & Rao K.N. Design and analysis of filament wound composite pressure vessel with integrated-end domes. *Defence Science Journal*, **59**(1), 73-81, 2009.

[2] Tam W.H., Griffin P.S. & Jackson A.C. Design and manufacture of a composite overwrapped pressurant tank assembly. 38th AIAA/ASME/SAE/ASEE Joint Propulsion Conference & Exhibit, Indiana, USA, 7-10th July, 2002.

[3] Kim E., Lee I. & Hwang T.K. Impact response and damage analysis of composite overwrapped pressure vessels. 52nd AIAA/ASME/ASCE/AHS/ASC Structures Dynamics and Materials Conference, Colorado, USA, 4-7th April, 2011.

[4] Mian H.H., Wang G., Dar U.A. & Zhang W. Optimization of composite materials system and lay-up to achieve minimum weight pressure vessel. *Applied Composite Materials*, **20**(5), 873-889, 2013.

[5] Grimsley B.W., Cano R.J., Norman J.J., Loos A.C. & McMahon W.M. Hybrid Composites for LH2 Fuel Tank Structure, NASA Langley Research Center, Virginia, USA, 2001.

[6] Ju J., Pickle B.D., Morgan R.J., & Reddy J.N. An initial and progressive failure analysis for cryogenic composite fuel tank design. *Journal of Composite Materials*, **41**(21), 2545-2568, 2007.

[7] Kang S., Kim M., Park S., Kim C. & Kong C. Damage analysis of a type 3 cryogenic propellant tank after LN_2 storage test. *Journal of Composite Materials*, **42**(10), 975-992, 2008.

[8] Sonmez F.O., Hahn H.T. & Akbulut M. Analysis of process-induced residual stresses in tape placement. *Journal of Thermoplastic Composite Materials*, **15**(6), 525-544, 2002.

[9] Croft K., Lessard L., Pasini D., Hojjati M., Chen J. & Yousefpour A. Experimental study of the effect of automated fiber placement induced defects on performance of composite laminates. *Composites Part A: Applied Science and Manufacturing*, **42**(5), 484-491, 2011.

[10] Aoki T., Ishikawa T., Kumazawa H. & Morino Y. Mechanical Behaviour of CF/Polymer Composite Laminates under Cryogenic Environment. Proceedings of the 12th International Conference on Composite Materials, Paris, France, 1997.

[11] Yoon H. & Takahashi K. Mode I interlaminar fracture toughness of commingled carbon fibre/PEEK composites. *Journal of Materials Science*, **28**(7), 1849-1855, 1993.

[12] Stokes-Griffin C. M., Matuszyk T. I., Compston p. & Cardew-Hall M.J.. Modelling the automated tape placement of thermoplastic composites with in-situ consolidation. *Sustainable Automotive Technologies*, 61-68, 2012.

[13] Kilroy J.P., Ó Brádaigh C.M. & Semprimoschnig C.O.A. Mechanical and physical evaluation of new carbon fibre/peek composites for space applications. S.A.M.P.E Journal, **44**(3), 22-34, 2008.

[14] Comer A.J., Ray D., Obande W.O., Jones D., Rosca I, O' Higgins R.M. & McCarthy M.A. Mechanical characterisation of carbon fibre–PEEK manufactured by laser-assisted automated-tape-placement and autoclave. *Composites Part A: Applied Science and Manufacturing*, **68**, 10-20, 2015.

[15] Jeronimidis G. & Parkyn A.T. Residual Stresses in Carbon Fibre-Thermoplastic Matrix Laminates. *Journal of Composite Materials*, **22**(5), 401-415, 1988.

[16] Kumazawa H. & Whitcomb J. Numerical Modelling of Gas Leakage through Damaged Composite Laminates. *Journal of Composite Materials*, **42**(16), 1619-1638, 2008.

[17] Bois C., Malenfant J.C., Wahl J.C. & Danis M. A multiscale damage and crack opening model for the prediction of flow path in laminated composite. *Composites Science and Technology*, **97**, 81-89, 2014.

[18] Kam T.Y., Liu Y.W. & Lee F.T. First-ply failure strength of laminated composite pressure vessels. *Composite Structures*, **38**(1-4), 65-70, 1997.

[19] Chang R.R. Experimental and theoretical analyses of first-ply failure of laminated composite pressure vessels. *Composite Structures*, **49**(2), 237-243, 2000.

[20] Mallick K., Cronin J., Ryan K., Arzberger S., Munshi N., Paul C. & Welsh J.S. An integrated systematic approach to linerless composite tank development. 46th AIAA/ASME/ASCE/AHS/ASC Structures, Structural Dynamics, and Materials Conference, Texas, USA, 18-21st April, 2005.

[21] Ryan K., Cronin J., Arzberger S., Mallick K., Munshi N., Yazdani F., Kallmeyer A., Arritt B. & Welsh J.S. Prediction of pressure cycle induced microcrack damage in linerless composite tanks. 47th AIAA/ASME/ASCE/AHS/ASC Structures, Structural Dynamics, and Materials Conference, Rhode Island, USA, 1-4th May, 2006.

[22] [3]Suprem Victrex IM7 , The Irish Centre for Composites Research (ICOMP), private communication, 2015.

[23] [1]Suprem Victrex AS4, [4]Suprem Victrex IM7, ÉireComposites Teo, private communication, 2012

[24] [2]Cytec APC-2/IM7, Cytec Engineered Materials. APC-2 PEEK Thermoplastic Polymer Technical Data Sheet. www.cytec.com, 2012.

[25] Wang C. & Sun C.T. Thermoelastic behaviour of PEEK thermoplastic composite during cooling from forming temperatures. *Journal of Composite Materials*, **31**(22), 2230-2248, 1997.

[26] Melo J.D.D & Radford D.W. Elastic properties of peek/IM7 related to temperature. Journal of Reinforced Plastics and Composites, 22(12), 1123-1139, 2003.

[27] Holmes S.T. & Gillespie J.W. Thermal analysis for resistance welding of large-scale thermoplastic composite joints. *Journal of Reinforced Plastics and Composites*, **12**(6), 723-736, 1993.

[28] Sonmez F.O. & Hahn H.T. Simulation of crystallization behaviour during thermoplastic tape placement process. Proceedings of ICCM-10, Whistler, Canada, August, 1995.

[29] Comer A., Hammond P., Ray D., Lyons J., Obande W., Jones D., O' Higgins R. & McCarthy M. Wedge peel interlaminar toughness of carbon-fibre/PEEK thermoplastic laminates manufactured by laser-assisted automated-tape-placement (LATP). SETEC 14 Conference, Tampere, Finland, September 10-11th, 2014.

[30] Grogan D.M., Leen S.B., Semprimoschnig C.O.A. & Ó Brádaigh C.M. Damage characterisation of cryogenically cycled carbon fibre/PEEK laminates. *Composites Part A: Applied Science and Manufacturing*, **66**, 237-250, 2014.

[31] Murray B.R., Leen S.B. & Ó Brádaigh C.M. Void distributions and permeability prediction for rotationally moulded polymers. *Proceedings of the Institution of Mechanical Engineers, Part L: Journal of Materials: Design and Applications*, 2014. DOI: 10.1177/1464420714525135.

[32] Stokes-Griffin C.M., Compston P., Matuszyk T.I. & Cardew-Hall M.J. Thermal modelling of the laser-assisted thermoplastic tape placement process. *Journal of Thermoplastic Composite Materials*, 1-18, 2013.

[33] Akula V.M.K & Schubert M.K. Analysis of debonding of filament wound composite pressure vessels. *Proceedings of the American Society of Composites – 28th Technical Conference*, 2013.

[34] Tam W., Hersh M. & Ballinger I. H. Hybrid propellant tanks for spacecraft and launch vehicles. 39th AIAA Propulsion Conference, Alabama, USA, 21st July, 2003.

[35] Grogan D.M., Leen S.B & Ó Brádaigh C.M. An XFEM-based methodology for fatigue delamination and permeability of composites. *Composite Structures*, **107**, 205-218, 2014.

[36] Grogan D.M., Ó Brádaigh C.M. & Leen S.B. A combined XFEM and cohesive zone model for composite laminate microcracking and permeability. *Composite Structures*, **120**, 246-261, 2015.

[37] Feerick E.M., Liu X. & McGarry P. Anisotropic mode-dependent damage of cortical bone using the extended finite element method (XFEM). *Journal of the Mechanical Behaviour of Biomedical Materials*, **20**, 77-89, 2013.

[38] Hashin Z. Failure criteria for unidirectional fiber composites. *Journal of Applied Mechanics*, **47**(2), 329-334, 1980.

[39] Huang H. & Talreja R. Effects of void geometry on elastic properties of unidirectional fiber reinforced composites. *Composites Science and Technology*, **65**(13), 1964-1981, 2005.

[40] Christensen R.M. Effective properties of composite materials containing voids. *Proceedings of the Royal Society of London A: Mathematical, Physical and Engineering Sciences*, **440**(1909), 1993.

7. Discussion and conclusions

7.1 Chapter summary

This chapter presents the main conclusions of the thesis. **Section** 7.2 summarises the research outcomes from the individual articles, as well as outlining the connection between the works. Ideas for future work are provided in **Section** 7.3 and overall conclusions for the work are given in **Section** 7.4.

7.2 Thesis overview

In order to significantly reduce launch costs, the next generation of reusable launch vehicles (RLVs) will require the adoption of novel weight-saving designs. The development of lightweight composite cryogenic fuel tanks for these vehicles is central to achieving this goal. Given the complexity and scale of these tanks, new experimentally validated numerical techniques are necessary in order to ensure safe and reliable designs. This thesis outlines a novel combined experimental and numerical approach to predicting composite laminate permeability with the aim of improving cryogenic tank design.

Existing methods of predicting composite laminate permeability rely on a unit cell approach based on pre-defined microcrack density and fixed delamination length. These analysis techniques have been constrained by a lack of experimental insight

into crack network and delamination formation, as well as a lack of flexibility due to the constraints of previously-utilised numerical methods. In Chapter 3, a novel extended finite element method (XFEM)-based methodology for the combined simulation and prediction of thermal fatigue delamination for identification of delaminated crack opening displacement (DCOD) and, hence, composite laminate permeability was presented. This method represents an important advancement in laminate permeability prediction, as it does not require the initial delamination to be pre-defined in terms of location or size. The need for continual re-meshing in order to capture crack propagation is also removed, significantly reducing computational cost and enhancing the scalability of the approach. The methodology was validated through simulation of standardised static and fatigue delamination tests and compared with experimental work and results from the literature. The method was also used to predict trends in the relationship between initial delamination length, crack growth behaviour and permeability. For short initial defect lengths, of the same order as ply thickness, high growth rates were predicted, whereas a distinct levelling-off in growth rate was predicted for longer initial delamination lengths. This suggests that interlaminar defects with dimensions of the same order as ply thickness are of greater concern with regard to crack growth rate for low cycle applications. It was shown that DCOD increases with delamination length for a given ply thickness. This has direct implications for gas leakage potential due to an increase in crack overlap area.

Novel, high-performance, thermoplastic composite materials such a CF/PEEK have not been investigated in-depth. Understanding and, hence, predicting the response of these materials to cryogenic conditions is crucial to the development of advanced analysis techniques. Chapter 4 describes detailed experimental testing to characterise damage formation in cryogenically cycled CF/PEEK laminates. A combination of optical microscopy and 3-D X-ray CT (computed tomography) was used to provide an insight into the interaction between transverse microcracking and delamination. This approach permitted observation of detailed networks of through-thickness cracks with a level of detail not previously achieved. The scope and complexity of these crack networks require full 3-D modelling to predict laminate permeability. The presence of defects such as voids were found to influence microcrack initiation

and growth. CT scans were used to quantitatively characterise void morphology and spatial distribution for modelling.

The important role of residual stress in damage formation was observed in thicker laminates, prior to cryogenic cycling, indicating significant stress build-up from the material processing temperature to room temperature. All damage formation, independent of laminate thickness or lay-up, was found to occur after the first cryogenic cycle, despite the laminates being exposed to over 50 thermal cycles. This has a significant impact on tank design using CF/PEEK in that fatigue loading associated with re-fuelling is not anticipated to be a significant factor in damage accumulation. As shown in Chapter 3, the predicted DCOD of transverse microcracks was found to increase with length of adjacent inter-ply delaminations. Large crack openings were observed in thicker laminates, particularly in the outer plies. Crack opening in inner and off-axis ply groups was found to be significantly less than in outer plies; this highlights the importance of these plies for limiting laminate permeability.

The experimental work of Chapter 4 highlighted the need for a 3-D permeability prediction methodology capable of simulating random microcrack initiation. To this end, Chapter 5 describes a novel computational methodology for predicting three-dimensional microcracking, delamination and permeability in composite laminates. This method represents a significant improvement over existing techniques which rely on repeating unit cell geometries and pre-defined crack locations and growth paths. The methodology combines the use of XFEM for random microcrack initiation with a cohesive zone model for delamination, allowing for the first time discrete damage modelling of through-thickness leak paths in multi-ply laminates. This facilitates direct computation of DCOD values and crack overlap areas for permeability prediction throughout the entire model space. Two distinct methods of simulating microcrack initiation due to the presence of defects were also introduced: the first based on a stochastic distribution of material fracture strengths and the other on the defect distribution measured in Chapter 4. These methods aim to directly link experimental observations with the modelling process for random crack nucleation. The methodology was used to predict damage and leak rates of laminates similar to those tested in Chapter 4. A qualitative comparison of the damage formation in the models and the X-ray CT scans of the specimens showed similar overlapping crack

patterns, with damage forming after a single cycle. A quantitative comparison of DCOD values through the thickness for the model and experimental specimens again matched closely. Measured leak-rates were also found to be within the range of experimental test data from ÉireComposites Teo.

To date, no detailed design of a linerless composite cryogenic fuel tank has been published, despite significant work in the area of composite overwrapped pressure vessels (COPVs). In Chapter 6, a combined experimental and numerical approach to the design and analysis of tape-laid composite cryogenic tanks was presented. Many of the experimental techniques introduced in Chapter 4 were used to characterise tape-laid CF/PEEK, a material which has received little attention in the literature. Void content for the tested laminates was found to be on average an order of magnitude higher than comparable autoclave specimens, in-part due to the presence of gaps in the laminates. The general production quality of the tape-laid laminates was also found to be lower, primarily due to the novelty and the complexity of the in-situ consolidation process. Transverse microcracking was again observed after a single cryogenic cycle. Measured defect distributions and temperature-dependant properties were used, in conjunction with an improved version of the numerical methodology outlined in Chapter 5, to predict damage formation and leakage in a large cryogenic fuel tank. An optimised tank design was presented which represented a significant step beyond conventional COPV design. A lay-up comprising hoop and high-angle helical plies was found to offer superior resistance to transverse stress build-up in the tank under cryogenic and internal pressure loading. This is important due to the increased likelihood of transverse microcracking with increased transverse stress. A damage sub-model for the optimised lay-up showed significantly improved performance over conventional lay-ups under estimated operating loads; the optimised lay-up was predicted to be free of through-thickness crack networks and, hence, leak paths. The methodology was also shown to be scalable to a previously unseen level for a meso-scale discrete damage prediction technique.

7.3 Future work

This work provides a framework for simulating meso-scale discrete damage in composite laminates for permeability prediction. Given the complexity and novelty of this area, significant research into both experimental and numerical methods is required to ensure the robustness and accuracy of the approach.

One of the main sources of potential inaccuracy in damage simulation is the material properties which are used as inputs. Modelling the material response from processing to cryogenic temperatures requires access to a vast range of temperature-dependant material properties. Although significant effort has been made in this work to accurately characterise the behaviour of CF/PEEK throughout the temperature ranges used in simulations, gaps exist in the data. The fracture behaviour of CF/PEEK, or even more common epoxy materials, remains understudied at cryogenic temperatures. Methods for predicting residual stress gradients in autoclaved laminates remain underdeveloped and practically non-existent for tape-laid laminates. This has serious implications for the accurate modelling of high-processing temperature thermoplastics such as CF/PEEK, where the magnitude of residual stress is seen as having a major effect on the damage accumulation in cryogenically cycled laminates. Experimental data relating to the permeability of CF/PEEK also remains sparse. It is envisaged that combining conventional leak tests with advanced non-destructive testing methods such as 3-D X-ray CT could lead to further calibration and validation of permeability predictions.

The combination of XFEM and cohesive zone modelling has been shown to offer a flexible and scalable approach to intra- and inter-laminar damage modelling for composites. However, the simplicity of the method somewhat compromises the accuracy of the solution. Research is ongoing into developing traction laws and cohesive zone models which are more capable of capturing the interaction between intra- and inter-laminar damage modes. Due to the scale of the structures being modelled, an approach comprising of a single element through the ply thickness, along with a single cohesive element is required to minimise computational time. An improved XFEM implementation for the damage models is also required. Significant convergence problems were encountered for high-damage simulations, often resulting from issues with XFEM crack surface determination. Although of minimal

importance to permeability predictions due to its catastrophic implications for the structure, XFEM fibre failure criteria could also be included in order to expand the utility of the methodology.

There have been very few studies on overwrapped or linerless cryogenic fuel tanks. This work has sought to outline an approach to the design and analysis of such structures, based on available data and materials. However, comprehensive experimental testing of actual scale model tanks, manufactured using tape-laid composites is required. The material, processing and loading complexities involved in such designs can only be fully addressed in this way.

7.4 Conclusions

The aim of this thesis was to understand and predict the damage and permeability of composite cryogenic tanks for the next generation of RLVs. A novel combined experimental and numerical approach was used to achieve this aim involving the testing, characterisation and modelling of composite laminates. This work has resulted in an improved understanding of cryogenic damage formation in composite materials and the development of a 3-D numerical methodology for predicting permeability of large composite structures. The main research outcomes are summarised below:

- The existing unit cell approach to laminate permeability prediction has been improved upon using a novel, experimentally-validated, XFEM-based approach. Delamination growth at crack openings can now be directly predicted rather than estimated from experimental data. In addition, the delamination initiation point and growth path are no longer required to be defined a-priori. This leads to more accurate permeability predictions using this method.

- Extensive experimental testing and characterisation of cryogenically-cycled laminates have improved understanding of through-thickness crack network formation, crack morphology, manufacturing defects, residual stress,

thickness effects and the role of material type and stacking sequence on damage formation.

- A novel 3-D combined XFEM-cohesive zone methodology has been developed, allowing discrete damage and permeability prediction of large structures including random microcracking. The method facilitates simulation of overlapping crack networks, DCOD and crack density, removing the constraints of the existing pre-defined unit cell approach.

- Based on experimental observations and numerical simulations, an optimised tape-laid cryogenic fuel tank design has been presented. The tank represents a significant departure from conventional composite pressure vessel design, with the reduction of thermally induced stress being the critical design criterion. Using the developed permeability prediction methodology, the design has been shown to predict cryogen leakage at maximum expected operating loads.

A. Appendices

A.1 Finite element implementation of the VCCT

In Chapter 3, the VCCT is used in conjunction with XFEM to model delamination in composites. The following describes the general VCCT implementation within the finite element mesh using a 2-D four-noded element at the crack tip, shown in Fig. 3.3 and A.1.
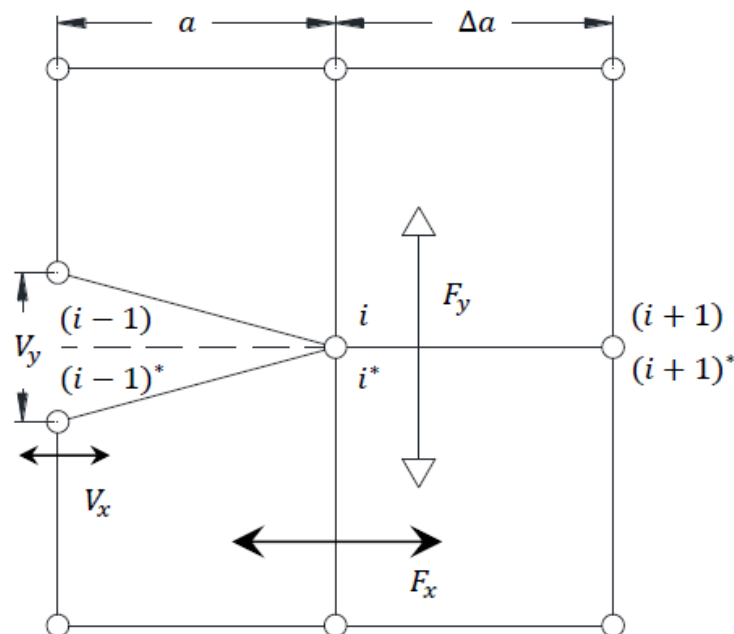

Figure A.1 Implementation of the VCCT for a four-noded element.

A. Appendices

The strain energy release rate at the crack tip is calculated as a function of the force at the tip and the COD. The relation for a Mode I crack growth situation is given by Eq. A.1 [1],

$$G_I = \frac{1}{2\Delta a}(F_y V_y) \tag{A.1}$$

where G_I is the Mode I energy release rate, Δa is the crack extension, F_y is the vertical force between nodes i and i^*, and V_y is the vertical displacement between nodes $(i-1)$ and $(i-1)^*$ as shown in Fig. A.1. The relation for a Mode II crack growth simulation is given by Eq. A.2 [1],

$$G_{II} = \frac{1}{2\Delta a}(F_x V_x) \tag{A.2}$$

where G_{II} is the Mode II energy release rate, Δa is the crack extension, F_x is the horizontal force between nodes i and i^*, and V_x is the horizontal displacement between nodes $(i-1)$ and $(i-1)^*$ as shown in Fig. A.1. The reader is directed to [1] for a more detailed treatment of the VCCT implementation within the finite element mesh. For a combination of normal and shear forces, such as in a mixed-mode loading case, then effective nodal separations are defined, based on the location of the crack surface. Within *Abaqus*, the effective separation, δ_m, is given by the following [2]:

$$\delta_m = \sqrt{\langle \delta_n \rangle^2 + \delta_s^2 + \delta_t^2} \tag{A.3}$$

where δ_n is the separation normal to the crack surface and δ_s and δ_t are the two shear separations along the crack surface. These separations are analogous to the aforementioned nodal separations described in Eqs. (A.1) and (A.2) and are used to describe the traction-separation behaviour of damaged elements in conjunction with the equivalent mixed-mode energy release rate described in Chapter 3.

A.2 DCB and ENF experimental data

Both the DCB and ENF experimental test data in Chapter 3 were generated by ÉireComposites Teo [3] for Suprem Victrex-150 AS4 CF/PEEK. The comparisons between the XFEM-generated data and experimental curves shown in Fig. 3.10 and Fig. 3.12 are based on mean material properties (including the G_{IC} and G_{IIC} fracture toughness values and the material elastic constants (Table 3.1)) and test specification dimensions (including specimen width, thickness and pre-crack length). The properties and dimensions of individual test specimens can vary and these natural variances can explain some of the differences between the XFEM model response and the experimental data. For instance, differences in the elastic moduli can influence the slope of the linear-elastic section of the curve. Differences in the initial pre-crack length can influence the peak loads at damage initiation. Variation of fracture toughness can lead to variations in crack propagation behaviour. For completeness, the full set of available experimental data is provided in the following graphs and tables for both the DCB and ENF tests.

Figure A.2 Load-displacement curve for the XFEM DCB model and six experimental DCB tests.

Table A.1 Available test specimen geometry and properties for each DCB test shown in Fig. A.2.

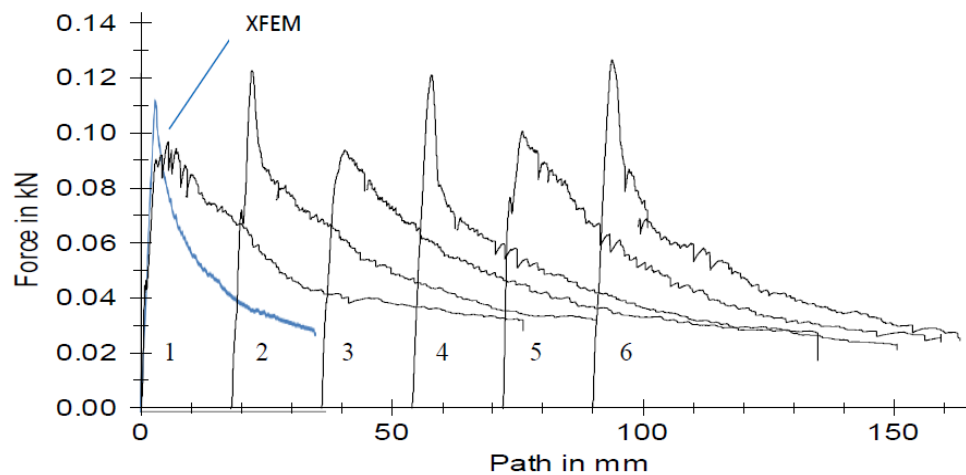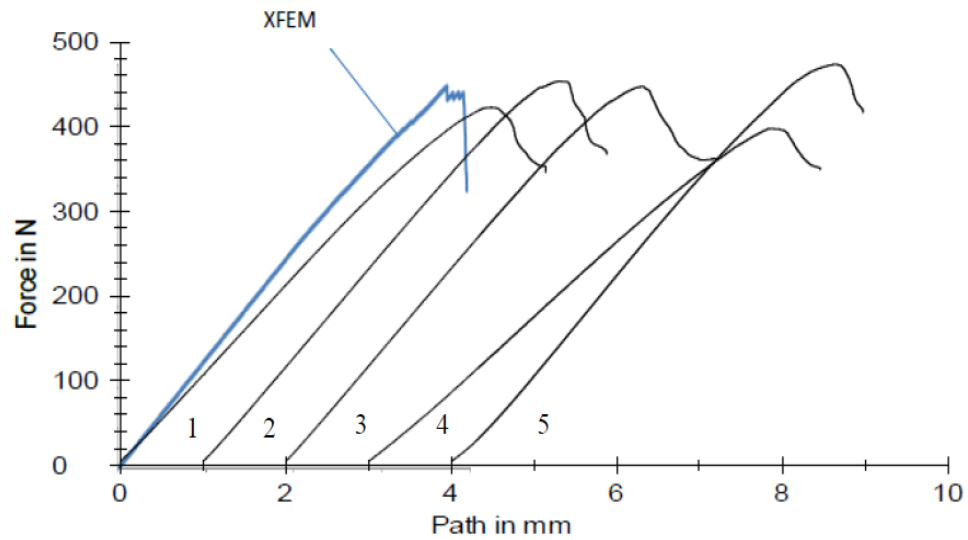| Specimen #	Thickness (mm)	Width (mm)	G_{IC} (jm^{-2})
XFEM	2.50	25.00	1062
1	2.40	25.01	1058
2	2.50	25.03	1144
3	2.48	24.75	1099
4	2.43	24.87	1017
5	2.52	24.92	1081
6	2.54	24.96	975

Figure A.3 Load-displacement curve for the XFEM ENF model and five experimental ENF tests.

Table A.2 Available test specimen geometry and properties for each DCB test shown in Fig. A.3.

Specimen #	P (N)	a (mm)	Thickness (mm)	Width (mm)	G_{IIC} (jm^{-2})
XFEM	410	35.00	2.50	25.00	999
1	375	35.83	2.50	25.02	821
2	432	35.11	2.46	24.95	979
3	430	35.40	2.45	24.75	1003
4	390	35.25	2.57	24.75	1079
5	455	35.13	2.54	24.96	1116

A.3 Mesh density and convergence controls

This appendix details the mesh density and convergence criteria used for numerical simulations in Chapter 3. The reader is directed to Krueger's extensive work on these topics [4], which was used as a basis for many of the mesh and convergence criteria used in this work.

A.3.1 Element type

2-D CPE4R plane strain elements were used for all simulations in Chapter 3. These elements are described as 4-node bilinear, reduced integration elements, with hourglass control [2]. The effect of element type on VCCT crack growth was investigated in detail by Krueger [4], with the CPE4 elements showing excellent agreement with established crack growth benchmark tests. Negligible differences in performance were predicted between plane strain and plane stress (CPS4) elements, although the plane strain elements exhibited a slightly more compliant behaviour.

A.3.2 Mesh density

For the VCCT, both the element crack tip length, Δa, and the number of elements through the ply thickness of the composite can influence the accuracy of crack

growth simulations. The technique itself is relatively robust, particularly for coarse meshes, although for meshes with a low element crack tip length to ply thickness ratio, solution oscillation is known to occur [5]. Thus, an optimum range of mesh densities exists for obtaining converged solutions. For the 2-D DCB fatigue test, Krueger recommends using approximately six elements through the thickness of specimens and an element crack tip length between 0.25 mm (lower bound constrained by computational expense) and 1.67 mm. For this range of mesh densities, the maximum deviation of the solution from the converged benchmark is expected to be less than 10%, both in terms of the critical load at crack initiation and in terms of the subsequent crack growth behaviour.

For the static DCB test case modelled in Chapter 3, six elements were used through the thickness of the specimen. Mesh densities of 1,000 ($\Delta a = 1.500$ mm), 10,000 ($\Delta a = 0.150$ mm) and 113,000 elements ($\Delta a = 0.013$ mm) were used to examine the effects of mesh convergence. As expected, even the relatively coarse mesh of 1,000 elements achieved a solution within 9% of the converged simulation (113,000 elements), based on deviation of the critical load point. For the static test case, the 10,000 element model was chosen as the ideal comprise between solution accuracy (within 3% of the converged solution) and model simulation time (less than 15 mins.). A similar mesh density was employed for the ENF test case, with a 7,200 element mesh being used due to the smaller length of the ENF specimen (160 mm long as opposed to 250 mm long for the DCB specimen). This resulted in approximately the same crack tip element length for both the static DCB and ENF simulations.

Given the increased computational expense of fatigue simulations, where over 1×10^7 loads cycles were modelled, a reduced mesh density of 1,800 elements ($\Delta a = 0.833$ mm) was used for the DCB fatigue case. This drop in mesh density allowed an order of magnitude reduction in computational time when compared to the mesh density used for the static tests (10,000 elements), whilst keeping within the required element crack tip length range necessary for accurate implementation of the VCCT. A total of 2,240 elements were used for the thermal fatigue test case, with eight elements used through the thickness due to the non-standard test specimens used in the literature. The element crack tip length was 0.5 mm, again within the prescribed range and similar to the DCB fatigue test case. A denser mesh of 16,256 elements

was used for the FLM fatigue case. A total of four elements were used to model each ply in order to ensure accurate DCOD measurements. This corresponded to an element crack tip length of 0.005 mm. Although this element length is far below those used for the DCB, ENF and thermal test cases, the total specimen length of the FLM is 5 mm. Scaling the element crack tip length to the DCB test case dimensions (specimen length of 250 mm) would give an equivalent element length of 0.25 mm.

It should be noted that for all test cases examined in this work, the minimum mesh density required for accurate solution convergence (within 10% of measurable output) was determined, before increasing the mesh density until computational expense became the primary constraint. This approach was carried out in keeping with the general bounds of element sizes outlined in Krueger's VCCT benchmark.

A.3.3 Convergence controls

An initial time increment of 0.001 was used in simulations, based on recommendations from Krueger to ensure a prompt, yet accurate solution. In general, smaller time increments were found to yield more accurate crack propagation predictions due to the non-linear nature of the analyses. The downside of using small time increments is the corresponding increase in computation time. During the analyses in Chapter 3, dynamic cutback of the time increment was allowed, down to a minimum time increment of 1×10^{-12}. The general solution controls within the *Abaqus implicit* software were also modified to allow for a discontinuous analysis. Such an approach is recommended for complex crack growth problems [2]. The two time incrementation parameters, I_0 and I_R, were increased from there default values and have a direct effect on convergence. I_0 is the number of equilibrium iterations after which the check is made that the residuals are not increasing in two consecutive iterations. The value of this parameter was increased from 4 to 8. I_R is the number of equilibrium iterations after which the logarithmic rate of convergence check begins. The value of this parameter was increased from 8 to 10. The combined effect of increasing these parameters can also help to prevent premature cutbacks in time increment. I_A, the number of time increment cutbacks allowed for a given increment, was also increased from 5 to 20 to increase the chances of solution convergence.

These changes to the time increment convergence controls are not expected to affect the accuracy of the solutions presented in Chapter 3.

A.4 Materials and processing techniques

CF/PEEK is an advanced thermoplastic carbon-composite, widely used in the aerospace industry due to its superior properties. The composite consists of carbon fibres, on the order of 5 to 7 μm in diameter, embedded in a matrix of polyether ether ketone (PEEK). The carbon fibres give the composite its characteristic high strength and stiffness, while the matrix holds the fibres together. CF/PEEK is supplied as a raw material in the form of a pre-impregnated (pre-preg) tape, where the fibres are all aligned in the same direction. Given the extremely high aspect ratio of long-strand fibres, they generally only offer high strength and stiffness properties in a single direction, with matrix properties dominating in the out-of-plane directions. Therefore, multiple sheets, or plies, of pre-preg must be stacked to form laminates in order to achieve desirable multi-directional properties. Processing of these laminates can be carried out by methods including autoclave and automated tape-laying (ATL), both of which were used for this work.

Autoclave processing is widely used for manufacturing high performance composite structures. The equipment typically consists of a secure pressure vessel with an associated heat source. The method relies on the application of heat and pressure to a part placed in the autoclave in order to achieve consolidation of the plies. A major benefit of using an autoclave is the high part quality which is obtained, particularly in terms of a low void content and good resin distribution. However these come at the price of a large initial capital investment for the equipment, as well as high operating costs.

Three types of CF/PEEK from three different material suppliers were processed by autoclave for cryogenic cycling: (i) Suprem T/60%/IM7/PEEK/Victrex-150, (ii) Cytec APC-2 IM7 and (iii) Tencate CF/PEEK CETEX TC1200 AS4. The first two material use intermediate modulus IM7 carbon fibres, while Tencate uses AS4. The prepreg ply thickness for each material was approximately 0.14 mm. The Suprem

prepreg came in a roll 150 mm wide, while the Tencate and Cytec came in rolls 305 mm wide. Tables A.3 and compares the main properties of the fibres. Table A.4 provides manufacturers PEEK property data. Note, to the author's best knowledge, Victrex-150 is the matrix material used for Cytec APC-2 prepreg. The specific fibre surface treatments used for each material type are not available.

Table A.3 Comparison of carbon-fibre properties for the composites processed.

Property	AS4 [6]	IM7 [7]
Tensile Modulus (GPa)	231	276
Density (g/cm^3)	1.79	1.78
Filament Diameter (μ)	7.1	5.2
Specific Heat (cal/g°C)	0.27	0.21
Thermal Expansion (ppm/°C)	-0.63	-0.64
Thermal Conductivity (W/mK)	6.83	5.4

Table A.4 Comparison of PEEK properties for the composites processed.

Property	Cytec APC-2 [8]	Cetex MC1200 [9]	Victrex-150 [10]
Tensile Strength (MPa)	100	100	100
Tensile Modulus (GPa)	3.6	3.7	3.7
Flexural Modulus (GPa)	4.1	4.1	4.1
Glass transition temperature (°C)	143	143	143
Melt Viscosity (Pa.s)	N/A	N/A	130 (@400 °C)

Identical sets of rectangular laminates measuring 150 mm × 70 mm for each material type were laid-up by hand at ÉireComposites Teo (Indreabhán, Ireland). Prior to being processed in the autoclave, a polyimide film was placed over the laminates. Custom cut metal caul plates were cut to the laminate dimensions and then placed over the film above each laminate. The caul plates were made from mild steel to limit the mismatch in thermal expansion with the composite laminates. The laminates and caul plates were then sealed in a vacuum bag and placed under

vacuum (atmospheric pressure). The caul plates transmit a normal pressure to the surface of the laminate and ensure a smooth part surface. The vacuum was kept in place for the duration of processing. Several thermocouples were also placed within the vacuum bag to monitor the temperature during processing. Up to 6 parts at a time were then sealed in the autoclave, as shown in Fig. A.4.
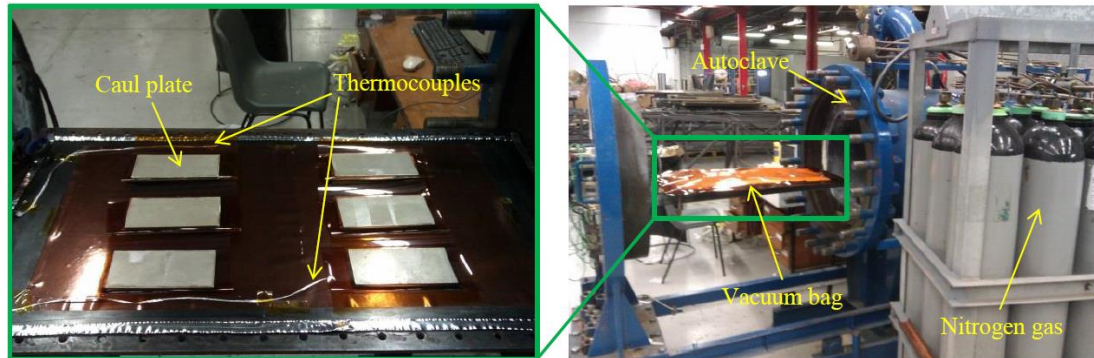

Figure A.4 Autoclave processing of composite laminates at ÉireComposites Teo.

Nitrogen gas was used to increase the pressure acting on the vacuum bag while the parts were heated to a temperature of 385 °C for the Cytec and Tencate materials and 375 °C for the Suprem material. The laminates were held at processing temperature at a pressure of approximately 6.5 bar. for 25 minutes in order to ensure full consolidation. The average cooling rate and peak cooling rate were 3.8 °C/min and 4.9 °C/min respectively. Upon removal from the autoclave, the laminates underwent ultrasound testing to ensure no major defects were present. Each laminate was then partitioned into 6 individual specimens of size 34 mm × 27 mm using a water-jet, as shown in Fig. A.5. A compact specimen size was chosen in order to facilitate detailed non-destructive testing. The crystallinity level for the specimens was not directly measured; however, previous measurements on similarly processed autoclave specimens gave crystallinity levels of approximately 35%.
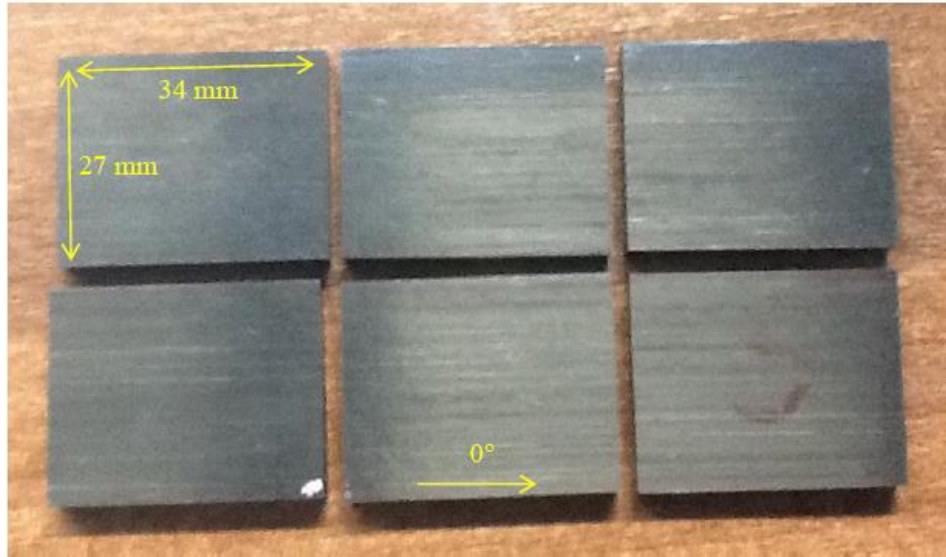
Figure A.5 CF/PEEK specimens cut from an autoclaved laminate.

ATL is a relatively new method of out-of-autoclave processing of composite materials based on the in-situ consolidation of plies. In the case of thermoplastic composites such as CF/PEEK, this means that the material lay-up and bonding can occur simultaneously. Given that the process is fully automated, significant labour and time savings are possible by using this method. ATL is carried out by a computer controlled robot which typically applies pre-preg tape to a heated mould placed on a revolving mandrel. Thus, the technique is well suited to producing components such as pressure vessels. Like autoclave processing, heat and pressure are used to consolidate the plies. However, consolidation occurs at a point, specifically where the head of the robot is placed, as opposed the entire laminate simultaneously, as shown in Fig. A.6.
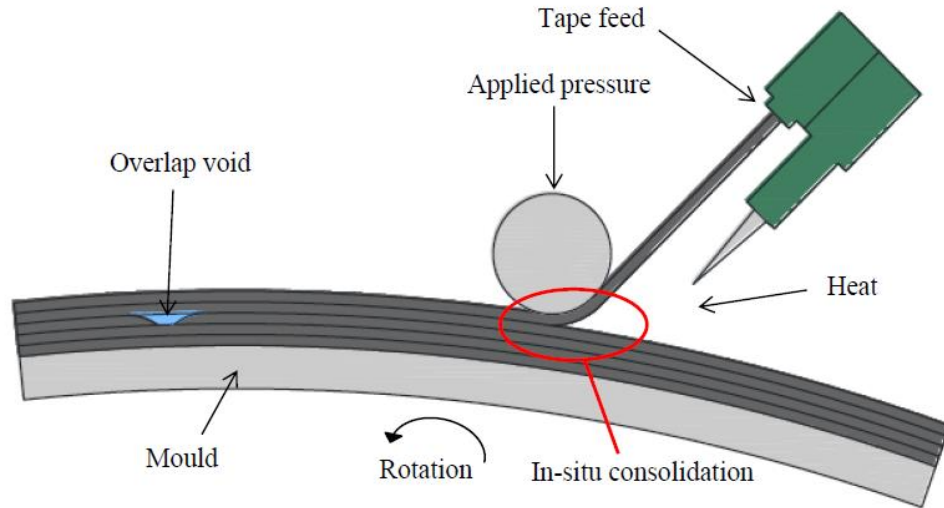
Figure A.6 Schematic of the ATL process showing in-situ ply consolidation.

The main drawbacks of this technique include the potential for poor ply adhesion due to insufficient bond time and the presence of significant residual stress gradients due to non-uniform cooling. The laying process itself can also result in gaps due to overlapping plies which can result in high void contents. These issues can often lead to composite laminates of a lower general quality than those produced in an autoclave. The tape laid specimens used in this work were manufactured at the University of Limerick in conjunction with ÉireComposites Teo and ICOMP using the ATL robot shown in Fig. A.7. A tape-grade version of the intermediate modulus Suprem T/60%/IM7/PEEK/150 was used for the ATL specimens. Consolidation is achieved using a 3,000 W laser-line diode laser module, with parts up to 2 m in diameter being catered for.
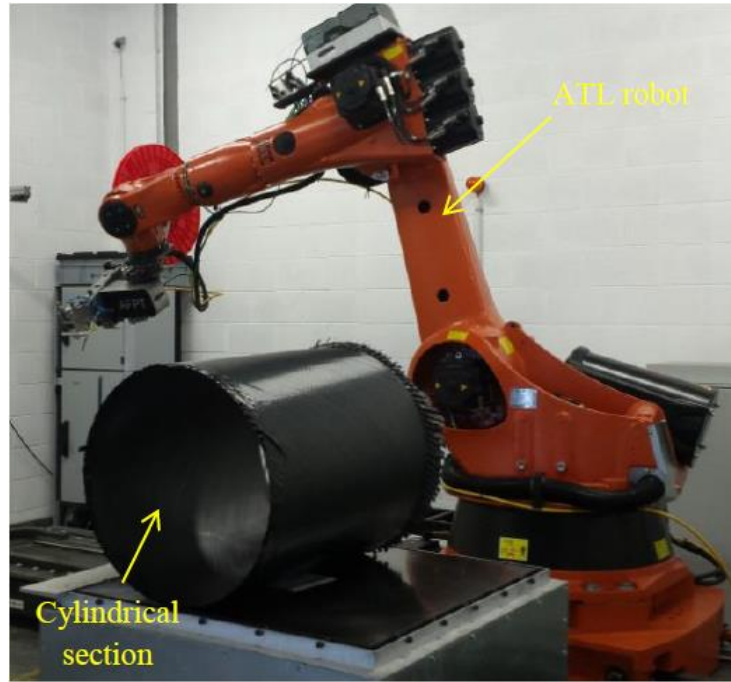
Figure A.7 The ICOMP ATL robot used to manufacture the tape-laid specimens used in testing. Shown is a 500 mm diameter CF/PEEK cylinder.

Specimens from both flat-plate laminates and cylindrical sections were extracted for testing. The flat-plate laminate was sectioned into rectangular coupons 34 mm × 27 mm, similar to the autoclave specimens shown in Fig. A.5. Uni-directional and quasi-isotropic cylindrical sections, shown in Fig. A.8, were also extracted from 500 mm diameter cylinders in order to investigate the effect of part geometry on processing defects and damage formation.
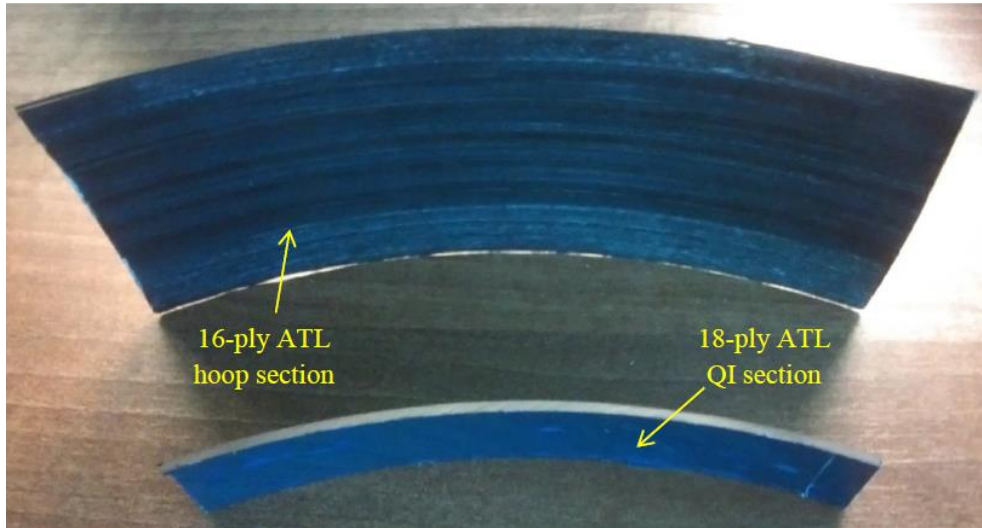
Figure A.8 CF/PEEK cylindrical sections manufactured using the ATL robot.

A.5 Cryogenic cycling

CF/PEEK laminates were cryogenically cycled in order to simulate the thermal fatigue loading experienced by fuel tank materials used in RLVs due to multiple refuellings. Observing and quantifying physical damage accumulation in cycled laminates provides the basis for detailed FE damage simulations and subsequent predictions of laminate permeability. Test specimens were cycled manually and automatically via direct immersion in a cryogen as well as by controlled cooling of a single specimen to cryogenic temperatures.

Manual cycling was carried out in order to investigate crack initiation and growth in laminates due to direct immersion in a cryogenic liquid. Testing took place at ESTEC, allowing access to the aforementioned specialised NDT equipment for continuous specimen damage monitoring. Due to cost and safety concerns associated with using open containers of LH_2 and LO_2, LN_2 (liquid nitrogen) was used to represent the contents of a RLV fuel tank for cryogenic cycling. LN_2 is widely used in many industrial applications and can be sourced in large quantities at a relatively low cost. It has a boiling point between that of LH_2 and LOX at -196 °C, allowing a realistic approximation of the cryogenic cycle which occurs during the fuelling process. The cryogenic cycle consisted of immersing a batch of the specimens directly into an open Dewar of LN_2 before placing them in warm air flow at 40 °C

from a fan, giving a total ΔT of -236 °C. This cycle was carried out a total of 50 times for all specimens during the course of manual testing. In order to accurately trace the thermal history of cycled laminates, a thermocouple was embedded in the centre of a cryogenically cycled 8-ply CF/PEEK laminate at ÉireComposites Teo, as shown in Fig. A.9.
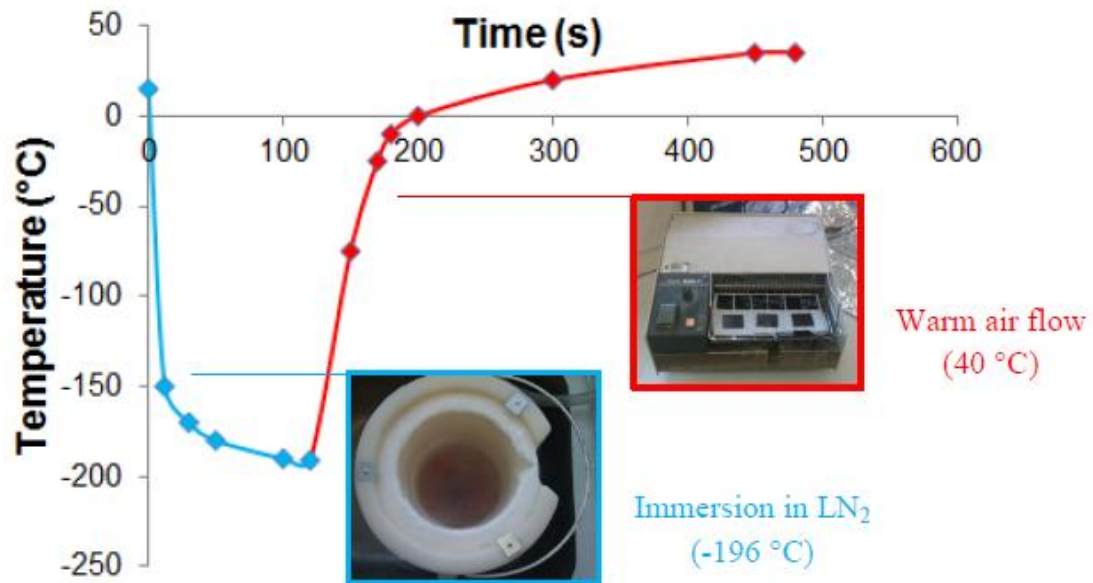

Figure A.9 Cryogenic cycle of an 8-ply CF/PEEK laminate immersed in LN_2 and heated in a warm air flow.

In order to continue the cryogenic cycling of the specimens beyond the initial 50 manual cycles, an automated fatigue rig was commissioned at NUI Galway. The aim of this project was to examine damage growth at several hundred fatigue cycles, with minimal interaction required in the cycling process. Automation of the manual process required development of an electro-mechanical system to reliably cycle specimens over extended periods of time.

The main components of the fatigue rig are shown in Fig. A.10 and include:

— LN_2 Dewar

— Specimen holder

— Stepper motor and pulley system

— Arduino Uno microcontroller

— Thermocouple and thermal amplifier

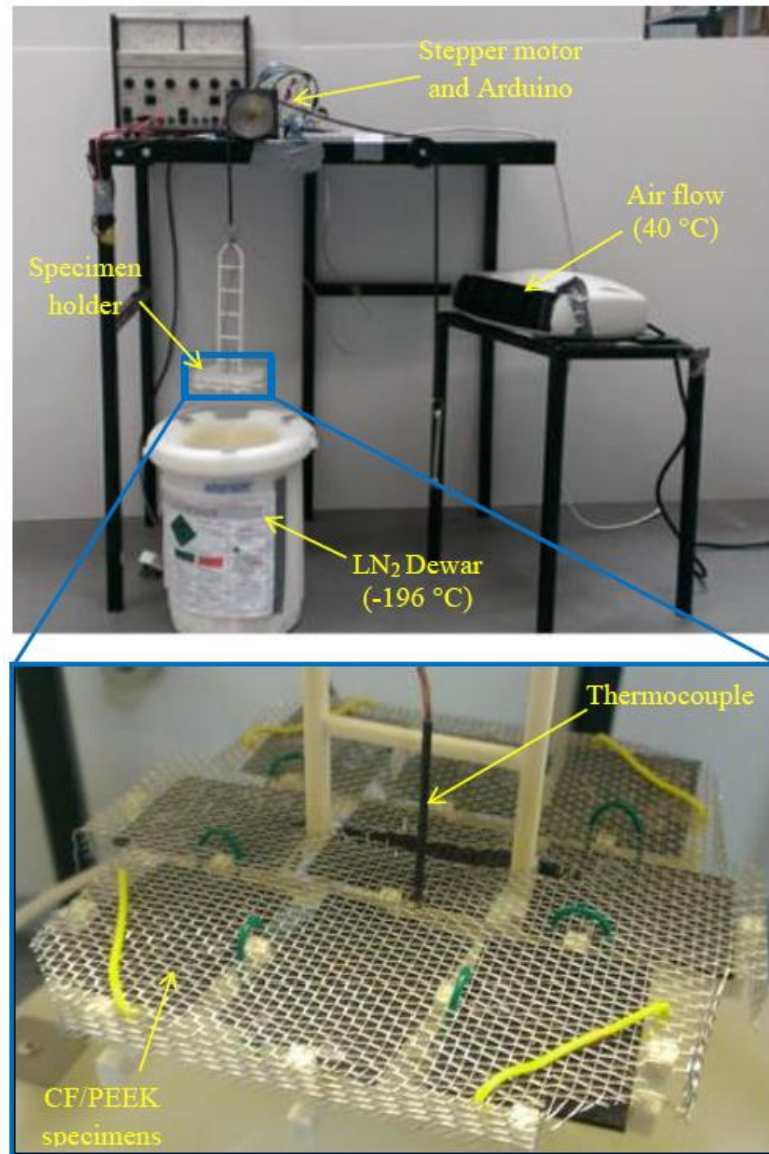— Heating fan and direct control socket

Figure A.10 The automated cryogenic fatigue rig developed at NUI Galway for cycling of CF/PEEK laminates.

The thermal history of both manually and automatically cycled laminates was identical, with specimens being directly immersed in LN_2 before being heated in an air flow of 40 °C. The rig facilitated up to 9 specimens to be cycled simultaneously,

whilst being held in a custom made 3-D printed Nylon specimen container. The holder was designed to keep the specimens well-spaced apart for consistent heat transfer between the laminates and the cryogen. The use of light-weight Nylon in place of a metallic material ensured minimal LN_2 boil-off during cycling, increasing the rig operation time between Dewar refills.

A stepper motor and pulley system, controlled by an Arduino Uno, was used to raise and lower the specimen holder between the Dewar and the warm air flow provided by the heater. The dwell position and times were pre-programmed, with thicker specimens requiring extended hold times during the cooling and heating phases. In order to ensure reliable unattended operation of the system, a thermocouple was connected to the specimen holder, allowing the temperature trace for each cycle to be logged on an adjoining desktop computer. Depending of the specimen thickness, between 6 and 24 cryogenic cycles could be carried out before the 4 litre Dewar had to be manually refilled. Despite some specimens being exposed to an additional 250 cycles, no further microcracking or delamination was detected.

A.6 Non-destructive testing

Understanding damage initiation and growth in CF/PEEK test specimens is essential to the development of accurate predictive models. Material and damage characterisation were carried out before, during and after cryogenic cycling of the CF/PEEK laminates using two non-destructive testing (NDT) techniques: optical microscopy and 3-D X-ray computed tomography (CT). These techniques allow a material to be inspected in detail without altering the physical attributes of the test specimen, providing an insight into the basic structure of the laminates as well as damage formation.

Optical microscopy is based on the reflection of visible light from the surface of a specimen. Detailed, high magnification micrographs of composite cross-sections can be obtained using this technique. Microscopy is widely used in the characterisation of composite materials and can be helpful in determining void and resin contents as well as monitoring damage growth. In particular, micrographs offer unrivalled clarity

when viewing a composite cross-section, allowing for accurate crack opening displacement and crack density measurements. A highly reflective and smooth surface is required for inspection, meaning careful specimen preparation is required.

Prior to cryogenic cycling, specimens were prepared for optical microscopy by a procedure involving the grinding, polishing and cleaning of laminate sides. The specimens were first mounted in quick-set epoxy resin holders in order to ensure a level surface when grinding and polishing, as shown in Fig. A.11.
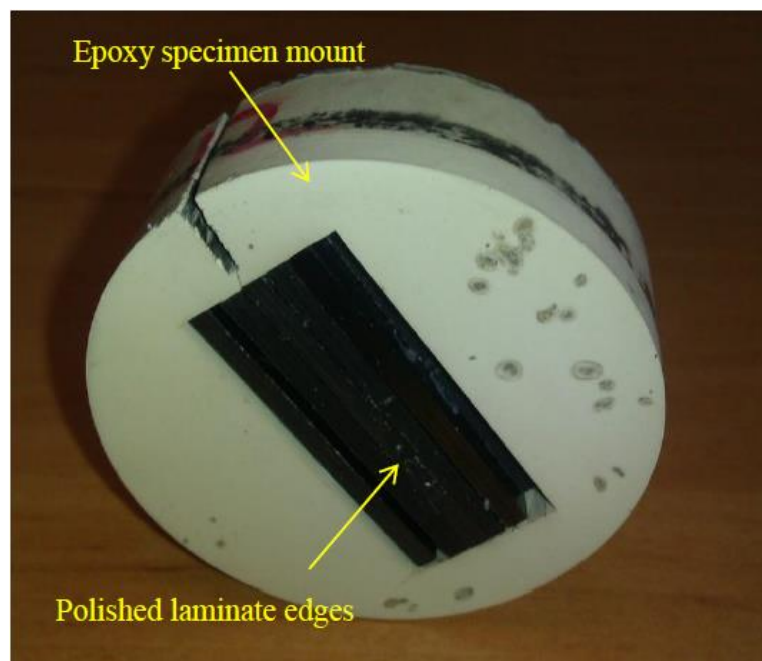

Figure A.11 CF/PEEK laminates set in an epoxy mount with sides exposed for grinding and polishing.

The specimens were hand ground using successively finer grit paper ranging from P180 to P2400, before being machine polished on cloth using diamond solutions ranging from 6 μm to 0.25 μm. The specimens were thoroughly cleaned with water, soap solution and isopropyl alcohol between each grinding and polishing stage. The sides were viewed before and during cycling, under magnifications ranging from 12.5× to 200×, in order to characterise the internal structure of the laminates and to observe subsequent crack growth. The effect of the grinding and polishing procedure on a laminate edge is shown in Fig. A.12.
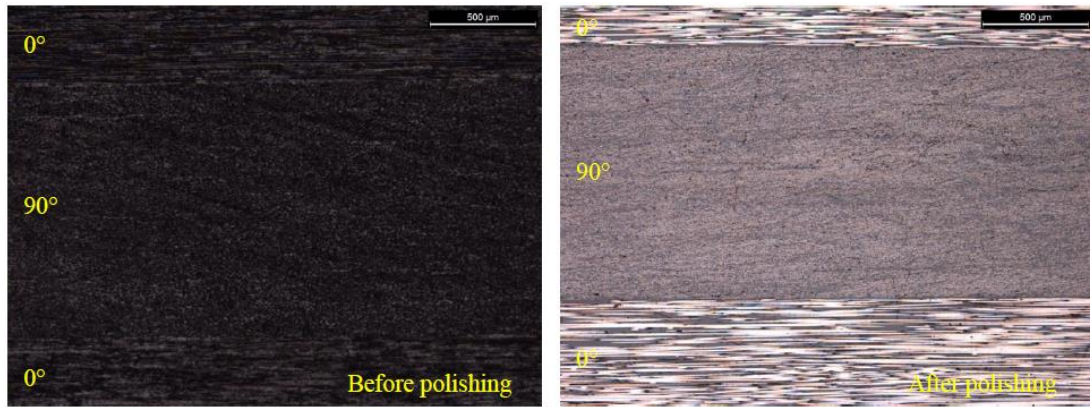
Figure A.12 The difference in surface reflectivity for a CF/PEEK sample before and after polishing.

3-D X-ray CT is increasingly becoming a viable testing technique due to technological advances and reduction in equipment costs. This technique allows a full 3-D characterisation of the damage modes within a specimen, as well as void and defect identification by isolating the various phases within a material, including air gaps. This capability provides a platform for direct comparison with 3-D FE damage simulations, giving unprecedented insight into crack network formation within laminates and simplifying model calibration and validation. In this work, 3-D X-ray CT has been used to quantitatively analyse defects present in CF/PEEK laminates and to observe damage formation during and after cryogenic cycling.

X-ray CT is a NDT technique which can be used to view the internal structure of an object without physically opening it. The main components of an X-ray CT system are the X-ray source, the X-ray detector and a rotating holder for the specimen to be scanned. The fundamental principle of operation is the attenuation of X-rays as they pass from the source through the various substances within an inhomogeneous object. The difference in X-ray intensities can then be detected via scintillators. For instance, within a composite material the fibre and matrix phases will absorb a different amount of the X-rays passing through them, allowing the distinct phases of the material to be identified. Fig. A.13 shows the main components in an X-ray CT system.
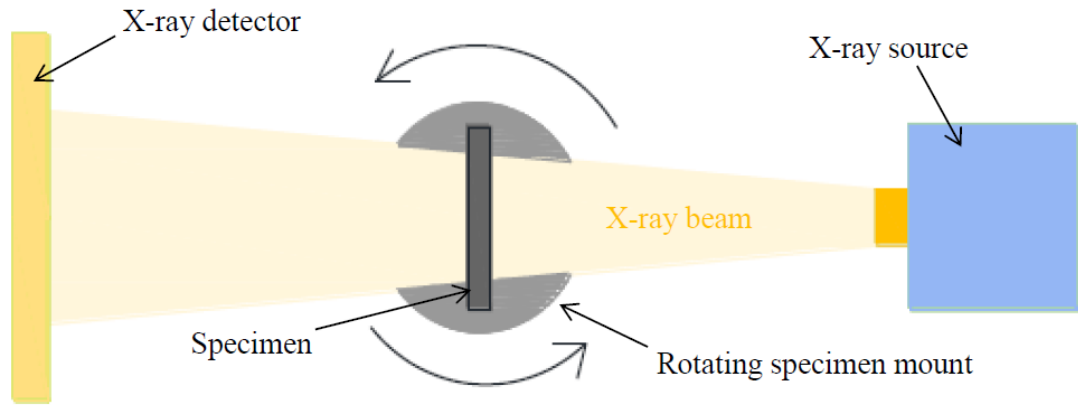
Figure A.13 Main components of an X-ray CT system with a stationary source and rotating specimen.

The specimen is incrementally rotated through 360° whilst 2-D radiographic images are taken, providing a sliced view through the scanned object. High-performance computing techniques are then used to generate tomographic images and to reconstruct them into a 3-D representation of the specimen. Volume rendering and subsequent analysis of the internal structure can then be carried out. Unlike optical microscopy, X-ray CT does require any specific specimen preparation before scanning. Fig. A.14 shows the main steps in the generation of a 3-D image from the initial 2-D scans.
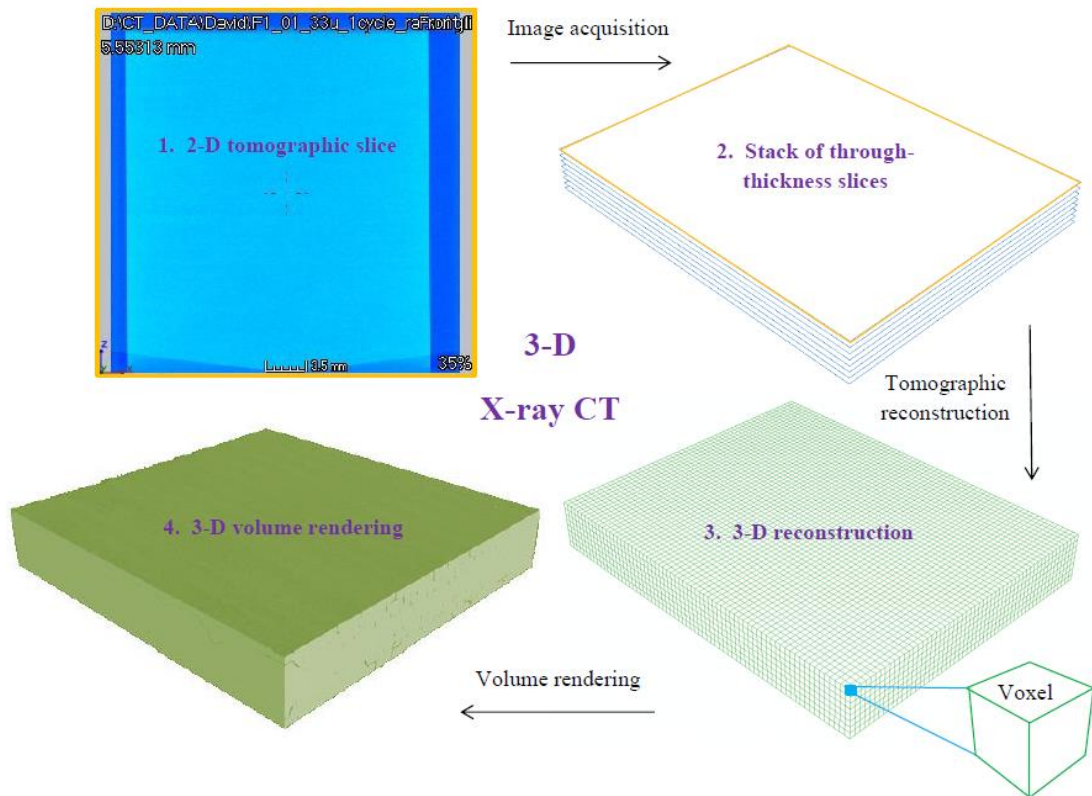
Figure A.14 The main steps involved in the generation of 3-D images from 2-D tomographic slices.

A GE Phoenix M nano/microtom, based in the European Space Research and Technology Centre (ESTEC, The Netherlands), was used to scan the CF/PEEK laminates before, during and after cryogenic cycling. The X-ray gun, or source, was rated at 180 kV, with scans being carried out at 160 kV and 28 μA, giving a scan power of 4.5 W. A total of 1,000 tomographic images were generated for each scan over a 360° field of view, for a total scan time of 67 minutes. The tomographical reconstruction was carried out using Davos software, whilst volume rendering was completed using *VGStudio MAX 2.2* (Volume Graphics GmbH, Germany). Two primary scan resolutions were used in this study: 15 μm and 33 μm. The scan resolution is related to the minimum length scale discernible in the resulting reconstruction. For 3-D images this would correspond to voxels, or 3-D pixels, of side 15 μm and 33 μm respectively. Although the voxel is the base unit of a 3-D reconstruction, advanced rendering techniques allow prediction of phase changes within a voxel, based on the status of the connecting voxels. However, features are generally only discernible using this technique if one of their dimensions exceeds the

scan resolution, as is the case with narrow but long transverse microcracks or elongated, ellipsoidal inter-ply voids.

A.7 Weibull distribution Python script

The following is the Python script used to distribute random Weibull fracture strengths to elements within a finite element mesh, as described in Chapter 5. The script can be used to ensure proper implementation of the volume adjusted distribution by outputting a list of low fracture strength elements. This allows the number of low strength elements below a given threshold to be compared across multiple simulations to ensure consistent crack density results for a specific mesh density.

```
from abaqus import *
from abaqusConstants import *
import random
import regionToolset
aModel=mdb.models['']
aPart=aModel.parts['']
i=
print '*****************************'
for eachElement in aPart.elements:
        elSeq=aPart.elements.sequenceFromLabels(labels=(eachElement.label,),)
        region = regionToolset.Region(elements=elSeq)
        i=i+1
        MaterialName = 'Material-' + str(i)
        SectionName = 'section-' + str(i)
        aModel.Material(name= MaterialName)
        fs = random.weibullvariate( , )
        if fs > :
         fs =
        if fs < :
         print fs
        aModel.materials[MaterialName].Elastic(type=ENGINEERING_CONSTANTS, table=(( , ,
 , , , , , , ), ))
        aModel.materials[MaterialName].MaxsDamageInitiation(direction= ,table=(( , , ), ))
        aModel.materials[MaterialName].maxsDamageInitiation.DamageEvolution(
    type=ENERGY, mixedModeBehavior= , power= , table=(( , ,
    ), ))
        aModel.materials[MaterialName].maxsDamageInitiation.DamageStabilizationCohesive(
    cohesiveCoeff= )
        aModel.HomogeneousSolidSection(name=SectionName,            material=MaterialName,
thickness=None)
        aPart.SectionAssignment(region=region, sectionName=SectionName, offset=0.0,
                        offsetType=MIDDLE_SURFACE, offsetField='',
                        thicknessAssignment=FROM_SECTION)
```

A.8 Appendices references

[1] Kumar A., Gopalakrishnan S. & Chakraborty A. Modified virtual crack-closure technique using spectral element method. International Journal of Computational Methods, 4(1), 109-139, 2007.

[2] Hibbitt, Karlsson & Sorensen. *Inc. ABAQUS/Standard User's Manual, v. 6.11.* Pawtucket, Rhode Island, 2011.

[3] Kilroy J. New carbon fibre/PEEK composites for space applications final test report. Doc. No. 02/025. CTL Tástáil Teo, Indreabhán, Co. Galway, Ireland, 2006.

[4] Krueger R. Development of a benchmark example for delamination fatigue growth prediction. NIA Report No. 2010-04. National Institute of Aerospace, Hampton, Virginia, 2010.

[5] Camanho P.P., Dávila C.G. & Ambur D.R. Numerical simulation of delamination growth in composite materials. NASA/TPN-2001-211041. National Institute of Aerospace, Hampton, Virginia, 2001.

[6] Data from Hexcel Corporation. Available online at:
http://www.hexcel.com/resources/datasheets/carbon-fiber-data-sheets/as4.pdf
Accessed August 2014.

[7] Data from Hexcel Corporation. Available online at:
http://www.hexcel.com/resources/datasheets/carbon-fiber-data-sheets/im7.pdf
Accessed August 2014.

[8] Data from Cytec. Available online at:
http://www.cemselectorguide.com/pdf/APC-2_PEEK_031912.pdf Accessed August 2014.

[9] Data from Tencate Advanced Composites. Available online at:
http://www.tencate.com/emea/Images/MC1200_DS_Web28-23482.pdf Accessed August 2013.

A. Appendices

[10] Data from Victrex. Available online at:

http://www.materialdatacenter.com/ms/en/Victrex/Victrex+plc/VICTREX%C2%AE+PEEK+150G/4a0ac74c/2553 Accessed August 2014.